AFRL-RY-WP-TR-2012-0331

ENHANCED PERFORMANCE & FUNCTIONALITY OF TUNABLE DELAY LINES

Alan E. Willner

University of Southern California

AUGUST 2012
Final Report

AIR FORCE RESEARCH LABORATORY
SENSORS DIRECTORATE
WRIGHT-PATTERSON AIR FORCE BASE, OH 45433-7304
AIR FORCE MATERIEL COMMAND
UNITED STATES AIR FORCE

NOTICE AND SIGNATURE PAGE

Using Government drawings, specifications, or other data included in this document for any purpose other than Government procurement does not in any way obligate the U.S. Government. The fact that the Government formulated or supplied the drawings, specifications, or other data does not license the holder or any other person or corporation; or convey any rights or permission to manufacture, use, or sell any patented invention that may relate to them.

This report was cleared for public release by the USAF 88th Air Base Wing (88 ABW) Public Affairs Office (PAO) and is available to the general public, including foreign nationals. Copies may be obtained from the Defense Technical Information Center (DTIC) (http://www.dtic.mil).

AFRL-RY-WP-TR-2012-0331 HAS BEEN REVIEWED AND IS APPROVED FOR PUBLICATION IN ACCORDANCE WITH ASSIGNED DISTRIBUTION STATEMENT.

*//Signature//

KENNETH L. SCHEPLER
EO CM Technology Branch
Multispectral Sensing & Detection Division

//Signature//

JOHN F. CARR, Chief
EO CM Technology Branch
Multispectral Sensing & Detection Division

//Signature//

TRACY W. JOHNSTON
Multispectral Sensing & Detection Division
Sensors Directorate

This report is published in the interest of scientific and technical information exchange, and its publication does not constitute the Government's approval or disapproval of its ideas or findings.

*Disseminated copies will show "//Signature//" stamped or typed above the signature blocks.

REPORT DOCUMENTATION PAGE

Form Approved
OMB No. 0704-0188

1. REPORT DATE *(DD-MM-YY)*	2. REPORT TYPE	3. DATES COVERED *(From - To)*
August 2012	Final	5 March 2008 – 5 June 2012

4. TITLE AND SUBTITLE
ENHANCED PERFORMANCE & FUNCTIONALITY OF TUNABLE DELAY LINES

5a. CONTRACT NUMBER
FA8650-08-1-7820

5b. GRANT NUMBER

5c. PROGRAM ELEMENT NUMBER
62716E

6. AUTHOR(S)
Alan E. Willner

5d. PROJECT NUMBER
ARPR

5e. TASK NUMBER
YJ

5f. WORK UNIT NUMBER
Y0HB

7. PERFORMING ORGANIZATION NAME(S) AND ADDRESS(ES)
University of Southern California INC
Dept. of Contracts and Grants
University Gardens Ste 203
Los Angeles, CA 90089-0001

8. PERFORMING ORGANIZATION REPORT NUMBER
AFRL-RY-WP-TR-2012-0331

9. SPONSORING/MONITORING AGENCY NAME(S) AND ADDRESS(ES)
Air Force Research Laboratory
Sensors Directorate
Wright-Patterson Air Force Base, OH 45433-7320
Air Force Materiel Command
United States Air Force

10. SPONSORING/MONITORING AGENCY ACRONYM(S)
AFRL/RYMWA

11. SPONSORING/MONITORING AGENCY REPORT NUMBER(S)
AFRL-RY-WP-TR-2012-0331

12. DISTRIBUTION/AVAILABILITY STATEMENT
Approved for public release; distribution unlimited.

13. SUPPLEMENTARY NOTES
This work was funded in whole or in part by Department of the Air Force contract FA8650-08-1-7820. The U.S. Government has for itself and others acting on its behalf an unlimited, paid-up, nonexclusive, irrevocable worldwide license to use, modify, reproduce, release, perform, display, or disclose the work by or on behalf of the U.S. Government. PAO Case Number 88ABW-2012-5927, Clearance Date 7 November 2012. Report contains color.

14. ABSTRACT
We demonstrated dramatic enhancements in the performance and functionality of tunable optical delay lines. We used tunable wavelength conversion combined with inter-channel chromatic dispersion and intra-channel dispersion compensation to achieve continuously tunable optical delays. Extremely long delays at very high bit-rates were demonstrated with minimal data distortion. We demonstrated delays for different data modulation formats, including on-off-keying and spectrally efficient DQPSK (differential - quadrature-phase-shift-keying .We used: (i) low dispersion slope, highly nonlinear fiber to achieve wide-bandwidth wavelength conversion based on four-wave mixing and (ii) a highly dispersive element with low dispersion slope to introduce a large linear change in time delay as a function of wavelength. Since the dispersive element also introduces data-destroying intra-channel chromatic dispersion, we made use of spectrally efficient DQPSK which increased the tolerance to all orders of dispersion. We demonstrated that tunable optical delays can potentially be used in a dynamic, reconfigurable, and heterogeneous optical system.

15. SUBJECT TERMS
telecommunications, nonlinear optics

16. SECURITY CLASSIFICATION OF:			17. LIMITATION OF ABSTRACT:	18. NUMBER OF PAGES	19a. NAME OF RESPONSIBLE PERSON (Monitor)
a. REPORT	b. ABSTRACT	c. THIS PAGE			Kenneth L. Schepler
Unclassified	Unclassified	Unclassified	SAR	144	19b. TELEPHONE NUMBER *(Include Area Code)* N/A

Table of Contents

List of Figures

List of Tables

1. Summary

We have demonstrated dramatic enhancements in the performance and functionality of tunable optical delay lines. Fundamentally, we used tunable wavelength conversion combined with inter-channel chromatic dispersion and intra-channel dispersion compensation to achieve continuously tunable optical delays. Extremely long delays at very high bit-rates were demonstrated with minimal data distortion that met the

Parametric Optical Processes and Systems (POPS) program goals. We also demonstrated delays for different data modulation formats, including on-off-keying (OOK) and spectrally efficient differential-quadrature-phase-shift-keying (DQPSK).

We used: (i) low dispersion slope, highly nonlinear fiber (HNLF) to achieve wide-bandwidth wavelength conversion based on four-wave mixing (FWM), and (ii) a highly dispersive element with low dispersion slope to introduce a large linear change in time delay as a function of wavelength. Since the dispersive element also introduces data-destroying intra-channel chromatic dispersion, we mitigated dispersion in order to achieve a low bit-error-rate (BER). Towards this end, we made use of spectrally efficient DQPSK which increased the tolerance to all orders of dispersion.

In general, we studied various high-data-rate signal-processing applications that make use of POPS-enabled tunable optical delays. We demonstrated that tunable optical delays can potentially be used in a dynamic, reconfigurable, and heterogeneous optical system.

Table 1 shows a comparison of the program milestones and the achievements

Table 1 Comparison of achievements to program milestones.

	Milestone	Results
Multicasting at 40 Gb/s	16x	24x (OOK) 7x (DQPSK) 8x (DPSK) 8x (Pol-Mux OOK)
Optical Amplifier Bandwidth	200 nm	203 nm
Maximum Delay	3 μs	3.6 μs (100 Gb/s)
Data Multiplexing	16 by 40 Gb/s to 1 by 640 Gb/s	16 by 40 Gb/s to 1 by 640 Gb/s 8 by 40 Gb/s to 1 by 320 Gb/s
Demultiplexer Granularity	10 Gb/s	640 Gb/s to 10 Gb/s
Sampling Resolution and Jitter	100 fs and 50 fs	100 fs and 30 fs
System Performance	1E-9	1E-9

2. Introduction

Signal processing is a powerful enabler and performance enhancer for a host of communications functions, and performing processing in the optical domain reduces any optical-electronic conversion inefficiencies. One of the most basic elements needed to achieve efficient and high throughput signal processing is a continuously-tunable optical delay line, and yet this element has historically been difficult to realize. Applications of such a delay line include: (a) accurate synchronization for bit-level interleaving, (de)multiplexing and time switching, and (b) data packet synchronization, switching, time-slot interchange, and buffering. Moreover, a continuous tuning capability enables signal processing for heterogeneous, variable bit-rate systems. A partial "wish list" of tunable-delay attributes include: (i) wide bandwidth, (ii) amplitude, frequency, and phase preservation (i.e., modulation format independent), and (iii) high dynamic range. Such delays provide flexible time domain data grooming in the optical domain.

At its core, many of the key goals of the entire POPS program can be critically affected and dramatically enhanced by significant advancements in the ability to have continuously tunable optical delay subsystems over large dynamic ranges and while accommodating extremely high bit rates. The absence of such a capability would substantially impair the overall efficiency and performance of any data processing. Historically, optical delays were based on switching between a discrete set of different path lengths, which do not provide the ability to continuously tune the delay. The delay granularity of such an approach is fine for low bit rates, such that a small fraction of a bit time at 1 Gb/s is still > 1 cm long. However, the granularity required in the differential path lengths for a 1 Tb/s would be an extremely challenging mere ~10 μm. Therefore, highly accurate and continuously tunable delays are of great value, and extremely fast optical nonlinear properties can achieve this.

In this POPS program, we have demonstrated dramatic enhancements in the performance and functionality of continuously tunable optical delay lines.

3. Methods, Assumptions, and Procedures

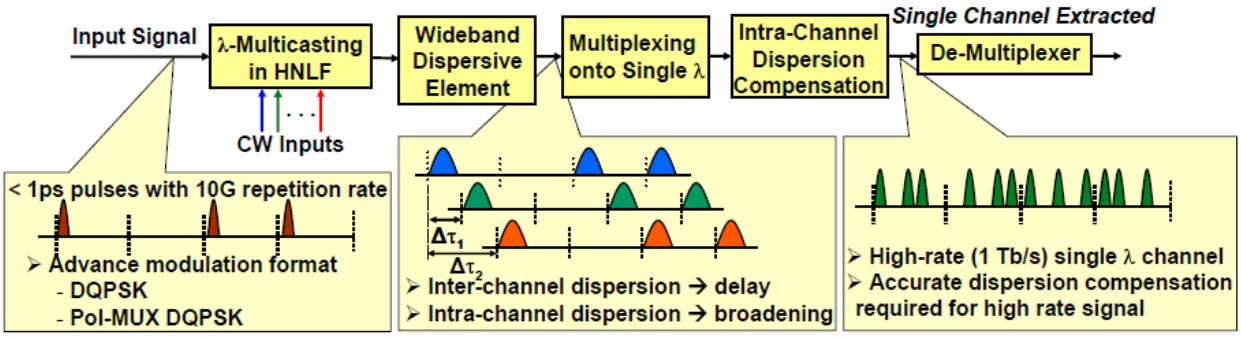

Figure 1. Block diagram of optical multiplexing using wide BW tunable delay lines

Figure 1 shows a system level block diagram of the method by which this high-rate multiplexed channel will be generated. Signal multicasting is a process in which the information of an input signal is copied to many new wavelengths. When the delays between the multicast copies are appropriately selected, the result is a high-rate pseudo random bit sequence (PRBS). To obtain PRBS data, the copies must have integer number of delays of Tword/M, where Tword is the length of the PRBS word and M is the number of multicast signals. The temporal length of a PRBS word is given by (2N-1)*Tbit, where N is the PRBS order (e.g. 7, 15, 31) and Tbit is the duration of a bit. The maximum achievable length of the PRBS sequence is limited by the maximum achievable delay. We point out that current electronic pattern generators which use a split / delay / combine method are presently limited to ~100 Gb/s rate PRBS generation. The advanced delays of the work reported here will enable optical PRBS generators reaching 1 Tb/s in data rate, corresponding to an order of magnitude increase over today's electronic systems.

Our scheme consists of the following blocks:

Signal Generation: A narrow pulse width laser source modulated by 40 GHz data. To meet the demanding goals of this program, OOK along with other more advanced modulation formats have been used, including multi-level phased-based modulation formats, such as DQPSK. Additionally, we will utilize polarization multiplexing as a method to achieve high single channel data rates with higher spectral efficiency. These allowed for broader pulse widths due to the decreased symbol rate, thereby increasing tolerance to chromatic dispersion and intra-channel nonlinearities.

Multicasting: A multi-caster to create copies of the original data onto multiple (up to 32) wavelength channels using four-wave mixing (FWM) in highly nonlinear fiber. HNLF with high nonlinear coefficient and low dispersion slope were required to meet the program goals of FWM efficiency flatness versus wavelength and noise figure.

Parametric Amplification: A wide-bandwidth fiber optical parametric amplifier (FOPA), with bandwidth extending up to 300 nm and gain of at least 20 dB.

Delay via Dispersion: A highly dispersive element to impose a relative delay between the different multicast channels through inter-channel dispersion. To limit the amount of intra-channel dispersion (i.e. dispersion over the bandwidth of an individual channel) a dispersive element with low dispersion slope was required.

Multiplexing (serializer): A multiplexer (also referred to as a serializer) to convert each of the

wavelength channels with different relative delays onto a single high-rate channel. The multiplexing was performed using four-wave mixing in HNLF.

Dispersion Compensation: The dispersive delay element can result in intra-channel dispersion (i.e. dispersion within a single channel). At extremely high bit rates, 3rd and 4th order dispersion are no longer negligible and must be accurately compensated. Moreover, polarization effects such as polarization-mode-dispersion (PMD) become acute at these high rates and were addressed in support of the proposal.

Demultiplexing (deserializer): In order to measure BER, a demultiplexer (also referred to as a deserializer) was required. This demultiplexer can utilize the fast response time of four-wave mixing in highly nonlinear fiber. Super-continuum generation could be necessary to achieve the 100 fs pulse widths required for >640 Gb/s.

3.1. Components of Delay Module

3.1.1 Signal Generation

Achieving high data rates approaching 1 Tb/s in an optical time division multiplexed (OTDM) system requires a transmitter capable of producing narrow pulses at a sub-rate that is still relatively high. Even when composed of 32 sub-channels, a 1 Tb/s system still requires a subrate of ~40 Gb/s. At 1 Tb/s, each data bit must occupy <1 ps for an OOK signal using 1 bit/symbol. We used a mode locked laser (MLL), whose pulses can be externally modulated [14]. Fig. III.A.7 shows the transmitter for generating 40 GHz modulated data. A MLL with 10 GHz repetition rate gives ~1 ps pulses which are compressed using an optical pulse compressor. To increase the repetition rate from 10 to 40 GHz, a fiber delay-line multiplexer is used. Finally, data is modulated onto the optical pulse train at a rate of 40 Gb/s. As will be discussed, various modulation formats were used.

A pulsed source is also necessary to drive the demultiplexer and extract a lower rate channel from a multiplexed high-rate channel. The requirements on the demultiplexer pulsed source are more stringent when compared to the transmitter.

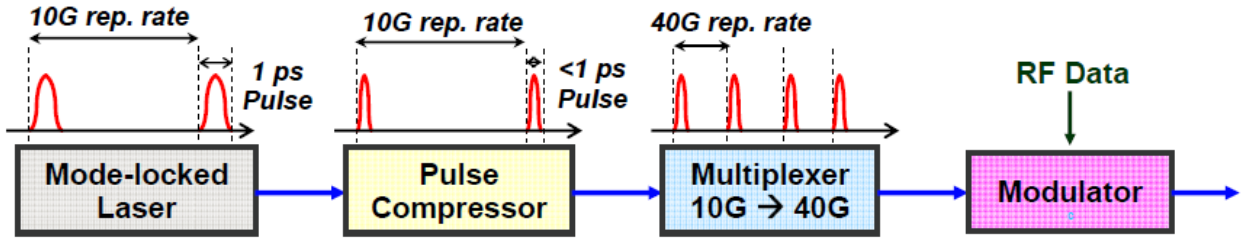

Figure 2. Block diagram of transmitter for generating narrow pulse width, 10 or 40 GHz repetition rate, modulated signals

Our laboratory at USC uses a tunable pulse compressor that can achieve compression down to 250 fs, exceeding the phase I requirement and coming close to the phase II requirement. Note that the spectral width further increases after pulse compression and places a limit on how close multicast channels can be located. Furthermore, the tolerance of the signal to residual dispersion is greatly reduced due to the wide spectral BW. This decreased tolerance motivates the use of spectrally-efficient modulation formats.

Return-to-Zero Differential Quadrature-Phase-Shift-Keying (RZ-DQPSK) is similar to

DPSK in that the data is stored in the phase relation between adjacent bits. However, DQPSK has the advantage of storing 2 bits per transmitted symbol. This allows for broader pulse widths due to the lowered symbol rate making it twice as spectrally efficient and more tolerant to chromatic dispersion and intra-channel nonlinearities.

Polarization-Multiplexing (Pol-Mux) DQPSK takes advantage of both principal states of polarization (PSPs) and allows 2 bits to be transmitted in each time slot. When combined with DQPSK, the spectral efficiency is increased to 4 bits/symbol while the symbol rate is decreased by a factor of four. Polarization insensitive FWM, parametric amplification and demultiplexer were used.

3.1.2. Parametric Four-Wave Mixing in HNLF for Wavelength-Multicasting and Multiplexing

FWM is one of many 3rd order parametric processes resulting from the third order susceptibility. In non-degenerate FWM, two pumps, with propagation constants k_1 and k_2, are utilized to create two new photons with propagation constants k_3 and k_4, where $k_i = \omega_i/c$. The annihilation of two pump photons requires the following phase matching condition be satisfied: $k_1+k_2 = k_3+k_4$. FWM can also be performed using a single pump, with propagation constant k1, given that $2k_1 = k_2+ k_3$ is satisfied. In such a configuration, referred to as degenerate FWM, the energy of two photons from the pump with propagation constant k_1 is transferred to two new photons with propagation constant k_2 and k_3. In both schemes, phase matching is the critical condition for efficient FWM. A number of parameters lead to phase mismatch, and therefore reduce the conversion efficiency, including: polarization misalignment, zero-dispersion wavelength (ZDW) fluctuation, dispersion slope and PMD. We combated all of these limitations.

Parametric four-wave mixing (FWM) in highly nonlinear fiber (HNLF) was utilized in a number of locations throughout the delay module. Initially, multiple copies of a single low-rate channel were multicast into multiple wavelength channels using multiple CWs inserted into the HNLF. As illustrated below, each CW produced a replica of the input signal at a new converted location. This type of multicasting has been demonstrated previously in both HNLF and periodically poled lithium niobate (PPLN).

Figure 3 illustrates our multicasting scheme using FWM in HNLF. Also shown are simulation results using a HNLF with dispersion slope of 0.0002 ps/nm^2. An 8-fold multicaster is simulated for a 2 ps pulse width, 40 Gb/s data rate, resulting in flatness of ~3dB in efficiency over the bandwidth of the channels.

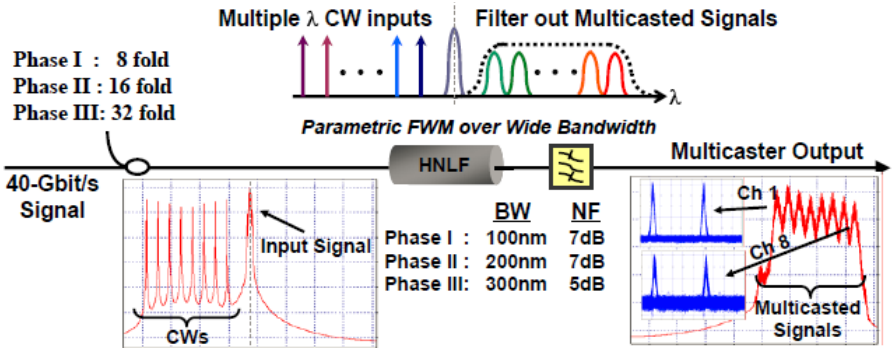

Figure 3. Illustration of signal multicasting of a single channel onto multiple wavelengths utilizing FWM in HNLF

After multicasting and applying a relative delay between wavelengths via dispersion, a multiplexer (referred to as a serializer) can convert all the delayed signals back to the original wavelength. This multiplexer can be performed by using parametric FWM in another piece of HNLF. When the wavelengths are appropriately delayed, a pulse can exist at only one wavelength at any given instant in time. By inserting sequentially clocked multiple pumps into the HNLF, we can convert each of the multicast / delayed signals back to the original wavelength. We can also utilize pulsed pump sources (pulsed at 40 Gb/s) in the multiplexer. Because only one channel can be ON at a given time, the pumps cannot interact, thereby reducing pump-to-pump crosstalk.

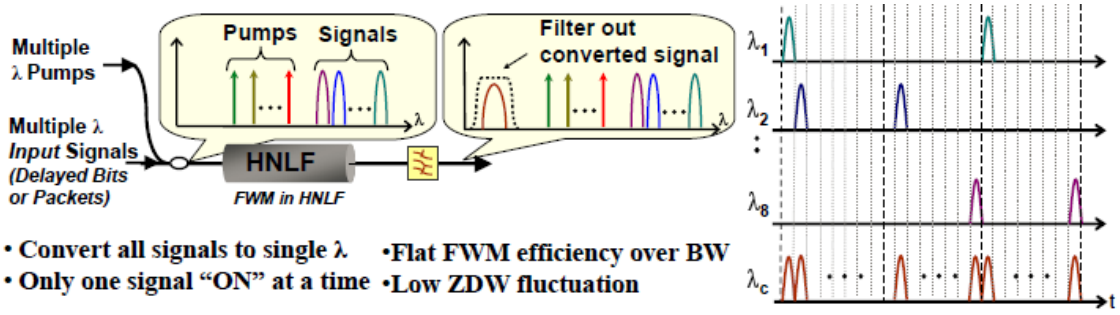

Figure 4. Multiplexer (serializer) using FWM in HNLF. Multiple ! delayed and converted to single wavelength

The primary concerns in the wavelength-conversion stages are FWM conversion efficiency, pump-to-pump crosstalk, and bandwidth. To achieve efficient multicasting and multiplexing over a wide bandwidth requires a low dispersion slope fiber. In addition, the zero-dispersion wavelength (ZDW) fluctuation must also be limited.

4. Results and Discussion

In the following, experimental results on tunable optical delays and their applications in multicasting and multiplexing are presented.

4.1. Experimental demonstration of 105 ns delay for multiple modulation formats

Signal processing is a powerful enabler and performance enhancer for a host of communications functions, and performing processing in the optical domain reduces optical-electronic conversion inefficiencies. One of the most basic elements needed to achieve efficient and high-throughput signal processing is a tunable optical delay line, but this element has historically been difficult to realize. Applications of such a delay may include: (a) synchronization for bit interleaving or (de)multiplexing (b) time-slot interchange (TSI), and (c) data packet synchronization.

We have demonstrated an optically-controlled delay element based on tunable wavelength conversion, dispersion compensating fiber (DCF), and intra-channel dispersion compensation, enabling a delay of up to 105 ns using 80 Gb/s RZ-DQPSK, 40 Gb/s RZ-OOK and 40 Gb/s RZ-DPSK modulation formats. A bit error rate (BER) < 10^{-9} was obtained for all formats. The experimental block diagram of the setup is shown in Figure 6. [2]

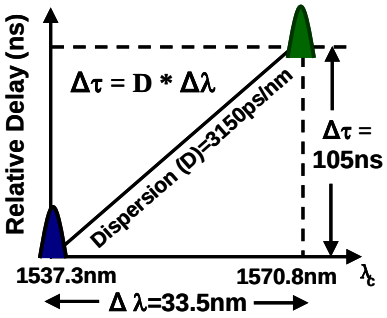

Figure 5. The amount of delay depends on the wavelength conversion range and the total dispersion of the DCF

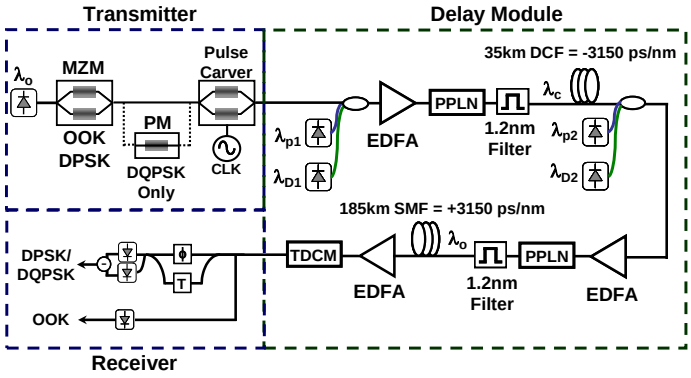

Figure 6. Experimental setup. Transmitter is capable of generating 80-Gb/s RZ-DQPSK, 40-Gb/s RZ-DPSK and 40-Gb/s RZ-OOK modulation formats. Phase demodulation at the receiver for DPSK/DQPSK is performed with a single interferometer tuned to the appropriate location

Various delay values has been experimentally demonstrated in Figure 7. For illustration purposes, a data packet of length 12 ns was used. Note that all other performance data was performed using PRBS data of sequence length 2^{15}-1. A maximum delay value of 105 ns was achieved in the first set of experiments, which is in agreement with the bandwidth-dispersion product of (33.5 nm) x (3150 ps/nm). This maximum delay was limited by the 33.5 nm amplification bandwidth of the erbium doped fiber amplifier (EDFA) following the first wavelength conversion.

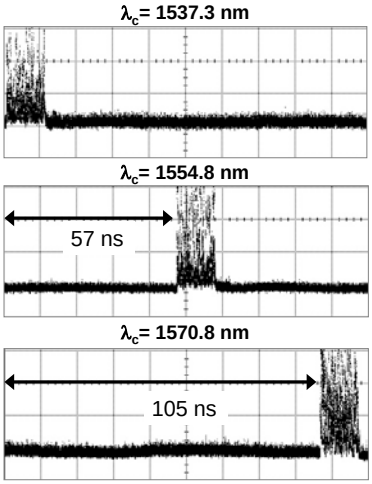

Figure 7. Experimental demonstration of 57 and 105 ns delay using a data packet of ~12 ns duration

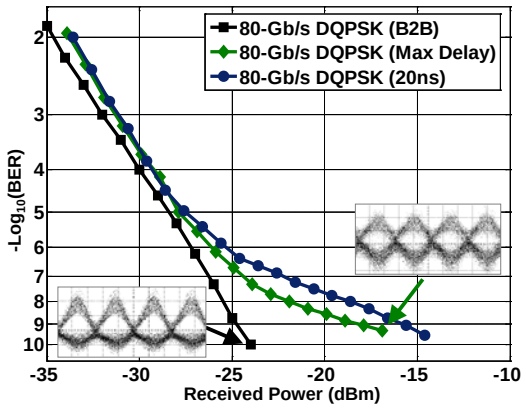

Figure 8. Bit error rate performance for 80 Gb/s RZ-DQPSK

To assess the impact of the delay module on data quality, we measured the BER both before and after the delay element for 80 Gb/s RZ-DQPSK, 40 Gb/s RZ-DPSK and 40 Gb/s RZ-OOK modulation formats as shown in Figs II.4-6. Power penalties ranging from 3 to 7 dB were observed down at BERs of 10^{-9}, while little power penalty was observed at higher BERs. Despite BER flaring, no error floor existed and BER < 10^{-9} was obtained for all modulation formats at various delay settings. No penalty was observed after the first wavelength conversion and we believe the system penalty to be due to the cascaded filters and amplifiers throughout the delay module, along with finite residual dispersion. We note that it is possible to reduce the complexity of the setup by double-passing through the same span of DCF for both delay and dispersion compensation.

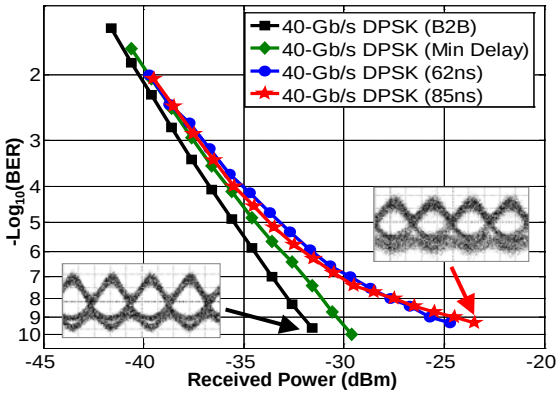

Figure 9. Bit error rate performance for 40 Gb/s RZ-DPSK

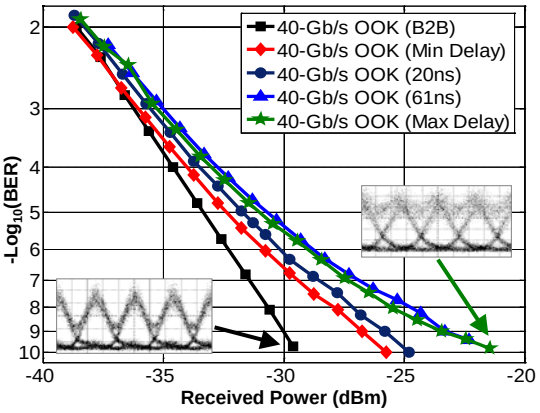

Figure 10. Bit error rate performance for 40 Gb/s RZ-OOK

4.2. Experimental demonstration of time-slot interchanger for variable packet lengths via tunable delays

A key function in time-based networks is the ability to manipulate data in the time domain in order to avoid output-port contention and increase throughput efficiency. This manipulation can

occur on the bit or packet level. For packet-switched networks, delaying and possibly interchanging full data packets in the time domain might require optical delays that are tunable over reasonably wide ranges and that are transparent to the data modulation format. In general, time-slot interchange (TSI) affords the network greater flexibility, similar to wavelength interchange for a wavelength-switched network. It might be desirable to perform such signal processing optically to reduce any optical-electronic conversion inefficiencies.

We have demonstrated tunable TSI of 40 Gb/s optical data packets using a conversion/dispersion-based optical delay element. Tunability was demonstrated by varying the packet length, which requires a different amount of relative delay. Packets of 182 bits were extracted to different wavelengths using FWM in HNLF. The packets were delayed relative to each other in a dispersion module, before being converted back to the original wavelength using a PPLN waveguide. The resulting signal remained intact with the exception of the swapping between the two packets. Tunability was demonstrated by operating with two different packet lengths, 182 and 288 bits/packet, and BER < 10^{-9} was achieved. [3]

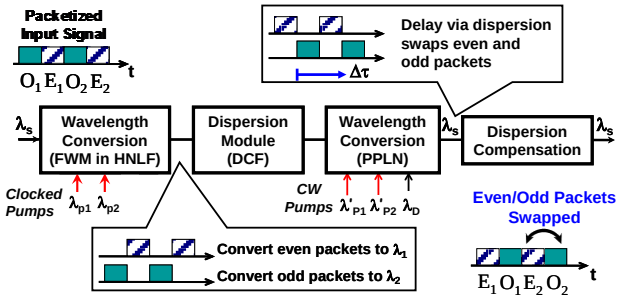

Figure 11. Concept of the time slot interchange. Even packets are delayed relative to the odd packets in the dispersion module. The proposed method allows tuning of the packet length through delay tuning via wavelength selection

Shown in Fig. 11 is the conceptual block diagram of the TSI technique. Clocked pumps were launched into HNLF, along with a packetized input signal located at the zero dispersion wavelength of the HNLF. FWM between the clocked pumps and signal generates replicas of the odd/even packets at new wavelengths, given by $f_{conv} = 2 f_{sig} - f_{pump}$.

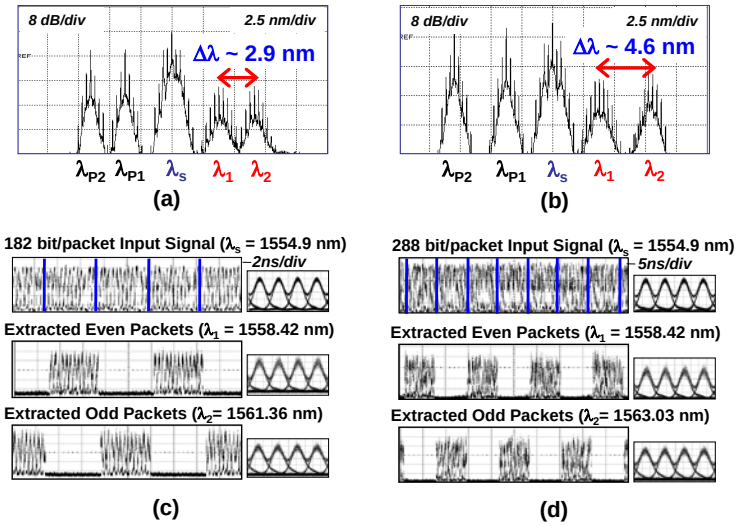

Figure 12. Optical spectra and packets after first wavelength conversion stage in the HNLF for two different packet lengths. (a) Spectra after HNLF for 182 bit-long packet extraction via FWM. Clocked pumps are located at 1551.38 nm and 1548.48 nm for even and odd packets, respectively; (b) Spectra after HNLF for 288 bit-long packet extraction via FWM. The clocked pump corresponding to odd packets is tuned to 1546.78 nm; (c) 182 bit-long input packets and extracted even/odd packets; (d) 288 bit-long input packets and extracted even/odd packets

Converted signals passed through a dispersion module thereby experiencing a wavelength-dependent delay. They were both converted back to the original wavelength using a PPLN waveguide operated in a 2-pump configuration followed by intra-channel chromatic dispersion compensation. This approach lends itself to delay tuning, and therefore to variable length packet swapping through modification of the conversion wavelengths.

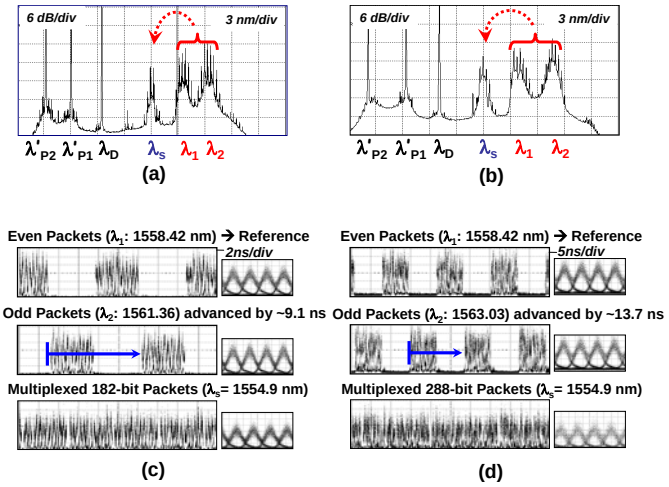

Figure 13. Optical spectra and packets following multiplexing in the PPLN for two different packet lengths. (a) Spectra after PPLN for 182-bit long packet multiplexing; (b) Spectra after PPLN for 288-bit long packet multiplexing; (c) Multiplexed 182-bit long packets to the original signal wavelength with swapped even/odd packets; (d) Multiplexed 288-bit long packets to the original signal wavelength with swapped even/odd packets

To assess the performance of the system, we measure the BER of the multiplexed signal, along with a 2^{15}-1 pseudo-random bit sequence (PRBS). Figure 14 shows the BER curves for the multiplexed and PRBS signals compared with the back-to-back performance. In the PRBS case, a single channel was wavelength converted, delayed, and converted back to the original wavelength. There is a slight flaring using a 40 Gb/s PRBS sequence attributed to cascaded optical filtering and EDFA's throughout the system. A higher flaring is observed for the multiplexed packets. We believe that this is due to the residual dispersion between the odd and even channels and can be reduced by using a DCF with a flatter dispersion profile.

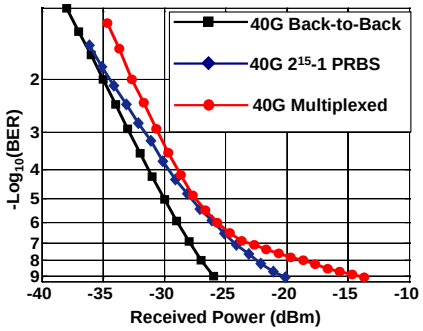

Figure 14. BER performance of the system for 40 Gb/s PRBS signal and multiplexed packets. Back to back performance is also shown

4.3. Experimental demonstration of optical PRBS data multiplexing via tunable delays.

In general, high-speed multiplexing can be used to generate pseudo-random bit sequences (PRBS). In order to achieve a true PRBS, which is the standard for accurate system performance characterization; there is a requirement to accurately delay the different data paths by specific

amounts. As is well known, accurate delays and multiplexing of parallel streams represent a significant part of the complexity and high cost of electronic high-speed data generation. Optical time-division multiplexing (OTDM) has been typically performed using fixed fiber delay lines to split a single lower rate channel into multiple copies that are time shifted by a required amount before being re-combined into a single, higher-rate channel. Unfortunately, once the delay lines are fixed this method produces a true PRBS only for the specifically designed data rate and PRBS order.

We have also demonstrated bit-rate-tunable, all-optical 2^7-1 PRBS multiplexing from 10-to-20 Gb/s and from 20-to-40 Gb/s using a conversion/dispersion based tunable optical delay element. The input signal was multicast to two wavelengths in a PPLN waveguide. The converted signals were delayed relative to each other using a dispersion module before they were converted back to the same wavelength using another PPLN waveguide. A BER $<10^{-9}$ was achieved for both 10-to-20 and 20-to-40 Gb/s multiplexing. The RF spectra before and after multiplexing were measured and showed the expected PRBS spectral characteristics.

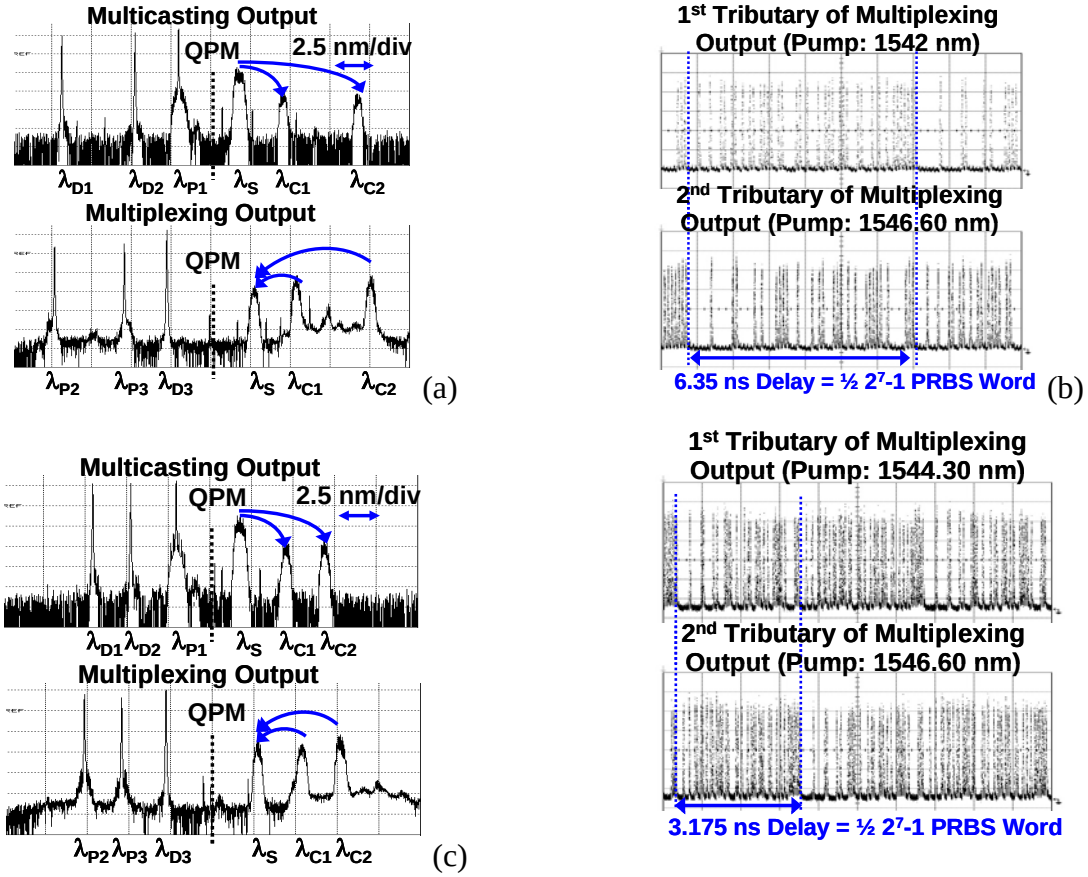

Figure 15. Optical spectra after both wavelength conversion stages and the delay between the tributaries corresponds to ½ of a 2^7-1 PRBS word. (a) 10-to-20 Gb/s spectra; (b) 10-to-20 Gb/s delay between tributaries; (c) 20-to-40 Gb/s spectra; (d)20-to-40 Gb/s delay between tributaries

Shown in Figure 15 are the optical spectra and multiplexed bit patterns after both multicasting and multiplexing stages for 10-to-20 Gb/s and 20-to-40 Gb/s PRBS generation. We measured the BER of the multiplexed signals, as well as the lower rate tributaries for both 10-to-20 Gb/s and

20-to-40 Gb/s multiplexing. Shown in Figure 16 and 17 are the BER curves and the corresponding eye diagrams. For 10-to-20 Gb/s multiplexing we observed < 2 dB penalty at lower BERs, beyond the expected 3 dB shift due to the rate doubling, while almost no penalty was observed at higher BERs. The slight difference of performance between the two converted tributaries is attributed to the different amount of residual dispersion. For 20-to-40 Gb/s multiplexing a ~4 dB penalty was observed in the lower BER region, while there was negligible penalty in the higher BER region.

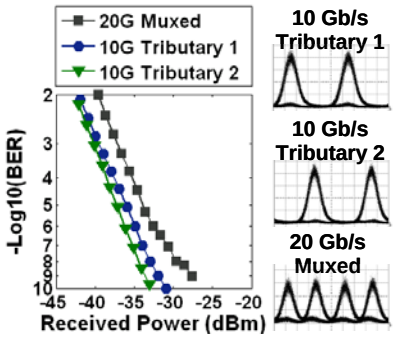

Figure 16. Bit error rate performance of the multiplexed signals and their tributaries

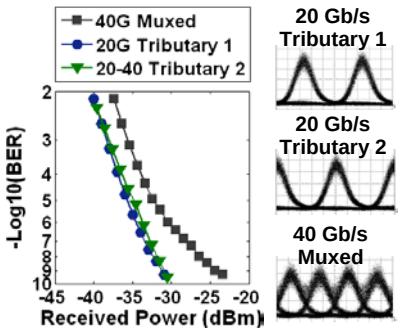

Figure 17. Bit error rate performance of the multiplexed signals and their tributaries

Figure 18. (a) and (b) show the RF spectra before and after PRBS multiplexing from 10-to-20 Gb/s. Prior to multiplexing, the RF spectra consists of equally spaced tones separated by ~79 MHz, i.e. (10 Gb/s)/(127). Following multiplexing, the tone spacing increases to ~158 MHz, i.e. (20 Gb/s)/(127), demonstrating that proper multiplexing is achieved. Note that for inaccurate bit shifts the tones at odd integers of 79 MHz increase rapidly, as shown in Figure 18. (c) and (d).

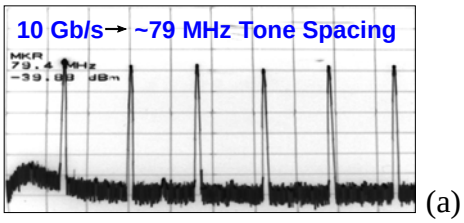

(a)

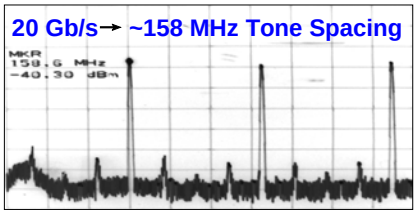

(b)

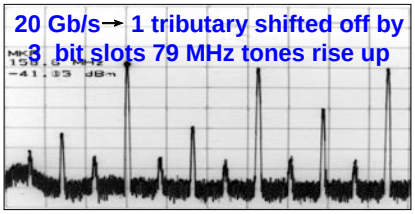

(c)

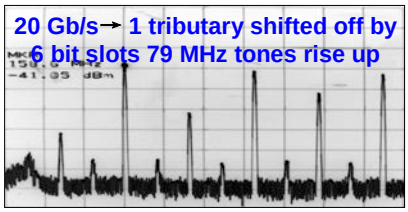

(d)

Figure 18. RF spectra before and after multiplexing. (a) 10 Gb/s 2^7-1 PRBS RF spectra before multiplexing; (b) Multiplexed 20 Gb/s 2^7-1 PRBS RF spectra; (c) Multiplexed 20 Gb/s RF spectra: 1 tributary shifted off by 3 bit slots; (d) Multiplexed 20 Gb/s RF spectra: 1 tributary shifted off by 6 bit slots

4.4. Experimental demonstration of 503 ns delay for 40 Gbit/s RZ- OOK data

There has been increased recent interest in the ability to produce tunable optical delays such that fine granularity can be achieved to improve the performance of many types of optical signal

processing functions. For data rates ≥40 Gb/s in which the length/time scales of a single bit time are fairly short, accurate optical timing can be critical in time multiplexing, synchronization, switching, equalization, correlation, and time-slot interchange. At high bit rates, switching between a set of discrete delay lines lacks the fine granularity needed for efficient performance. Therefore, finely tunable delay lines, which are crucial for electronic signal processing, might become important elements for optical systems. Desirable features of such tunable optical delays include the ability to handle high data rates, transparency to data modulation formats, and accommodation of a large range of delays to enable the delay of a large data blocks.

We have demonstrated a method in which we achieve a 503 ns, continuously tunable delay of a 40-Gb/s RZ-OOK signal using an additional λ-conversion stage to reduce residual 2nd and 3rd order dispersion. This corresponds to a delay-to-bit-rate product of over 20,000 for 40 Gb/s. A BER of 10^{-9} was obtained over the extent of the delay tuning range. [4]

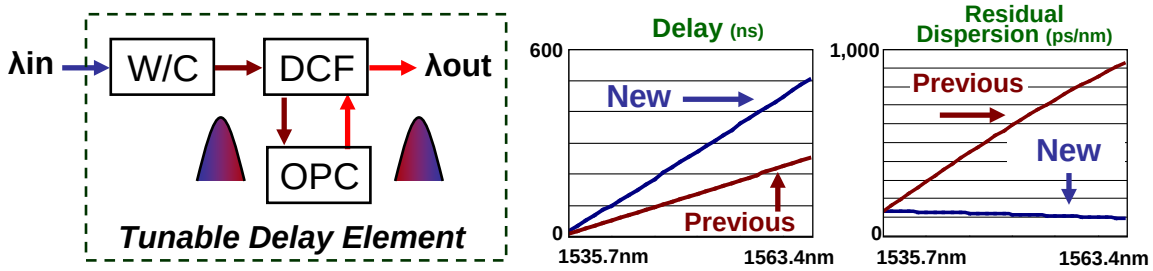

Figure 19. Conceptual diagram of tunable delay using wavelength conversion (W/C), dispersion compensating fiber (DCF), and optical phase conjugation (OPC). Near wavelength maintaining phase conjugation allows for double group delay and minimized 3rd order dispersion compared to previous methods

Shown in Figure 19 is a conceptual block diagram of this technique. Dispersion compensating fiber (DCF) is used to generate a wavelength-dependent group delay, in addition to intra-channel dispersion. By varying the wavelength through the DCF, the signal experiences a variable delay. A wavelength converter after the DCF is used to phase conjugate the signal, before it is passed through the DCF a second time. This double-pass allows for compensation of the 2nd order dispersion. Furthermore, by only phase conjugating the signal a few nano-meters and allowing it to return at nearly the same variable wavelength, the signal undergoes a second group delay while the 3rd order residual dispersion is minimized. The maximum amount of delay ($\Delta\tau$) through the system can determined by the product of the wavelength conversion bandwidth ($\Delta\lambda$) and the dispersion (D): $\Delta\tau = 2*\Delta\lambda*D$, where the factor of two comes from taking advantage of the group velocity variation on both passes through the DCF.

An experimental block diagram of our setup is shown in Figure 20. RZ-OOK is generated using a Mach-Zehnder modulator (MZM) driven by a 42 Gb/s PRBS 2^{15}-1 data stream. Full-rate 42 Gb/s pulse carving is used to produce a 50% return-to-zero (RZ) waveform. Tunable wavelength conversion is achieved using a ~400 m piece of dispersion flattened highly nonlinear fiber (HNLF) with a ZDW of ~1550 nm. A 1-pump four-wave-mixing approach is used where the high power pump is swept in wavelength to control the location of the converted signal. The signal ($\lambda_0 \approx 1534$ nm) was up converted from 1535.7 nm to 1563.4 nm.

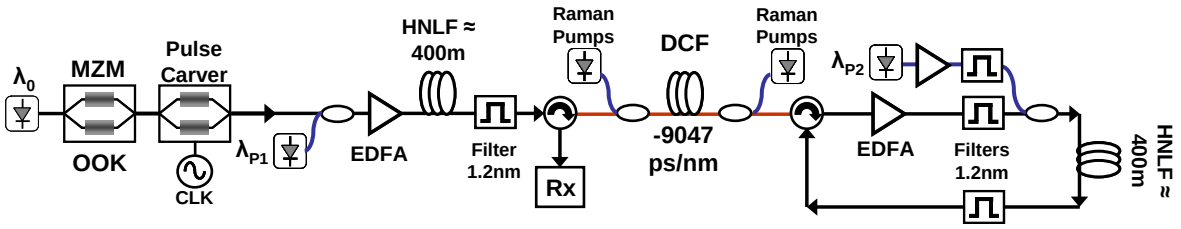

Figure 20. Experimental setup. 40 Gb/s RZ-OOK is wavelength converted and passed thorough the DCF. The DCF is Raman pumped to compensate for the fiber loss. The signal is phase conjugated and shifted by ~4nm before passing back through the DCF for detection and error rate measurements

The converted signal was then filtered out and sent through the DCF (-9047 ps/nm of dispersion) to impose a wavelength-dependant delay. The DCF was Raman pumped to compensate for the 22 dB of loss in the fiber. Following the DCF, the delayed signal was phase conjugated using a second piece of ~400 m HNLF with a ZDW of ~1560 nm. Again, a 1-pump FWM approach was used to convert the signal ~4 nm up in wavelength. To compensate for the significant intra-channel dispersion, the signal is passed backwards through the DCF a second time. Since the return trip is at nearly the same wavelength, the conjugated signal sees both a similar group velocity, giving more delay, and a similar dispersion profile allowing for 3rd order residual dispersion to be minimized. Wavelength preserving phase conjugation is possible and would further improve the dispersion compensation. The remaining residual dispersion ranged from 170 ps/nm to 40 ps/nm depending on wavelength, and was removed using a commercially available tunable dispersion compensator with a resolution of 10 ps/nm and a range of ±400 ps/nm.

Shown in Figure 21(a) is the relative delay of the system as a function of the conversion wavelength. The total delay achieved is 503 ns covering 27.7 nm from 1535.7 to 1563.4 nm. The delay is limited by the amount of dispersion available and the wavelength bandwidth. The amount of dispersion is limited by the loss of the medium. Our DCF had a loss of ~22 dB on top of the system losses from couplers and filters. The DCF was Raman pumped to eliminate much of this loss. Further increases in the amount of fiber lowered our signal power to an unsuitable level for efficient wavelength conversion. Higher power Raman pumps along with lower loss fiber would allow for the increase of the dispersive element. Similarly, the wavelength range is directly limited by the conversion bandwidth of the fiber we have. In order to achieve relatively high conversion efficiency, large pump powers are required. This limited us to the bandwidth of our available EDFAs and to the region of Raman gain in our DCF. Further extending our Raman region as well as broadband amplifiers, including parametric optical amplifiers, would allow us to extend our delay.

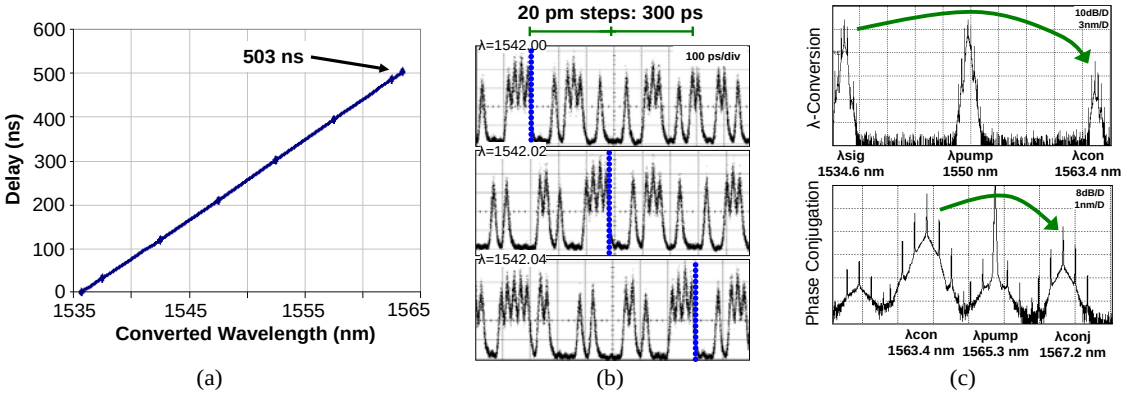

(a) (b) (c)

Figure 21. (a) Relative delay versus converted wavelength through the DCF. (b) Experimental demonstration of delay using 20 pm steps equivalent to 300 ps delay. (c) Experimental optical spectra after both wavelength conversion stages

In Figure 21(b) 20 pm laser steps are used to show a delay of 600 ps and illustrate the granularity of our delay. A 0.1 pm laser tuning resolution translates into a delay resolution of ~1.8 ps, which is adequate for time-multiplexing of 40-Gbaud signals of bit period 25 ps. However, as the delay and data rate increases, finer control over laser resolution may be necessary. It should be noted, that our new method allows for both the first stage λ-conversion pump and the OPC pump to affect the delay giving greater control over the delay value. Shown in Figure 21(c) are sample optical spectra at the output of the first and second wavelength conversion stages for the worst case, stage 1 is over the largest conversion bandwidth (λconv = 1563.4 nm) and the signal conversion efficiency is at its lowest. Similarly, the stage 2 phase conjugation has the smallest input signal giving its lowest conversion efficiency.

BER both before and after the delay element for 40-Gb/s RZ-OOK is shown in Figure 22(a). A power penalty of 1.9 and 3.3 dB respectively was observed at 1E-9. Similarly, Figure 22(b) shows the power penalty for the closest, middle and farthest converted wavelengths with penalties of 3.7, 1.7 and 2.8 dB respectively. Virtually no power penalty was observed at higher BERs. We attribute this flaring of the BER to the cascaded amplifiers and filters throughout the delay module, along with a finite residual dispersion.

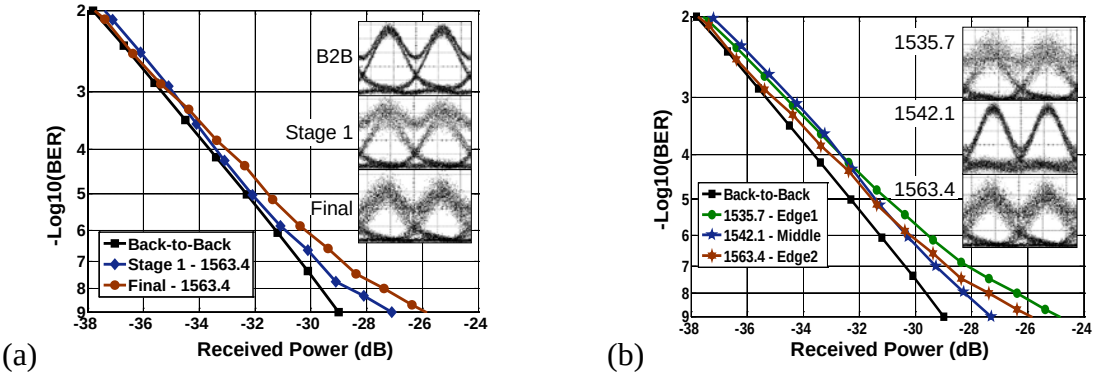

(a) (b)

Figure 22. Bit error rate performance for 40 Gb/s RZ-OOK. (a) Back-to-back performance compared against the performance after stage 1 and after the final system at the maximum delay, and (b) compared to the delay edges and the delay center

4.5. Experimental demonstration of 40 Gbit/s to 160 Gbit/s Multiplexing and 160 Gbit/s to 40 Gbit/s demultiplexing

Optical fiber communications can accommodate a very high-data-rate channel whose data stream originates and terminates in the electrical domain. However, multi-user networks tend to manipulate (i.e., multiplexing, demultiplexing) multiple lower-data-rate channels in order to facilitate efficient routing and to optimally utilize links of differing capacities. This granularity adds to the usefulness of a network, and optics does enable such granularity in the wavelength domain. However, time manipulation has presented a greater implementation challenge. Functions such as multicasting and time (de)multiplexing can be considered key building blocks when considering a future optically-switched network.

A potential candidate for all-optical approaches has been using optical nonlinearities in highly nonlinear fiber (HNLF) which tend to accommodate very-high-speed operation, data-format transparency, and wide spectral ranges. A key goal for any optical system is to ensure that the data bits are not degraded by the in-line optical-signal-processing subsystem modules. This can be challenging for even a single module, and it is especially true for a cascade of data-manipulating subsystem elements that can operate on 40 and 160-Gbit/s data channels.

We have demonstrated good performance for optically concatenated 4-fold 40-Gbit/s multicasting, 4-fold 40-to-160-Gbit/s multiplexing, and 160-40-Gbit/s demultiplexing using highly nonlinear fiber. Supercontinuum generation plus spectrum slicing was used to get 4-fold 40-Gbit/s multicasting and XPM plus offset filtering was used for 4-fold 40-to-160-Gbit/s multiplexing, and 160-to-40-Gbit/s demultiplexing. Error-free performance was achieved after these nonlinear processes, with 5-10 dB power penalty at 10^{-9} bit error rate (BER). [6]

Figure 23 shows the experiment setup. At the transmitter, a short pulse laser with repetition rate of 10 GHz and pulse width of 2 ps was used. The 10 GHz pulses were multiplexed to 40 GHz by an optical multiplexer. Data modulation was applied using a Mach-Zehnder modulator (MZM) driven by a 215-1 pseudo-random binary sequences (PRBS) at 40-Gbit/s. Then the signal was amplified and sent to a 500 m HNLF, with zero dispersion wavelength (ZDW) at ~ 1565 nm for supercontinuum generation. 4 portions of the broadened spectrum of interests were filtered out by different optical bandpass filters (BPF) to obtain 4 multicast channels each at 40-Gbit/s. The delay between the 4 channels was adjusted by using optical tunable delay lines (TDLs). A 17 nm BPF was used to filter out the ASE noise before going into another 1 km HNLF, with ZDW at ~1552 nm, for multiplexing to one 160-Gbit/s channel. XPM plus offset filtering was used for the multiplexing process. A tunable bandwidth/wavelength was inserted after the HNLF to optimize the multiplexed signal. The 160-Gbit/s signal was demultiplexed through another 3 km HNLF, with ZDW at ~1554 nm, using XPM induced phase shift plus offset filtering. The 40 GHz pump pulses used in the DEMUX stage were tapped off after the MUX in the transmitter. The DEMUXed signal was then set to a 40-Gbit/s pre-amplified receiver for BER measurement.

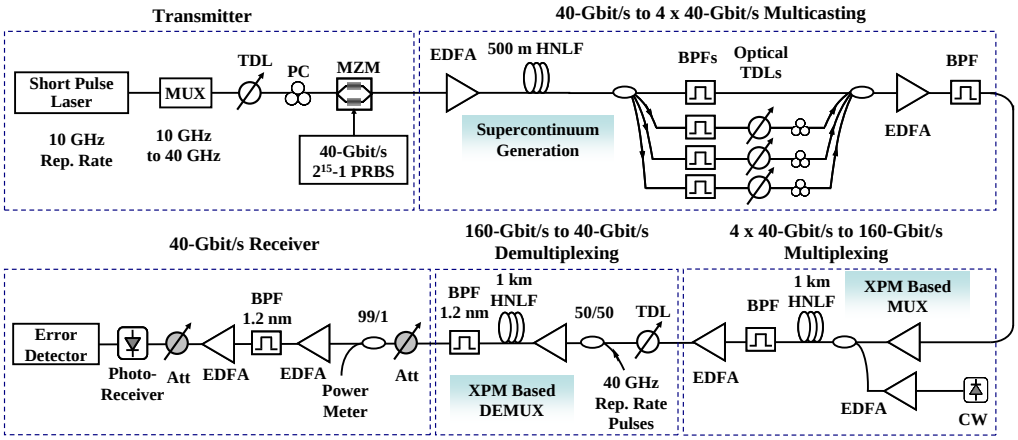

Figure 23. Experimental setup. MUX: optical multiplexer; MZM: TDL: tunable delay line; Mach-Zehnder modulator; BPF: bandpass filter; Att: optical attenuator; CW: continuous wave

Figure 24 (a) shows the supercontinuum after the 500 m HNLF (top) and the combined 4 multicast channels (bottom) before going to the XPM-based multiplexing stage. Figure 24 (b) shows the BER performance and the corresponding eye diagrams for each multicast channel. <2.5 dB penalty at 10^{-9} BER was observed for all 4 multicast replicas. Considering the bandwidth of our sampling scope was limited to 40 GHz, we only kept 2 multicast channels on at the beginning and test the performance of two 40-Gbit/s signal multiplexing to one 80-Gbit/s signal. Figure 24 (c) shows an example of the spectrum after the 1 km HNLF (top) and the following offset filtering for two 40-Gbit/s signal to 80-Gbit/s signal multiplexing. The bandwidth of the offset filter after the HNLF was varied and the optimal value was found to be 2.6 nm. Figure 24 (d) shows the BER curves after the 80-Gbit/s signal was demuxed to 40-Gbit/s. ~ 5 dB penalty was observed compared to the back to back (BB) signal.

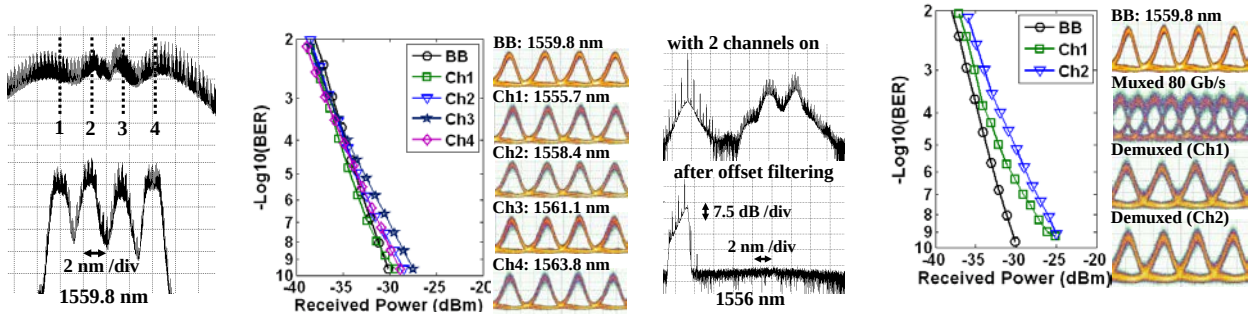

(a) (b) (c) (d)

Figure 24. 40-Gbit/s to 4 x 40-Gbit/s signal multicasting and 2 x 40-Gbit/s to 80-Gbit/s multiplexing results. (a) spectra after supercontinuum generation and filtering; (b) BER performance of each tributary after supercontinuum; (c) spectra after multiplexing and offset filtering; (d) BER performance after demux of each tributary of the 80-Gbit/s multiplexed signal

To further investigate the pulse evolution during the nonlinear processes, we used an autocorrelator to measure the pulse width after each stage. Due to the four 1.2 nm filters we used after supercontinuum, the pulse width of each multicast signal was broadened to ~ 4 ps before going to the XPM-based multiplexing stage. The 3 dB pulse width was broadened to ~5.5 ps after the multiplexing stage, which shows that the pulse width is good for 80-Gbit/s signal, but is

relatively wide for 160-Gbit/s due to the adjacent pulse overlapping.

Based on the experimental results and analysis above, we modified the multicasting setup according to what we had in the lab, as shown in Figure 25 (a). Instead of using four 1.2 nm filters, we used two wider filters, one ~5 nm and one ~4 nm after supercontinuum and got two corresponding multicast signals. The other two channels were obtained by tapping off the original modulated signal and adding in another pulse source. The repetition rate of the newly added source was 10 GHz, which was considered to be the emulation of a 40-Gbit/s signal with the programmed pattern "1000". The pulse width was ~2 ps for the three 40-Gbit/s channels and ~2.3 ps for the emulated 40-Gbit/s channel. Figure 25 (b) shows the optical spectrum after the multicasting stage. In the time domain, the delay between each of the four 40-Gbit/s signal was adjusted to be interleaved.

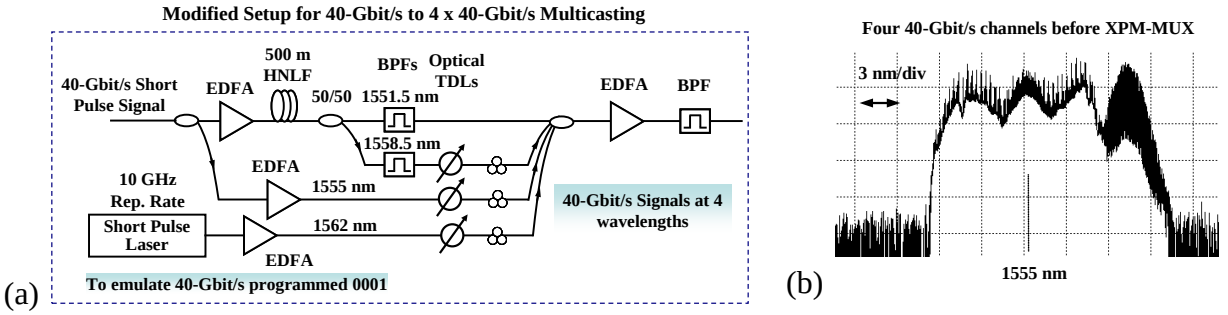

Figure 25. Modified multicasting setup and the output of the multicasting stage

Figure 26 (a) shows the optical spectrum after the multiplexing stage (top) and after offset filtering (bottom). The 4 multicast channels were sent to a high bandwidth optical sampling scope after adjusting the delay between each other. Figure 26 (b) shows the eye diagram of the multiplexed 160-Gbit/s signal before and after the offset filtering. Again, we demuxed the signal based on XPM induced frequency shift plus offset filtering, the spectra of which are shown in Figure 26 (c). Note that the 40 GHz pump happened to be close to the ZDW of the HNLF. We can also obtain the demux by filtering out the FWM product on the right-hand side of the spectrum. Figure 26 (d) shows the corresponding BER performance and the eye diagrams for each channel.

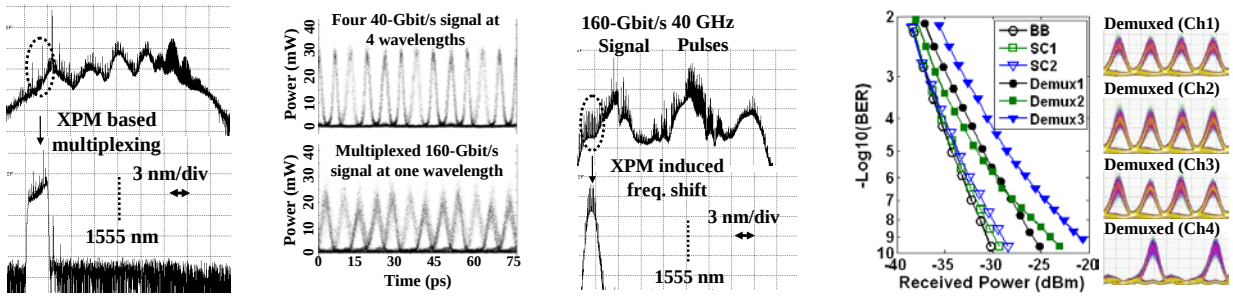

Figure 26. Experimental results for 4-fold 40-Gbit/s signals to 160-Gbit/s multiplexing. (a) spectra after multiplexing and the offset filter; (b) eye diagrams before and after multiplexing; (c) spectra after the demux and offset filter; (d) BER performance the 160-Gbit/s tributaries

4.6. Experimental demonstration of multiplexing of two DPSK signals to a single DQPSK signal and simultaneous 7-fold multicasting

It is well known that data signal processing can enhance the efficiency and performance of a communication system. Examples of such functions include multiplexing two data streams together on a single channel, multicasting a single data stream into many copies, and converting the data modulation format to optimally use the channel medium. These three functions can effectively utilize system bandwidth, decrease network latency, and provide requested data granularity. Moreover, performing these functions at the line rate can further enhance system efficiency, and yet achieving multiplexing and multicasting in the electronic domain is a severe challenge as data rates rise to 100-Gbit/s/channel. Therefore, optical implementations of transparent multiplexing and multicasting have garnered much interest, especially with regards to advanced data modulation formats such as highly sensitive differential-phase-shift-keying (DPSK) and spectrally efficient differential-quadrature PSK (DQPSK).

We have demonstrated optical multiplexing of two 21.5-Gbit/s DPSK signals into a single 43-Gbit/s RZ-DQPSK channel with simultaneous 7-fold multicasting in a single PPLN waveguide. The use of a dual-pump wavelength conversion scheme in PPLN allows preservation of signal phase information and therefore multiplexing of two phase-modulated signals. This method can also be extended in simultaneous multicasting of phase-modulated data by using additional continuous wave (CW) lasers. A BER of 10^{-9} was obtained for all multicast RZ-DQPSK channels with 100 GHz channel spacing with power penalties lower than 5 dB. [5]

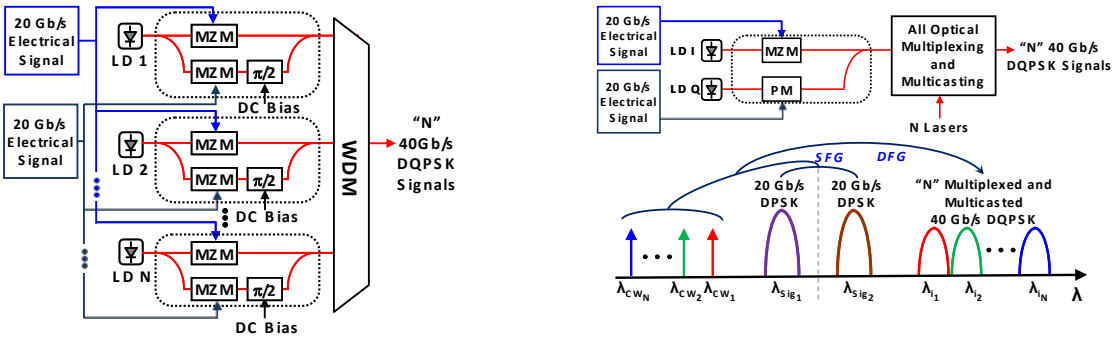

Figure 27. Conceptual block diagram of simultaneous multiplexing and multicasting of two DPSK signals

Shown in Figure 27 is a conceptual block diagram of this technique. A dual-pump wavelength conversion scheme in PPLN is utilized to generate idler signals. The cascaded $\chi^{(2)}$: $\chi^{(2)}$ processes of sum frequency generation (SFG) between the input pumps (with electric fields $\mathbf{E_{Sig1}}$ and $\mathbf{E_{Sig2}}$) and difference frequency generation (DFG) between the CW pump ($\mathbf{E_{CW,N}}$), respectively, generates the idler with $\mathbf{E_{i,N} \sim E_{Sig1} \times E_{Sig2} \times E_{CW,N}^{*}}$. The phase of the resulting idler will be $\sim \phi_{Sig1} + \phi_{Sig2} - \phi_{CW,N}$. Hence, by using two input DPSK signals with phases modulated from $\{0, \pi\}$ and $\{0, \pi/2\}$, respectively, we achieve quaternary phase states of $\{0, \pi/2, \pi, 3\pi/2\}$, hence multiplexing of the two input data streams into a single DQPSK signal. Using multiple CW pump lasers, multiple copies of the multiplexed DQPSK signal can be generated at desired wavelengths in the same PPLN waveguide.

An experimental block diagram of our setup is shown in Figure 20. One of the 20-Gbit/s DPSK

input signals was generated using a Mach-Zehnder modulator (MZM) driven by a 20-Gb/s PRBS 2^7-1 data stream with an amplitude of $2V_\pi$, yielding a 20 Gbit/s DPSK signal with $\{0, \pi\}$ phase swing. To generate the other 20 Gbit/s DPSK input signal with $\{0, \pi/2\}$ phase swing, a phase modulator (PM) driven with an inverted and delayed version of the original data was employed, where the amplitude of the input level was tuned to $V_\pi/2$. Full-rate 20-Gb/s pulse carving was used for this input signal to produce a 50% return-to-zero (RZ) waveform. Simultaneous multiplexing and multicasting was achieved using a PPLN waveguide with a quasi-phase matching location of 1552.3 nm. A 2-pump scheme was used in which the input DPSK signal (λ_{Sig1} = 1550.6 nm) serves as the first pump and the other RZ-DPSK input (λ_{Sig2} = 1554.0 nm) is placed equidistant to the first input signal, relative to the PPLN QPM. Seven CW lasers were combined with an arrayed waveguide grating (AWG), then amplified, and coupled to the PPLN along with the two DPSK signals. The CW lasers were separated by 100 GHz (~0.8 nm) channel spacing and positioned at ITU-T grid wavelengths. The multiplexed RZ-DQPSK signal copies were generated at wavelengths equidistant and opposite to the QPM of the PPLN.

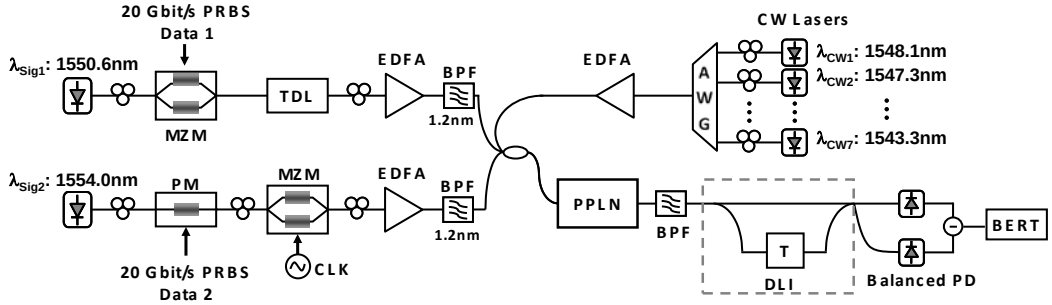

Figure 28. Experimental setup. TDL: tunable delay line; MZM: Mach-Zehnder modulator; BPF: bandpass filter

Each multicast copy of the multiplexed 40 Gbit/s RZ-DQPSK signals was then filtered for BER measurements. A preamplified receiver was used for the detection. A 50 ps delay line interferometer (DLI) was used for phase demodulation prior to detection using a balanced photoreceiver. Because we were limited to a single DLI at the receiver, the in-phase (I) and quadrature (Q) channels for DQPSK were detected at different times through tuning of the DLI phase to +/- 45 degrees, respectively.

The spectrum after simultaneous multiplexing and 7-fold multicasting is show in Figure 29 (a). The output 43 Gbit/s DQPSK signals are located at wavelengths from 1556.5 nm to 1561 nm with ~0.8 nm (100 GHz) channel spacing. The multicasting flatness was measured to be less than 2 dB. Shown in Figure 29 (b) are the demodulated eyes of the multicast signals after detection with a balanced photodiode. We also investigated the power penalty induced by the number of multicast channels as shown in Fig 29 (c). We observed that single channel operation (multiplexing of two input DPSK channels with single CW pump) yielded a power penalty of ~1.2 dB (at BER of 1E-9) with respect to back-to-back operation of a 43 Gbit/s RZ-DQPSK transmitter. Introducing more CW pumps to generate multiple copies increased the power penalty on the multicast channels due to the decreasing peak power of the CW pumps as the gain of the booster EDFA was split between the CW pumps. In addition to this, another source of the power penalty was the decrease in the power of the SFG product of two DPSK channels per CW pump to generate the multicast copies via DFG. For 7-fold multicasting, we observed a

maximum of 4.8 dB power penalty for the worst case.

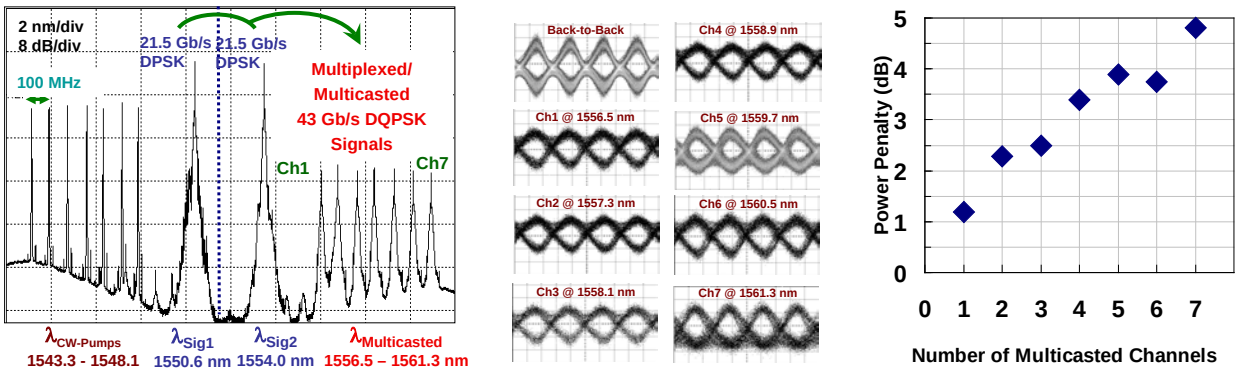

(a) Spectrum after PPLN

(b) Eyes for each multicast

(c) Power penalty at BER of 1E-9 as a function of number of multicast copies

Figure 29. Experimental results for 7-fold multicasting of multiplexed 43 Gbit/s RZ- DQPSK Signals

BER measurements were obtained for all seven multicast RZ-DQPSK channels with all channels on at a given time. The receiver sensitivity was observed to be around -25 dBm for a BER of 10^{-9}. We obtained similar BER performance for all of the channels. Figure 30 (a) shows the BER curves for all multicast channels along with a 43 Gbit/s RZ-DQPSK transmitter BER performance for comparison. We observed a very slight change in performance among the multicast copies. The power penalty as a function for each channel is shown in Figure 30 (b) with power penalties ranging from 3.7 dB to 4.8 dB.

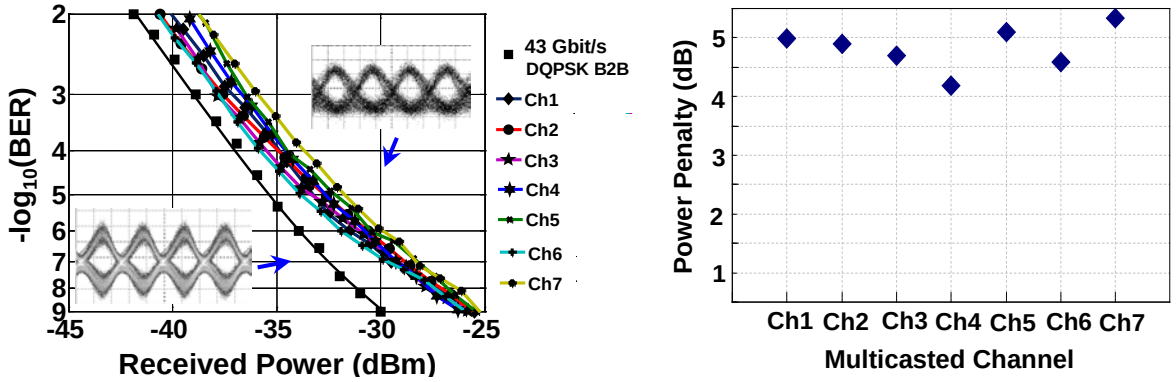

(a) BER measurement s for multicast 43 Gbit/s RZ DQPSK signals. Back to back performance of a 43 Gbit/s RZ-DQPSK transmitter is shown as well for comparison.

(b) Power penalty for each multicast channel with 100 GHz channel spacing.

Figure 30. Performance for the multicasting of multiplexed channels and power penalty induced per channel

4.7. Experimental demonstration of 8-fold multicasting of 40 Gbit/s RZ-OOK signals in HNLF via FWM

We have also demonstrated 8-fold multicasting of RZ-OOK signal via four-wave mixing (FWM) in highly nonlinear fiber (HNLF). The RZ input signal was located at the zero dispersion wavelength of the HNLF (~1550.4 nm) and 8 CW lasers were used to generate 8 copies of the input signal. The multicast signals were equally spaced by ~2.4 nm and located from 1553.1 nm to 1569.8 nm. Figure 31 (a) shows the spectrum after the HNLF. The powers of the CW pumps were adjusted such that a multicasting flatness of < 2 dB was achieved. To assess the performance of the multicast signals BER measurements were performed on each copy as shown in Fig 31(b). A maximum of ~4 dB penalty was observed at a BER of10^{-9}. This was mainly due to the limitations of filter used in the receiver.

Furthermore, we measured the pulse width of the multicast signals with a free-space autocorrelator as shown in Figure 32 below. The input pulses were compressed due to the nature of the FWM scheme used. The output pulse width was measured to be 8.7 ps for all multicast signals.

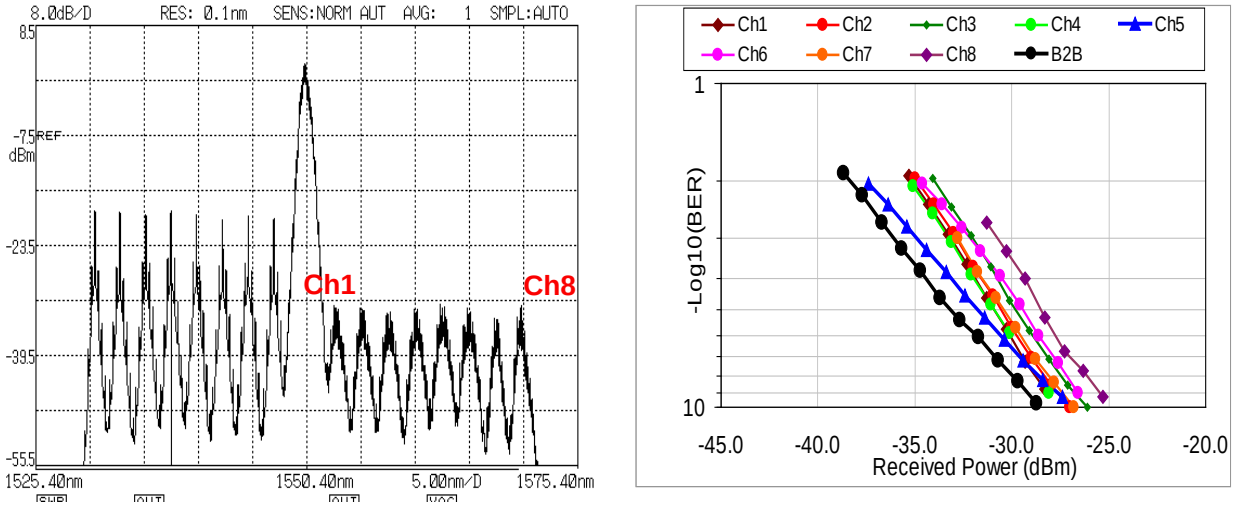

(a) Spectra after multicasting (b) BER performance

Figure 31. Spectrum after the HNLF and bit error rate performance for 40-Gb/s RZ-OOK. Back-to-back performance compared against the performance of the multicast copies of the signal

	CRO	Pulsewidth
Signal	*2.44ms*	*12.65ps*
Channel1	*1.68ms*	*8.7ps*
Channel2	*1.68ms*	*8.7ps*
Channel3	*1.68ms*	*8.7ps*
Channel4	*1.68ms*	*8.7ps*
Channel5	*1.68ms*	*8.7ps*
Channel6	*1.68ms*	*8.7ps*
Channel7	*1.68ms*	*8.7ps*
Channel8	*1.68ms*	*8.7ps*

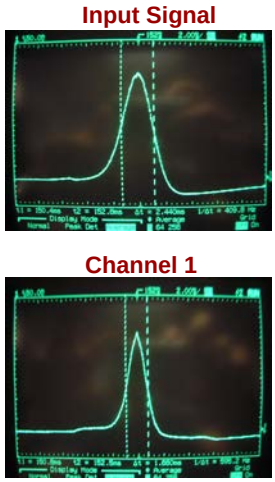

Figure 32. Pulse width measurements for each multicast channel along with the input signal for comparison

4.8. Experimental demonstration of wavelength conversion over 100 nm in HNLF via FWM.

We have also demonstrated wavelength conversion over 100 nm of bandwidth in a HNLF via FWM. The FWM efficiency is given in the Figure 33 (a) below. We achieved 80 nm of bandwidth with 3 dB of conversion flatness. A bandwidth of 103 nm was achieved with 9 dB flatness. Sample spectra after the HNLF depicting the FWM are given in Figure 33 (b).

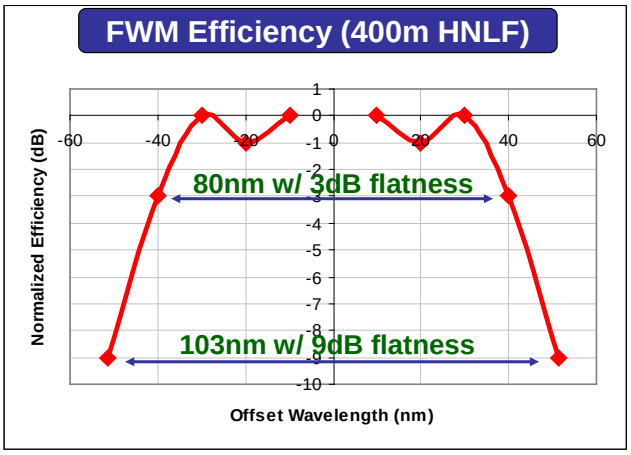

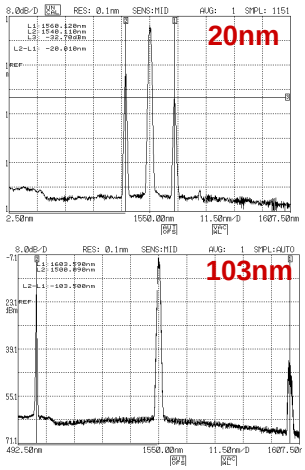

(a) Normalized FWM efficiency for 400 m HNLF, (b) Spectrum for wavelength conversion for 20 nm and 103 nm.

Figure 33. FWM efficiency as a function of conversion bandwidth and samples of the spectra after the HNLF

4.9. Fine (<0.5 ps) and Course Tuning (>15 ps) of Optical Delays using Acousto-optic Mixing with a 1-pm Tunable Laser

We have demonstrated fine (<0.5 ps) and course (>15 ps) tuning of optical delays using acousto-

optic mixing with a 1 pm (125 MHz) resolution tunable laser. Coarse tuning was performed using the tunable laser source to reach a maximum delay of 256 ns for a 40 Gb/s return-to-zero on-off-keying (RZ-OOK) signal. Cascaded acousto-optic modulators (AOMs) were used to precisely control the laser center wavelength and achieve a delay resolution of <0.5 ps. Spectral mixing data showed ~10 kHz control of laser wavelength granularity. This fine tuning was coupled with the coarse tuning to provide a nearly continuous range of delays with no extra system penalty. [9, 19]

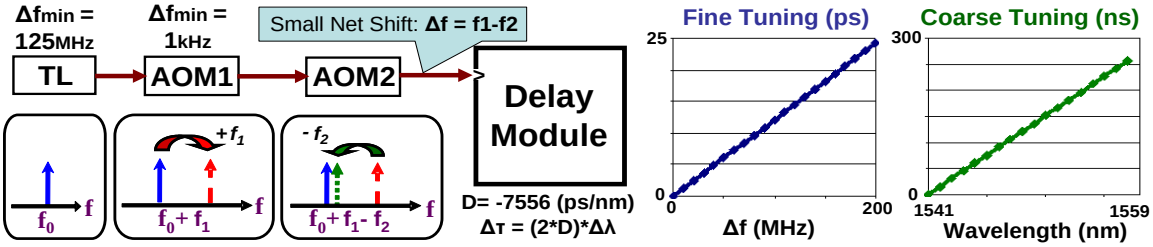

Figure 34. Conceptual block diagram. A tunable laser (TL) with 1pm = 125MHz resolution is used to coarse tune the optical delay from 0 to 256 ns. Cascaded acousto-optic modulators (AOMs) shift the laser center frequency with 1kHz resolution, fine tuning the delay from 0 to 25ps

The conceptual diagram of our technique is shown in Figure 34. Inside the delay module, an input signal was wavelength converted before passing through dispersion compensating fiber (DCF). The DCF was used to generate a wavelength-dependent group delay. A wavelength converter after the DCF was used for near-wavelength maintaining phase conjugation of the signal, before it was passed through the DCF a second time. This double-pass allowed for compensation of the residual dispersion and a second relative group delay. The maximum amount of delay ($\Delta\tau$) can be determined by the product of the wavelength conversion bandwidth ($\Delta\lambda$) and the dispersion (D): $\Delta\tau \approx 2*D*\Delta\lambda$, where the factor of two comes from our taking advantage of the relative group velocity variation on both passes through the DCF. Accurate control of the delay requires accurate control over the wavelength of one of the pump lasers. Typical tunable laser sources can be tuned in steps of 1pm (~125 MHz) at 1550 nm. This translates into a delay resolution of ~15 ps for our system. For accurate control of wavelength, one of the pump lasers was passed through a pair of cascaded AOMs to precisely tune the laser's center wavelength using acousto-optic mixing. By cascading the AOMs, a frequency resolution of 1 kHz, far less than the 125 MHz of the laser, can be obtained.

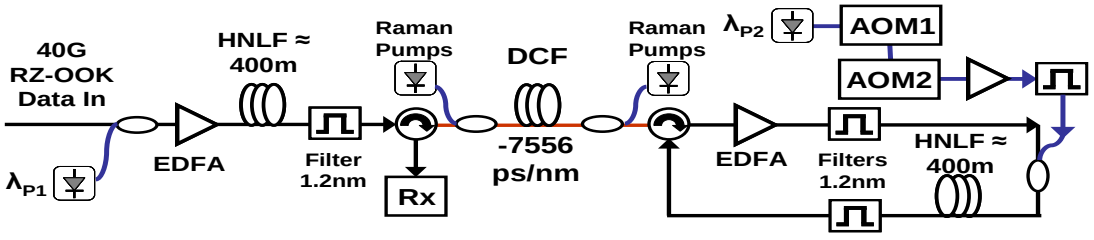

Figure 35. Block diagram. Dispersion compensating fiber (DCF), acousto-optic modulator (AOM), receiver (RX), and highly nonlinear fiber (HNLF)

An experimental block diagram of our setup is shown in Figure 35. A 40 Gb/s RZ-OOK signal was wavelength converted using highly nonlinear fiber (HNLF). A 1-pump four-wave-mixing

approach was used where the high power pump was swept in wavelength to control the location of the converted signal. The signal ($\lambda_0 \approx 1537$ nm) was up-converted from 1541 to 1558 nm. The converted signal was then filtered out and sent through the DCF (D = -7556 ps/nm) to impose a wavelength-dependent delay. Raman amplification in the DCF was used to compensate for the 22 dB of loss in the fiber. Following the DCF, the delayed signal was phase conjugated using a second piece of HNLF. Again, a 1-pump FWM approach was used to convert the signal ~4 nm up in wavelength. The signal was passed through the DCF a second time to compensate residual dispersion and to undergo a second wavelength dependent delay.

The wavelength of the second pump laser (λ_{P2}) was precisely controlled using two AOMs. The first modulator performs a +595 MHz ± 70MHz while the second performs a -530 MHz ± 65 MHz frequency shift. Frequency was controlled to a 1 kHz resolution. This gives a total frequency shift of $\Delta f = f_1 - f_2 = 0$ to 200 MHz. By adjusting the laser wavelength, coarse tuning from 0 to 256 ns of delay was achieved with ~15 ps resolution. By adjusting the AOMs, fine tuning of 0 to 25 ps was performed with <0.5 ps resolution.

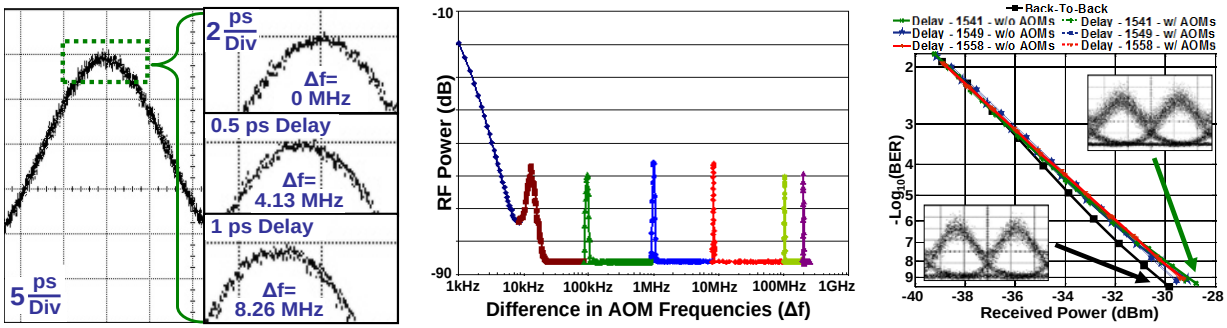

Figure 36. (a) 0, 0.5 ps, and 1 ps delay resolution of a single 40 Gb/s RZ-OOK bit. (b) RF-spectra showing optical mixing for different AOM frequency offsets. (c) Bit-error-rate curves for varying delay values with and without the AOMs

Figure 36(a) shows the fine tuning of our delay. A single 40 Gb/s RZ-OOK bit was delayed by 0, 0.5, and 1 ps using a frequency shift of 0, 4.13, and 8.26 MHz, respectively. Finer control of laser wavelength is shown in Figure 36(b) where the pump laser was split and recombined in a photodiode to show beat terms for varying frequency shifts. Due to the low frequency cutoff of the RF-spectrum analyzer, a minimum shift of 10 kHz is shown. Figure 36(c) shows bit-error-rate curves with and without the AOMs. No system penalty was induced by the use of the cascaded AOMs. A 1.2 dB penalty was noticed for the minimum and maximum delay values.

4.10. Tunable N-Fold Multicasting and Pulsewidth of 40 Gb/s Channels by Variable Periodic Slicing of a Supercontinuum

We have also demonstrated tunable n-fold multicasting and tunable temporal pulsewidth of 40 Gb/s channels using variable periodic slicing of a supercontinuum. A supercontinuum was generated and then filtered with a periodic filter, comprising a tunable differential group delay (DGD) element and a polarizer, to generate multicast copies of the original data. Continuous tuning of the DGD value provided continuous selection of the channel width/spacing and pulsewidth. In addition, polarization tuning within the tunable periodic filter gave the flexibility to tune the channel center wavelengths. We achieved 2-, 4-, 8-fold multicasting of the 40 Gb/s RZ-OOK waveform with average penalties of 0.1, 0.26, 0.44 dB, respectively, at 10^{-9} BER. [8]

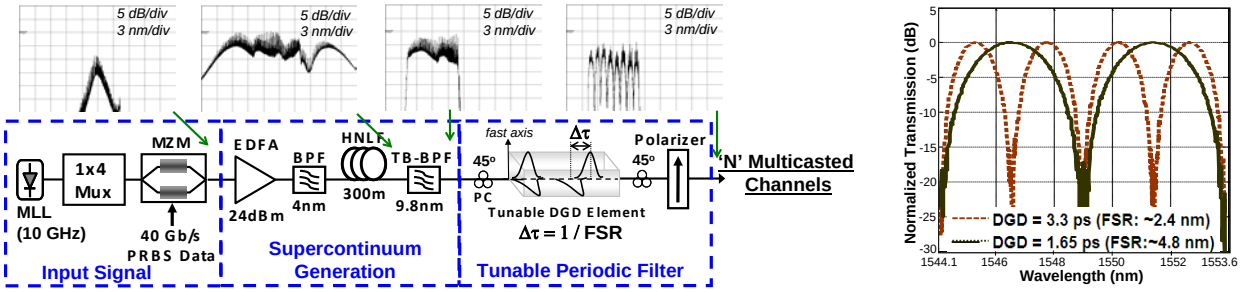

(a) (b)

Figure 37. (a) Conceptual and experimental diagram. A portion of the generated supercontinuum is sliced into channels by a tunable periodic filter. Tuning the differential group delay (DGD = $\Delta\tau$) tunes the free spectral range (FSR) of the filter which changes the multicasting order. (b) The filter transmission response for two DGD values. BPF: bandpass filter; MZM: Mach-Zehnder modulator; PC: polarization controller

The conceptual and experimental block diagram of our technique is shown in Figure 37(a). A short-pulse laser (at 1554.9 nm) with a repetition rate of 10 GHz and pulsewidth of ~2 ps was used at the transmitter. Following multiplexing to 40 GHz by an optical multiplexer (Mux), pulses were modulated using a Mach-Zehnder modulator driven by a 2^{15}-1 PRBS at 40 Gb/s. The modulated signal was then amplified and sent though a 300 m HNLF with a zero dispersion wavelength at ~1561 nm for supercontinuum generation. A portion of the generated supercontinuum was filtered with a tunable bandwidth bandpass filter (TB-BPF) set to ~9.8 nm bandwidth. This was then filtered by a tunable periodic filter (TPF) to achieve multicasting. A commercially available tunable DGD element and a polarizer were used to realize the TPF. In the TPF, we split the signal into orthogonal polarization states, delayed one using the tunable DGD element, and then beat the signals together at a polarizer resulting in a periodic raised-cosine filter. Figure 37(b) shows two settings of the DGD element (τ), which was tuned to change the number of output channels (multicasting order) since free spectral range (FSR) was equal to $1/\tau$. Multicasting order can also be varied by selection of the TB-BPF bandwidth. Furthermore, the center wavelength for the pass-bands can be changed by adjusting both polarization controllers in the TPF as shown in the inset of Figure 38(b). The TPF can be tuned to a narrower (wider) FSR to increase (decrease) the pulsewidth while preserving the multicasting order using a narrower (wider) portion of the supercontinuum by tuning TB-BPF.

Shown in Figure 38 are the experimental spectra of three different multicasting orders; 2-fold (a), 4-fold (b), 8-fold (c); along with the eye diagrams of the multicast channels. The DGD values were set to 1.65 ps, 3.3 ps, and 6.6 ps, respectively. Tunable slicing of the spectrum enabled changing the multicasting order where >25 dB channel crosstalk suppression was maintained. The inset in Figure 38(b) shows the tunability of the center wavelengths of the multicast channels by polarization tuning for the 4-fold multicasting case. Therefore, the multicast channels can be located at any wavelength within the supercontinuum portion.

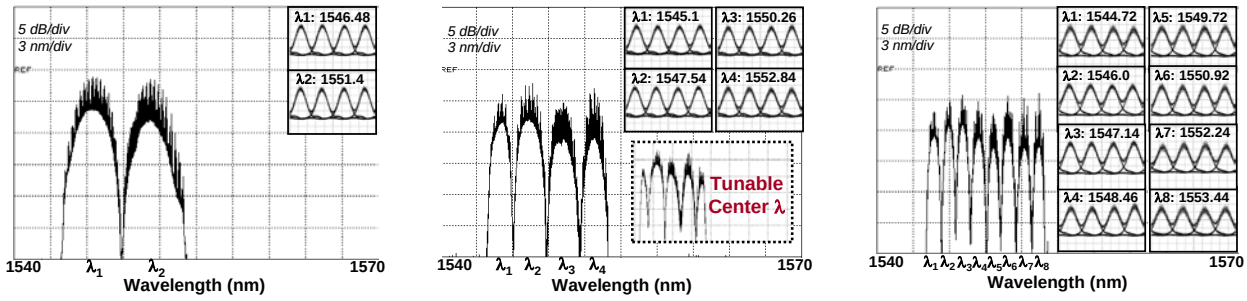

(a) (b) (c)

Figure 38. Multicast channel spectra and eye diagrams (after tunable periodic filter): (a) 2-fold (~4.8 nm/channel); (b) 4-fold (~2.4 nm/channel) Inset shows the tunability of the channel wavelengths by tuning polarization into and after the DGD element; (c) 8-fold (~1.2 nm/channel)

BER measurements were obtained for all multicast channels for 2-fold, 4-fold, and 8-fold multicasting by filtering each channel with a 4.8 nm, 2.4 nm, and 1.2 nm filter, respectively. Figure 39(a) shows the BER curves for the best and worst case performances along with the back-to-back (B2B) performance. Three different B2B curves were obtained by filtering the transmitted signal with the same filter used to extract the multicast channels. Figure 39(b) shows the power penalty (at BER of 10^{-9}) with respect to the relevant B2B performance. We have observed an average penalty of 0.1, 0.26, and 0.44 dB (0.2, 0.5, and 1.1 dB maximum) for 2-, 4-, and 8-fold multicasting, respectively. Shown in Figure 39(c) is the pulsewidth vs. DGD for a fixed supercontinuum portion (9.8 nm) along with the eye diagrams from an optical sampling scope.

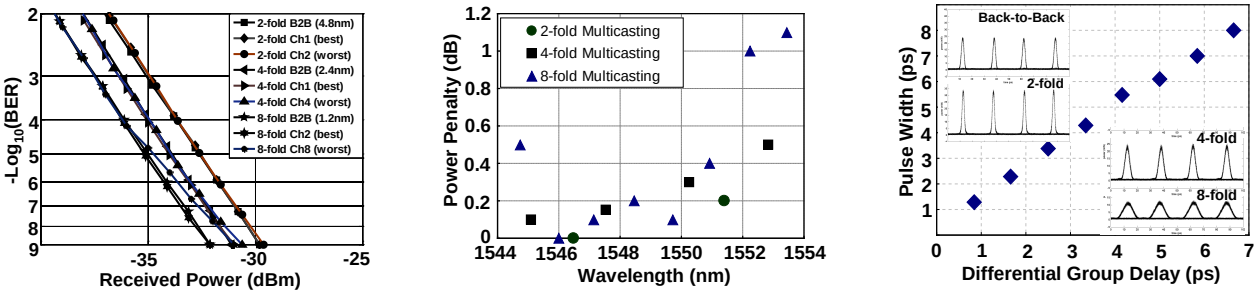

(a) (b) (c)

Figure 39. (a) BER performances (best and worst) for 2-, 4-, 8-fold multicasting. (b) Power penalty with respect to B2B of each channel for 2-, 4-, 8-fold multicasting. (c) Pulsewidth as a function of DGD along with eye diagrams of 2-, 4-, 8-fold multicast channels

4.11. 320-Gbit/s Optical Time Multiplexing of Two 160-Gbit/s Channels Using Supercontinuum Generation to Achieve High-Speed WDM-to-TDM

We have also demonstrated 320-Gbit/s optical time multiplexing of two 160-Gbit/s channels in a HNLF to achieve high-speed WDM-to-TDM conversion. Supercontinuum generation plus filtering, which eliminated the use of any pump, was used for the multiplexing process, and the

320-Gbit/s signal was then demultiplexed to 10-Gbit/s for BER measurement. Error free operation was achieved with < 3 dB power penalty at 10^{-9} BER. [7]

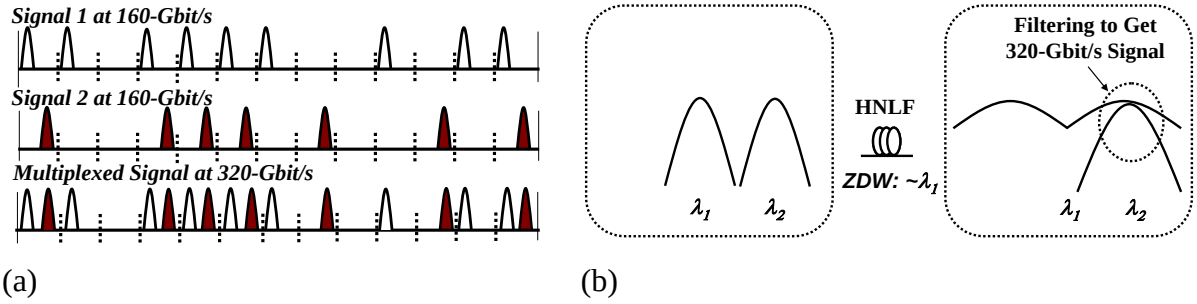

Figure 40. Concept. (a) time domain; (b) supercontinuum generation-based multiplexing in highly nonlinear fiber (HNLF) (frequency domain). ZDW: zero-dispersion wavelength

Figure 40(a) shows the concept of data multiplexing in the time domain while Figure 40(b) shows a conceptual diagram of the supercontinuum generation-based multiplexing scheme in the frequency domain. Two 160-Gbit/s signals (at λ_1 and λ_2), delayed relative to each other, were sent to an HNLF. At the output of the fiber, the spectra of both signals got broadened. By adjusting the power levels and choosing an appropriate HNLF, one spectrum got more broadened than the other and they got overlapped in the frequency domain, as shown on the right side of Figure 40(b). The two signals were offset in time so no interaction happened between them. By subsequently filtering out the overlapped portion, multiplexing of the signals could be achieved.

Figure 41 shows the experimental setup. At the transmitter, a short pulse laser at 1557 nm with a repetition rate of 10 GHz and pulse width of ~1.8 ps was used. Data modulation was applied using a MZM driven by a 2^{15}-1 PRBS at 10-Gbit/s. The signal was then amplified and sent into a 500 m HNLF for supercontinuum generation. Two portions of interest were filtered out by two ~5 nm optical bandpass filters (BPFs), centered at 1553 nm and 1561 nm respectively, to obtain two 10-Gbit/s signals at different wavelengths. The 10-Gbit/s signals were delayed relative to each other and multiplexed into two separate 160-Gbit/s signals using an optical multiplexer. Then the two 160-Gbit/s signals were sent to a 200 m HNLF, the zero-dispersion wavelength of which was ~1553 nm, followed by a 6 nm BPF at 1561 nm. The multiplexed 320-Gbit/s signal was then demultiplexed to 10-Gbit/s through a 1 km HNLF exploiting XPM induced frequency shift plus optical filtering. The 10 GHz pump pulses at 1547 nm used for the demultiplexing were generated by filtering the supercontinuum of the pulse source at the transmitter. The demultiplexed signal was then sent to a 10-Gbit/s pre-amplified receiver for BER measurement.

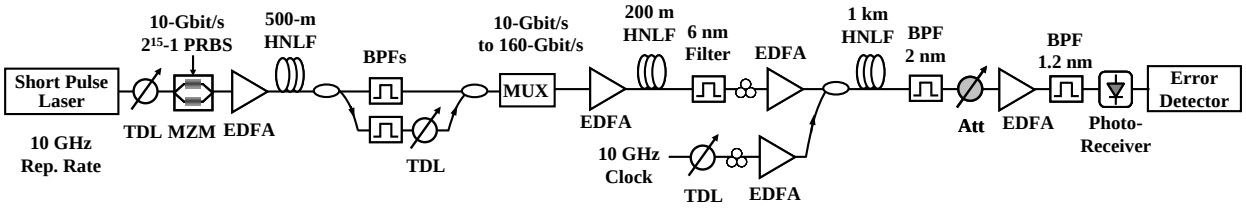

Figure 41. Experimental setup. TDL: tunable delay line; MZM: Mach-Zehnder modulator; BPF: bandpass filter; MUX: optical multiplexer; Att: optical attenuator

Figure 42(a) (left) shows the spectra before and after the 160-to-320-Gbit/s multiplexing. Figure

42(a) (right) shows the eye diagrams of the two 160-Gbit/s and the multiplexed 320-Gbit/s signals. The pulse width of the 160-Gbit/s signals was ~1.8 ps. The filtered 320-Gbit/s signal (with a pulse width of ~2 ps) at 1561 nm was coupled with a 10 GHz optical clock at 1547 nm (with a pulse width of ~1.5 ps) and then sent to the HNLF for demultiplexing. Figure 42(b) (left) shows the spectra before and after demultiplexing. Figure 42(b) (right) shows the eye diagrams of the demultiplexed 10-Gbit/s signals from 160-Gbit/s and 320-Gbit/s. Figure 42(c) shows the BER curves. A ~1 dB penalty at 10^{-9} BER was observed after the 10-Gbit/s supercontinuum generation for both channels. Around 4 dB penalty was then observed after the multiplexing to 160-Gbit/s and the subsequent demultiplexing to 10-Gbit/s. Note that we only show the BER curves for one channel in each stage. The penalty variation was within 1 dB, which was mainly due to the unequal power levels after the 10-to-160-Gbit/s multiplexing. The penalty of the 160-to-320-Gbit/s multiplexing was observed to be less than 3 dB. The BER curves of two demultiplexed channels are shown. The penalty variation between channels was observed to be less than 2 dB.

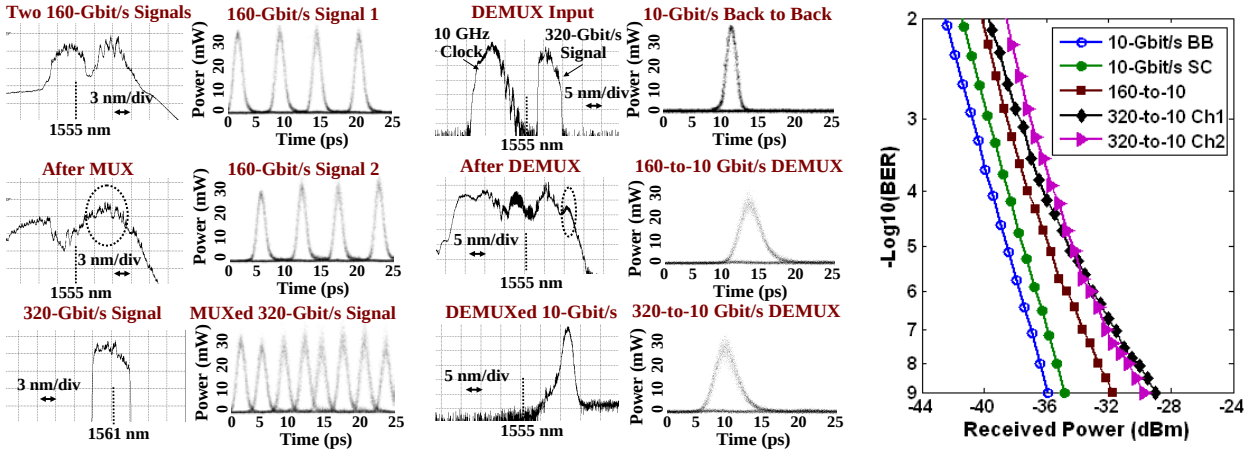

(a) (b) (c)

Figure 42. Experimental results. (a) spectra and eye diagrams before and after the multiplexing (MUX) stage; (b) spectra and eye diagrams before and after the demultiplexing (DEMUX) stage; (c) BER performance. BB: back to back; SC: supercontinuum generation

4.12. Optical Parametric Amplifier with >20 dB Gain over 110 nm Bandwidth

We have also demonstrated an optical parametric amplifier (OPA) with >20 dB gain over 110 nm bandwidth in a HNLF. A single pump operation was utilized where gain was measured by using a tunable seed laser. The gain was flattened by tuning the laser to a slightly shorter wavelength than the ZDW of the highly nonlinear fiber used. The gain flatness of ~4 dB was measured for 110 nm of 20 dB gain bandwidth.

Figure 43 shows the experimental setup used for the OPA experiment. A 100 m HNLF was used as the parametric gain medium. The HNLF has a ZDW of 1558.2 nm and the nonlinear coefficient is ~ 25 $(W.km)^{-1}$. The dispersion slope of the HNLF is 0.02 ps/nm and β4 is 0.2 10^{-55} s^4/m. A low β4 is essential for high bandwidth operation. Therefore, we have tested this HNLF prior to the use in the OPA. The measured four-wave mixing (FWM) efficiency over bandwidth is shown in Figure 44. The experimental setup used for the FWM test is similar to the OPA setup shown in Figure 43. However, the power levels were kept lower (~ 0-10 dBm). Wavelength

conversion efficiencies with ~3 dB flatness over ~210 nm was achieved with the 100 m HNLF as shown in Figure 44. The conversion efficiency had only ~1.5 dB fluctuations for the 100 nm proximity around the pump wavelength.

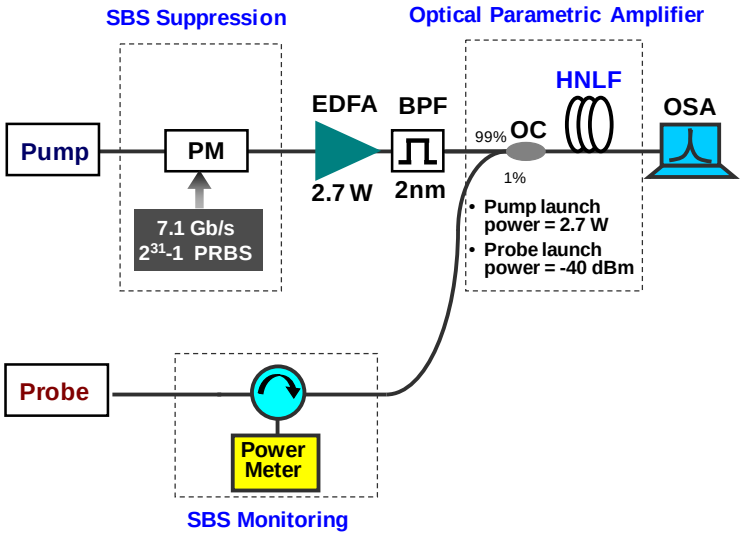

Figure 43. Experimental setup for the optical parametric amplifier

Figure 45 shows the measured gain profile of the parametric amplifier for three different pump wavelengths. The flattest gain was achieved with the pump laser located at 1558.05 nm. The measured gain was larger than 20 dB for over ~110 nm. The effect of the pump wavelength on gain and gain flatness can be seen in Fig. 45. The pump laser wavelength closer to the ZDW (1558.15 nm) provided much higher gain. However, the gain profile was not flat for this pump wavelength. When a pump laser further from the ZDW was used (1557.95 nm) the gain was flatter, however, the gain bandwidth and gain were both decreased. We have observed this tradeoff between the gain and the flatness and therefore we operated our OPA with a pump located at 1558.05 nm which provided >20 dB of parametric gain over ~110 nm with flatness ~ 4.5 dB.

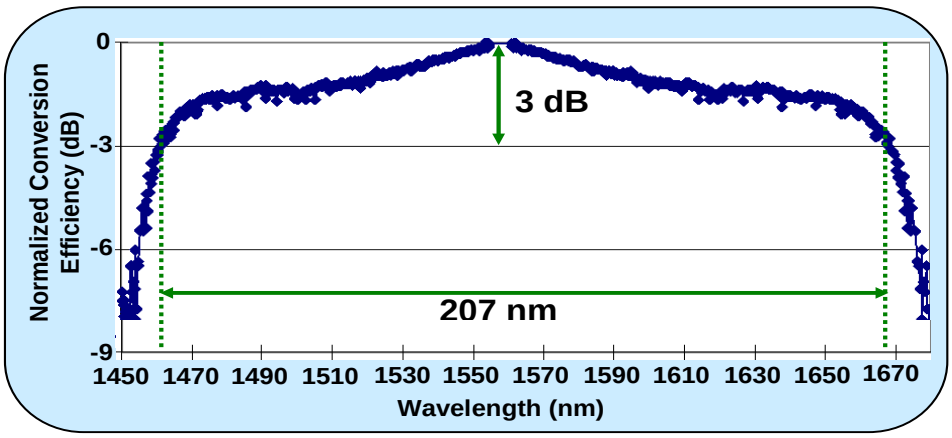

Figure 44. FWM efficiency test with the 100 m HNLF.

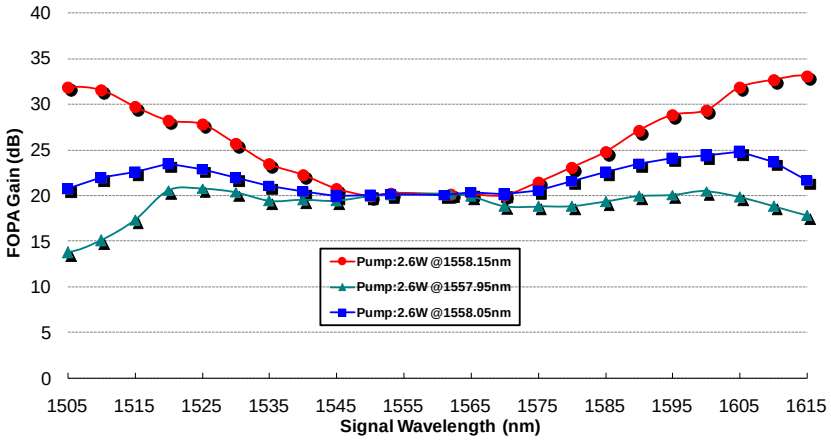

Figure 45. Gain profile of the OPA with three different pump wavelengths

For the OPA operation a tunable laser was used for the pump which was phase modulated with a 7.1 GHz PRBS signal generated by a signal generator to suppress the stimulated Brillouin scattering (SBS). The back reflected light due to SBS was monitored via a circulator placed in the signal arm. The SBS threshold was constantly monitored and the pump power was kept below the threshold. The phase modulated laser output was then amplified to 2.7 W and filtered with a 2 nm filter. It was then coupled with an idler signal with power ~ -40 dBm and both were sent to the HNLF and the output was monitored with an optical spectrum analyzer (OSA).

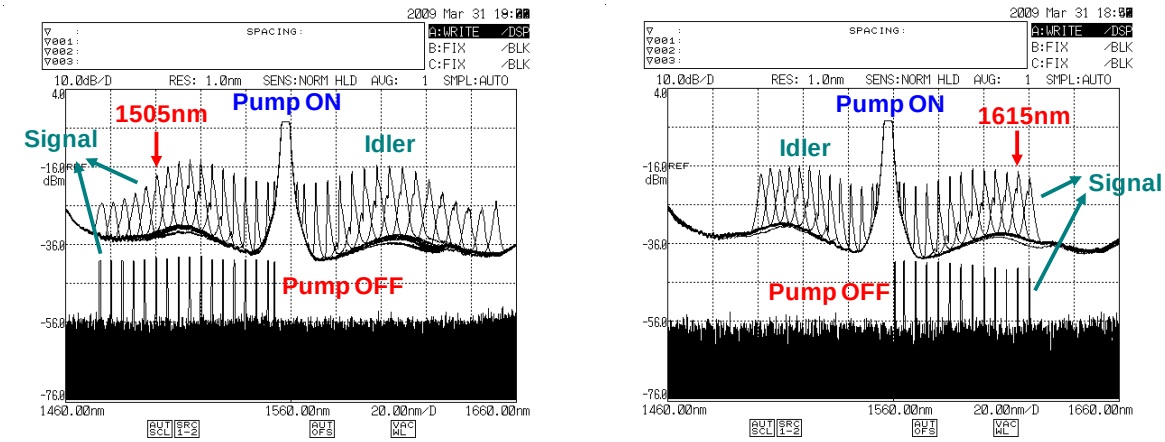

Figure 46. Generation of idler signal and amplified signal for various signal wavelengths. (a) Up-conversion; (b) Down-conversion

The parametric amplification results for signals at lower wavelengths and for signals at higher wavelengths than the pump wavelength are shown in Figure 46. Figure 46 (a) shows the up-conversion of the input signals where the generated idlers are located at symmetric wavelengths with respect to the pump. Similarly, for the case of input signals located at higher wavelengths, the idlers are generated at lower wavelengths symmetric to the pump as shown in Figure 46 (b). These results are taken with pump laser at 1558.05 nm, which results in the flattest gain profile over 100 nm.

4.13. 9-fold Multicasting of 21.4 Gbit/s DPSK Signal via Supercontinuum Generation

We have demonstrated 9-fold multicasting of a 21.4 Gbit/s time-division multiplexed (TDM) DPSK data channel using supercontinuum generation. A 12 nm supercontinuum out of DPSK modulated short pulses is generated in a HNLF and then filtered with a periodic filter, comprised of a tunable differential group delay element and a polarizer, to generate multicast copies of the original data. We achieved ~ 1.2 dB average penalty for the 9-fold multicasting of the 21.4 Gbit/s DPSK signal at 10^{-9} BER. [10]

The conceptual block diagram of supercontinuum multicasting is shown in Figure 47. A pulsed input data stream was encoded with DPSK data where each pulse had equal amplitude but the relative phase between adjacent pulses was either flipped by π to denote a "1" or kept constant for a "0". The signal was inserted close to the zero-dispersion wavelength (ZDW) of a HNLF. This allowed the spectral broadening to produce a supercontinuum based primarily on self-phase modulation (SPM) of the signal especially for low launch powers to the HNLF. The nonlinear phase shift of the signal due to the SPM when propagating through the fiber can then be approximated as $\varphi_{spm} = 2\gamma L_{eff} P_{in}$, where P_{in} is the total power of the signal into the fiber, L_{eff} is the effective length of the fiber, and γ is the nonlinear coefficient. This effectively creates a power dependent phase shift across each bit. As adjacent pulses had approximately the same envelope, the same phase shift profile (φ) was induced to the bits. At the output of the highly nonlinear fiber, the generated supercontinuum maintained the phase encoded data with only an identical phase shift for each bit for relatively low launch powers. Therefore, even with the time-varying phase shift, the relative 0 or π shift between the bits was maintained. The supercontinuum was then spectrally sliced by a tunable periodic filter (TPF) to produce the

multicast copies. By changing the bandwidth and center wavelength of the filter, the channel locations, bandwidths, and pulse widths of the multicast copies can be also tuned with this scheme.

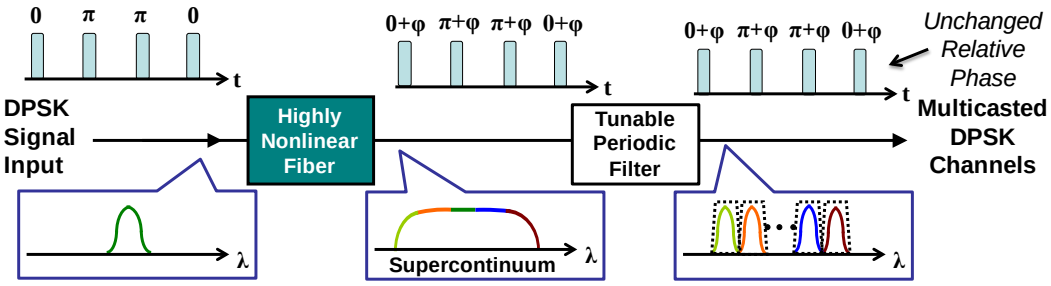

Figure 47. Conceptual block diagram of supercontinuum based wavelength conversion/multicasting of differentially phase encoded signals

An experimental block diagram of our setup is shown in Figure 48. A short-pulse laser (1558.6 nm, ~2.2 ps) with a repetition rate of 10.7 GHz was used at the transmitter. The pulses were first modulated using a phase modulator driven by a 2^{15}-1 PRBS at 10.7 Gbit/s. The modulated signal was then optically multiplexed to 21.4 Gbit/s by a polarization maintaining optical MUX. The 21.4 Gbit/s TDM DPSK signal was amplified to an average power of ~18 dBm and sent through a 500 m HNLF with a ZDW of ~1565 nm for supercontinuum generation. The spectrally broadened signal was sent to the TPF realized with a commercially available tunable differential group delay (DGD) unit and a polarizer. The polarization was tuned to be 45^{o} linear with respect to the fast/slow axis of the DGD element. The signal component projected on the slow axis was delayed by the DGD amount ($\Delta\tau$) with respect to the fast axis component. The two principal polarizations were then mixed back together using a polarizer also at 45^{o} linear to the DGD element. This can be thought of as a delay line interferometer (DLI) in the polarization domain and has a raised cosine transfer function with a free spectral range (FSR) of ~$1/\Delta\tau$. Thus, the output of the periodic filter spectrally slices the supercontinuum defining the multicast channels. The signals were spaced by ~150 GHz for a 6.6 ps DGD value. This can be tuned to modify the number of multicast channels at the output. The multicast signals were filtered by a 1.2 nm filter and sent to the receiver for BER measurements. In the receiver, a 10.7 GHz DLI was used for the demodulation of the 21.4 Gbit/s signal due to the non-phase stabilized nature of the MUX. The bit rate was matched to the FSR of the DLI for proper demodulation as the DPSK data was encoded in pulses as short as 2.2 ps. The demodulated DPSK signal was detected by a thresholding balanced receiver and sent to a BER tester (BERT).

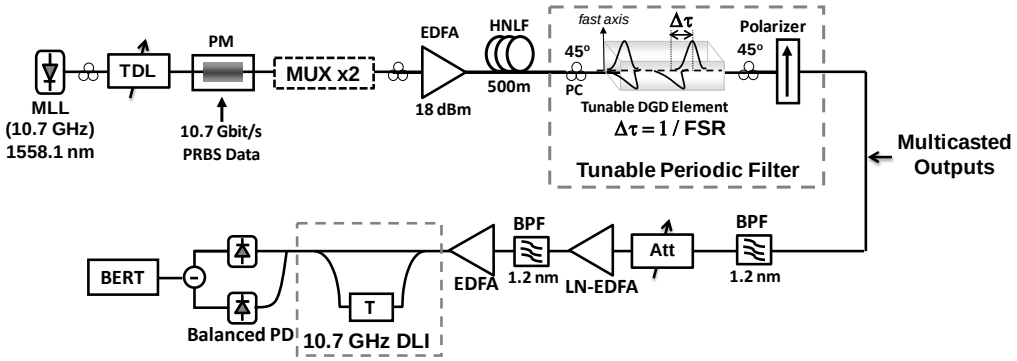

Figure 48. Experimental setup for wavelength conversion/multicasting of differentially encoded phase modulated signals using supercontinuum. A 10.7 Gbit/s DPSK signal is multiplexed to 21.4 Gbit/s using an optical multiplexer (MUX) prior to multicasting (TDL: tunable delay line; PM: phase modulator; BPF: bandpass filter; DLI: delay line interferometer, Att: attenuator; HNLF: highly nonlinear fiber)

For wavelength conversion of the 10.7 Gbit/s DPSK signal, the optical MUX was not employed. A similar setup was used for generation of the supercontinuum with an average launch power of ~15 dBm into the HNLF. Instead of the TPF, a 1.2 nm filter was used to slice a 10.7 Gbit/s DPSK channel out of the supercontinuum. For proper comparison of the BER performance, the back-to-back signal was also filtered by the 1.2 nm filter to match the received power.

Figure 49 shows the spectrum of a 10.7 GHz pulsed source before (a) and after (b) modulation and multiplexing to 21.4 Gbit/s. The generated supercontinuum of ~12 nm is shown in Figure 49(c) prior to periodic filtering. Figure 49(d) shows the nine channels multicast at the output of the TPF. The DGD setting was kept at 6.6 ps to generate channels with ~1.2 nm spacing. The multicast channels of the 21.4 Gbit/s DPSK signal were at wavelengths from 1553.7 nm to 1563.3 nm with 1.2 nm of separation. The eye diagrams of the multicast signals detected by a balanced photoreceiver are given in Figure 50. Traces obtained by an optical sampling scope of the phase modulated pulse train and the demodulated alternate-mark-inversion (AMI) signal right after the transmitter are shown in Figure 51(a), and (b), respectively. After demodulation the AMI signal had a pulsewidth of 2.7 ps. Figure 51(c) shows the demodulated AMI signals after filtering by a 1.2 nm filter and (d) the demodulated AMI signal of the channel 5 copy. The filtered signal at Figure 51(c) had a pulsewidth of 4.6 ps. The pulses of the multicast signals were further broadened to ~6 ps due to the additional filtering.

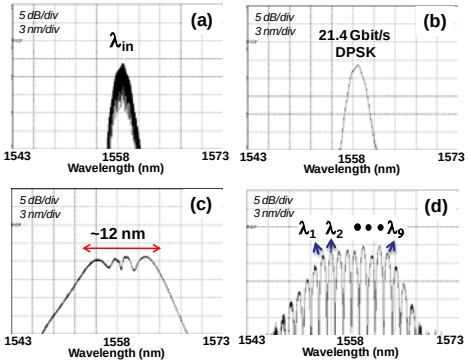

Figure 49. Spectra before (a) and after (b) DPSK modulation, after SC generation (c), and after multicasting by periodic filtering (d)

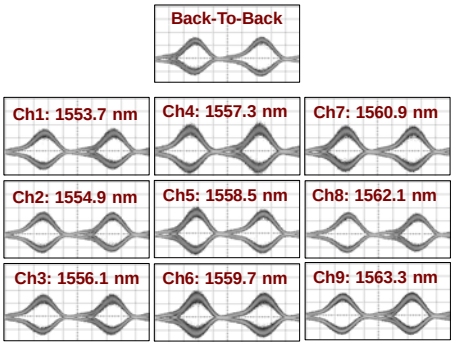

Figure 50. Eye diagrams of the multicast signals along with the transmitter signal detected by a 35 GHz balanced photoreceiver

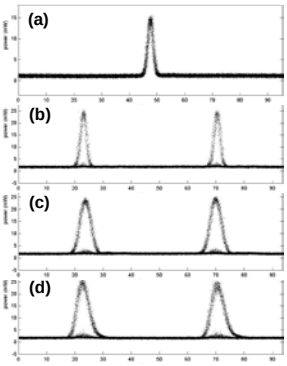

Figure 51. Optical sampling traces after modulation, demodulation, filtering, and multicasting (a-d)

BER measurements were obtained for all nine multicast RZ-DPSK channels as shown in Figure 52. The power penalty varied across the 12 nm supercontinuum from 0.5 dB to 2.8 dB. The power penalties for the multicast DPSK signals at a BER of 10^{-9} are shown in Figure 52(c). The output channels at or close to the dips in the supercontinuum spectrum exhibited relatively higher power penalty. Moreover, increasing the launch power into the HNLF resulted in significant degradation of the output signals. Figure 52(b) shows single channel wavelength conversion BER performances of a 10.7 Gbit/s DPSK signal and for the 21.4 Gbit/s TDM DPSK signal. We have not observed additional penalty due to the time multiplexing to 21.4 Gbit/s.

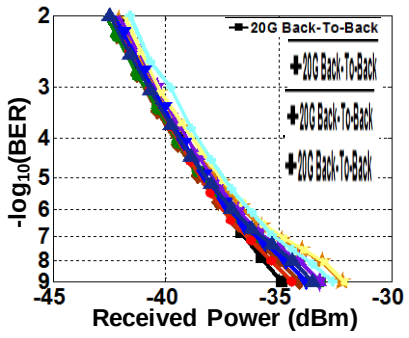

(a) 9-fold multicasting of a 21.7 Gbit/s DPSK signal to 1.2 nm spaced channels.

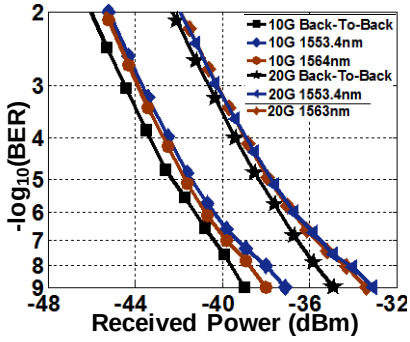

(b) Single channel wavelength conversion of 10 Gbit/s DPSK and 21.7 Gbit/s DPSK signal.

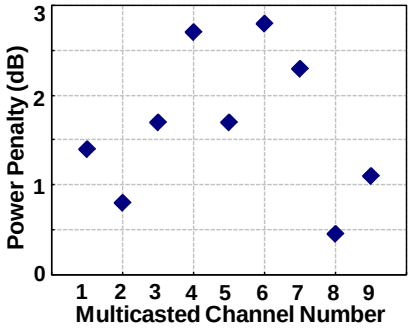

(c) Power penalty compared to the back-to-back performance for the multicast channels.

Figure 52. BER performances of the DPSK multicasting and wavelength conversion using supercontinuum generation

4.14. Controllable Optical Demultiplexing Using Continuously Tunable Optical Parametric Delay at 160-Gbit/s with <0.1 ps Resolution

We experimentally demonstrated the use of continuously tunable optical parametric delay at 160-Gbit/s based on the conversion/dispersion technique for 160-to-40-Gbit/s optical demultiplexing.

A 15.2 ns delay was shown for a 160-Gbit/s signal, with <0.1 ps resolution achieved by inserting cascaded acousto-optic modulators (AOMs) after the pump laser for delay fine tuning. 3-6 dB penalty was introduced by the delay line. [11]

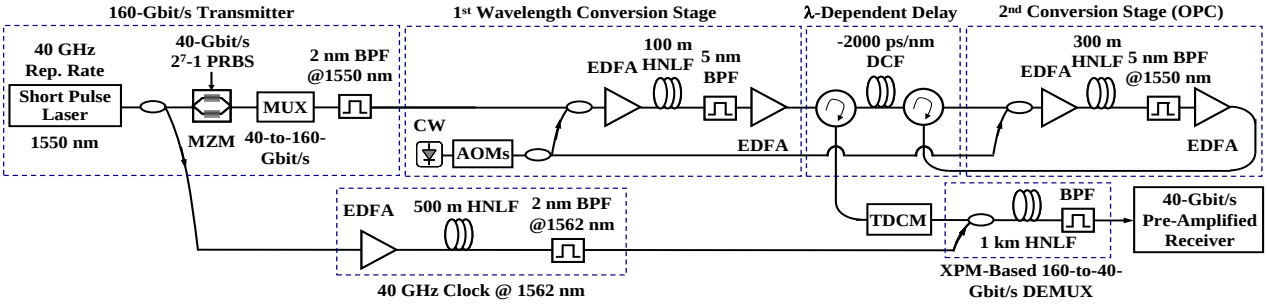

Figure 53. Experimental setup: MUX: multiplexer, BPF: bandpass filter, AOM: acousto-optic modulator, HNLF: highly non-linear fiber, DCF: dispersion compensating fiber, OPC: optical phase conjugation, XPM: cross-phase modulation, DEMUX: demultiplexer

The experimental setup is shown in Figure 53. A short pulse laser at 1550 nm with a repetition rate of 40 GHz and pulse width of ~1.5 ps was modulated using a MZM driven by a 40-Gbit/s 27-1 PRBS. Then a 40-to-160-Gbit/s fiber-based PRBS maintaining multiplexer was used to produce the 160-Gbit/s signal. The signal was then converted via FWM in a 100 m piece of HNLF. After being filtered out, the converted signal was then sent through ~6.8 km of DCF (-2000 ps/nm) to impose a wavelength-dependant delay. The delayed 160-Gbit/s signal was converted back to the original wavelength using FWM in a 300 m HNLF. The wavelength of the continuous wave (CW) pump laser, which had a resolution of 1 pm (corresponding to ~ 4 ps (>1/2 160-Gbit/s bit) delay resolution), was precisely controlled using a pair of cascaded AOMs [7, 8], which gave a resolution of ~1 kHz (corresponding to <1 fs delay resolution). Note that OPC was realized in the wavelength conversion scheme, so that dispersion was compensated when passing back through the same dispersive element. Since the dispersion slope could not be compensated by double passing, a tunable dispersion compensating module (TDCM) at 1550 nm with a +/- 30 ps/nm tuning range and 1 ps/nm resolution was used to minimize residual dispersion. The compensated 160-Gibt/s output was combined with a 40 GHz optical clock with ~2.3 ps pulsewidth for demultiplexing using cross-phase modulation (XPM) introduced frequency shift and BER measurements. The optical clock was obtained by SPM spectral broadening the original short pulse laser in a 500 m HNLF and then filtering at 1562 nm.

Shown in Figure 54 (a) is the relative delay of the system as a function of the converted wavelength. The 160-Gbit/s delay achieved was ~15.2 ns covering 7.5 nm from 1559 to 1566.5 nm, which was mainly limited by the wavelength of the TDCM, EDFA bandwidth and filter tuning range. The pump laser had a resolution of 1 pm (~125 MHz), which corresponded to 2 pm in converted wavelength change and translated into a delay resolution of ~4 ps in our system. By inserting a pair of AOMs after the pump laser, a much finer resolution could be achieved. Figure 54 (b) shows the fine tuning of the delay, in which the top is a 160-Gbit/s signal as reference, the middle is after the AOMs with a shift of ~3.12 MHz (~0.1 ps delay), and the bottom is when the pump laser is shifted by 1 pm (~4 ps delay). Shown in Figure 54 (c) are the optical spectra after both the 1st and 2nd conversion stages at 0 ns relative delay. The signal was converted to ~1559 nm in the 1st stage. After passing through the DCF, the signal was phase conjugated and converted back to the original wavelength in the 2nd stage. Similarly, Figure 54 (d) shows the

optical spectra at ~14 ns relative delay.

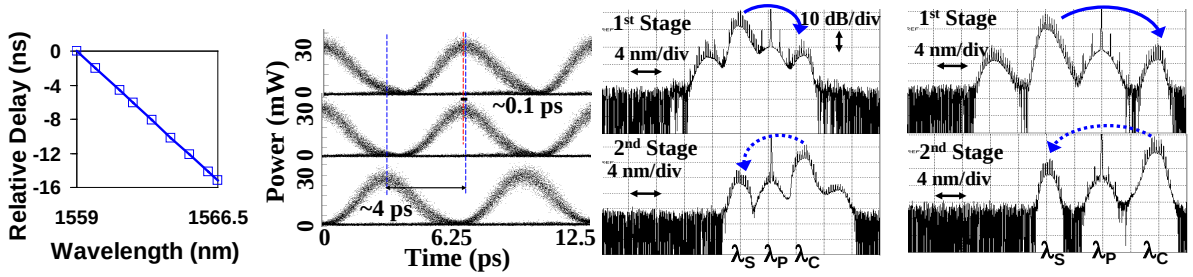

(a) Relative delay vs. wavelength (b) Fine tuning of delay (c) λ_C=1559 nm (0 ns delay) (d) λ_C=1566 nm (14 ns delay)

Figure 54. (a) Relative delay vs. converted wavelength (λ_C), (b) Fine tuning of delay: (top) a 160-Gbit/s signal as reference, (middle) AOMs shifted by ~3.12 MHz, (bottom) laser shifted by 1 pm (~125 MHz), and (c)-(d) Optical spectra at different converted wavelengths. λ_S: 1550 nm, λ_P: pump wavelength

To assess the performance of the tunable delay, we demultiplexed the 160-Gbit/s signal to 40-Gbit/s and measured the BER. Shown in Figure 55 are the BER curves of the back to back 40-Gbit/s signal and the 160-Gbit/s signals before and after the tunable delay, and the corresponding eye diagrams. A ~3 dB penalty was observed after the 160-Gbit/s signal (without passing through the delay) demultiplexed to 40-Gbit/s, mainly due to the non-ideal sampling pulses generated by filtering the SPM broadened spectrum and the long HNLF (1 km) used for demultiplexing. The tunable delay line introduced another 3-6 dB penalty. We attributed the penalty to the nonlinear processes and residual dispersion and dispersion slope in the tunable delay line. Note, for clarity, we only plot the BER curve of one tributary at a specific converted wavelength. The penalty variations were within 1 dB, partially due to the non-ideal optical multiplexing at the transmitter.

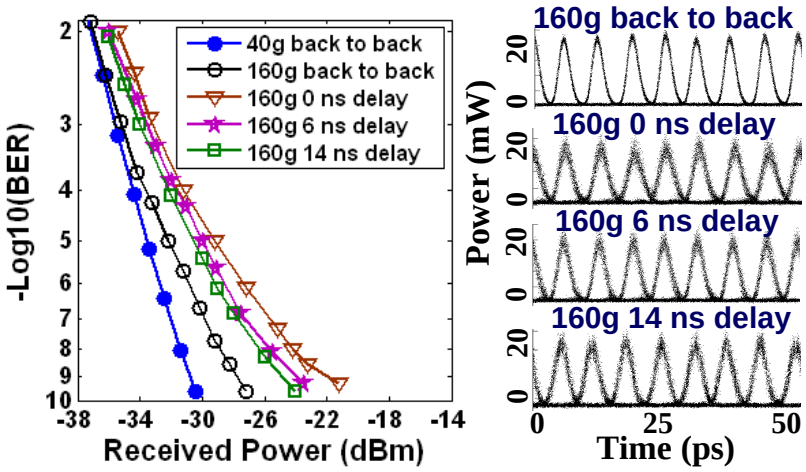

Figure 55. BER performance of the 160-Gbit/s parametric delay

We then used the conversion/dispersion based tunable optical delay for controllable optical demultiplexing. Figure 56 shows the importance of a fine delay control and quantifies the power penalty versus the delay offset between the 160-Gbit/s signal and 40 GHz sampling pulses. We

observed ~3 dB penalty when the delay was off by ~1.2 ps. As the delay offset increased, the power penalty grew rapidly, resulting in a ~8.5 dB power penalty when the offset was ~2.5 ps. The eye diagrams corresponding to 3 different offsets are inserted in the figure. Clearly, fine control of delay was critically important in maintaining the system performance especially in high-speed optical systems, i.e. beyond 100-Gbit/s.

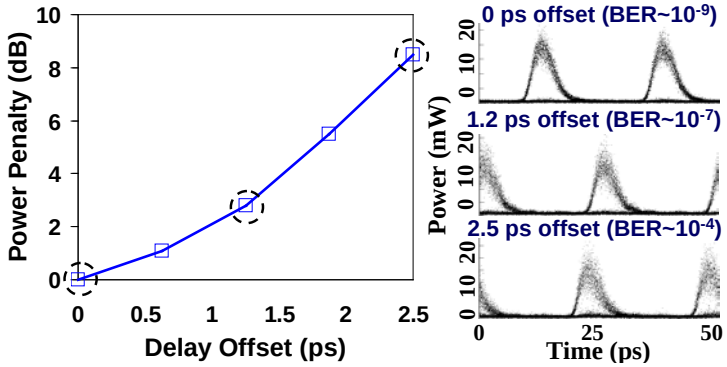

Figure 56. Controllable optical demultiplexing: penalty vs. delay offset between 160-Gbit/s signal and 40 GHz sampling pulses, and the corresponding demultiplexed 40-Gbit/s eye diagrams

4.15. Bit-Rate-Variable and Order-Switchable Optical Multiplexing of 160-Gbit/s PRBS Data Using Tunable Optical Delays

We further demonstrated bit-rate-variable and order-switchable optical multiplexing of 160-Gbit/s PRBS data. By using switchable optical delays and conversion dispersion based tunable delay, we were able to switch the order between 7 and 15, and tune the bit rate to accommodate up to 7% forward-error-correction (FEC) overhead, i.e. rate tuning from 160-Gbit/s to 171.2-Gbit/s. [12]

OTDM is typically performed using fixed fiber delay lines to split a lower rate channel into multiple copies that are time shifted by a required amount before being re-combined into a single, higher-rate channel. Unfortunately, once the delay lines are fixed, this method produces a true PRBS only for the specifically designed rate and PRBS order. Figure 57 is the conceptual diagram of the proposed PRBS generation scheme. A short-pulse optical PRBS signal was split into two copies, delayed relative to each other via switchable optical delay lines. Each delay had ~1 ns tunability. The multiplexed signal was then split into two paths again, one of which had a fixed delay and a conv./disp. based tunable delay. Inside the conv./disp. tunable delay, the original signal was wavelength-converted and passed through a dispersive element. Depending on the converted wavelength, the signal experienced a wavelength-dependent group delay. Then the signal was converted back to the original wavelength for dispersion compensation. When the wavelength separation and therefore delay was appropriately selected, the result was a true PRBS data stream with a tunable rate. For PRBS orders lower than 15, the delays required to maintain the PRBS were relatively small and could easily be achieved by tuning the 2^{15}-1 PRBS multiplexer.

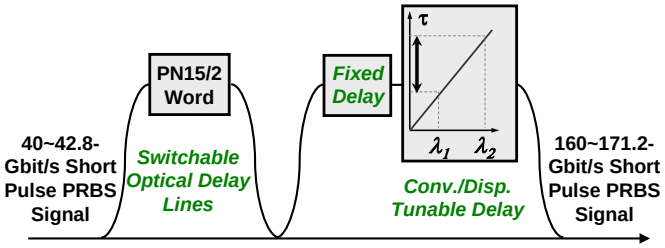

Figure 57. Conceptual block diagram of tunable PN order multiplexing

The experimental setup is shown in Figure 58. At the transmitter, a short pulse laser at 1550 nm with a repetition rate of 40~42.8 GHz and pulse width of ~1.5 ps was used. Data modulation was applied using a MZM driven by a 2^{15}-1 or 2^{7}-1 PRBS at the appropriate rate. After passing through the stage with switchable delays, the 80~85.6 Gbit/s signal was then split into two paths, one of which passes through the conv./disp. based tunable delay. The signal was converted via FWM in a 100 m piece of HNLF. After being filtered out, the converted signal was then sent through ~6.8 km of DCF (-2000 ps/nm) to impose a wavelength-dependant delay. The delayed signal was converted back to the original wavelength using FWM in a 300 m HNLF. Note that phase conjugation was realized

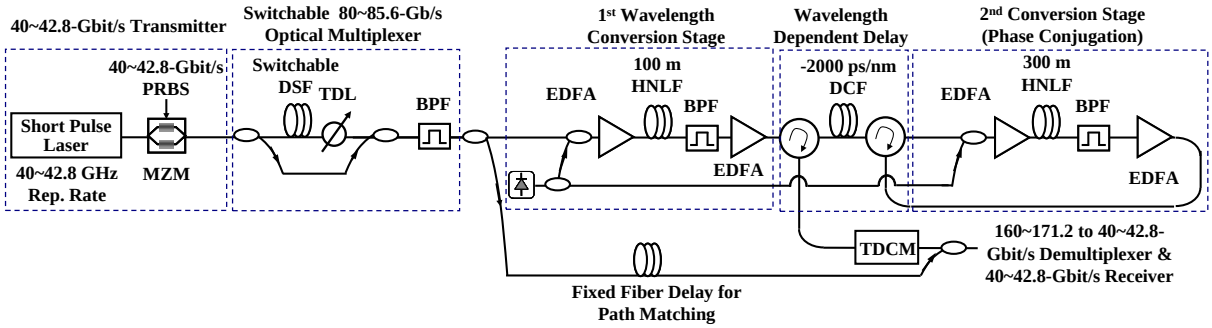

Figure 58. Experimental setup: TDL: tunable delay line, DSF: dispersion shifted fiber, BPF: bandpass filter

in the wavelength conversion scheme, so the dispersion was compensated when passing back through the same dispersive element. Since the dispersion slope could not be compensated by double passing, a TDCM with +/- 30 ps/nm tuning range and 1 ps/nm tuning resolution was used to minimize residual dispersion. The output of the TDCM was combined with the undelayed 80~85.6- Gbit/s tributary to generate a 160~171.2-Gbit/s PRBS, which is then demultiplexed for BER measurements. Shown in Figure 59 (a) is the relative delay of the system as a function of the converted wavelength. Note that we utilized just a portion of the delay curve for the PRBS multiplexing. We first considered 1558.5 nm as a reference and adjust the path (fixed delay in Figure 57) to give 2^{15}-1 PRBS at 160-Gbit/s. The required delays were ~6 ns and ~13.4 ns to add 3% (i.e. 164.8-Gbit/s) and 7% FEC (i.e. 171.2-Gbit/s) respectively. This corresponded to ~3 nm and ~6.7 nm shifts from 1558.5 nm. Shown in Figure 59 (b) are the optical spectra after both the 1st and 2nd wavelength conversion stages for 160-Gbit/s 2^{15}-1 PRBS multiplexing. The signal was converted to ~1558.5

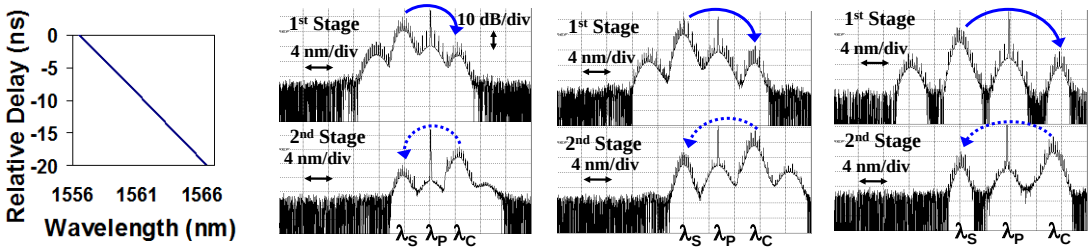

(a) Conv./disp. optical delay (b) 160-Gbit/s (c) 164.8-Gbit/s (d) 171.2-Gbit/s

Figure 59. (a) Relative delay vs. converted wavelength (λ_C) and (b)-(d) Optical spectra at different converted wavelengths for PRBS rate tuning: (b) λ_C=1558.5 nm, (c) λ_C=1561.5 nm, (d) λ_C=1565.2 nm, with λ_S fixed at 1550 nm

nm by placing the pump at ~1554.25 nm in the 1st stage. After passing through the DCF and by sharing the same pump, the signal was phase conjugated and converted back to the original wavelength in the 2nd stage. Similarly, shown in Figure 59 (c) and (d) are the optical spectra for 164.8-Gbit/s and 171.2-Gbit/s 2^{15}-1 PRBS multiplexing, respectively. By slightly tuning the pump wavelength, 2^7-1 PRBS at different rates could be achieved similarly.

To assess the performance of the multiplexed PRBS, we demultiplexed the signal to 40~42.8-Gbit/s and measured the BER. Shown in Figure 60 are the BER curves of 160-Gbit/s 2^{15}-1 PRBS and corresponding eye diagrams. For the tributaries that did not pass through the conv./dips. delay line, ~5 dB penalty was observed, mainly from demultiplexing and the beating with the noise from the tributaries that pass through the tunable delay line. A ~9 dB penalty was observed for tributaries that pass through the tunable delay line. We attributed the extra ~4 dB penalty to the nonlinear processes and residual dispersion in the delay line. Figure 61 shows the RF spectra before and after PRBS multiplexing for different cases. Prior to multiplexing, the RF spectrum consisted of equally spaced tones separated by ~(symbol rate)/(word length), i.e. (80-Gbit/s)/(2^{15}-1). After multiplexing, the tone spacing was increased by a factor of 2, i.e. (160-Gbit/s)/(2^{15}-1), showing that proper multiplexing was achieved. Note that for inaccurate bit shifts the tones at odd integers of tone spacing increased rapidly, as shown in Figure 61.

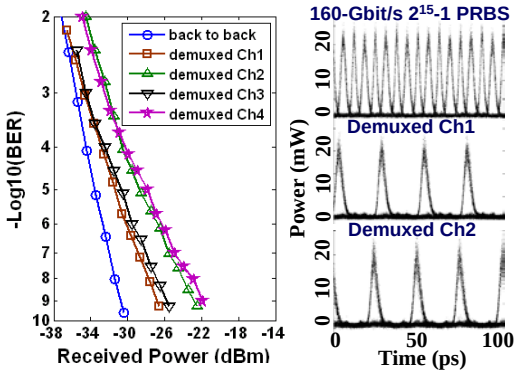

Figure 60. 160-Gbit/s 2^{15}-1 PRBS BER performance

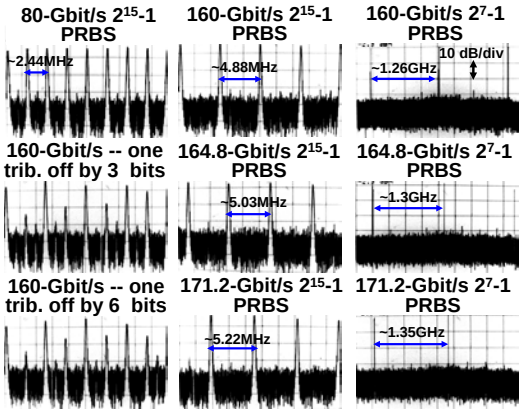

Figure 61. RF spectra showing the successful multiplexing to 160~171.2-Gbit/s PRBS with the order of 15 and 7

4.16. 8-Fold Multicasting of a 100 Gb/s Polarization-Multiplexed OOK Signal using Highly Nonlinear Fiber

We experimentally demonstrated 8-fold multicasting of a 100 Gb/s polarization-multiplexed OOK data signal to 200 GHz spaced copies using HNLF. DFWM in a bi-directional wavelength conversion scheme was employed for multicasting. This scheme allows for the signal polarizations to be treated independently for multicasting of a Pol-Mux'ed signal. Wavelength conversion over 45 nm with ~1 dB multicasting flatness and 8-fold multicasting with an average power penalty of ~4 dB at a BER of 10^{-9} was obtained. Furthermore, the effect of multicasting order and crosstalk on the multicasting performance was measured.

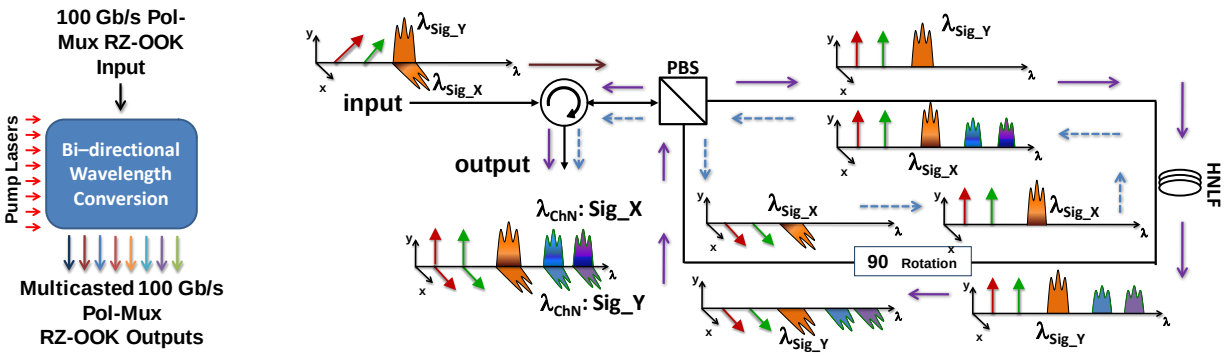

Figure 62. Conceptual block diagram and optical spectrum of the bi-directional wavelength conversion scheme used for multicasting

The conceptual block diagram of this technique is illustrated in Figure 62. A polarization multiplexed signal and continuous wave (CW) pumps aligned at 45° linear relative to the signal axis are inserted into the bi-directional four-wave-mixing (FWM) setup through a circulator. A polarizing beam splitter/combiner (PBS/PBC) separates the signal into the X and Y polarizations while the CW pumps are split between the two polarizations. The X-polarization traverses the loop counterclockwise following the path of the dashed arrows. It first undergoes a 90° rotation so that the pumps and signals are aligned to the Y-polarization axis before passing through the

HNLF. After passing through the HNLF, copies of the data are generated according to the degenerate FWM relationship, $f_{Ch\_X} = 2 f_{Sig\_X} - f_{CW\_X}$. Similarly, the Y-Polarization travels in the opposite direction (clockwise) as shown by the solid arrows. It first passes through the HNLF to generate the multicast copies of its data before being rotated by 90° so that it can pass backwards through the PBC. After passing back through the polarizing beam combiner, the recombined signal is directed out by the circulator. This output signal now contains the multicast copies of the original Pol-Mux'ed signal and scalable by the number of CW pumps. The setup yields polarization insensitive wavelength conversion.

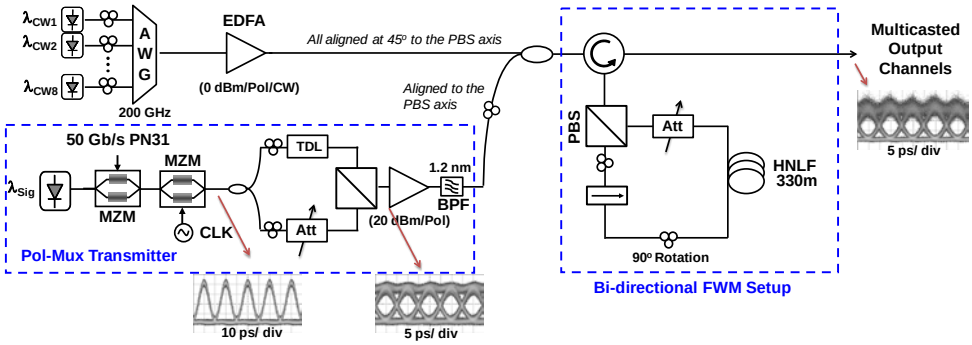

Figure 63. Experimental setup for the 8-fold multicasting of the 100 Gb/s Pol-Mux'ed RZ-OOK signal. (PBS: polarization beam splitter; TDL: tunable delay line; BPF: bandpass filter; Att: attenuator)

An experimental block diagram of our setup is shown in Figure 63. A 50 Gb/s OOK signal (λ_{Sig} = 1562 nm) was generated using a MZM driven by a 2^{31}-1 PRBS data. Full-rate pulse carving by an MZM was used to produce a 50% return-to-zero (RZ) waveform. The signal was split by a 3-dB coupler and one copy is delayed by a TDL in order to decorrelate and insert a half-bit time offset between the two copies prior to multiplexing in a PBC. An attenuator was used to equalize the two signal components of the resulting 100 Gb/s Pol-Mux RZ-OOK signal. The polarization extinction ratio of the PBC was measured to be ~22 and ~23 dB for the two ports. Eight CW lasers separated by 200 GHz (λ_{CW1} ~1549.6 nm to λ_{CW8} ~1538 nm) were coupled by an arrayed waveguide grating (AWG) and amplified by an EDFA. The Pol-Mux'ed signal was amplified by an EDFA and filtered by a 1.2 nm BPF prior to coupling with the CW lasers using a 3-dB coupler. A circulator followed by a PBS was used to send (receive) the signal and the pumps to (from) the 330 m HNLF. The HNLF zero dispersion wavelength is ~1562 nm with a dispersion slope of 0.026 ps/nm^2/km and has a nonlinearity coefficient of 25 (W×km)$^{-1}$. The polarization of the input Pol-Mux signal was aligned to the principal axis of the PBS. The polarizations of the CW lasers were also tuned to be linearly polarized at 45^o to the PBS axis. Hence, the two components of the input Pol-Mux'ed signal were counter propagated along with 8 pumps in the HNLF. A polarizer aligned with one of the PBS axis was also inserted in the resulting loop in order to increase the polarization extinction ratio. The multicast copies of each polarization component were generated at the corresponding output of the HNLF by the degenerate FWM process. A polarization controller (PC) was used in order to rotate the signal polarizations by 90^o in the loop. A tunable attenuator was used to match the power of the two directions. The launch power of each polarization component was approximately 20 dBm while the CW laser powers were ~0 dBm.

The multicast polarization components of the 100 Gb/s Pol-Mux signal were combined by the PBS and collected at the output of the circulator. The multicast channels (Ch1 – Ch8) were then filtered individually by a 1.2 nm filter. Each polarization component was demultiplexed by a PBS and sent to a preamplified receiver for BER measurements, while the other was monitored on a sampling scope.

The optical spectrum at the output of the circulator for the 8-fold multicasting is shown in Figure 64(a). The multicast copies of the 100 Gb/s Pol-Mux'ed RZ-OOK signal (Ch1 to Ch8) were located at wavelengths from 1574.35 nm to 1586 nm with 200 GHz channel spacing. The multicasting flatness was measured to be less than 1 dB. Shown in Figure 64(b)-i are the close-up spectrum of the multicast output channels, where Figure 64(b)-ii shows the same when λ_{CW4} is turned off. The presence of an undesired mixing product(s) with a power ~25 dB less than the multicast channel outputs is visible from the Figure 64(b)-ii. The Figure 64(c) shows the captured time elapsed eye diagrams of both polarization components (polarization X and polarization Y) of the eight multicast 100 Gb/s Pol-Mux'ed signals along with those of the input 100 Gb/s Pol-Mux'ed signal.

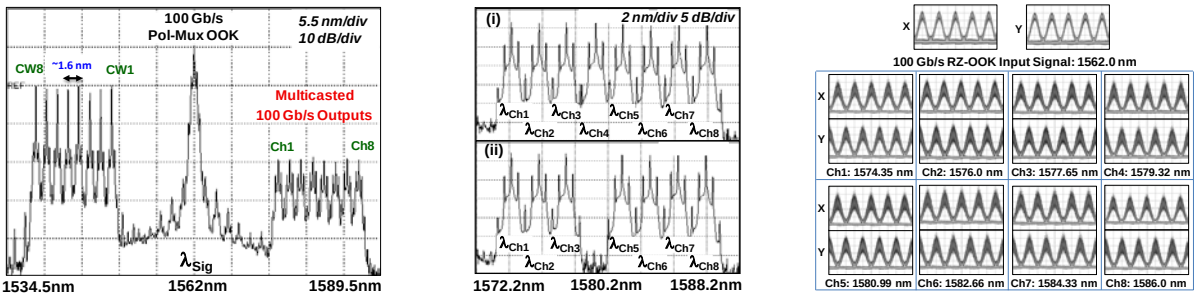

(a) (b) (c)

Figure 64. Experimental results for 8-fold multicasting. (a) Spectrum at the circulator output (after the HNLF) showing eight copies of the 100 Gb/s RZ-OOK signal; (b) i-close-up of the output channel spectrum, ii-close of the output channel spectrum when channel 4 (Ch4) is off; (c) Eye diagrams of both polarizations of the multicast copies

BER measurements were obtained for all eight multicast 100 Gb/s channels. Figure 65(a) shows the BER curves for both polarization components of the output channels along with the back to back performance of each polarization. We observed an average of ~4 dB power penalty (at a BER of 10^{-9}) for the 8-fold multicasting scheme. The power penalties for the both components of the multicast Pol-Mux'ed signals are shown in Figure 65(b). The worst performance was for Ch4 with a 4.6 dB power penalty. Figure 65(c) shows the results of power penalty (for Ch4) vs. multicasting order measurements, where the CW powers were kept constant at 0 dBm. The single channel wavelength conversion power penalty was ~1.8 dB. The triangles show the power penalty when closest neighboring channels – Ch3, Ch5, Ch2, Ch6…- are turned on in sequence. The circles show the power penalty when Ch3 and Ch5 were kept off. A slight increase in the power penalty is observed when Ch2 and Ch6 were turned on (triangles), suggesting a contribution of the crosstalk from those channels. This crosstalk contributed to a ~0.8 dB additional power penalty on Ch4 when compared to multicasting when the neighboring channels were off.

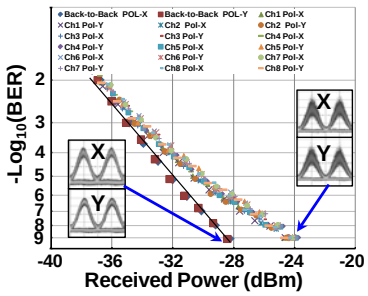

(a) BER measurements of the eight 100 Gb/s multicast channels.

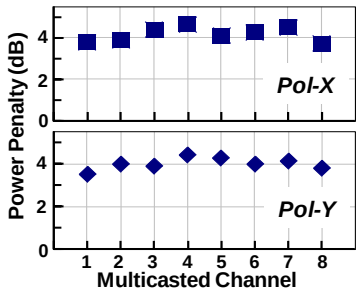

(b) Power penalty (10^{-9} BER) of both polarization components for multicast copies.

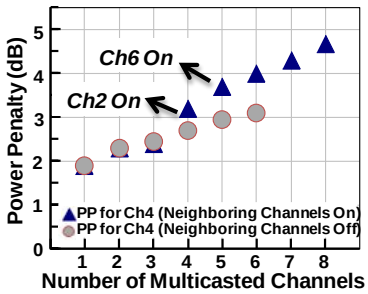

(c) Power penalty (for Ch4) vs. number of multicast channels (multicasting order).

Figure 65. Performance of the 8-fold multicasting of 100 Gb/s Pol-Mux'ed RZ-OOK signals

4.17. Demonstration of All-Optical Polarization Multiplexing and Polarization Demultiplexing between Two 50 Gb/s Channels and a Single 100 Gb/s Channel

We experimentally demonstrated all-optical polarization multiplexing and polarization demultiplexing between two 50 Gb/s channels and a single 100 Gb/s channel. Orthogonal pumps in a bidirectional highly nonlinear fiber (HNLF) loop were used to both demultiplex a single 100 Gb/s Pol-Mux channel into two 50 Gb/s WDM channels and multiplex two 50 Gb/s WDM channels into a single 100 Gb/s Pol-MUX channel. Both OOK and DPSK were shown with no measurable penalty for demultiplexing and <2 dB penalty for multiplexing. [18]

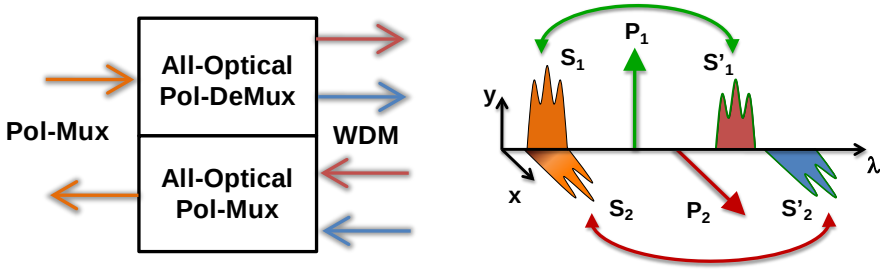

Figure 66. Conceptual diagram of all optical polarization demultiplexing and polarization multiplexing

Shown in Figure 66 is a conceptual diagram of our technique. Two orthogonally polarized pumps, P_1, P_2, are separated in wavelength and used to independently operate on each of the polarization channels of a Pol-MUX signal. Using FWM in HNLF, the X- and Y-polarized channels, S_1 and S_2, are demultiplexed and converted to two new wavelengths resulting in the WDM channels S'_1 and S'_2. The reverse process is also available where the two WDM signals, S'_1, S'_2, are converted and multiplexed to a single wavelength except on orthogonal polarizations. In this manner, WDM channels can be combined into a single Pol-MUX channel to double their spectral efficiency while a Pol-MUX channel can be demultiplexed for use in a traditional WDM network or for independent routing or processing of its sub-channels.

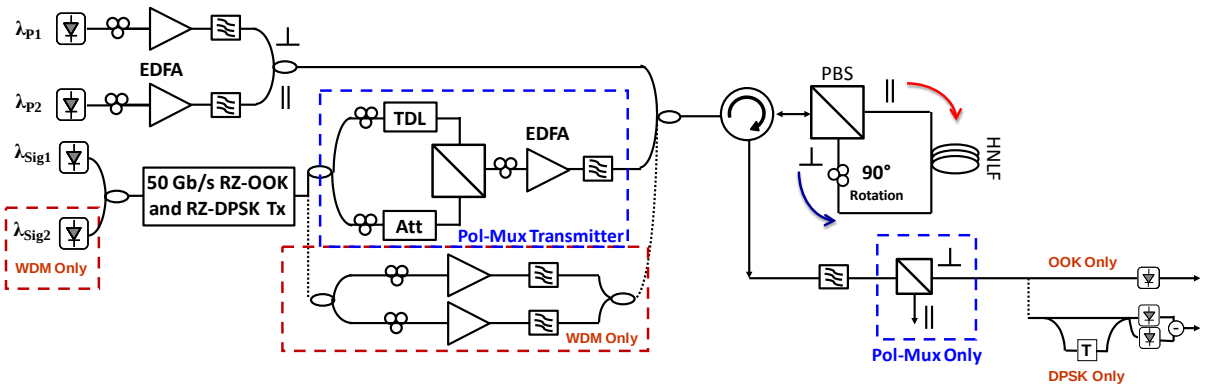

Figure 67. Experimental setup. A 100 Gbit/s Pol-Mux signal is generated and combined with two orthogonal pumps for demultiplexing to two 50 Gbit/s WDM channels. Similarly, two 50 Gbit/s WDM channels are generated and combined with two orthogonal pumps for multiplexing into a single 100 Gbit/s Pol-Mux channel

An experimental block diagram of our setup is shown in Figure 67. A MZM driven by a 50 Gb/s PRBS 2^{31}-1 data stream was used to generate both OOK and DPSK signals. Full-rate pulse carving was used to generate both 50% RZ waveforms generating RZ-OOK and RZ-DPSK. Polarization multiplexing was achieved by splitting the signal into two paths, de-correlating with a fiber delay, and recombining the signals using a PBC/PBS to ensure orthogonality. For the case of WDM channels, two CW sources were combined and modulated before being split and independently amplified, filtered, and de-correlated. Four-wave-mixing was achieved in a bidirectional fiber loop consisting of 330 meters of HNLF with a zero dispersion wavelength of 1562 nm, a PBS, a polarization controller set to rotate 90°, and a circulator to separate the data moving into and out of the loop. The incoming channels and pumps were aligned to the PBS such that the X and Y polarization travel in opposite directions around the loop. One channel and one pump travel in each direction. After one pass around the loop, the pumps, signals, and converted channels were recombined by the PBS and routed by the circulator to the receiver. The appropriate wavelength was filtered off and sent to a pre-amplified receiver for BER measurements. A PBS was used to separate the Pol-Mux data channels for detection while a delay-line interferometer with a 20 ps delay and balanced photo-receiver were used for DPSK detection.

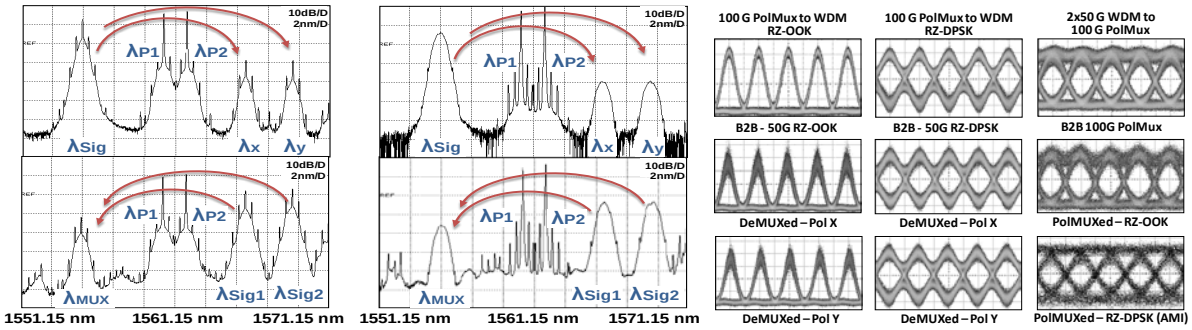

(a) (b) (c)

Figure 68. (a) Experimental spectra for demultiplexing (top) and multiplexing (bottom) between 100 Gbit/s Pol-Mux RZ-OOK and 2 x 50 Gbit/s RZ-OOK. (b) Experimental spectra for the demultiplexing (top) and demultiplexing (bottom) when using RZ-DPSK. (c) Back-to-Back eyes and demultiplexed/multiplexed eyes for comparison

For the case of demultiplexing 100 Gb/s Pol-Mux to two 50 Gb/s WDM channels, the signal, $\lambda_{Sig} \approx 1555$ nm, was combined with two pumps, $\lambda_{P1} \approx 1560$ nm and $\lambda_{P2} \approx 1562$ nm. The signal and pumps were independently amplified and filtered with 2 nm bandpass filters to suppress the ASE noise from the amplifiers. The polarization of the Pol-Mux signal was adjusted so that the X-polarized and Y-Polarized channels were separated and sent in opposite directions around the bi-directional FWM setup. The pumps were also polarized such that λ_{P1} travels in the same direction as the X-polarization while λ_{P2} travels with the Y-polarization. Two converted signals were generated via degenerate FWM at $\lambda_X = 2\times\lambda_{P1} - \lambda_{Sig} \approx 1565$ nm and $\lambda_y = 2\times\lambda_{P2} - \lambda_{Sig} \approx 1569$ nm respectively. This degenerate FWM process was phase conjugating, but it was also inherently phase maintaining allowing for both OOK and DPSK data to be demultiplexed to two different WDM channels, top of Figure 68(a) and Figure 68(b).

For the reverse case of multiplexing two 50 Gb/s WDM channels to a single 100 Gb/s Pol-Mux channel, two WDM signals, $\lambda_{Sig1} \approx 1565$ nm and $\lambda_{Sig2} \approx 1569$ nm were combined with the two pumps at λ_{P1} and λ_{P2} respectively. Again the polarization of the signals and pumps were aligned so that only one signal and one pump travel in the same direction around the loop. This time, DFWM produces two converted signals at the same wavelength, $\lambda_{MUX} = 2\times\lambda_{P1} - \lambda_{Sig1} = 2\times\lambda_{P2} - \lambda_{Sig2} \approx 1555$ nm. The two converted signals were also orthogonally polarized resulting in a single 100 Gb/s Pol-Mux channel at λ_{MUX}. Again the phase transparent nature of the FWM process allows for both OOK and DPSK data to be multiplexed into a single Pol-Mux channel, bottom of Figure 68(a) and Figure 68(b).

Figure 68(c) shows a comparison of the transmitted or back-to-back eye diagrams with the eye diagrams after demultiplexing and multiplexing when using RZ-OOK and RZ-DPSK. Demultiplexing of RZ-OOK and RZ-DPSK are shown in the first two columns respectively. Multiplexing of RZ-OOK and RZ-DPSK to a single channel are shown in column three. Note that the Pol-Mux sub-channels were offset by half of a bit-time for better comparison of the multiplexed eye-diagrams.

BER curves were used to assess the performance of both the demultiplexing and multiplexing functions. Figure 8(a) shows the performance of RZ-OOK compared to the back-to-back case. For demultiplexing, of the 100 Gb/s Pol-Mux channel, <0.5 dB penalty was observed for either

converted channel. Multiplexing of the two WDM channels into a single 100 Gb/s Pol-MUX resulted in a penalty of <2 dB. Similarly, Figure 69(b) shows the performance of RZ-DPSK. As expected, RZ-DPSK performed ~3 dB better than RZ-OOK due to the use of balanced detection. Pol-Mux to WDM demultiplexing showed penalties of 0.4 and 0.9 dB for the X and Y polarization respectively. Again, an additional ~ 2 dB penalty was observed for the case of WDM to Pol-Mux multiplexing. We believe this penalty is due to the finite extinction ratio of the polarizing beam combiners which may result in a small amount of power from the orthogonal data channel being converted onto the other polarization.

To further assess the quality of the multiplexed 100 Gb/s Pol-Mux channel, it was propagated over 1 km of uncompensated SMF-28 fiber. For comparison, the back-to-back signal was also propagated over the same distance. Both the back-to-back and the multiplexed signal experienced an additional ~1.5 dB penalty following propagation.

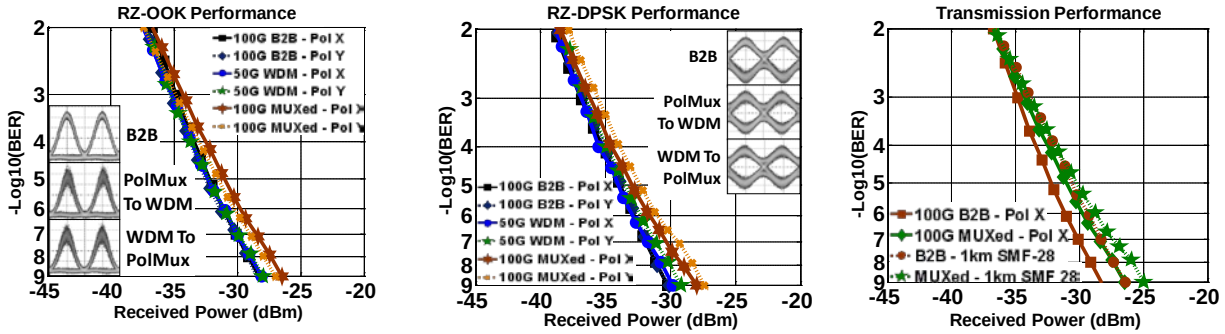

(a) (b) (c)

Figure 69. Conceptual diagram of all optical polarization demultiplexing and polarization multiplexing

4.18. 8-Fold 40-to-320 Gb/s Phase-Coherent WDM-to-TDM Multiplexing and 320-to-40 Gb/s Demultiplexing Using Highly Nonlinear Fibers

We experimentally demonstrated the use of XPM in HNLF to achieve phase-coherent WDM-to-TDM multiplexing of 40 Gb/s data channels at different wavelengths into a single 320 Gb/s data channel. The 320 Gb/s signal was then demultiplexed to 40 Gb/s for performance evaluation. An average penalty of approximately 7 dB at 10^{-9} BER was observed for all 8 tributaries. [17]

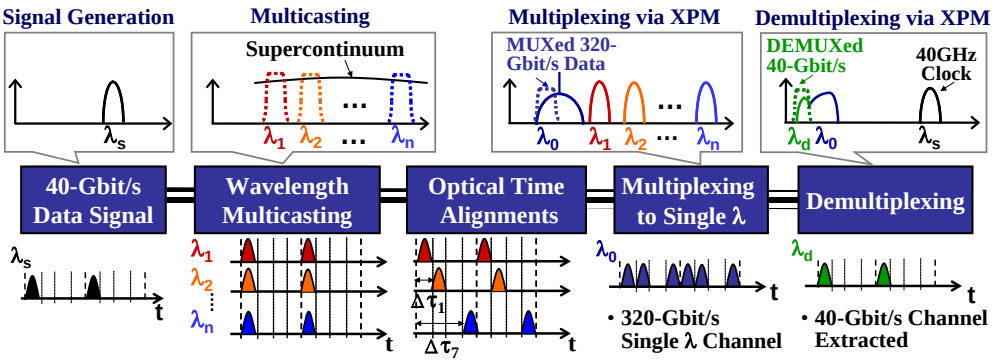

Figure 70. System block diagram. MUX: multiplex; DEMUX: demultiplex; XPM: cross-phase modulation

Figure 70 shows a system level block diagram of the scheme for signal multicasting, multiplexing, and subsequent demultiplexing. A short pulse 40 Gb/s signal was used to multicast the original data onto multiple wavelength channels using supercontinuum generation in an HNLF, which was followed by spectrum slicing. Then, the multicast copies were shifted in time for the time multiplexing. They were combined with a CW laser output and sent through another HNLF for WDM-to-TDM multiplexing via XPM. A single high-rate channel can be obtained after offset filtering the phase modulated CW. The multiplexed high-rate signal was then combined with a 40 GHz pulse train and demultiplexed to 40 Gb/s using XPM-induced frequency shift in another HNLF. Note that the purpose of the multicasting stage is to emulate the 8 WDM channels. For practical implementation of WDM-to-TDM multiplexing, in order to obtain the return-to-zero (RZ) signals with short pulsewidth, optical samplers would possibly be required to sample the original WDM channels.

Figure 71 shows the experimental setup. A 40 GHz mode locked laser (MLL) at ~1558 nm with a pulse width of ~2 ps was used. Data modulation was applied using a Mach-Zehnder modulator (MZM) driven by a 2^{31}-1 pseudo-random bit sequence (PRBS) at 40 Gb/s. The signal was then amplified and sent to a 500 m piece of HNLF, with a zero dispersion wavelength (ZDW) of 1565 nm and a dispersion slope (s) of ~0.017 ps/nm^2/km, for supercontinuum generation. Eight optical bandpass filters (BPFs) were inserted for spectrum slicing. The delay between the signals was adjusted by using optical tunable delay lines (TDLs). The multicast 40 Gb/s copies were then combined with a CW at 1543 nm and sent to a 100 m HNLF, with nonlinear coefficient (γ) = 25 W^{-1}·km^{-1}, ZDW = 1558.2 nm, and s = 0.026 ps/nm^2/km, for WDM-to-TDM multiplexing. Two offset BPFs were cascaded after the HNLF to optimize the multiplexed 320 Gb/s signal. 320-to-40 Gb/s demultiplexing is realized in another piece of 330 m HNLF, with γ = 25 W^{-1}·km^{-1}, ZDW = 1562.2 nm, and s = 0.026 ps/nm^2/km. The 40 GHz pump pulses used in the demultiplexing were tapped off from the MLL. The demultiplexed signal was then filtered by a 1 nm filter and sent to a 40 Gb/s pre-amplified receiver for BER measurement. Note that the multicasting stage was polarization insensitive; the multiplexing and demultiplexing stages were polarization dependent and we use polarization controllers (PCs) to maximize the conversion efficiency for each stage.

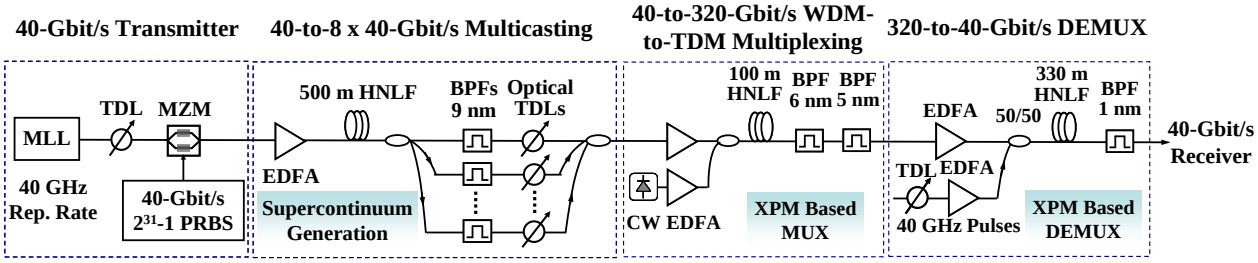

Figure 71. Experimental setup. MLL: mode locked laser; TDL: tunable delay line; MZM: Mach-Zehnder modulator; BPF: band-pass filter; CW: continuous wave; MUX: multiplexing; DEMUX: demultiplexing

Figure 72 shows the supercontinuum. To obtain multicast copies after supercontinuum generation, 8 filters with ~9 nm bandwidth were used, with the center from ~1551 nm to 1565 nm in steps of 2 nm. A pulse width of ~1.2 ps was obtained for each channel. Shown in Figure 72 (b) is the optical spectrum after the XPM-based WDM-to-TDM multiplexing stage. The 320 GHz tones in the broadened pump spectrum show the successful multiplexing to 320 Gb/s. The CW pump power into the 100 m HNLF was ~23 dBm and the total average power of the 8 signals was ~18 dBm. A square shape offset filter with a 3 dB bandwidth of 6 nm, centered at ~1540 nm, followed by another 5 nm filter was used to filter out the multiplexed 320 Gb/s signal and optimize its pulse width and shape. Figure 72 (c) shows the spectrum after demultiplexing. The power levels of the 40 GHz sampling pulses and the 320 Gb/s signal power into the 330 m HNLF were ~20 dBm and ~17 dBm, respectively. The signals at different stages were sent to a commercial optical sampling oscilloscope with ~0.8 ps resolution. Shown in Figure 72 (d) is the eye diagram of the multiplexed 320 Gb/s signal, which has a pulse width of ~1.8 ps. Note that the spectrum of the 40 GHz sampling pulses was broadened, which gives pulse compression in the time domain. The pulsewidth of the sampling pulse train after the 330 m HNLF was measured to be ~0.8 ps, with a root-mean-square (RMS) jitter of ~100 fs.

After demultiplexing the 320 Gb/s signal to 40 Gb/s, BER measurements were performed to characterize the nonlinear processes. Figure 73 shows the BER performance of the 8 multicast copies and 8 demultiplexed tributaries. The eye diagrams for each demultiplexed 40 Gb/s tributary are also given. An average penalty of approximately 2 dB at 10^{-9} BER was observed for the multicasting copies when compared to 40 Gb/s back to back performance. An extra penalty of approximately 7 dB is observed after the 40-to-320 Gb/s WDM-to-TDM multiplexing process and the following 320-to-40 Gb/s demultiplexing, mainly due to the pulse broadening through fiber, optical filters and EDFAs, and the slow phase drift of the signal and sampling pulse train induced by fluctuations of the HNLF length. The silica-HNLFs used in the demonstration can be replaced by special HNLFs or some integrable devices, having much shorter lengths and thus reducing the phase drift significantly.

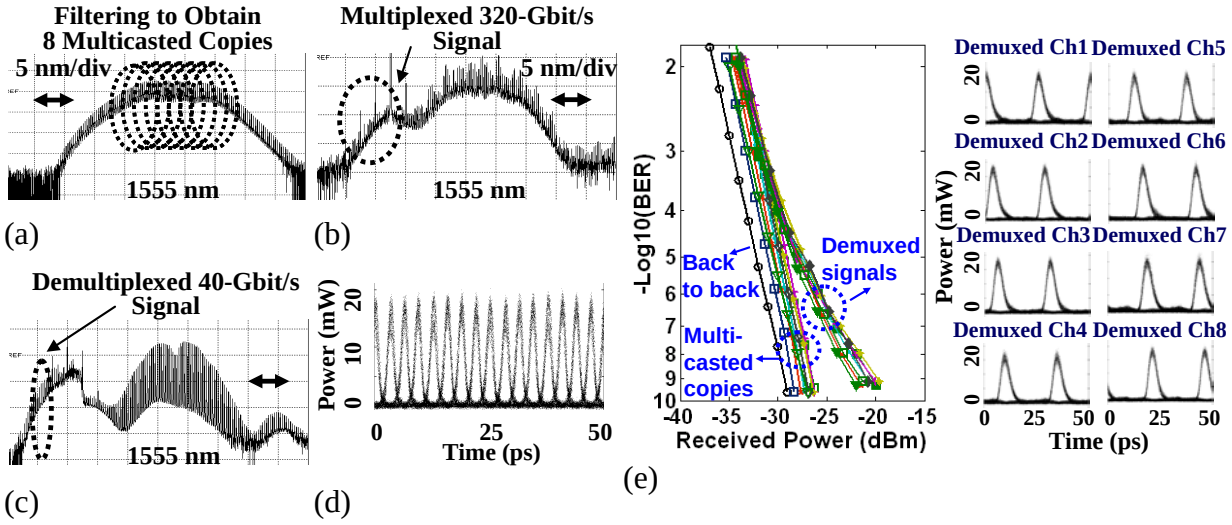

Figure 72. Experimental results. (a) supercontinuum; (b) optical spectrum after WDM-to-TDM multiplexing; (c) optical spectrum after demultiplexing; (d) eye diagram of the multiplexed 320 Gb/s signal, BER performance of the multicast copies and the 40 Gb/s tributaries of the multiplexed 320 Gb/s signal

It is observed from Figure 72(b) right hand side that the frequency tones of the eight time-delayed 40 Gb/s channels were not well defined, which was a result of the poor phase correlation between channels. The spectrum after WDM-to-TDM multiplexing exhibits clear 320 GHz tones, which showed high phase coherence. To verify the improved phase coherence, we used a differential group delay (DGD) based delay-line interferometer (DLI) with the DGD set to be 6.25 ps, which corresponded to a 2-bit delay at 320 Gb/s, to characterize the signal before and after the WDM-to-TDM multiplexing stage. The signal before multiplexing showed considerable amplitude noise due to the poor phase correlation, as shown in Figure 73(a). Figure 73(b) shows the interferometer output with the 320 Gb/s WDM-to-TDM multiplexed signal, which exhibited significantly lower amplitude noise and much better phase coherence. A similar measurement was performed for a 320 Gb/s pulse train. Figure 73(c) shows the interferometer output without passing through the XPM-based WDM-to-TDM multiplexer, and Figure 73(d) shows the interferometer output after the XPM process, which exhibits high phase coherence.

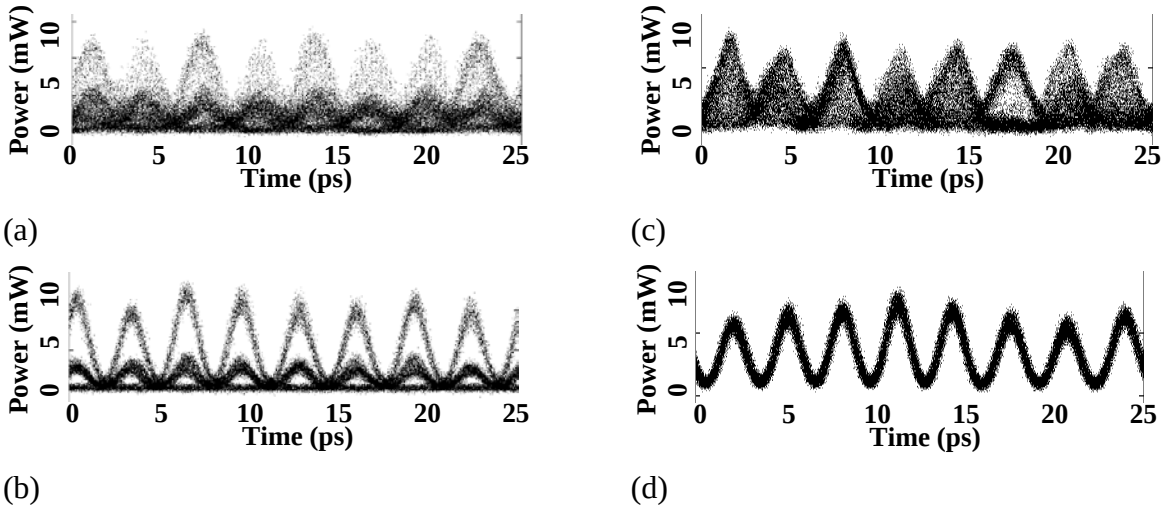

Figure 73. Experimental verification of the phase-coherence characteristics. (a) Data channels before WDM-to-TDM multiplexing after the DLI; (b) 320 Gb/s WDM-to-TDM multiplexed signal after the DLI; (a) 320 Gb/s clock after the DLI without passing through the XPM-based WDM-to-TDM multiplexer; (b) DLI output with the 320 Gb/s clock after the XPM process

4.19. Phase-Transparent Optical Data Exchange of 40 Gb/s DPSK Signals Using Four-Wave-Mixing in a Highly Nonlinear Fiber

We demonstrated phase-transparent optical data exchange by exploiting non-degenerate FWM in an HNLF. 40 Gb/s DPSK optical data exchange is demonstrated with ~4.5 dB power penalty. [16]

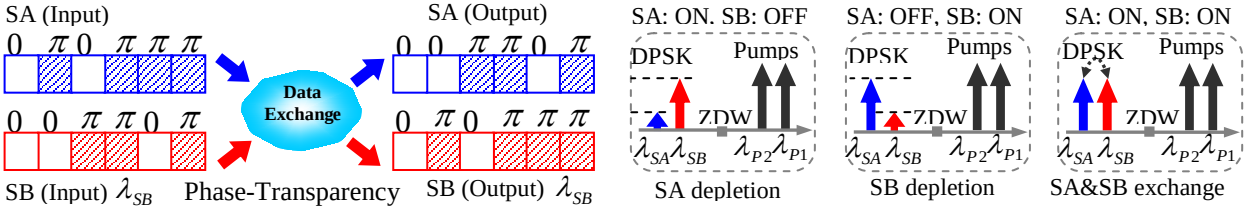

Figure 74. Concept and operation principle of phase-transparent optical data exchange

Figure 74 depicts the conceptual diagram of FWM-based phase-transparent data exchange. Two DPSK signals (SA: λ_{SA}, SB: λ_{SB}) and two CW pumps ($\lambda_{P1}, \lambda_{P2}$) are set to be symmetric with respect to the zero-dispersion wavelength of an HNLF. SA (SB) can be depleted and converted to SB (SA) via non-degenerate FWM while preserving the phase-information by properly controlling the powers and polarization states of the pumps and signals, resulting in the phase-transparent optical data exchange between DPSK data signals.

To further explore the phase-transparent data exchange, we derive the following analytical solutions to the nonlinear interactions simultaneously involving two signals and two pumps.

$$A_{SA}^{'} = [A_{SA}\cos(gz) + A_{SB}\frac{2i\gamma}{g}A_{P1}^{*}A_{P2}\sin(gz)]e^{i[2\gamma(P1+P2)+\frac{k}{2}]z},\quad A_{SB}^{'} = [A_{SA}\frac{2i\gamma}{g}A_{P1}A_{P2}^{*}\sin(gz) + A_{SB}\cos(gz)]e^{i[2\gamma(P1+P2)-\frac{k}{2}]z}$$

where $g = \sqrt{4\gamma^2 P_1 P_2 + k^2/4}$, $k = \Delta\beta + \gamma(P_1 - P_2)$. $A_j\ (j = SA, SB, P1, P2)$ is the complex amplitudes of the signals

and pumps containing both amplitude and phase information. $A_{SA}^{'}$, $A_{SB}^{'}$ are complex amplitudes of the signals after swapping. γ is the nonlinear coefficient. k and g are constants related to phase mismatch ($\Delta\beta$) and pump powers ($P_{1,2}$). Under the condition $gz=(N+1/2)\pi$ $(N=0,1,2,...)$, it is expected that phase-transparent data exchange ($A_{SA}^{'} \propto A_{SB}$, $A_{SB}^{'} \propto A_{SA}$) can be achieved.

Figure 75 illustrates the experimental setup. Two DPSK signals (SA, SB) and two CW pumps were coupled into a 1-km piece of HNLF (ZDW: ~1552 nm) to participate in the non-degenerate FWM for phase-transparent data exchange. In order to suppress the stimulated Brillouin scattering (SBS), two CW pumps were phase modulated (PM) by a 10 Gb/s PRBS. Band-pass filters (BPFs) were used to separate two pumps and suppress amplified spontaneous emission (ASE) noise, while optical delay lines (ODL) were used to synchronize the two pumps. The polarization states of the signals and pumps were adjusted via polarization controllers (PCs) to optimize the performance of data exchange.

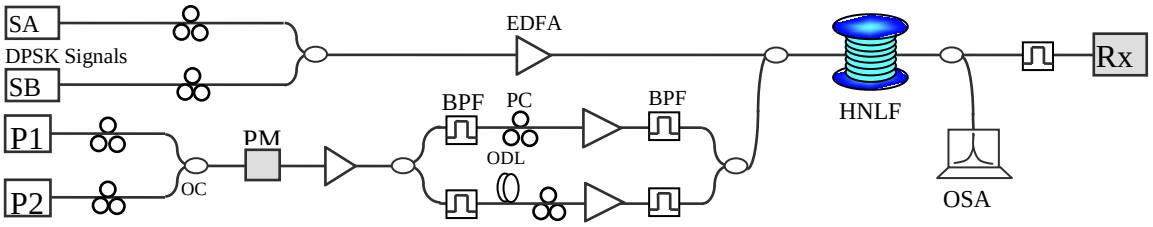

Figure 75. Experimental setup of DPSK data exchange. OSA: optical spectrum analyzer; OC: optical coupler

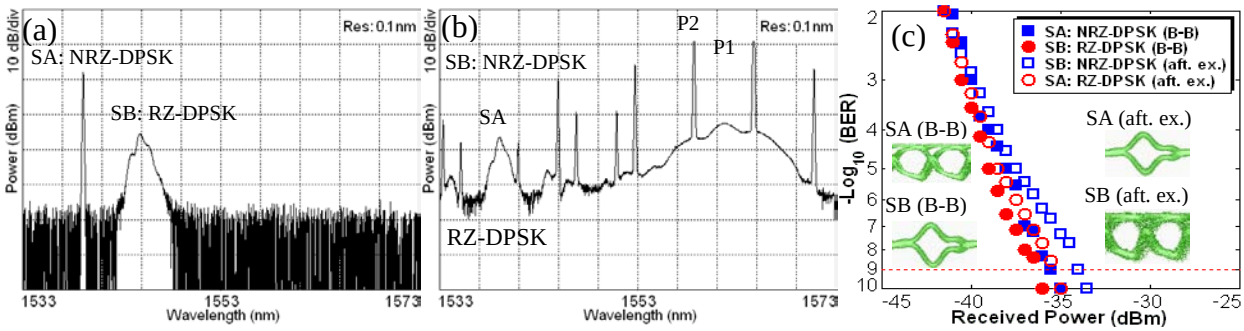

Figure 76. Data exchange between 10.7 Gb/s NRZ-DPSK and RZ-DPSK

Shown in Figure 76 is a data exchange between 10.7 Gb/s NRZ-DPSK (SA) and RZ-DPSK (SB). The NRZ-DPSK/RZ-DPSK signal was generated by adding a 10.7 Gb/s 2^{31}-1 pseudo-random binary sequence (PRBS) phase modulation after a CW laser/10.7 GHz mode-locked short-pulse laser. Figure 76(a) depicts the spectrum of the signals in the absence of the pumps. Figure 76(b) shows the spectrum after data exchange in the presence of the pumps (without ASE suppression), from which it can be seen that the information carried by the two signals was exchanged. Figure 76(c) presents the BER curves. The power penalty was ~1 dB for RZ-DPSK (SB to SA) and ~1.5 dB for NRZ-DPSK (SA to SB). Insets plot the eye diagrams detected by a 35-GHz balanced photoreceiver, which confirms the successful data exchange between NRZ-DPSK and RZ-DPSK.

We further demonstrated 40 Gb/s 2^{31}-1 PRBS NRZ-DPSK data exchange. The input power of

each signal and pump to the HNLF was about 3 dBm and 24 dBm. Figure 77(a) shows the spectrum with input SA (1539.5 nm) turned on and SB (1545.4 nm) off. We can clearly observe the depletion (~21.2 dB) of SA in the presence of the pumps (1558.4, 1564.5 nm), accompanied by the generation of SB. Similarly, with input SB turned on while SA off, SB depletion (~23.3 dB) together with SA generation are also obtained as shown in Figure 77(b). The dashed curves in Figure 77(a)(b) show the spectra of SA and SB with the pumps off. Figure 77(c) depicts the spectrum after data exchange when the two signals and the two pumps are simultaneously turned on (with pump ASE suppression).

In order to verify the 40 Gb/s NRZ-DPSK data exchange, Figure 78 displays the alternate-mark inversion (AMI) demodulated waveforms, from which we can clearly see the successful phase-transparent data exchange. Figure 78 plots the BER curves of 40 Gb/s NRZ-DPSK data exchange. The power penalty of wavelength conversion was less than 1.5 dB. An additional 3-dB penalty was induced when combining the converted and residual signals. Thus an approximate 4.5 dB penalty in total was obtained for 40 Gbit/s NRZ-DPSK data exchange and the performance degradation is mainly due to the beating effect between the newly converted and residual signals. With further improvement, it is possible to reduce the beating effects and improve the exchange performance with larger signal depletion. Figure 79 depicts the signal depletion as functions of the input pump powers and signal wavelength. It is expected that proper adjustment of pump powers and signal wavelengths is of great importance for optimizing the signal depletion and the performance of optical data exchange.

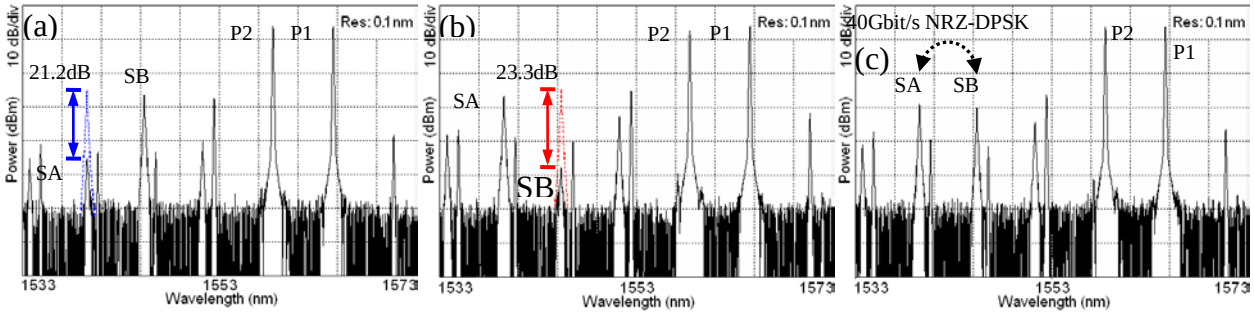

Figure 77. Optical spectra for 40 Gb/s NRZ-DPSK data exchange. (a) SA: ON, SB: OFF; (b) SA: OFF, SB: ON; (b) SA&SB: ON

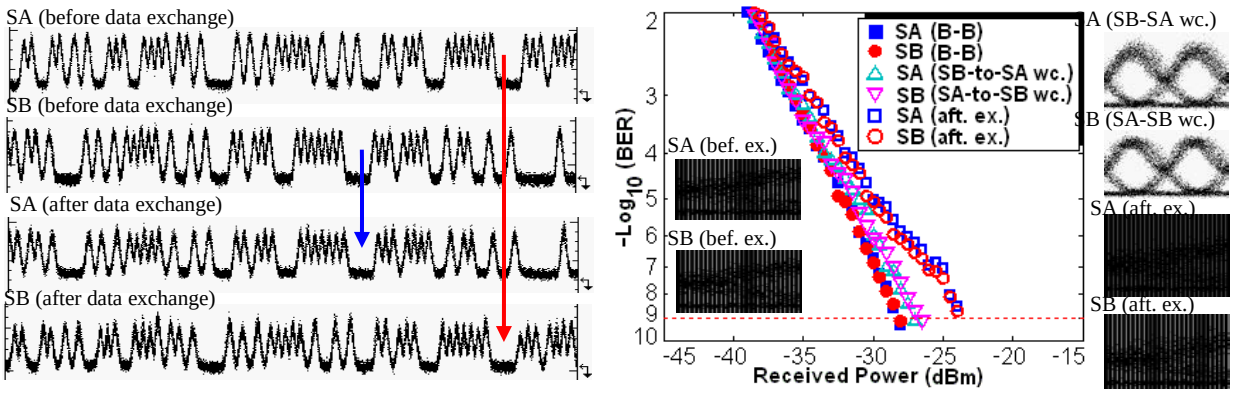

Figure 78. Waveforms for 40 Gb/s NRZ-DPSK exchange (AMI demodulation). BER and eyes (AMI demodulation) for 40 Gb/s NRZ-DPSK exchange.

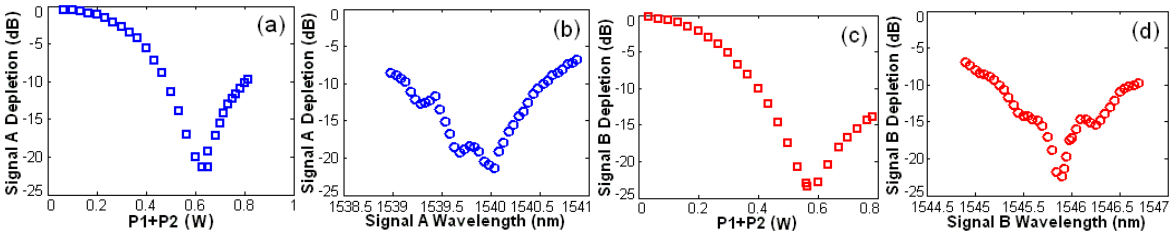

Figure 79. Signal depletion as functions of (a)(c) input pump powers and (b)(d) signal wavelengths. (a)(b) Signal A; (c)(d) Signal B

4.20. Demonstration of Data Traffic Grooming of a Single 10 Gb/s TDM Tributary Channel between Two 160 Gb/s WDM Channels

We also demonstrated data traffic grooming/exchange of a single 10 Gb/s TDM tributary channel between two 160 Gb/s WDM channels by using second-order nonlinearities in a PPLN waveguide. 16 tributary channel data grooming/exchange between two 160 Gb/s WDM signals was realized with a power penalty of ~4 dB. [21]

Figure 80 illustrates a conceptual diagram of a tributary channel data traffic grooming/exchange. Each of the two high-speed WDM signals (S1, S2) consists of many low-speed tributary TDM channels (e.g. 16-channel 10 Gbit/s for 160 Gbit/s). Two WDM signals (e.g. 160 Gbit/s) together with two synchronized sub-rate clock (10 GHz) pumps (P1, P2) are sent into a nonlinear device such as PPLN waveguide for tributary channel data traffic grooming. The wavelengths of two signals and two pumps are arranged to be symmetric (S1&P1, S2&P2) with respect to the quasi-phase matching (QPM) wavelength of PPLN. Due to the parametric depletion effect of the second-order nonlinearities inside the PPLN, S1 is depleted and converted to S2. Similarly, S2 is extinguished to produce S1. Thus data exchange between two WDM signals (S1, S2) can be realized. In particular, by exploiting two synchronized sub-rate (10 GHz) clock pumps which are aligned to one of the tributary channel of two WDM signals, it is possible to implement tributary channel data traffic grooming/exchange. As depicted in Figure 80, the tributary channel i (Ch i) of two high-speed WDM signals can be exchanged.

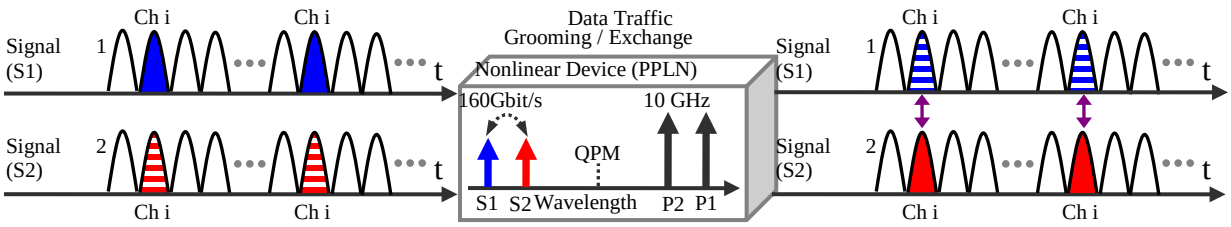

Figure 80. Concept of data traffic grooming/exchange.

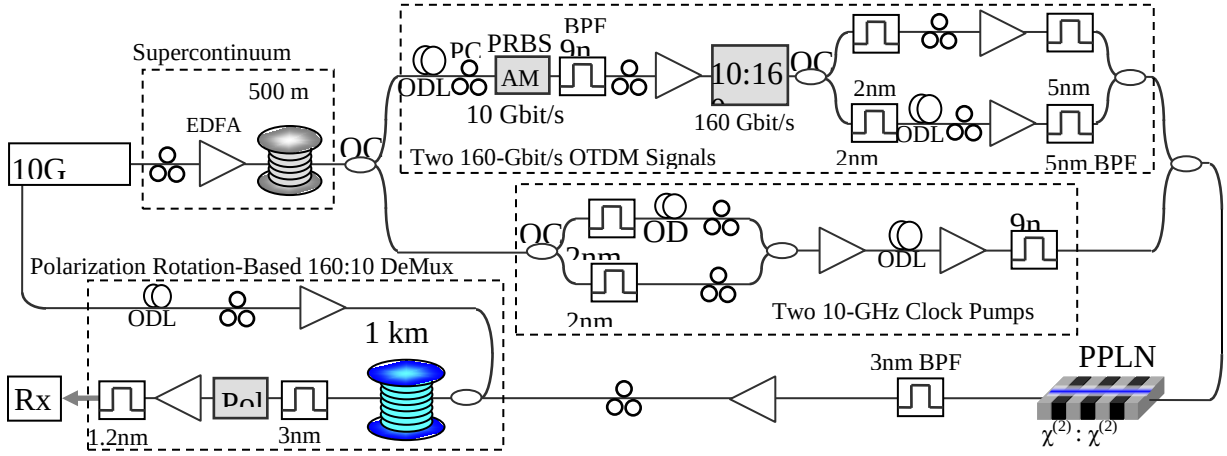

Figure 81. Experimental setup of tributary channel data grooming/exchange. AM: amplitude modulator; EDFA: erbium-doped fiber amplifier; ODL: optical tunable delay line; BPF: band-pass filter; PC: polarization controller; Pol.: polarizer; OC: optical coupler

Figure 81 shows the experimental setup. A 10-GHz mode-locked fiber laser (MLL) at ~1551 nm with a pulse width of ~1.9 ps was sent through a 500-m piece of HNLF for supercontinuum generation. The supercontinuum spectrum was divided into two branches. The 1st branch was modulated with a 10 Gb/s 2^{31}-1 pseudo-random binary sequence and multiplexed to 160 Gbit/s via a fiber-based polarization-maintained 10:160 multiplexer. Two 160 Gb/s WDM signals were then obtained by separately filtering the spectrum at 1535.6 (S1) and 1542.1 nm (S2). The 2nd branch was used to generate two synchronized sub-rate (10 GHz) clock pumps by directly slicing the supercontinuum spectrum at 1559.2 (P2) and 1565.3 nm (P1). Two 160 Gb/s signals and two 10-GHz clock pumps were then combined and launched into a 50-mm long PPLN waveguide for tributary channel data traffic grooming/exchange. The PPLN waveguide had a QPM wavelength of ~1550.52 nm when operating at 92.1 ^{o}C. The 160 Gb/s signal was demultiplexed to 10 Gbit/s for BER measurement using XPM induced polarization rotation in a 1-km piece of HNLF.

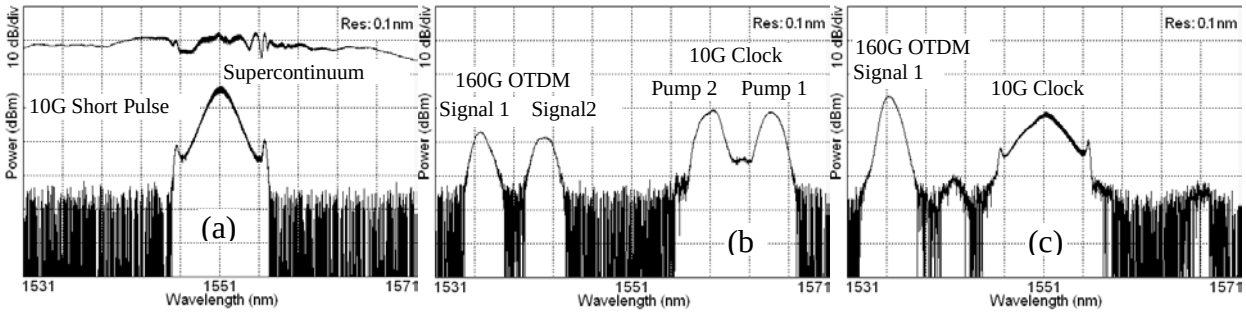

Figure 82. Optical spectra of (a) supercontinuum generation, (b) data grooming/exchange after PPLN, and (c) polarization rotation-based 160:10 demux

Figure 82(a) shows the supercontinuum spectrum over a 40 nm range with a total fluctuation of less than 7.7 dB. The spectral flatness within the signal and pump wavelength ranges was less than 2.1 dB. The average power of each signal and peak power of each pump into the PPLN were about 25 mW and 1.5 W. Shown in Figure 82(b) is the spectrum of tributary channel grooming after PPLN. The two 160 Gb/s signals and two 10-GHz clock pumps were symmetric in regard to the QPM wavelength of the PPLN. Figure 82(c) shows a typical spectrum of a polarization rotation-based 160:10 demux.

Figure 83 displays the eye diagrams of data grooming/exchange measured by an optical sampling scope. As shown in Figure 83(a), two 10-GHz clock pumps were aligned to the tributary Ch1 of two 160 Gb/s signals. The Ch1 of S1 was depleted (~19 dB) in the absence of S2 with proper adjustment of powers and polarization states. In the presence of S2, the tributary Ch1 of S2 was exchanged to S1. Similarly, the tributary Ch1 of S1 was also exchanged to S2. Figure 83(b)(c) shows the examples of tributary channel exchange for Ch5 and Ch15. In fact, it was easy to realize 16-channel data grooming/exchange simply by shifting the 10-GHz clock pumps to be aligned with the corresponding tributary channel.

Figure 84 plots the BER performance of data traffic grooming. As shown in Figure 84(a)(b), less than 3 dB power penalty was introduced for 160 Gb/s signal generation (before exchange) compared to 10 Gb/s back-to-back case. This was due to nonlinear effects during supercontinuum generation and the 160:10 demux. Approximately 4 dB power penalty was observed for the tributary channel data grooming/exchange which was caused by the nonlinear effects and the beating between converted and residual signals. Figure 84(c) shows the grooming/exchange impact on the neighboring channels with a power penalty of less than 1 dB. Figure 85 further presents the power penalty of 16-channel data traffic grooming/exchange. During the generation of 160 Gb/s signals, the average power penalty and fluctuation of 16 channels was about 2.6 and 0.9 dB for S1 and 2.7 and 0.7 dB for S2. During the tributary channel data traffic grooming/exchange, the average power penalty and fluctuation of 16 channels was around 3.7 and 1.1 dB for S1 (S2 to S1) and 3.9 and 1.1 dB for S2 (S1 to S2).

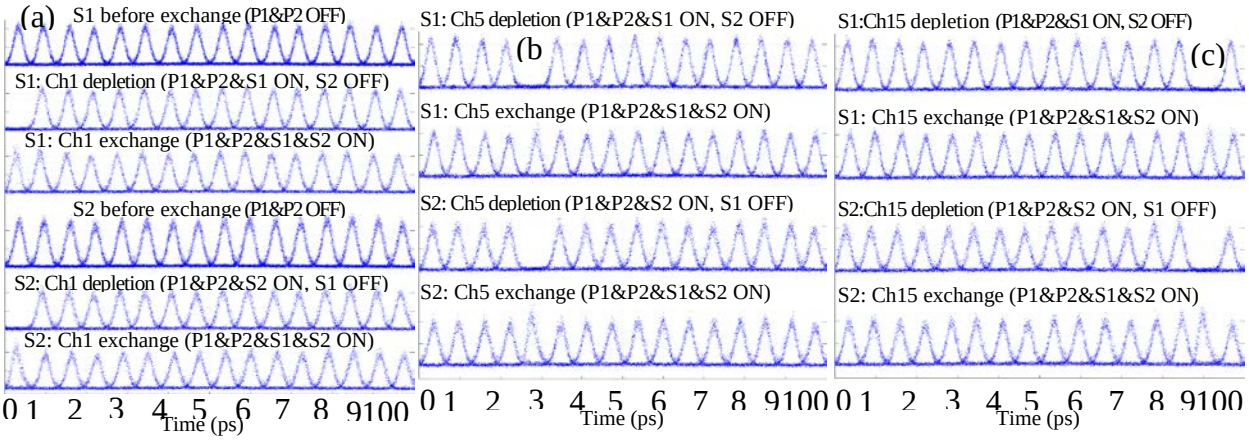

Figure 83. Eye diagrams of tributary channel data traffic grooming/exchange. (a) channel 1 (Ch1); (b) channel 5 (Ch5); (c) channel 15 (Ch15).

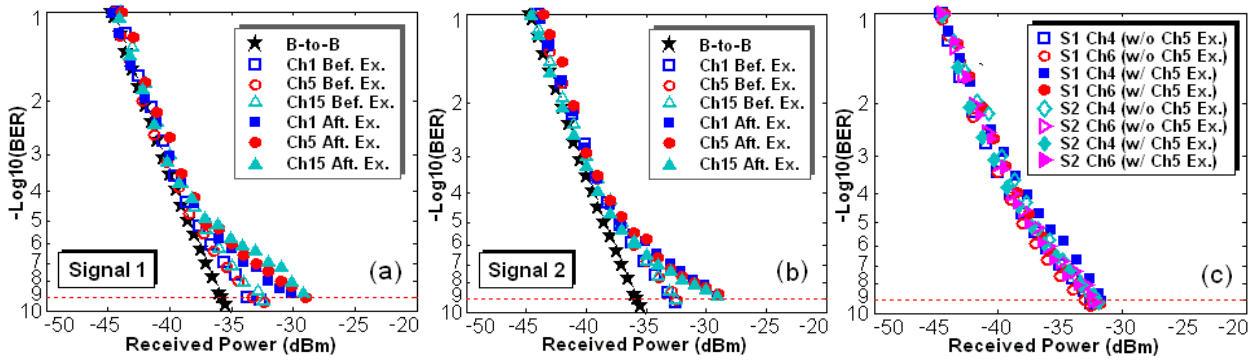

Figure 84. BER performance of tributary channel data trafic grooming/exchange. (a) S1; (b) S2; (c) data exchange impact on neighboring channels

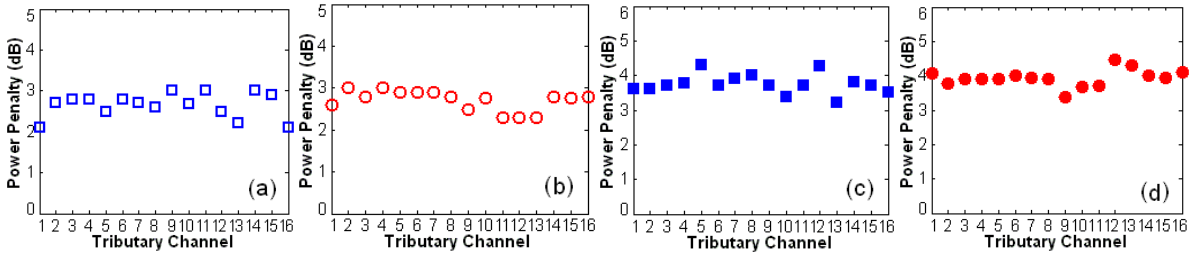

Figure 85. Power penalty of 16 channels during (a)(b) 160 Gb/s signal generation and (c)(d) tributary channel data trafic grooming/exchange

4.21. 1.16 µs Continuously Tunable Optical Delay of a 100-Gbit/s DQPSK Signal using Wavelength Conversion and Chromatic Dispersion in an HNLF

We demonstrated an optically-controlled tunable delay element using wavelength conversion in a highly nonlinear fiber, dispersion compensating fiber, and optical phase conjugation, enabling a continuous delay of up to 1.16-µs using 100 Gbit/s NRZ-DQPSK and 50 Gbit/s NRZ-DPSK modulation formats. This corresponds to a delay-to-bit-rate product exceeding 55,000 for 50 Gbit/s DPSK and 110,000 for 100-Gbit/s DQPSK. A BER=10^{-9} was obtained for all formats, over the extent of the delay tuning range. [22]

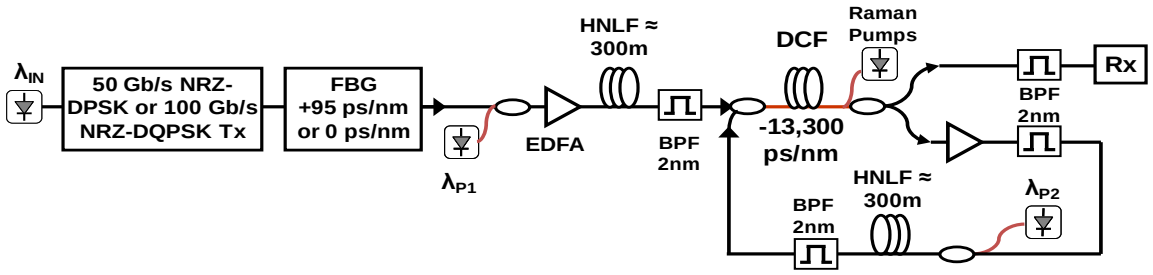

Figure 86. Block diagram. Dispersion compensating fiber (DCF), fiber Bragg grating (FBG), bandpass filter (BPF), transmitter (TX), receiver (RX), and highly nonlinear fiber (HNLF)

An experimental block diagram of our setup is shown in Figure 86. 100 Gbit/s NRZ-DQPSK was generated by driving two parallel integrated Mach-Zehnder modulators with 50 Gbit/s, 2^{31}-1, PRBS data. The data was shifted by 123 bits to de-correlate the two data streams. One data stream was removed to generate the 50 Gbit/s NRZ-DPSK signal. The optical signal was then wavelength converted using a 300m piece of HNLF with a zero-dispersion wavelength of ~1560 nm. A 1-pump degenerate FWM approach was used to convert the signal ($\lambda_{IN} \approx 1536$ nm) from 1540 to 1583 nm. The converted signal was then filtered out and sent through the DCF (D ≈ -13.3 ns/nm at 1550 nm) to impose a wavelength-dependent delay. Counter propagating Raman amplification in the DCF was used to compensate for the ~80 dB of loss. Following the DCF, the delayed signal was phase conjugated using a second piece of HNLF (ZDW ≈ 1558). Again, a 1-pump FWM approach was used to convert the signal ~4 to 14 nm up in wavelength. The signal was passed through the DCF a second time to compensate the intra-channel dispersion and to undergo a second wavelength dependent delay. A third wavelength conversion stage would be needed to return the output to its original wavelength, but was not implemented. The signal was received using a pre-amplified receiver with a 50 GHz delay-line interferometer (DLI) and balanced photo-receiver.

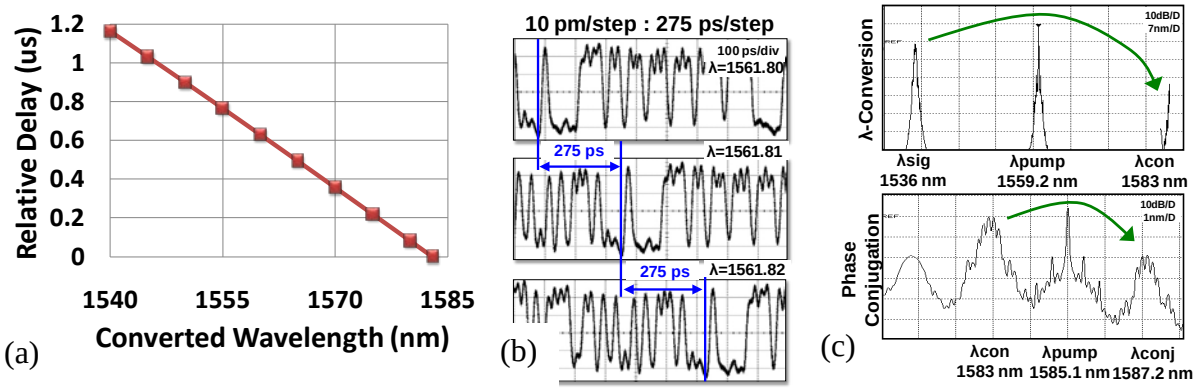

Figure 87. (a) Measured delay of 1.16 μs. (b) Received 50 Gbit/s ODB signal for 10 pm changes in laser wavelength showing ~275 ps changes in delay. (c) Experimental spectra of first and second wavelength conversion stages for the maximum delay value

As the dispersion profile is not linear with wavelength, several different types of fiber were combined to create a relatively flat profile. The residual dispersion was removed using a switchable FBG based dispersion compensator to pre-disperse the input signal with either +95 ps/nm, for converted wavelengths of 1540 to 1571 nm, or by 0 ps/nm, for wavelengths of 1568 to

1583 nm, and adjusting the phase conjugation distance. The total measured delay of 1.16 μs is shown in Figure 87(a) above. Figure 87(b) shows the received optical duo-binary (ODB) signal after the DLI as the first stage pump is varied in 10 pm steps. The expected ~275 ps changes in delay are easily seen. Figure 87(c) shows the experimental spectra of both wavelength conversion stages for the case of minimum delay.

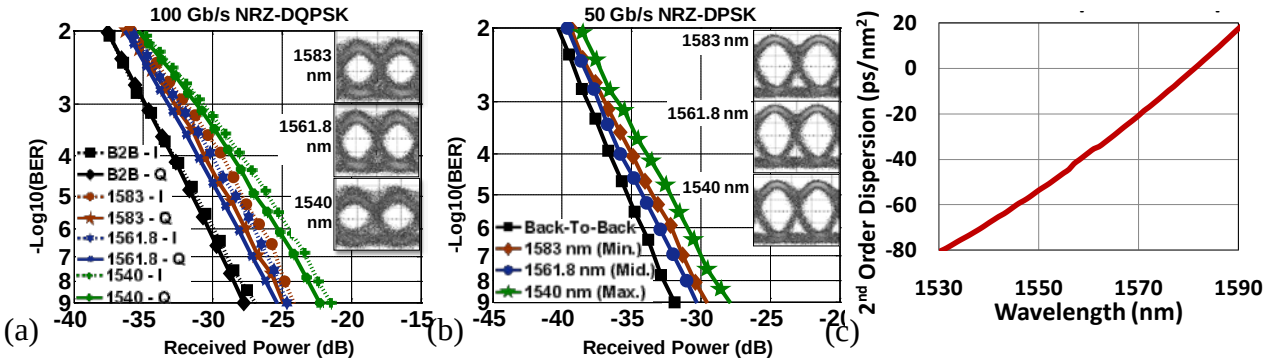

Figure 88. (a) 0, 0.5ps, and 1ps delay resolution of a single 40Gbit/s RZ-OOK bit. (b) RF-spectra showing optical mixing for different AOM frequency offsets. (c) Bit-error-rate curves for varying delay values with and without the AOMs

The performance of our delay system was assessed through BER measurements and is shown in Figure 88(a) and (b). Power penalties from 2.3 to 5.4 dB and 1.6 to 3.9 dB were observed for 100 Gbit/s DQPSK and 50 Gbit/s DPSK respectively. Figure 88(c) shows the calculated second-order residual dispersion (ps/nm^2) which was not compensated by the phase conjugation process. At the maximum delay value, ~68 ps/nm^2 of residual second order dispersion contributes ~1 dB of the observed penalty. This second order dispersion may prove to be a limiting factor for achieving larger delays and higher data rates.

4.22. Multicasting of 40-Gbit/s NRZ-OOK Data into 24 RZ Copies using a Single Pump and Supercontinuum Generation

We also demonstrated multicasting of 40-Gbit/s NRZ-OOK data into 24 RZ copies using a single pump and supercontinuum generation. The NRZ signal was optically sampled by a DFWM process and then a supercontinuum was generated using the sampled signal. The utilized optical sampling scheme inherently resulted in compressed pulses which facilitate the supercontinuum generation. A polarization based tunable periodic filter was used for slicing of the supercontinuum into 200 GHz channels with ~6 ps pulses. 24-fold Multicasting over a >36 nm bandwidth with an average power penalty of ~1.6 dB was achieved. [23]

The conceptual and experimental block diagram of our technique is shown in Figure 89. A 40-Gbit/s NRZ-OOK signal (λ_{SIG} ~1543.8 nm) was generated using a Mach-Zehnder modulator driven by a 2^{15}-1 pseudo-random binary sequence (PRBS). A fiber based mode-locked laser at a 40-GHz pulse repetition rate (λ_{CLK} ~1554 nm) was used as the sampling pulse source. The 2 ps pulses were amplified and filtered by a 9 nm band-pass filter (BPF) before being coupled with the NRZ signal in a 3 dB coupler, and launched into a 460 m highly nonlinear fiber (HNLF-1) with a ZDW of ~1555 nm. The pulsed signal was used as the pump in a DFWM configuration for the sampling of the NRZ signal in HNLF-1 to an appropriate wavelength for supercontinuum generation in HNLF-2. As the converted signal power depends on the square of the pulsed pump

power, the wavelength converted signal is a sampled copy of the input signal with compressed pulses. The sampled signal was then amplified, filtered and sent to the 500 m HNLF-2 with a ZDW of ~1565 nm for supercontinuum generation. A polarizer was used at the output of the HNLF-2 to ensure linear polarization of the supercontinuum. The supercontinuum was then sent to a polarization-based periodic filter for slicing of the supercontinuum and channel assignments. The filter comprised two PCs, a 5 ps differential group delay element and a polarizer to realize a delay line interferometer in the polarization domain. The resulting periodic filter with 200 GHz free-spectral range (FSR) sliced the supercontinuum defining the 200 GHz channels. Optical sampling enables multicasting via supercontinuum from an NRZ signal (at a variable wavelength) and pulse compression further assists for a wider supercontinuum.

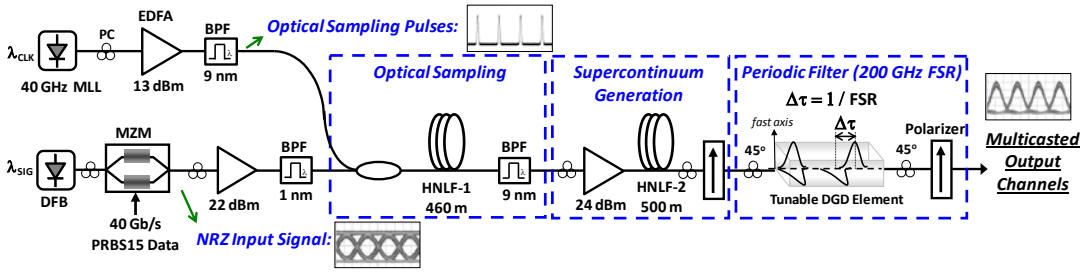

Figure 89. Conceptual and experimental diagram. A 40 Gbit/s NRZ signal is first optically sampled by 2 ps pulses and a supercontinuum is generated using the sampled data stream. The generated supercontinuum is sliced into channels by a tunable periodic filter. BPF: bandpass filter; MZM: Mach-Zehnder modulator; PC: polarization controller; MLL: mode-locked laser

Shown in Figure 90 are the spectra after each stage of the experiment. Figure 90(a) shows the sampling process in HNLF-1 which samples the NRZ input signal λ_{SIG} to λ_{SMP} at ~1564.2 nm. The spectrum before and after the HNLF-2 are shown in Figure 90(b). The sampled signal was amplified to an average power of ~24 dBm that resulted in a ~40 nm wide supercontinuum. Figure 90(c) shows the supercontinuum sliced into 200 GHz channels by the periodic filter. The multicast channel assignments were done starting from Ch1 at 1545.6 nm to Ch24 at ~1582.4 nm as shown.

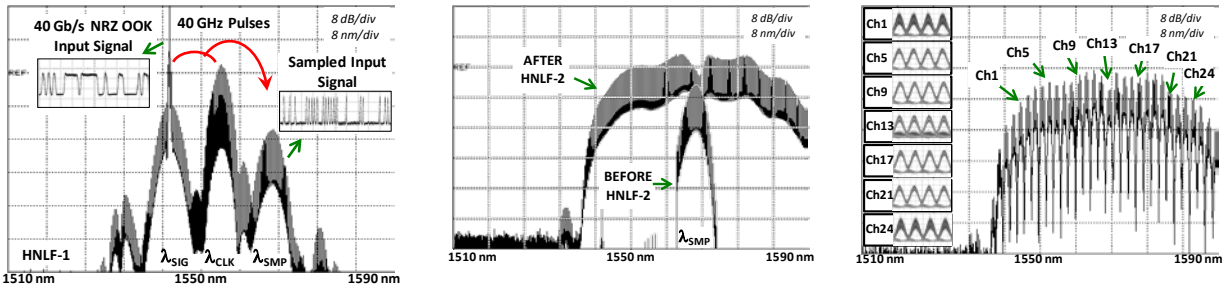

(a) (b) (c)

Figure 90. Experimental spectra: (a) Optical sampling in HNLF-1; (b) Sampled signal spectrum sent to the HNLF-2 and the generated supercontinuum; (c) The 24 multicast channels sliced from the supercontinuum spectrum along with eye diagrams of several channels

BER measurements were performed for all 24-fold multicast channels. Figure 91(a) shows the BER curves for the best and worst case performances along with the back-to-back performance

of the NRZ input signal and that of the sampled signal after HNLF-1. Figure 91(b) shows the power penalty (at 10^{-9} BER) for each channel with respect to the sampled input signal performance (filtered by a 200 GHz filter prior to receiver). While the reduced signal quality on the edges increased the power penalty, the worst cases were observed around the λ_{SMP} due to the amplified zero-levels of the sampled signal as seen from the Ch12 eye diagram in Figure 91(a). This mainly resulted from regeneration of the non-ideal zero levels due to the finite extinction ratio of the NRZ input signal. Figure 91(c) shows the eye diagrams from an optical sampling oscilloscope of the sampling pulses (~2 ps), sampled input signal (~1.6 ps), and a multicast channel (~ 6ps). Overall, 18 channels performed with < 2 dB power penalty over ~30 nm of bandwidth.

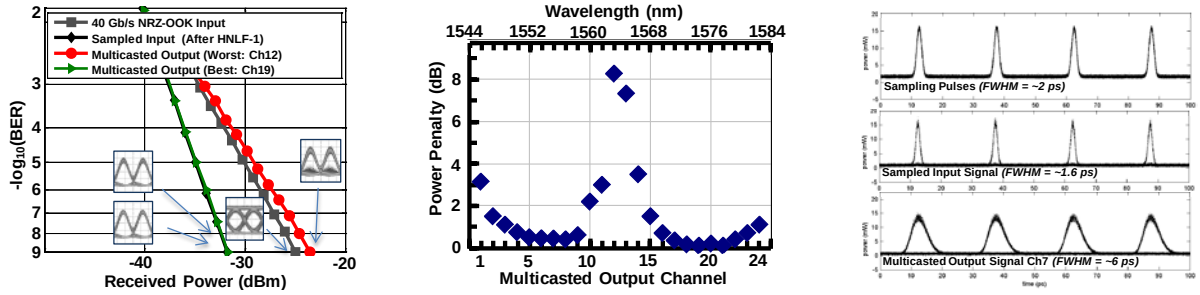

(a) (b) (c)

Figure 91. (a) BER performances for the best and worst cases; (b) Power penalty with respect to the sampled signal of each channel; (c) Eye diagrams from an optical sampling scope for the sampling pulses, sampled input signal and the multicast output Ch7

4.23. Data Traffic Grooming/Exchange of a Single 10-Gbit/s TDM Tributary Channel between Two Pol-Muxed 80-Gbit/s DPSK Channels

We also demonstrated data traffic grooming/exchange of a single 10-Gbit/s TDM tributary channel between two pol-muxed 80-Gbit/s DPSK channels using Kerr-induced nonlinear polarization rotation. 8 tributary channel data grooming between two pol-muxed 80-Gbit/s DPSK channels was realized with a power penalty less than 4 dB.

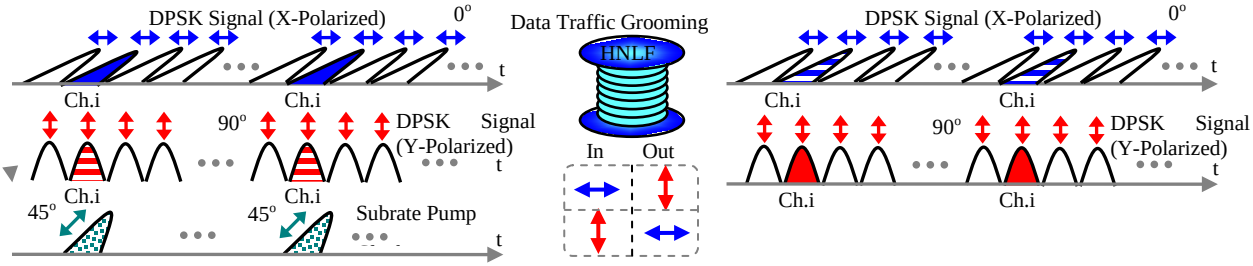

Figure 92. Concept of pol-muxed DPSK data traffic grooming/exchange

Figure 92 illustrates the concept and principle of tributary channel data grooming/exchange between two pol-muxed DPSK channels. A subrate pump clock is 45° linearly polarized with respect to the two pol-muxed channels. With proper control of pump power, the pump-induced birefringence causes nonlinear polarization rotation and exchanges the polarization states of the pol-muxed tributary channels where the subrate pump clock is present. [21]

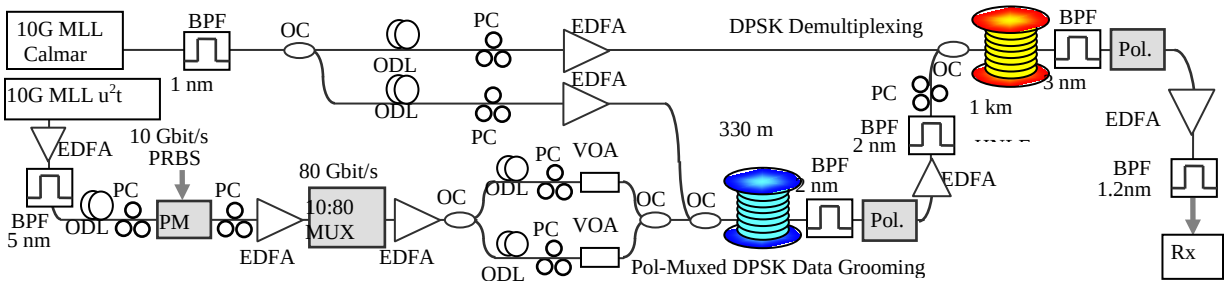

Figure 93. Experimental setup of pol-muxed DPSK data traffic grooming/exchange. EDFA: erbium-doped fiber amplifier; ODL: tunable optical delay line; PC: polarization controller; OC: optical coupler; VOA: variable optical attenuator; Rx: receiver

Figure 93 shows the experimental setup. A 10-GHz MLL at 1551.0 nm with a pulse width of ~2.4 ps was employed for 80-Gbit/s DPSK generation through a phase modulator (PM) driven by a 10-Gbit/s 2^{31}-1 PRBS and subsequent 10:80 multiplexer. Two pol-muxed DPSK channels were further obtained via splitting, separate control of delay, polarization state, and attenuation, and re-combination. Another 10-GHz Calmar MLL at 1559.7 nm with a pulse width of ~1.9 ps served as the subrate pump clock used for pol-muxed DPSK data grooming in a 330-m HNLF and DPSK demultiplexing (80:10) in a 1-km HNLF. A 1-nm BPF after the 10-GHz Calmar MLL was used to properly broaden the pump pulse width for performance optimization. The polarizers (pol.) after HNLFs were adopted to separate X-/Y-polarized channel (80-Gbit/s DPSK) after grooming and extract tributary channel (10-Gbit/s DPSK) after demultiplexing.

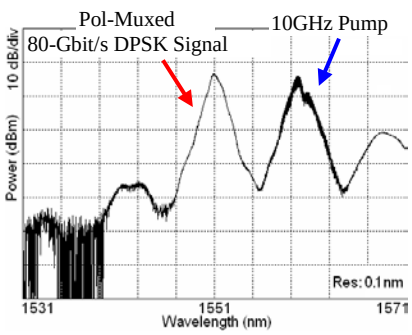

Figure 94. Spectrum of pol-muxed DPSK grooming

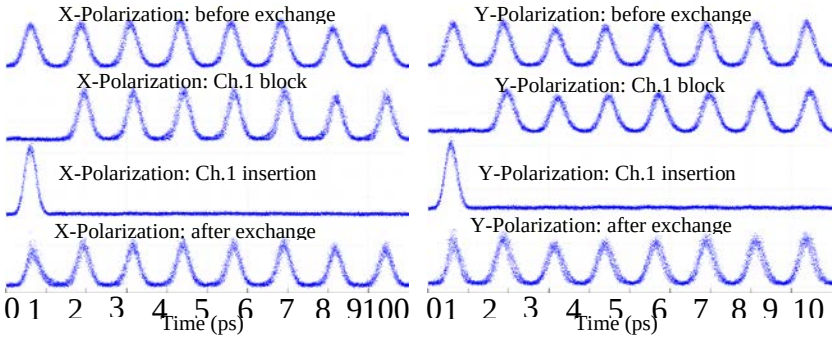

Figure 95. Eye diagrams of pol-muxed DPSK data grooming (tributary channel 1)

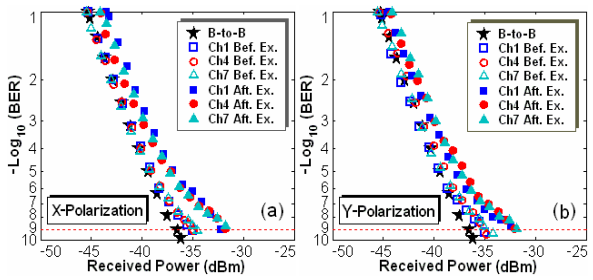

Figure 96. BER performance of pol-muxed DPSK data grooming

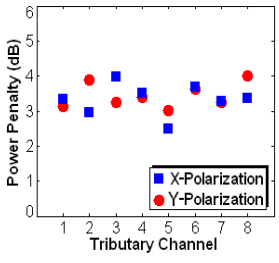

Figure 97. Penalty of 8 tributary channel.

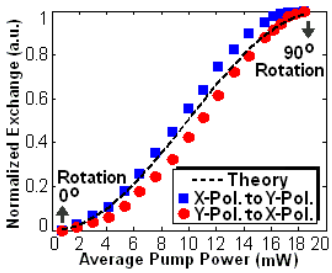

Figure 98. Pump power dependence

Figure 94 shows the spectrum of data grooming between two pol-muxed 80-Gbit/s DPSK channels. Figure 94 displays the eye diagrams of pol-muxed DPSK grooming measured by an

optical sampling scope. The input average power and peak power of the 10-GHz pump clock to the HNLF were ~19 and ~302 mW, respectively. As the 10-GHz pump clock was aligned to the tributary channel 1 (Ch.1) of 80-Gbit/s pol-muxed DPSK signal, in the absence of Y-polarization, the Ch. 1 of X-polarization was blocked by the polarizer (~18 dB) due to its rotation from X- to Y-polarization. When Y-polarization was turned on while X-polarization off, the Ch. 1 of Y-polarization was changed to X-polarization. In the presence of both X- and Y-polarization, the tributary Ch. 1 of Y-polarization was exchanged to X-polarization. Similarly, the Ch. 1 of X-polarization was also swapped to Y-polarization, resulting in tributary channel data grooming/exchange between two pol-muxed DPSK channels.

Figure 95 depicts the BER curves of pol-muxed DPSK data grooming. Approximately 3.3-dB power penalty was observed due to the beating effect between the newly inserted and residual signals. Figure 97 further shows the power penalty of 8 tributary channel data grooming. Less than 4 dB power penalty was obtained for all 8 tributary channels with a fluctuation <1.5 dB. Figure 98 presents the pump power dependence of power exchange (polarization rotation) between X- and Y-polarization. The experimental results were consistent with the theoretical calculations. Tributary channel data grooming/exchange between two pol-muxed DPSK channels was implemented under an average pump power of ~19 mW.

4.24. Demonstration of Reconfigurable 40-Gbit/s Tributary Selection from a 640-Gbit/s Signal using NOLM-based Cascaded Demultiplexing

We have experimentally demonstrated reconfigurable, multiple 40-Gbit/s tributary selection from a 640-Gbit/s signal using NOLM-based cascaded demultiplexing. Two arbitrary tributaries are selected using XPM in a NOLM controlled by two 40 GHz optical clocks with adjustable delay. The selected tributaries are then redistributed using a 2nd NOLM. An average penalty of ~3.5 dB at 10^{-9} BER is introduced by each NOLM.

As the network capacity increases, reconfigurably routing data tributaries becomes more challenging in optical networks. In order to enable the reconfigurability of manipulating data tributaries, it would be desirable for the network elements to agilely select tributary channels and complete the routing function. By incorporating a tributary selecting block, i.e. a tunable optical DEMUX stage, in each network node, a simple structure of a distributed optical network can be constructed, Figure 99(a). Two arbitrary tributaries of a high-speed signal from a core optical network are selectively routed to local area network #1 (LAN1) while the other two tributaries are sent to LAN2. LAN2 then distributes the data tributaries to local users C and D.

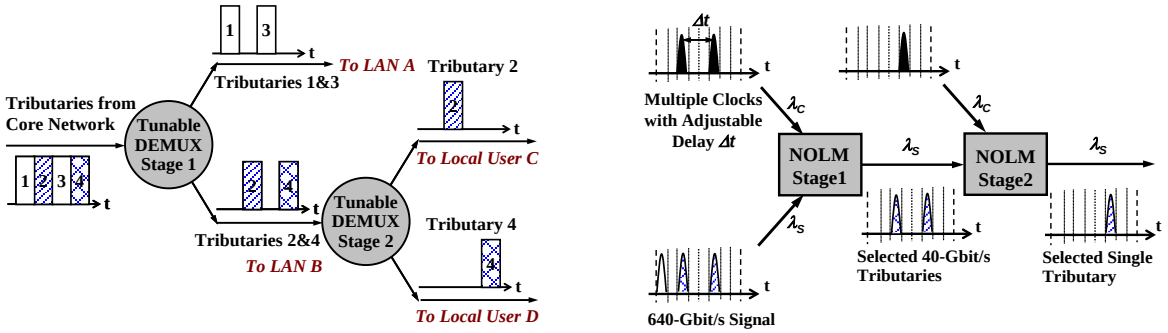

Figure 99. Concept. (a) A distributed optical network; (b) NOLMs for reconfigurable tributary selection. DEMUX: demultiplexing; LAN: local area network; NOLM: nonlinear optical loop mirror; λ_S: signal wavelength; λ_C: clock wavelength

Figure 99(b) shows the concept of using cascaded NOLMs for reconfigurable tributary selection from a 640-Gbit/s signal at λ_S. An NOLM is formed by connecting the two ends of a nonlinear element to a four-port fiber coupler to make a Sagnac interferometer. Demultiplexing is accomplished by introducing a relative phase shift between the two counter-propagating signal paths through XPM induced by a control pulse. With the clocked pumps off, the input 640-Gbit/s signal is suppressed at the output of the NOLM. When the tributary rate clocks @ λ_C are synchronized to the tributaries to be selected, the interaction between the signal and pumps results in a phase shift in the selected signal tributaries due to XPM. Therefore, at the output of the NOLM, the tributaries can be selectively separated. The scheme allows reconfigurably selecting arbitrary tributaries from a high-speed data stream by inserting/removing optical clocks at the tributary rate of the signal and adjusting the delay among the clock tributaries.

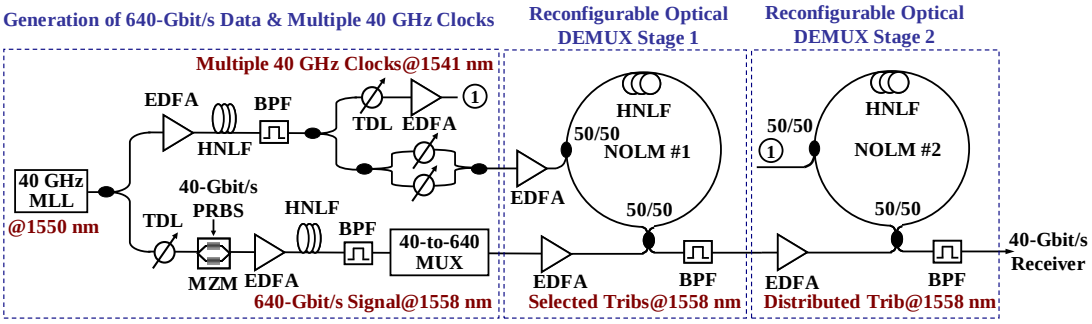

Figure 100. Experimental setup. MLL: mode locked laser; TDL: tunable delay line; MZM: Mach-Zehnder modulator; HNLF: highly nonlinear fiber; BPF: band-pass filter; (DE)MUX: (de)multiplexing; Trib: tributary

Figure 100 shows our experimental setup. A 40 GHz MLL at ~1550 nm with a pulse width of ~1.5 ps was used. Data modulation was applied using a Mach-Zehnder modulator driven by a 2^{15}-1 PRBS at 40-Gbit/s. The signal was then amplified and sent to a 200 m piece of HNLF, with a dispersion value of ~-0.85 ps/nm @1550 nm and a dispersion slope of ~0.01 ps/nm^2/km, for supercontinuum generation. A 9 nm optical BPF was inserted for spectrum slicing to obtain a compressed copy of the 40-Gbit/s data signal at ~1558 nm. The signal was then multiplexed to a 640-Gbit/s data stream using a passive optical multiplexer. A portion of the MLL output was tapped off to generate the optical clocks that are suitable for selecting multiple tributaries as well

as for tributary redistributing. The tapped portion is amplified before going through another 200 m piece of HNLF, which has the same parameters as the one used for obtaining the compressed data. A 5 nm filter was used to filter out the compressed 40 GHz clock at ~1541 nm. The clock was split into two copies. One copy was split a second time such that the copies can be adjustably delayed and recombined for reconfigurable two-tributary selection, while the other clock was for further tributary distribution. The multiplexed 640-Gbit/s signal and the combined optical clocks were then sent to an NOLM, which consisted of a 100 m HNLF, with a nonlinear coefficient of 11 W-1·km-1, a zero dispersion wavelength (ZDW) of ~1558 nm, and a dispersion slope of ~0.02 ps/nm^2/km. Another 9 nm BPF was used after the NOLM to filter out the selected tributaries. The filtered tributaries were then demultiplexed/redistributed in another NOLM, which consists of another piece of 100 m HNLF with the same parameters as the HNLF used in the 1st NOLM. The demultiplexed signal was then filtered by a 3 nm filter and sent to a 40-Gbit/s pre-amplified receiver for BER measurement. Note that the supercontinuum stage was polarization insensitive; the NOLM-based stages were polarization dependent and we used polarization controllers (PCs) to maximize the suppression ratio, defined as the ratio of the max and min output power of a NOLM without the clocks on, and XPM depth for each NOLM stage.

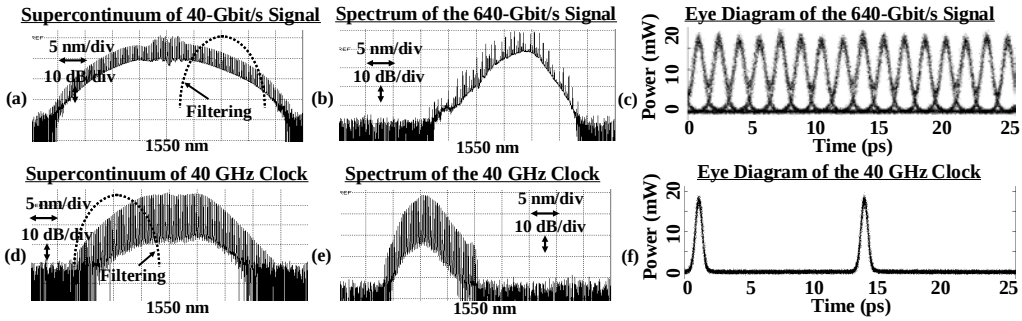

Figure 101. Experimental spectra and eye diagrams

Figure 101(a) shows the supercontinuum of the 40-Gbit/s signal. The input power to the 200 m HNLF for generating this supercontinuum was ~26 dBm. A converted and compressed copy at ~1558 nm was then obtained by filtering the supercontinuum, with a pulse width of ~0.8 ps, and then multiplexed to 640-Gbit/s. The residual dispersion from the components in the setup was carefully compensated by proper amount of DCF. Shown in Figure 101(b) was the optical spectrum after filtering the supercontinuum and subsequent 40-to-640-Gbit/s multiplexing. Figure 101(c) shows the corresponding 640-Gbit/s eye diagram. Similarly, the spectra and eye diagram for the 40 GHz clock supercontinuum are shown in Figure 101(d), (e) and (f), respectively. The power used for generating the clock supercontinuum was ~ 28 dBm. The obtained 40 GHz clock had a pulse width of ~0.8 ps. The 640-Gbit/s signal is amplified to had an average power of ~24 dBm before going through the 1st NOLM. The total power of the two 40 GHz optical clocks was ~22 dBm. After the tributaries were selected from the 640-Gbit/s data stream, further redistribution of the 40-Gbit/s channels was performed. The power of the selected two tributaries and the 40 GHz clock into the 2nd NOLM were ~14 dBm and ~20 dBm, respectively. The suppression ratios of the two NOLMs were measured to be ~30 dB and ~23 dB, respectively.

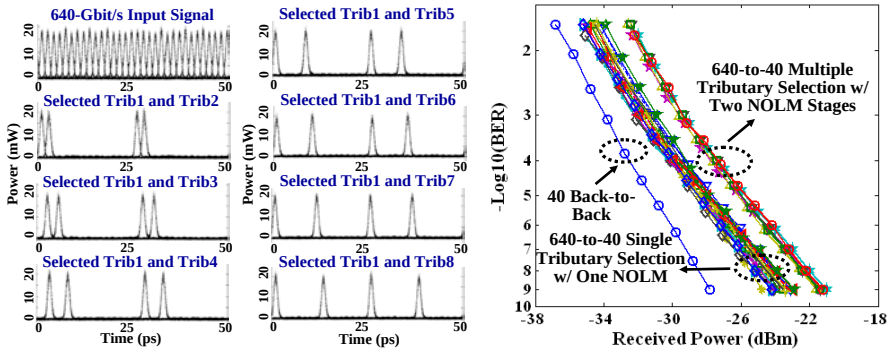

Figure 102. 640-Gbit/s BER performance for reconfigurable tributary selection and redistribution. (a) BER performance; (b) eye diagrams of the selected tributaries. Trib: tributary

Single tributary selection from the 640-Gbit/s signal was first carried out using one NOLM. BER measurements were performed to characterize the 640-Gbit/s signal without the reconfigurable two-tributary selection stage inserted. An average power penalty of ~4 dB was observed for all 16 tributaries. The reconfigurable two-tributary selection stage introduced an ~3 dB power penalty at 10^{-9} BER, as shown in Figure 102(a). The penalty was partially due to the slight pulse broadening through the fiber, optical filters and EDFAs, and the slow phase drift between the signal and the optical clocks induced by fluctuations of the HNLF lengths. The silica-HNLFs used in the demonstration can be replaced by specialty HNLFs or some integratable devices, having much shorter lengths and thus reducing the phase drift significantly. The corresponding eye diagrams of the selected two tributaries are shown in Figure 102(b). We clearly observed the pulse width and eye opening were maintained after the nonlinear operations.

4.25. Demonstration of 100-Gbit/s DQPSK Data Exchange between Two Different Wavelength Channels using Parametric Depletion in a Highly Nonlinear Fiber

We have also demonstrated 100-Gbit/s DQPSK data exchange between two different wavelength channels by exploiting the parametric depletion effect of non-degenerate FWM in an HNLF. Less than 5 dB power penalty was obtained for the 100-Gbit/s DQPSK data exchange. Furthermore, the tolerance of pump misalignment (+/-2 ps) and the dynamic range of input signal power (~20 dB) were investigated for the 100-Gbit/s DQPSK data exchange. [25]

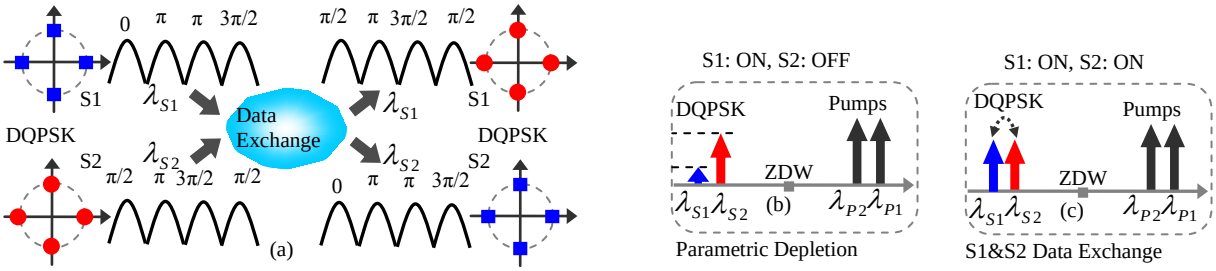

Figure 103. (a) Concept of DQPSK data exchange. (b)(c) Principle of parametric depletion and data exchange

Shown in Figure 103(a) is a conceptual diagram of DQPSK data exchange between two wavelength channels ($\lambda_{S1}, \lambda_{S2}$). In order to swap the quadrature-phase-modulated data, phase-transparent exchange is highly desirable, which can be realized using the parametric depletion

effect of non-degenerate FWM in an HNLF. Figure 103(b) illustrates the parametric depletion effect. Signal 1 (S1: λ_{S1}) and two pumps (P1: λ_{P1}, P2: λ_{P2}) are fed into the HNLF with S1 and P1 symmetric relative to the ZDW. During the non-degenerate FWM process, S1 and P1 photons are consumed to generate photons of P2 and S2 ($1/\lambda_{S2} = 1/\lambda_{S1} + 1/\lambda_{P1} - 1/\lambda_{P2}$). This causes parametric depletion of S1 with its data copied onto S2. When two signals (S1, S2) and two pumps (P1, P2) are simultaneously employed with S1(S2) and P1(P2) symmetric with respect to the ZDW of the HNLF, as shown Figure 103(c), S1(S2) can be depleted and converted to S2(S1) resulting in the data exchange between S1 and S2.

Under the non-depletion approximation, simple linear relationships of the output ($A_{S1}^{'}, A_{S2}^{'}$) and input ($A_{S1}, A_{S2}, A_{P1}, A_{P2}$) complex amplitudes are available ($A_{S1}^{'} \propto A_{S2} \cdot A_{P2} \cdot A_{P1}^{*}, A_{S2}^{'} \propto A_{S1} \cdot A_{P1} \cdot A_{P2}^{*}$) by the proper control of pump powers. Phase relationships of $\phi_{S1}^{'} = \phi_{S2} + \phi_{P2} - \phi_{P1}$ and $\phi_{S2}^{'} = \phi_{S1} + \phi_{P1} - \phi_{P2}$ are further obtained which clearly indicates the phase-transparent data exchange. Remarkably, pump phase modulation is always required to effectively suppress the stimulated Brillouin scattering (SBS) effect such that high-power pumps can be used for the effective parametric depletion. The pump phase transfer does not affect the OOK data exchange but may cause serious trouble during the DQPSK data exchange. Fortunately, according to the phase relationship, it is possible to cancel the pump phase transfer by applying the same phase modulation on the two pumps, which enables the phase-transparent DQPSK data exchange.

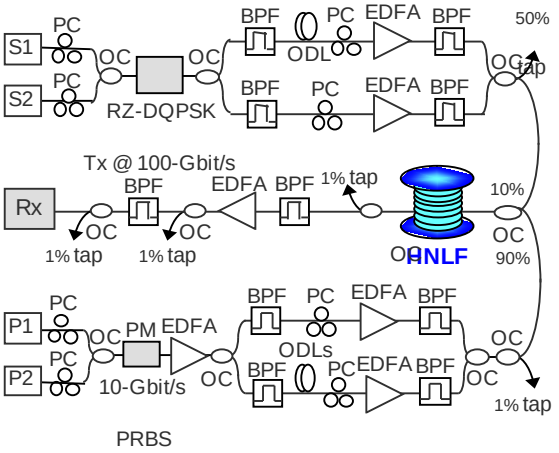

Figure 104. Experimental setup for 100-Gbit/s DQPSK data exchange. EDFA: erbium-doped fiber amplifier; OC: optical coupler; PC: polarization controller

Figure 104 shows the experimental setup for 100-Gbit/s DQPSK data exchange. Two 100-Gbit/s return-to-zero DQPSK (RZ-DQPSK) signals (S1, S2) and two pumps (P1, P2) were launched into a 1-km piece of HNLF (ZDW: ~1552 nm), in which DQPSK data exchange was realized based on the parametric depletion effect via the non-degenerate FWM process. Note that the two pumps were phase-modulated using the same phase modulator (PM) driven by a 10-Gbit/s PRBS. BPFs were then employed to separate the two pumps and suppress the amplified spontaneous emission (ASE) noise. The two pump branches needed to be accurately aligned using tunable optical delay lines (ODLs). Pump misalignment may cause significant performance degradation. The data exchange performance was optimized by the appropriate adjustment of pump powers and the pump and signal polarization states.

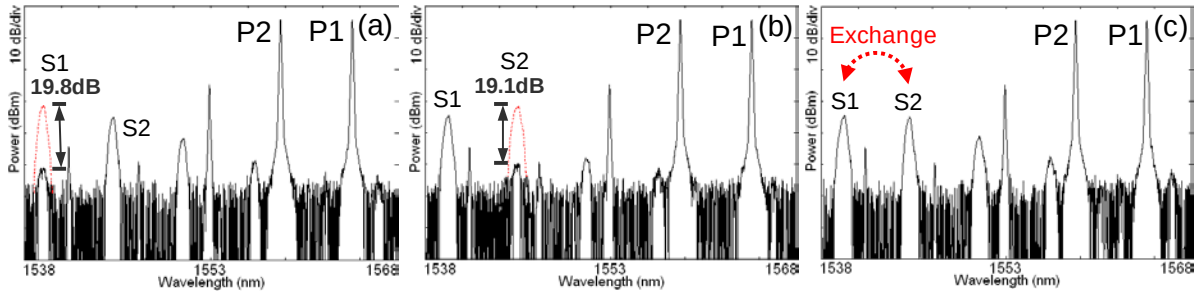

Figure 105. Optical spectra for 100-Gbit/s DQPSK data exchange. (a) S1:ON, S2:OFF; (b)S1:OFF, S2:ON; (C) S1&S2 ON

Figure 105 shows the measured spectra of parametric depletion and 100-Gbit/s RZ-DQPSK data exchange. Two 100-Gbit/s RZ-DQPSK signals (S1: 1539.4 nm, S2: 1545.4 nm) and two pumps (P1: 1564.4 nm, P2: 1558.6 nm) were used. The input power of each signal and pump coupled into the HNLF was about 0 and 23.8 dBm, respectively. As shown in Figure 105(a)(b), clear parametric depletion (S1: ~19.8 dB, S2: ~19.1 dB) was observed when only S1(S2) and the two pumps were turned on. Shown in Figure 105(c) was a typical spectrum of data exchange when the two signals and two pumps were all present.

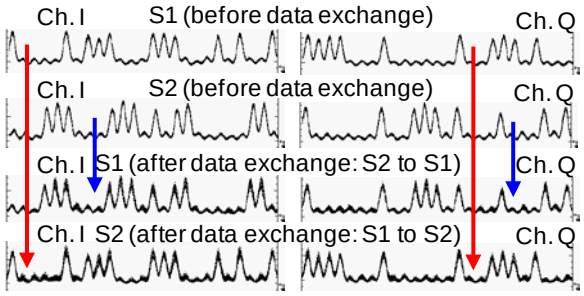

Figure 106. Demodulated waveforms (Ch. I and Ch. Q) for 100-Gbit/s DQPSK data exchange

Figure 106 depicts the temporal waveforms of the demodulated Ch. I and Ch. Q, from which we can clearly see that 100-Gbit/s DQPSK data exchange was successfully implemented. Figure 107 plots the constellation diagrams of different optical waves, from which we can see the four-phase levels of 100-Gbit/s DQPSK. Figure 108 plots the BER curves and balanced eye diagrams for 100-Gbit/s DQPSK data exchange. The power penalty of wavelength conversion with only one signal turned on was less than 1.2 dB at a BER of 10^{-9}. Less than 5 dB power penalty was obtained for 100-Gbit/s DQPSK data exchange. The extra penalty of data exchange compared to wavelength conversion mainly came from the beating effect between the newly converted and residual signals.

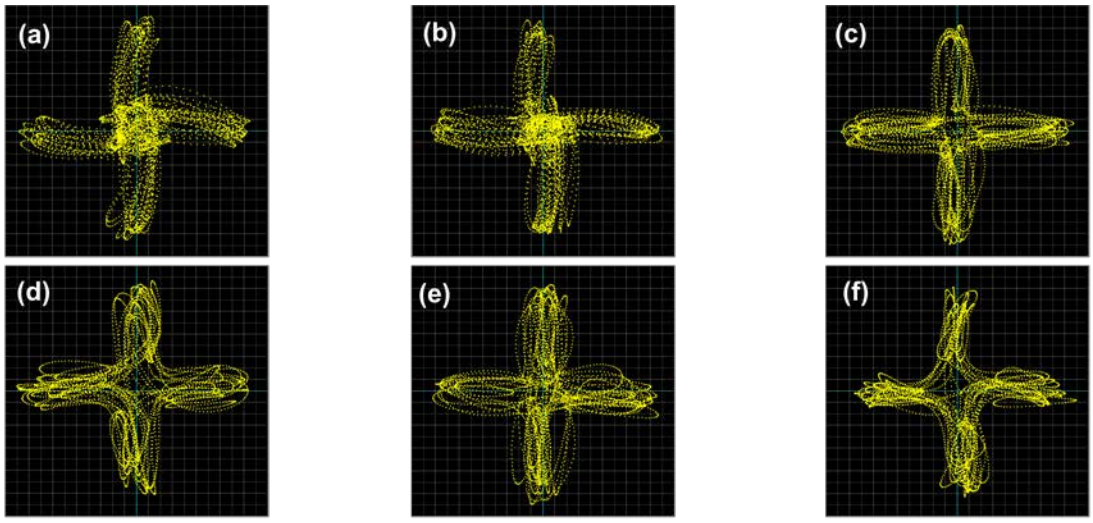

Figure 107. Constellation diagrams for 100-Gbit/s DQPSK data exchange. (a) S1: back-to-back; (b) S2: back-to-back; (c) Wavelength conversion (WC: S2 to S1) (S1: OFF, S2: ON); (d) Wavelength conversion (WC: S1 to S2) (S1: ON, S2: OFF); (e) Data Exchange (Ex.: S2 to S1) (S1, S2: ON); (f) Data Exchange (Ex.: S1 to S2) (S1, S2: ON)

For the 100-Gbit/s DQPSK data exchange, we further investigated the tolerance of pump misalignment and the dynamic range of input signal power. Figure 109 shows the relative power penalty as a function of pump misalignment. It can be clearly seen that the performance degraded quickly as the misalignment goes beyond +/- 2 ps. Such a phenomenon can be ascribed to the fact that large pump misalignment causes incomplete phase cancellation and resultant phase transfer to DQPSK signals. Therefore, accurate pump alignment was of great importance to achieve the optimized data exchange performance. Figure 109 further presents the received power at a BER of 10^{-9} versus input signal power. Approximately 20 dB of dynamic range of input signal power was achieved.

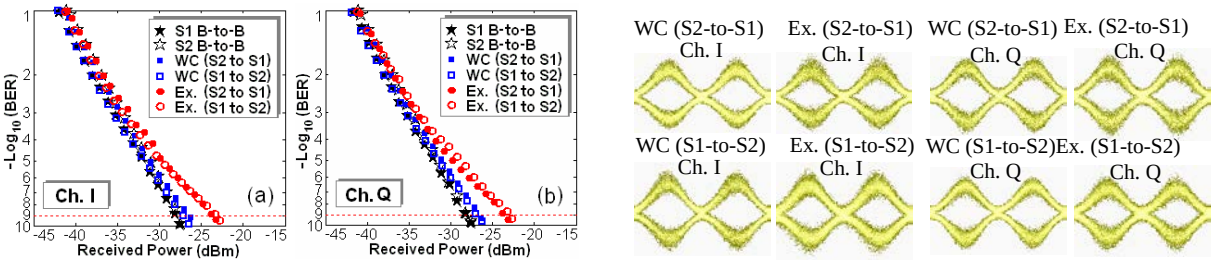

Figure 108. BER and balanced eye diagrams for 100-Gbit/s DQPSK data exchange

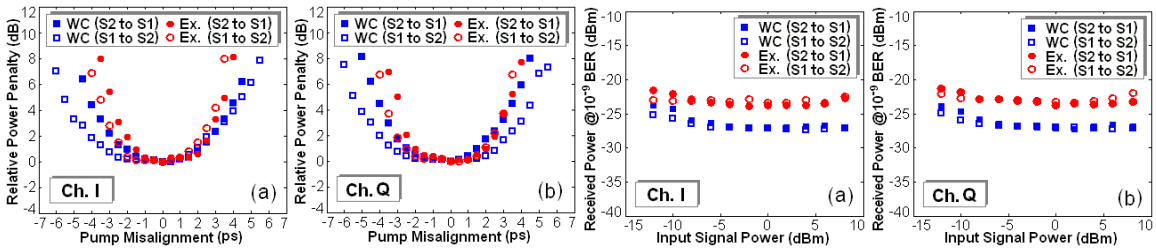

Figure 109. Pump misalignment tolerance and dynamic range of input signal power for 100-Gbit/s DQPSK data exchange. of 100-Gbit/s DQPSK data exchange

4.26. 3.6 µs of Continuously Tunable Optical Delay for a 100-Gbit/s DQPSK Signal Using Conversion/Dispersion and Higher-Order Dispersion Compensation

We have demonstrated 3.6 µs of continuously tunable optical delay for 100, 80, and 20 Gb/s RZ-DQPSK and 50, 40, 10 Gb/s RZ-DPSK signals using conversion/dispersion and higher-order dispersion compensation. Residual dispersion compensation was achieved using phase conjugation while higher-order dispersion compensation was achieved using fixed slope compensating fibber-Bragg-gratings (FBGs) and a liquid-crystal-on-Silicon (LCOS) spatial-light-modulator (SLM) for tunable slope compensation. Residual dispersion slope was reduced from a worst case -230 ps/nm^2 to ±10 ps/nm^2 enabling operation at 100 Gb/s. This corresponds to a delay-bit-rate product exceeding 360,000 at 100 Gb/s. [24]

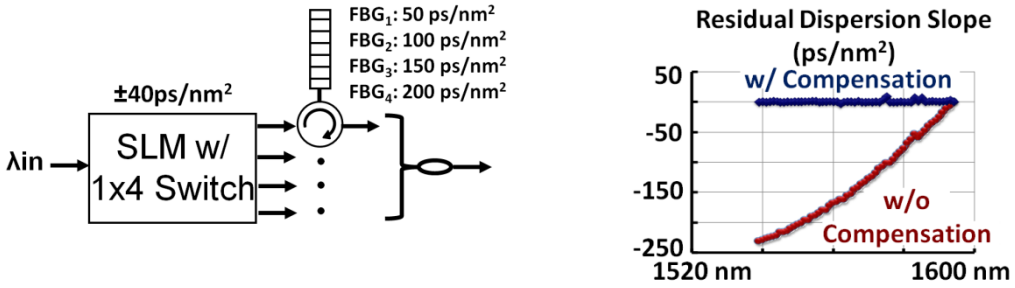

Figure 110. Conceptual diagram of dispersion slope compensation to enable 100 Gb/s operation. A 96% reduction in dispersion slope is achieved using fixed fiber-Bragg-gratings (FBGs) and a tunable Spatial light modulator (SLM)

As the phase-conjugation method used is not wavelength maintaining, the two passes through the dispersive element see different values of dispersion. It has been shown that pre-dispersing the original signal and allowing the phase conjugation distance to vary can compensate for this offset. However, odd-order dispersion coefficients, including dispersion slope, are not compensated by the phase conjugation process but accumulate on both passes. For high-rate signals where the residual dispersion slope cannot be neglected, higher-order compensation is required in addition to this pre-dispersion. A conceptual diagram of the higher-order compensation is shown in Figure 110. A commercially available SLM with an integrated 1x4 switch is combined with fixed FBGs to provide both the pre-dispersion and dispersion slope compensation simultaneously. The SLM is capable of generating both amplitude and phase transfer functions with a 5 GHz resolution. The maximum dispersion-bandwidth product is ±40 ps. For a 1 nm bandwidth, this translates into a tuning range of ±40 ps/nm of dispersion and ±40 ps/nm^2 for dispersion slope. The four FBGs provide: 1) +50 ps/nm and +50 ps/nm^2, 2) +140 ps/nm and +100 ps/nm^2, 3) +280 ps/nm and +150 ps/nm^2, and 4) +420 ps/nm and +200 ps/nm^2

respectively. Combined with the SLM, both residual dispersion and residual dispersion slope can be minimized to enable high-rate operation. Shown on the right side of Figure 110 is the measured residual dispersion slope before compensation and after compensation.

An experimental block diagram of our setup is shown in Figure 111. 100, 80, and 20 Gb/s DQPSK were generated by driving two parallel integrated MZMs with 50, 40, and 10 Gb/s, PRBS. A pulse carver was used to generate 50% RZ waveforms. The RF data was shifted by 33 bits at 100 and 80 Gb/s and 7 bits at 20 Gb/s to de-correlate the two data streams. One data stream was removed to generate the 50, 40, and 10 Gb/s RZ-DPSK signals.

The optical signal ($\lambda_{IN} \approx 1535.3$ nm) was first passed through the pre-dispersion and slope compensation element. Depending on the required delay value, one of the four FBGs was chosen and the SLM is set to provide the correct pre-dispersion and slope compensation values. The optical signal was then wavelength converted using a 460 m piece of HNLF with a ZDW of ~1556 nm. A 1-pump DFWM approach was used to convert the signal from 1539.3 to 1593.3 nm. The pump and signal powers varied over 15-21 dBm to provide a minimum -25 dB conversion efficiency. The converted signal was then filtered out and sent through dispersion compensating fiber (DCF) ($D \approx -32$ ns/nm at 1550 nm) to impose a wavelength-dependent delay. Co- and Counter-propagating Raman amplification in the DCF was used to compensate for the ~90 dB of loss. Launch powers into each section of fiber were kept below -5 dB and >27 dB OSNR was maintained at all times. Following the DCF, the delayed signal was phase conjugated using a second piece of 330 m HNLF ($ZDW \approx 1558$ nm). Again, a 1-pump DFWM approach phase conjugated the signal ~4 to 14 nm up in wavelength. Pump and signal powers were 10-14 dBm and required no SBS suppression. The signal was then passed through the DCF a second time to compensate the intra-channel dispersion and to undergo a second wavelength dependent

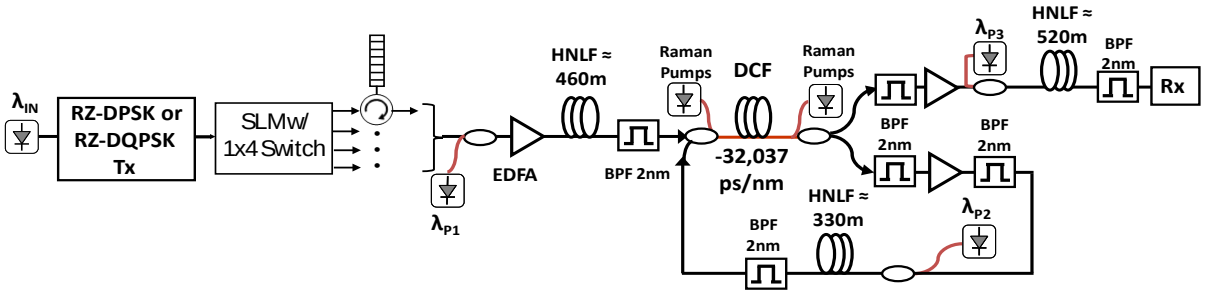

Figure 111. Experimental setup. 100, 80, and 20 Gb/s RZ-DQPSK and 50, 40, 10 Gb/s RZ-DPSK are pre-dispersed and dispersion slope compensated using a spatial light modulator (SLM) and matched fiber-Bragg-gratings (FBGs) prior to delay. Wavelength conversion in highly nonlinear fiber (HNLF) and propagation through dispersion compensating fiber (DCF) generate the 3.6 μs continuously tunable delay

delay. Finally, the signal was returned to the original wavelength using a third DFWM setup with ~450 m of HNLF ($ZDW \approx 1558$ nm). The pump and signal powers varied from ~17 to 21.5 dBm to return the conjugated signal in the range of ~1543.5 to 1597.1 nm back to the original wavelength of 1535.3 nm. Furthermore, the use of independent pumps for all three wavelength conversion stages allowed the output wavelength to be reconfigurable depending on the application of the delay line. The signal was received using a pre-amplified receiver with 50, 40, and 10 GHz delay-line interferometers (DLI) and a 32 GHz balanced photo-receiver.

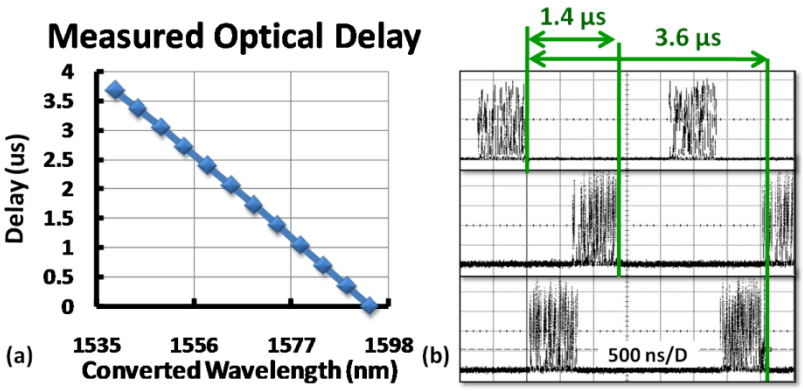

Figure 112. (a) Measured delay curve. A maximum 3.6 µs delay is achieved. (b) 7 Gb/s packets showing the full delay tuning range

A 500 bit packet at 7 Gb/s was used to measure the delay of 3.6 µs over an ~55 nm conversion range as shown in Figure 112a and b. Figure 112c shows the wavelength conversion and phase conjugation experimental spectra for the minimum delay of 100 Gb/s RZ-DQPSK. The conversion efficiency was -25 dB for the wavelength conversion case and -12 dB for the case of phase conjugation. Raising the conversion efficiency of either stage only increased phase noise and did not improve system performance.

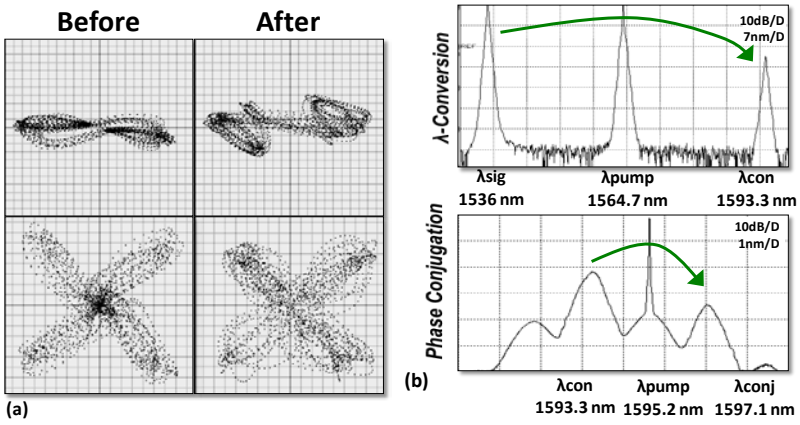

Figure 113. (a) Constellation diagrams for 50 Gb/s RZ-DPSK (top) and 100 Gb/s RZ-DQPSK (bottom) before and after the delay. (b) Experimental spectra of the first wavelength conversion stage (top) and the phase conjugation stage (bottom) for 100 Gb/s RZ-DQPSK

The dispersion slope compensation was also varied to assess its impact on the system. For the maximum -230 ps/nm^2 residual dispersion slope, at 10 Gbaud (10 GSymbol/second), there was less than 1 dB of improvement when adding the correct amount of higher-order compensation. However, at 40 and 50 Gbaud, the signals were not recoverable without proper slope compensation. Figure 113a shows the constellation diagrams of 50 Gb/s RZ-DPSK (top) and 100 Gb/s RZ-DQPSK (bottom) before and after the delay element captured by a complex optical spectrum analyzer. The addition of phase noise was visible following the multiple wavelength conversion and Raman amplified dispersion stages.

BER measurements were performed to assess the system performance of the different data-rates and formats. Figure 113(b) shows the performance curves for RZ-DQPSK while Figure 113(c) shows the performance curves for RZ-DPSK at the maximum (1539.3 nm), middle (1567 nm), and minimum (1593.3 nm) delay values. 10 Gbaud had the lowest penalty, as expected with <1dB for DPSK and ~1dB for DQPSK. 40 Gbaud and 50 Gbaud signals had respective maximum penalties of 4 and 4.4 dB for DPSK and 5.8 and 7 dB for DQPSK. The maximum delay had the worst performance in all cases due to inadequate filtering caused by the proximity to the pump in the first two wavelength conversion stages.

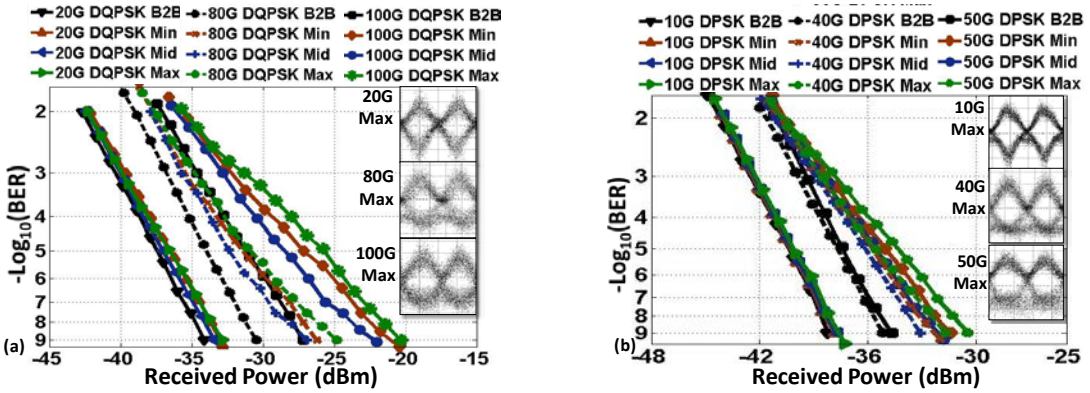

Figure 114. (a) 100, 80, and 20 Gb/s RZ-DQPSK performance curves for the back-to-back (B2B), minimum, middle, and maximum delay values. (b) 50, 40, 10 Gbs RZ-DPSK performance curves for B2B, minimum, middle, and maximum delay values

4.27. Multicasting of 50 Gb/s RZ-DPSK Signals using Self-Seeded FWM with Phase Modulated Pumps for SBS Suppression

We have also demonstrated a method to use phase modulated pumps for 9-fold multicasting of 50 Gb/s RZ-DPSK signals using a self-seeded FWM scheme. Phase modulation of the signal prior to wavelength conversion by the same RF tone used for SBS suppression enabled minimally distorted output copies after multicasting. An average of ~1.8 dB power penalty at a BER of 10^{-9} was observed. [31]

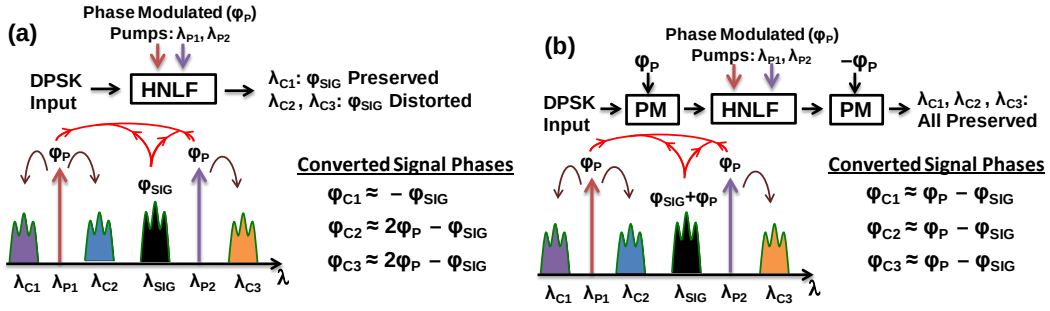

Figure 115. (a) Wavelength conversion using FWM and the resulting output phase information with phase modulated pumps. (b) Conceptual block diagram of the demonstrated multicasting scheme using phase modulated pumps

The conceptual block diagram of our scheme is given in Figure 115(b). An optical DPSK signal at λ_{SIG} (with phase φ_{SIG}) was multicast to several copies in an HNLF using self-seeded pump/

signal generation based on both degenerate and non-degenerate FWM. With high pump powers, generation of secondary pumps for wavelength conversion could be utilized, yielding multiple copies of the original signal. To achieve this, the two high power pumps were phase modulated with a tone (φ_P) to broaden the pump spectrum and increase the SBS threshold. As shown in the conceptual spectra in Figure 115(a), when phase modulated pumps are used in the given scheme, only the first copy, λ_{C1}, contains undistorted signal phase, i.e. $\varphi_{C1} \approx \varphi_{P1} - \varphi_{P2} + \varphi_{SIG} = \varphi_{SIG}$. For the other two outputs, λ_{C2} and λ_{C3}, the phases are $\varphi_{C2} \approx \varphi_{P1} + \varphi_{P2} - \varphi_{SIG}$, and $\varphi_{C3} \approx 2\varphi_{P1} - \varphi_{SIG}$. This results in $\varphi_{C2} = \varphi_{C3} \approx 2\varphi_P - \varphi_{SIG}$, which causes significant distortion in the converted signals due to the finite transition time during 0-π phase swings. However, if the input signal is also modulated with the same φ_P, all of the converted signals end up with phases $\varphi_{C1} = \varphi_{C2} = \varphi_{C3} \approx \varphi_P - \varphi_{SIG}$. The additional φ_P phase term could then be erased by modulation with $-\varphi_P$ as shown in the Figure 115(b). Hence, after the multicasting the converted signal copies were sent to a phase modulator driven 180° shifted from the original 375 MHz driving tone. This resulted in achieving copied signal phase information while enabling the use of phase modulated pumps in order to generate more copies by self-seeded FWM.

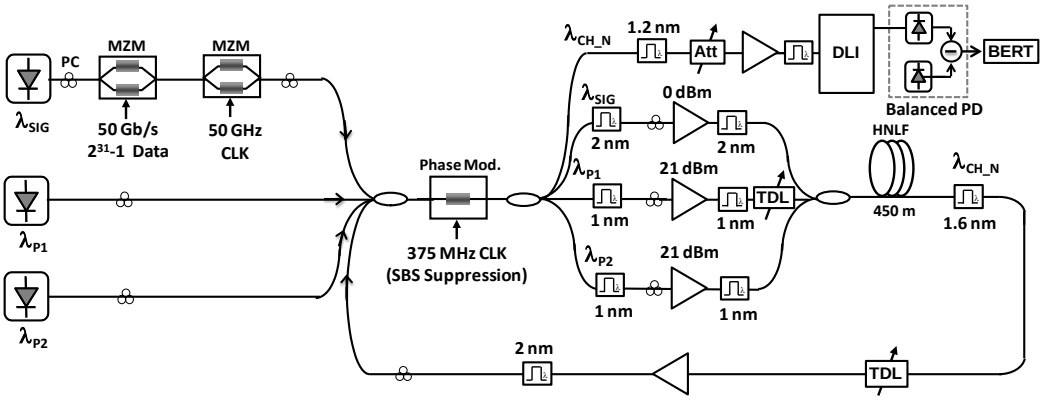

Figure 116. Experimental block diagram of the 50 Gb/s DPSK multicasting setup with phase modulated pumps used for self seeding. PC: polarization controller, BPF: band-pass filter, BERT: bit-error rate test-set, TDL: tunable delay line

An experimental block diagram of our 9-fold multicasting setup using phase modulated pumps is shown in Figure 116. A 50 Gb/s DPSK signal (λ_{SIG}~1556.8 nm) was generated using a MZM driven by a 2^{31}-1 PRBS. Full rate carving was used to generate the RZ waveform. The input signal was coupled with two CW pumps (λ_{P1}~1553.3 nm and λ_{P2}~1558.64 nm) in a 4x1 coupler and sent to a phase modulator (PM) driven by a 375 MHz tone for SBS suppression. The PM was driven by a full V_π swing. After being modulated by the 375 MHz tone, the input signal and the pumps were separated, individually amplified, and filtered to minimize unwanted ASE noise prior to being sent to a 450 m HNLF with a ZDW of ~1556 nm. A TDL was used to align the two pumps and ensure synchronized phase modulation in the HNLF. The dispersion slope of the HNLF was ~0.021 ps/nm^2/nm and the nonlinear coefficient, γ, was ~25 (W.km)$^{-1}$. The input power of the pumps into the HNLF were ~21 dBm while the DPSK signal power was ~0 dBm. After the multicast 50 Gb/s DPSK signal copies were generated in the HNLF by the FWM process, they were filtered off and sent to the same PM using the fourth input port of the 4x1 coupler. Hence, the multicast copies experienced the same 375 MHz tone modulation as the original signal. A TDL line was also employed to synchronize the phase modulation on the multicast copy such that it was 180° relative to the input signal. After the PM, each multicast

copy was filtered and sent to a preamplified receiver for detection. A 50 GHz delay line interferometer and a balanced photodiode are used for balanced detection. The signal was sent to a bit-error-rate test-set (BERT) for BER measurements.

The non-degenerate and degenerate FWM between the input DPSK signal, λ_{SIG}, and the two pumps, λ_{P1} and λ_{P2}, generated the DPSK signal copies at ~$2\lambda_{P1}$-λ_{SIG}, ~$2\lambda_{P2}$-λ_{SIG} , and at ~λ_{P1}+λ_{P1}-λ_{SIG}. In addition to these, new pumps were generated by the mixing of the two pumps at ~$2\lambda_{P1}$-λ_{P2}, and ~$2\lambda_{P2}$-λ_{P1}. These new pumps mixed with the signal copies in the HNLF to generate further copies of the signal according to the same FWM conditions. Nine copies of the 50 Gb/s RZ-DPSK signal were achieved by this self seeded multicasting scheme, limited by the self-seeding efficiency. Higher efficiency fiber, or a more complex RF tone combination, may allow for the generation of more copies.

The resulting spectrum after multicasting using phase modulated pumps for SBS suppression is shown in the Figure 117(a) below along with sample eye diagrams prior to detection. The generated multicast copies were at wavelengths ranging from ~1544.4 (λ_{CH1}) to ~1567.7 nm (λ_{CH9}). The spectrum given in Figure 117(b) was observed when the phase modulation was turned off while using the same input power levels. It can be seen from the comparison of Figure 117 (a) and (b) that as expected, the use of phase modulation resulted in an increase in the SBS threshold allowing the use of higher input pump powers and enabling self-seeding to achieve higher-order multicasting. In the case of Figure 117(b), the excessive power (more than the SBS threshold of ~16 dBm) was scattered causing significant distortion on the signal as shown in the eye diagram in Figure 117 (b). The eye diagrams (after the PM for deletion of the 375 MHz tone modulation) for all the output channels are given in Figure 118.

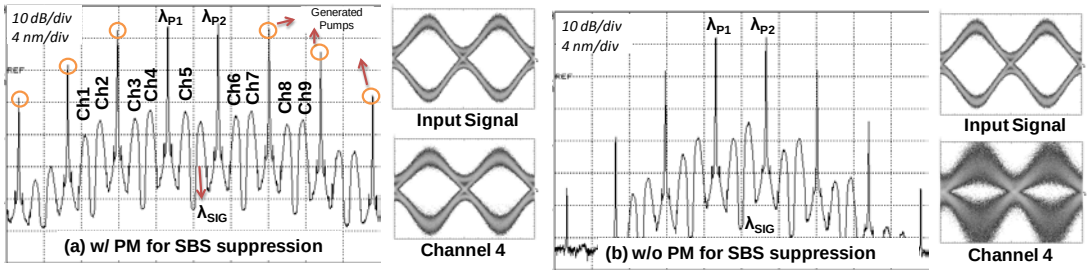

Figure 117. Spectra of the DPSK multicasting: (a) with phase-modulated signal/pumps; (b) without phase modulation

BER measurements were obtained on all nine multicast copies of the described multicasting scheme using a phase modulated signal and pumps. BER measurements showed an average of ~1.9 dB received power penalty (at a BER of 10^{-9}) for the multicast outputs. The maximum power penalty was observed for channel 9 with a ~2.3 dB penalty. Slightly higher penalties were observed for edge channels 1 and 9. The BER measurements along with the output channel balanced eye diagrams are given in the Figure 118.

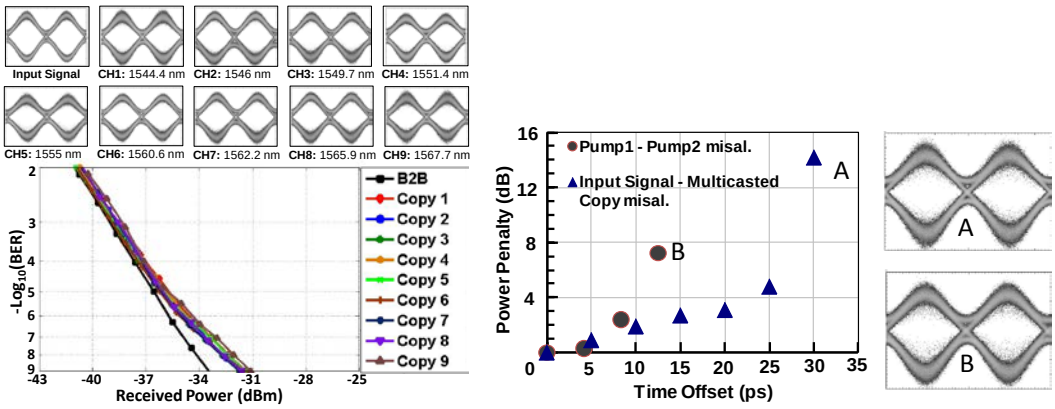

Figure 118. (a) BER performance of the multicast output copies, (b) Effect of timing offset between the Pump1 and Pump2 phases in the HNLF (circles); and between the converted signal and the 375 MHz RF tone (triangles) along with corresponding eye diagrams at points A and B

In order to achieve successful multicasting using phase modulated pumps, the 375 MHz tone phase modulation induced on the signal should be successfully erased after the multicasting. This requires the multicast copy to be precisely out of phase with the RF tone when passing through the PM. We observed that time misalignment of the multicast signal with respect to the RF tone results in significant degradation due to improper modulation removal. In addition, the two pumps also needed to be time aligned such that the 375 MHz tones were synchronized in the HNLF. The performance of the output channel 4 was investigated for any time misalignments between the two pumps and between the RF tone and multicast output as shown in the Figure 118 (b). An offset of ~30 ps between the RF tone and output signal phase modulation induced >10 dB penalty; while a similar penalty was observed for only ~15 ps offset between the two pumps.

4.28. Demonstration of 40-to-640-Gbit/s Multiplexing and Subsequent 640-to-10-Gbit/s Demultiplexing Using Cascaded Nonlinear Optical Loop Mirrors

We've experimentally demonstrated the use of XPM in a NOLM to achieve optical multiplexing of 40-Gbit/s data channels at different wavelengths onto a single 640-Gbit/s data channel. The 640-Gbit/s signal was then demultiplexed to 10-Gbit/s. An average penalty of approximately 3.5 dB at a 10^{-9} BER was observed after the nonlinear processes. Fiber-based NOLMs were used in our proof-of-concept demonstration. Potential implementations of NOLMs with some integrable nonlinear devices for signal (de)multiplexing are possible and will likely gain more interests in terms of practicality and power consumption.

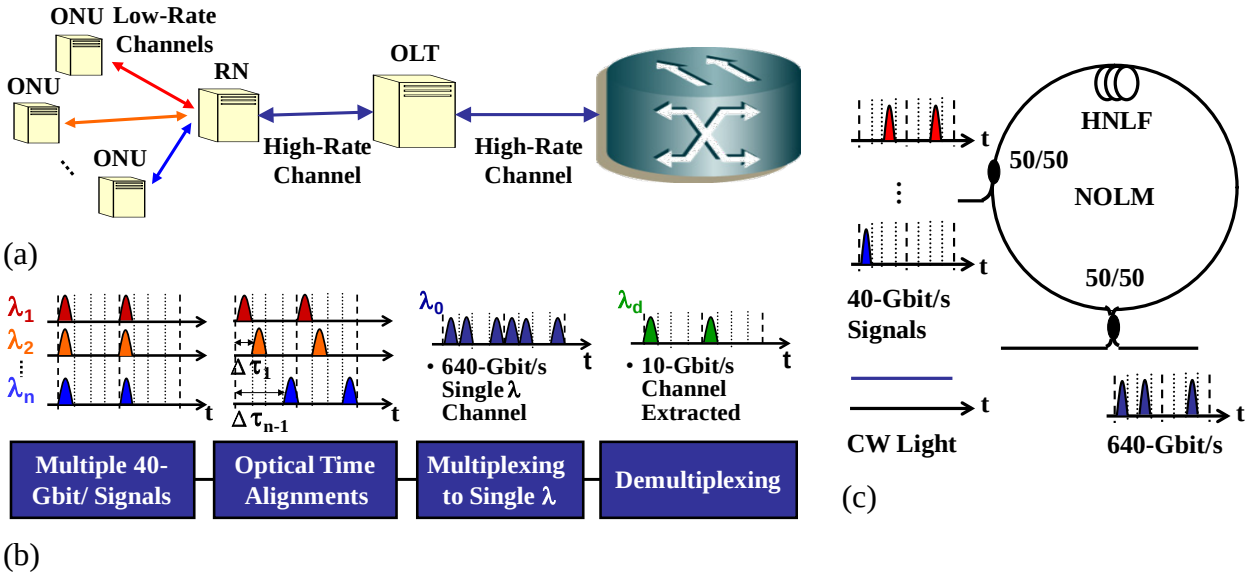

Figure 119. Conceptual diagrams. (a) A bidirectional optical link with conversion between low-rate channels and a high-rate channel; (b) system block diagram of signal multiplexing followed by demultiplexing; (c) concept of using an NOLM for optical multiplexing

In local area networks or long-haul systems, it is likely that many lower-rate signals exist. To efficiently utilize the available optical bandwidth, it may be desirable to convert different lower-rate channels onto a high-bit-rate single-wavelength channel. Figure 119(a) illustrates a bidirectional link to motivate optical (de)multiplexing. Low-rate signals from optical network units (ONUs) can be multiplexed to a high-rate signal in a remote node in order for further transmission. Similarly, a high-rate signal can be redistributed to low-rate users to obtain fine granularity.

Figure 119(b) shows a system-level block diagram of the scheme for signal multiplexing and subsequent demultiplexing. Multiple 40-Gbit/s signals at different wavelengths are shifted in time for optical multiplexing. A single 640-Gbit/s channel can be obtained through nonlinear interaction between the multiple signals and a continuous-wave (CW) laser. The multiplexed signal can then be demultiplexed to 10-Gbit/s for redistribution or performance evaluation. Note that we implement a multicasting stage in our demonstration in order to emulate multiple 40-Gbit/s channels. For practical implementations, in order to obtain the short pulsewidth signals, optical samplers would possibly be required to sample the original data channels.

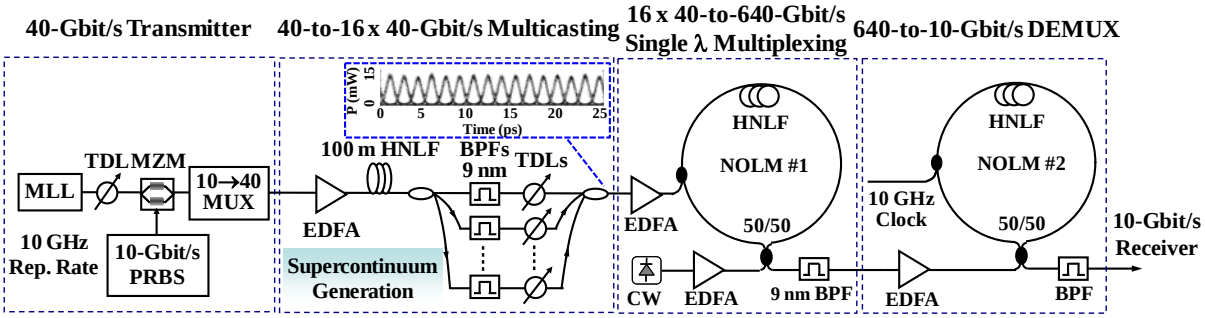

Figure 120. Experimental setup. The inset shows the eyes of the multicast 40-Gbit/s signals (time-interleaved) at different wavelengths. MLL: mode locked laser; TDL: tunable delay line; MZM: Mach-Zehnder modulator; MUX: multiplexer; BPF: band-pass filter

Figure 119(c) illustrates the concept of using an NOLM for optical multiplexing. An NOLM is formed by connecting the two ends of a nonlinear element to a four-port fiber coupler to make a Sagnac interferometer. With the signals off, the input CW is suppressed at the output of the NOLM. This is a consequence of destructive interference at the output port due to the static $\pi/2$ phase shift across the coupler. Multiplexing is accomplished by introducing a relative phase shift between the two counter-propagating CW paths through XPM induced by the signals to be multiplexed. Therefore, at the output of the NOLM, a multiplexed data stream can be obtained.

Figure 120 shows our experimental setup. A 10-GHz Erbium glass oscillating (ERGO) mode-locked laser (MLL) at ~1550 nm with a pulse width of ~1.5 ps was used. Data modulation was applied using a MZM driven by a pseudo-random bit sequence (PRBS) at 10 Gbit/s. The signal was then multiplexed to 40 Gbit/s using a passive optical multiplexer and sent to a 100-m piece of highly nonlinear fiber (HNLF), with a dispersion value of ~-0.9 ps/nm @ 1550 nm and a dispersion slope of ~0.01 ps/nm^2/km, for supercontinuum generation. Multiple 9-nm optical bandpass filters (BPFs) were inserted for spectrum slicing. The delay between the multicast signals was adjusted by using optical tunable delay lines (TDLs). The 40-Gbit/s signals and a CW at ~1535 nm were then sent to an NOLM, which consists of a 100-m HNLF, with a nonlinear coefficient of 11 W^{-1}·km^{-1}, a zero dispersion wavelength (ZDW) of ~1558 nm, and a dispersion slope of ~0.02 ps/nm^2/km. Another 9-nm BPF was used after the NOLM to filter out the multiplexed 640-Gbit/s signal. The 640-Gbit/s signal was then demultiplexed in another NOLM, which consists of another piece of 100-m HNLF with the same parameters as the HNLF used in the 1st NOLM. The 10-GHz optical clock used for demultiplexing was achieved by filtering the supercontinuum of the original MLL output with a 5-nm filter at ~1560 nm. The demultiplexed 10-Gbit/s signal was then filtered by a 2-nm filter and sent to a 10-Gbit/s pre-amplified receiver for BER measurement. Note that the NOLM-based stages were polarization dependent and we use polarization controllers (PCs) to maximize the extinction ratio, defined as the ratio of the max to min output power of an NOLM without the signals/clock on, and XPM depth for each stage.

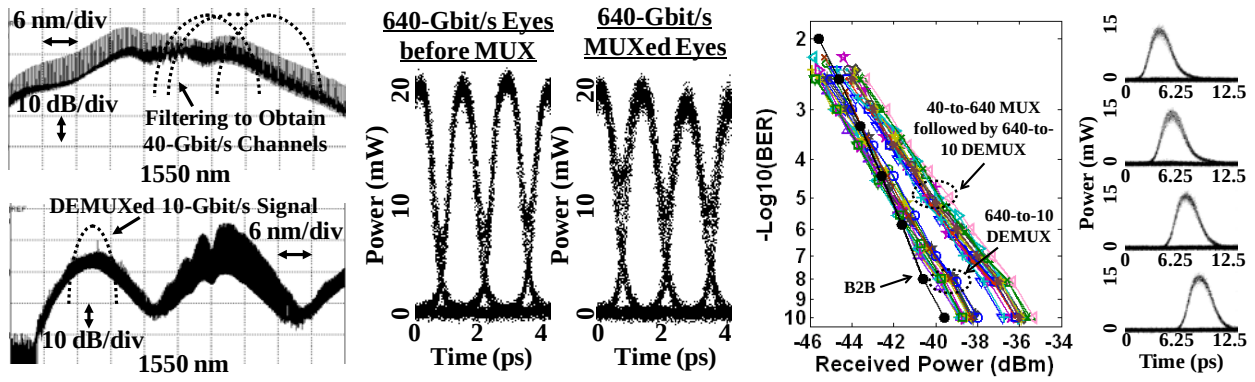

(a) (b) (c)

Figure 121. Experimental results. (a) Spectra after supercontinuum and 640-to-10-Gbit/s demultiplexing; (b) 640-Gbit/s eye diagrams before and after optical multiplexing; (c) 640-to-10-Gbit/s BER performance with and without 40-to-640-Gbit/s multiplexing

Fig.3 (a) (top) shows the supercontinuum after the 100-m HNLF. The average power launched into the HNLF was ~27 dBm. To obtain multicast copies after supercontinuum generation, an array of 2-cavity BPFs with ~9-nm bandwidth were used, with the center wavelengths from ~1555 nm to 1567 nm in steps of 0.8 nm. Note that different wavelengths see different frequency chirp, therefore, the pulses obtained were slightly different at each wavelength. We use different lengths of standard single mode fiber in each path to compensate the chirp, allowing signals with similar pulsewidth, ~0.8 ps, to be obtained. Note that these wavelength-multicast signals overlap in the frequency domain, but do not overlap in the time domain. The multicast signals were amplified to a total average power of ~28 dBm and then sent to the 1st NOLM to interact with the CW light. The power of the CW light into the NOLM was ~20 dBm. The required energy/bit for multiplexing was ~1.1 pJ/bit. A 9-nm 2-cavity BPF centered at ~1535 nm was used to filter out the multiplexed 640-Gbit/s signal. Subsequently, the 640-Gbit/s signal was demultiplexed to 10-Gbit/s and Figure 121(a) (bottom) shows the spectrum after demultiplexing. We can see that the multiplexed 640-Gbit/s signal was successfully suppressed at the output of the 2nd NOLM. The average power levels of the 10-GHz clock and the 640-Gbit/s multiplexed signal into the 2nd NOLM were ~20 and ~26 dBm, respectively. The energy/bit for demultiplexing was ~1.4 pJ/bit. The signals at different stages were sent to a sampling scope with a resolution of ~0.8 ps. The extinction ratios of the two NOLMs were measured to be ~ 31 dB and ~25 dB, respectively. The loss of each NOLM, measured across the two ports of the 2×2 coupler, was ~ 8 dB.

Shown in Figure 121(b) are the eye diagrams of the multiple time-interleaved 40-Gbit/s signals (left) and the multiplexed 640-Gbit/s signal (right). After demultiplexing the 640-Gbit/s signal to 10-Gbit/s, BER measurements were performed to characterize the nonlinear processes. Figure 121(c) shows the BER performance of the demultiplexed 10-Gbit/s tributaries with and without 40-to-640-Gbit/s multiplexing. Note for clarity we only show BER for 16 10-Gbit/s channels. A few eye diagrams of the demultiplexed 10-Gbit/s tributaries are also given. An average penalty of approximately 1 dB at 10^{-9} BER was observed for the 640-to-10-Gbit/s demultiplexing without inserting the multiplexing stage when compared to 10-Gbit/s back to back performance. An extra penalty of ~2.5 dB was observed with the 40-to-640-Gbit/s multiplexing process considered, mainly due to the pulse broadening through the optical fiber, filters and amplifiers. Better performance can be expected by using improved nonlinear devices.

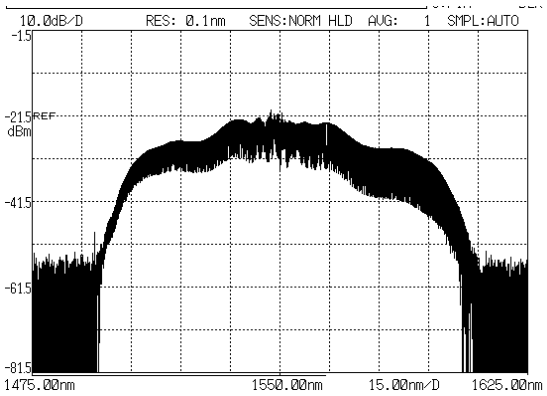

(a)

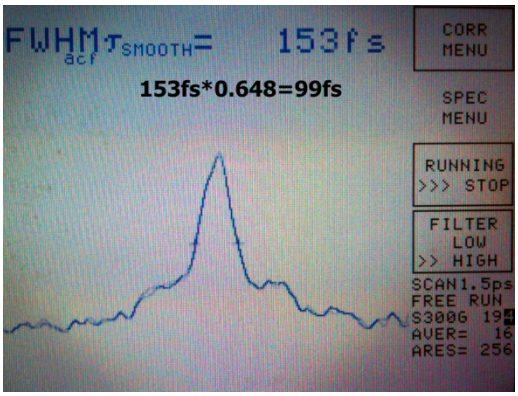

(b)

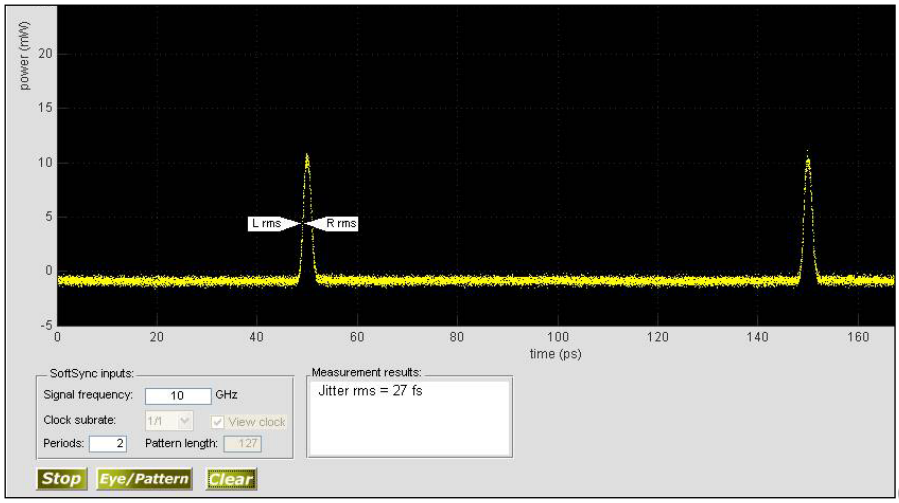

(c)

Figure 122. Experimental results. (a) Spectra after pulse-compression; (b) Autocorrelation-trace for the compressed pulses, 0.648 coefficient is used for correction for sech pulses for calculation of the correct FWHM (c) The jitter measurements of the sampling pulses

We have also demonstrated the sampling resolution of sub-100 fs by compressing the sampling pulses in an 100-m HNLF. The 10 GHz repetition rate pulses are amplified and sent to the HNLF to make use of self-phase modulation (SPM) based compression. After the HNLF adequate compensated fiber jumpers are used in order to maintain the compressed pulsewidth. The spectrum achieved at the output of the HNLF is shown in the Figure 122(a). A > 90-nm wide spectrum is observed for the compressed pulses. The pulsewidth of the compressed pulses are measured by a commercially available autocorrelator, and found to be < 100 fs as shown in the Figure 122(b). A correction factor of 0.648 is used for calcuation of the FWHM of the pulses that is widely used for $sech^2$ pulses. The sampling jitter is also shown in Figure 122(c). A jitter of ~30 fs is observed that is measured by a sampling scope. This low jitter is mostly attributed to the jitter characteristics of used Erbium Glass Oscillating MLL, owing to its single wavelength-long cavity and the low-jitter RF clock source.

4.29. Demonstration of a Fiber Optical Parametric Amplifier with > 200 nm of Gain Bandwidth with ~20 dB Gain

We have demonstrated a fiber optical parametric amplifier (OPA) with >200 nm of gain bandwidth with 20 dB of gain using a highly nonlinear fiber. A single pump is used in order to generate desired gain. Figure 5 shows the experimental setup of single-pump OPA. We use single-pump OPA in a piece of 100-m dispersion flattened HNLF to provide broadband wavelength conversion and OPA. Both amplitude modulator (AM) and phase modulator (PM) were used in order to increase the pump peak power and effectively suppress the SBS. The BPF after the EDFA was used to remove the ASE noise.

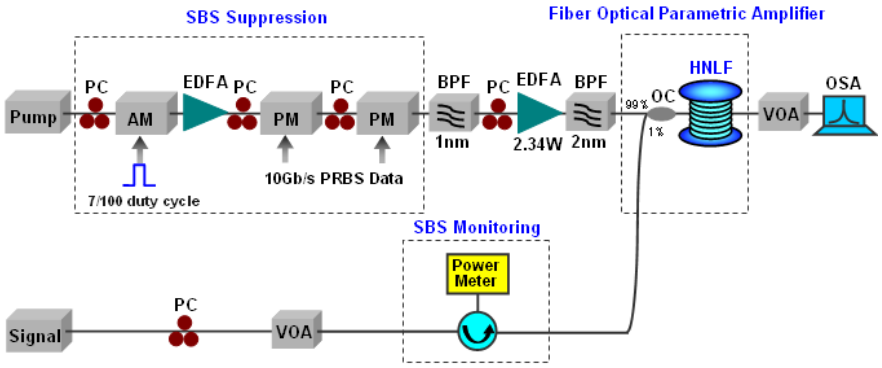

Figure 123. Experimental setup of single-pump OPA. AM: amplitude modulator; PM: phase modulator; EDFA: erbium-doped fiber amplifier; PC: polarization controller; BPF: band-pass filter; VOA: variable optical attenuator

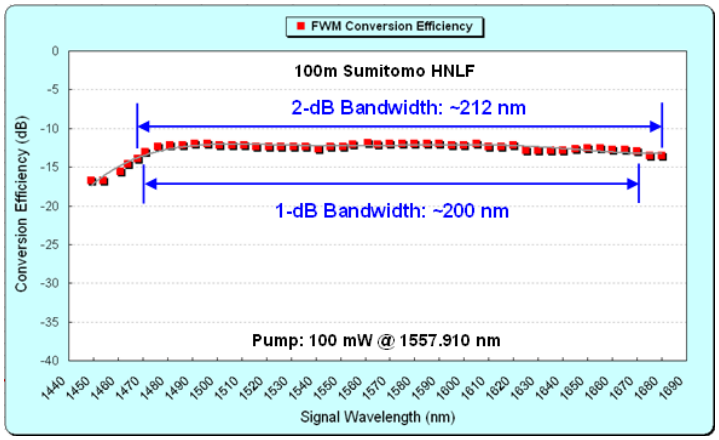

Figure 124. Broadband wavelength conversion

Figure 124 shows the broadband wavelength conversion using FWM in the 100-m spool of HNLF. The flat dispersion profile, allows for wavelength conversion and parametric amplification with high bandwidths. The pump power was 100 mW at 1557.910 nm. We measured the broadband wavelength conversion with 1-dB bandwidth of ~200 nm and 2-dB bandwidth of ~212 nm.

Figures 125-127 further depict the broadband single-pump OPA. When the pump power was 2.34 W at 1557.590 nm, we achieved a broadband single-pump OPA with a 3-dB bandwidth of ~172 nm. When the pump power was 2.34 W at 1557.632 nm, we observed a broadband single-

pump OPA with a 10-dB bandwidth of ~203 nm. Figure 125 shows the optical spectra of single-pump OPA in the presence/absence of the pump, from which we can clearly observe the flat broadband parametric gain applied to the signal when the pump is present.

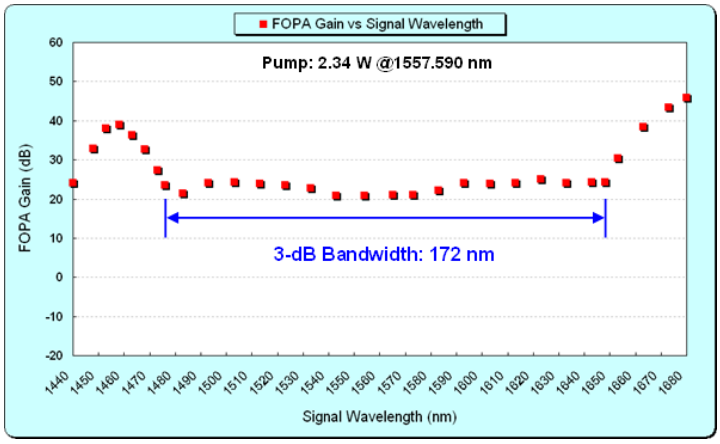

Figure 125. Broadband single-pump OPA (172-nm 3-dB bandwidth)

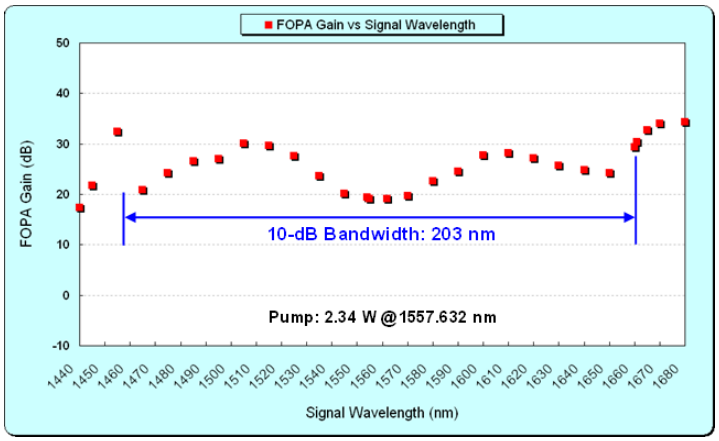

Figure 126. Broadband single-pump OPA (203-nm 10-dB bandwidth)

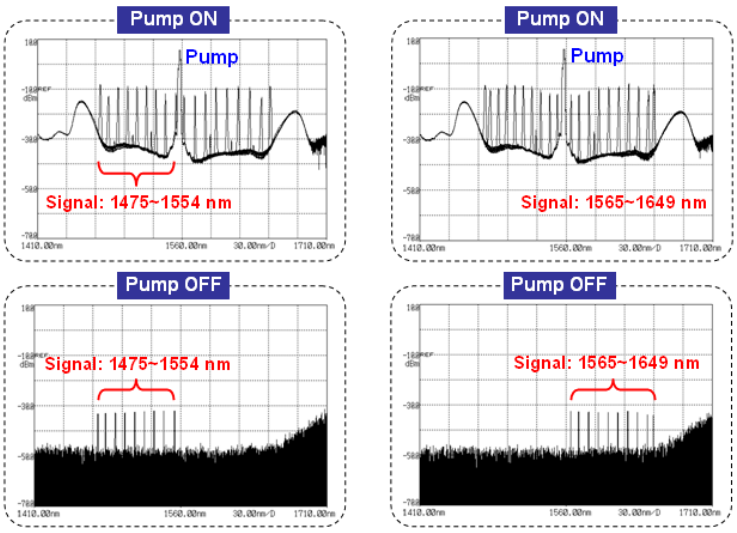

Figure 127. Measured optical spectra of single-pump OPA in the presence/absence of the pump

4.30. Demonstration of 80-Gbit/s DQPSK Optical Tapped-Delay-Line Equalization using Finely Tunable Delays, Phases and Amplitudes

We have demonstrated chromatic dispersion equalization using optical tapped-delay-lines with finely tunable delay, phase and amplitude. Using this technique, we observed >200% improvement in dispersion tolerance for 40 Gb/s RZ-DPSK and >50% improvement for 80 Gb/s RZ-DQPSK at ~3 dB power penalty. [34]

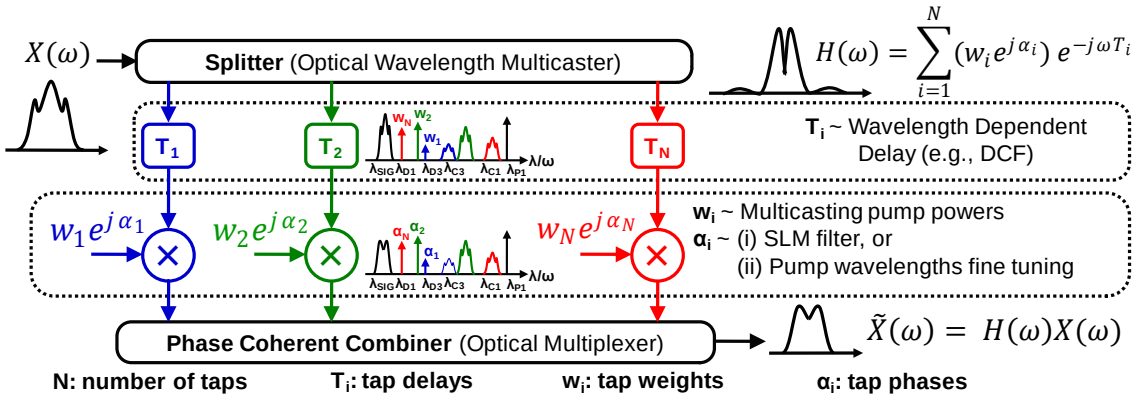

Figure 128. Conceptual block diagram of tunable optical tapped delay line implementation using conversion/dispersion delays

The conceptual block diagram of the tunable optical TDL with optical multiplexing is shown in Figure 128. An optical input signal at λ_{SIG} is multicast to several copies at different wavelengths ($\lambda_{C1\text{-}3}$) using a PPLN waveguide. The multicast copies are generated by the cascaded $\chi^{(2)}::\chi^{(2)}$ processes of SFG followed by DFG in a PPLN waveguide using the dummy pumps ($\lambda_{D1\text{-}3}$). The multicast signal copies are then sent through a spool of DCF to induce a small amount of wavelength dependent relative delay ($T\sim D\times\Delta\lambda$) between the multicast signals. Therefore, the number of taps, tap-delays, and tap-weight-magnitudes are directly controlled by the dummy pumps. In order to have control of the tap-phases (to realize complex valued weights), the

relative phases of the multicast copies with their corresponding dummy pumps need to be controlled before multiplexing. This can be achieved by an in-line phase/amplitude programmable filter, or by simply adding a fine offset to the pump wavelengths. Due to the dispersion, this small wavelength offset will result in a negligible change in the relative delay between the signal copies but induces phase difference between each copy and its dummy pump. This can be used to apply the tap phases prior to the optical multiplexing stage in another PPLN waveguide without the need for a spatial light modulator. Coherent multiplexing is achieved by keeping the dummy pumps from the first PPLN output ($\lambda_{D1\text{-}3}$) and using them as the SFG pumps to mix with their corresponding signal copies in the multiplexing stage. A pump ($\lambda_{P\text{-}2}$) is introduced to generate the output multiplexed signal via the DFG process in the PPLN waveguide. Therefore, the multiplexed output is a signal equalized according to the tap weights in this process.

The experimental setup we used for the equalizer is shown in Figure 129. A nested Mach-Zehnder modulator was used to generate the input of 40-Gbit/s RZ-DPSK data(PRBS 2^{31}-1) and the 80-Gbit/s RZ-DQPSK data (PRBS 2^{31}-1) at ~1540.7 nm. The signal was switched to 27-Gbit/s NRZ-DPSK for additional experiments. Full-rate pulse carving was used. A tunable dispersion compensation module (TDCM) was employed to emulate dispersion on the input signal. The input signal was amplified, filtered and sent to a 4-cm PPLN waveguide (PPLN-1) along with an amplified pump laser at ~1560.75 nm. Four CW pump lasers ($\lambda_{D1\text{-}4}$) were coupled together, amplified and launched to the PPLN waveguide. The quasi-phase matching (QPM) wavelength of the waveguide was set to ~1550.7 nm by temperature tuning. The signal copies at corresponding wavelengths ($\lambda_{C1\text{-}4}$) were generated by the cascaded SFG-DFG processes in the waveguide. The output of the PPLN-1 was sent to a liquid crystal on silicon based amplitude/phase programmable filter (the SLM) that was used to filter the dummy pump lasers and the generated signal copies, and to control the phases of the pump laser prior to the second wavelength conversion stage, as shown in Figure 129(b). Instead of using the SLM, the phases of the pumps were also controlled by fine tuning of the pump wavelength (~3°/ pm). The filtered pumps and the signals were then sent through a ~90-m DCF in order to induce the relative delay. The pump lasers and the signal copies were then amplified and sent to a 5-cm PPLN waveguide (PPLN-2) with QPM ~1550.7 nm (almost similar to PPLN-1). The pairs of pumps and signal copies that were symmetric to the QPM wavelength generate the phase coherent SFG signal based on the phases and the amplitudes of the pumps and the signal copies. A pump laser at ~1560.75 nm was used for generation of the multiplexed signal at ~1540.7 nm. The multiplexed signal was then filtered and sent to a preamplified receiver for BER measurements.

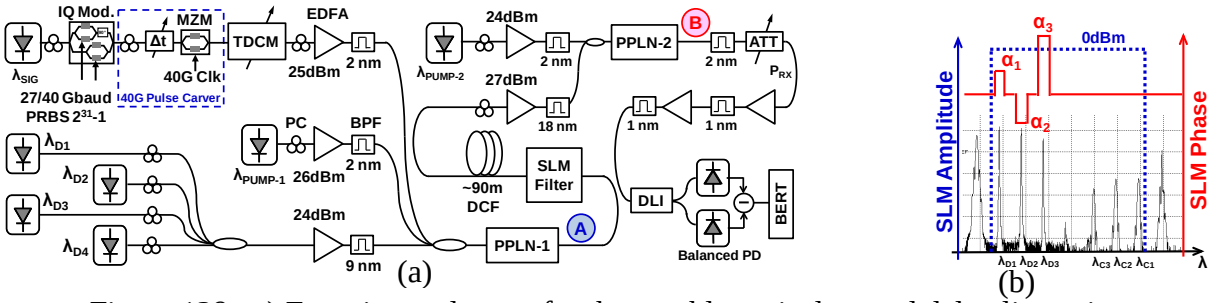

Figure 129. a) Experimental setup for the tunable optical tapped delay line using conversion/dispersion delays. TDCM: Tunable Dispersion Compensation Module, PPLN: Peridically Polled Lithium Niabate Waveguide, SLM: Spatial Light Modulator, DCF: Dispersion Compensating Fiber, PC: Polarization Controller, BPF: Bandpass Filter, ATT: Attenuator, DLI: Delay Line Interferometer, BERT: Bit Error Rate Tester. b) SLM filter amplitude and phase profile for applying phases on the pumps

The performance of the equalizer was tested by emulating dispersion using the TDCM. Figure 130 shows the spectra for the two stages of wavelength conversion (PPLN-1 and PPLN-2) of the optical tapped equalizer for equalization of 120 ps/nm dispersion emulated by the TDCM. Figure 130(a) shows the spectra for four-tap operation on a 40-Gbaud/s signal. The wavelength separation, $\Delta\lambda$, between the signal copies was set to ~1.6 nm, which corresponds to a ~12.5 ps. Therefore, $T_s/2$ tap-delays are achieved for the equalizer, where T_s is the symbol time. In Figure 130(b), the data was switched to 27-Gbit/s DPSK. Thus, in order to achieve the half bit tap delays (~18.8 ps), $\Delta\lambda$ was changed to ~2.4 nm.

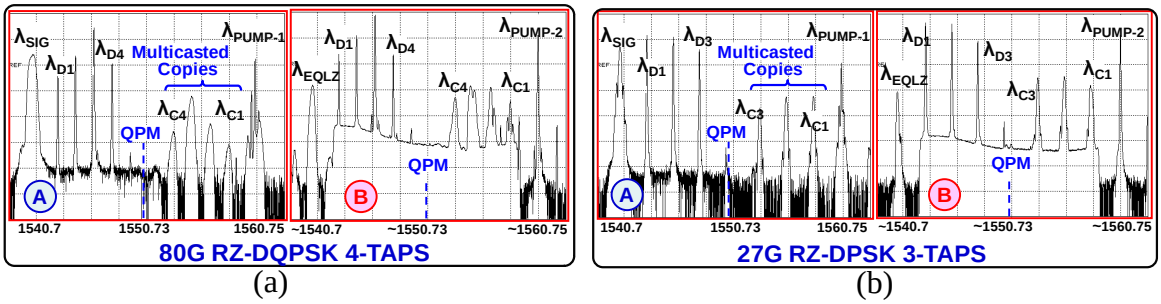

Figure 130. Experimental spectra for different conditions of operation for the tapped-delay-line equalizer, showing tunability to different bit rates and modulation formats

BER measurements were performed on the equalized signal and the input signal. The receiver sensitivity penalties (at a BER of 10^{-9}) for 3-tap and 4-tap equalization for 40-Gbit/s RZ-DPSK and three tap equalization for 27-Gbit/s NRZ-DPSK signal are shown in the Figure 131. We observed that 4-tap equalization results in improvements with respect to the 3-tap equalization. For a 3 dB receiver sensitivity penalty, the B2B signal had a tolerance of ~50 ps/nm of dispersion, while it improved to ~110 ps/nm with 3-taps, and to ~160ps/nm with 4-taps. The double wavelength conversion (0 ps/nm dispersion, single-tap operation) had an average penalty of ~1.5 dB. As shown in Figure 132, the equalization of dispersion on an 80-Gbit/s RZ-DQPSK was also demonstrated using four taps with $T_s/2$ spacing. At 3 dB power penalty, the improvement was from ~40 ps/nm to ~70 ps/nm and for dispersions as large as 120 ps/nm, BER rates of 10^{-9} were achievable with 7.8 dB penalty. Figure 133 shows the sensitivity of the 3-tap -

120 ps/nm equalizer to the variations of the CW pumps powers and tap phases. It was observed that the penalties were negligible for <20° phase change and <2 dB decrease in multicasting pump powers.

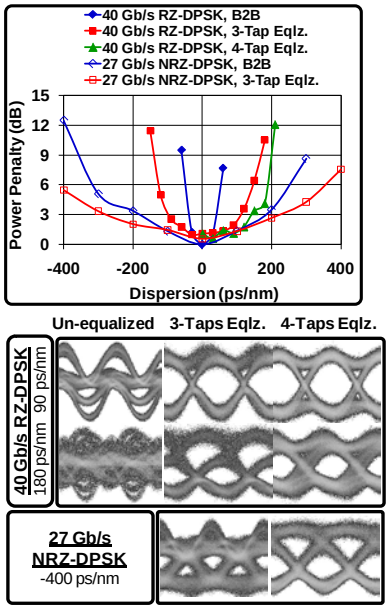

Figure 131. a) Receiver sensitivity penalties at 10e-9 BER. b) Eye diagrams

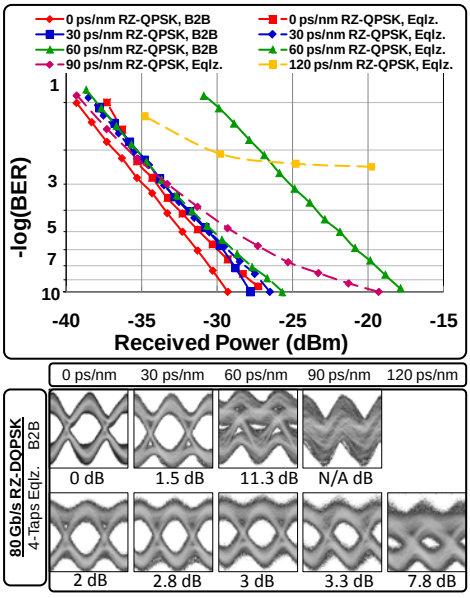

Figure 132. a) BER measurements for the 80 Gbit/s DQPSK signals. b) Back-to-back and equalized eye diagrams

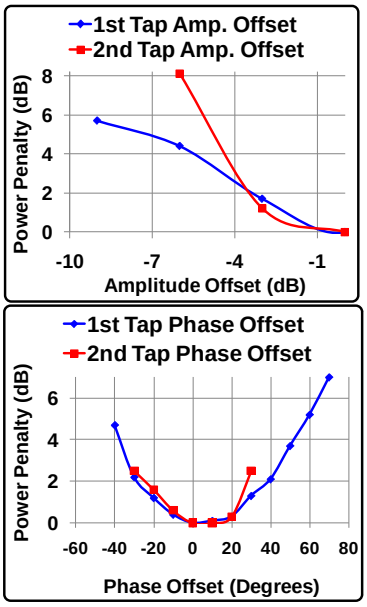

Figure 133. Equalizer sensitivity to tap variations for 3-tap -120 ps/nm equalization at 10e-9 BER

4.31. Demonstration of Baud-Rate-Variable and Channel-Spacing-Tunable Demultiplexing of 10-40-Gbaud OFDM Subcarriers using a Multi-Tap Optical DFT

We have also demonstrated error free demultiplexing of three different OFDM signals with two, three and four 20 Gbit/s NRZ-DPSK subcarriers in 20 GHz frequency spacing using a tunable multi-tap optical DFT based on finely tunable dispersion/conversion delays and coherent optical multicasting and multiplexing. Optical OFDM was generated by modulating odd and even subchannels of an optical comb. For demultiplexing of the four subcarrier 20-Gbit/s OFDM (80 Gbits/s), an average power penalty of ~7 dB was achieved at BER of 10^{-9}. By applying a 50% guard time and modulating the subcarriers at 10 Gbaud, the penalty reduced to ~3 dB. By changing the pump separations in the multicasting stage of the optical DFT, the DFT accommodated for 2, 3 and 4 taps at 20 GHz spacing and 2 taps at 40 GHz spacing, each requiring a different tap delay. [35]

An optically generated OFDM signal with N subcarriers can be represented by $s(t) = \sum_{n=0}^{N-1} x_n(t) e^{j2\pi(f_0+n\Delta f)t}$, in which $f_0, \Delta f$ and $x_n(t)$ are optical carrier frequency, optical frequency spacing and n-th subcarrier signal, respectively. To demultiplex $s(t)$ to its constituent subchannels the discrete Fourier transform (DFT) is required. Indeed, $x_n(t) = \sum_{n=0}^{N-1} s(t + k\tau/N) e^{j2\pi kn/N}$, where $t = m\tau$, $\tau = 1/\Delta f$ and m is any integer number.

The demonstrated optical tunable DFT is illustrated in Figure 134. At the first stage, a PPLN waveguide with quasi-phase matching wavelength of λ_{QPM} was utilized to wavelength multicast the OFDM signal to *N* copies. The OFDM signal, equally spaced ($\Delta\lambda$) N dummy pumps (λ_0 to λ_{N-1}) and a continuous wave (CW) pump at λ_p were sent into the PPLN waveguide to generate N copies at $2\lambda_{QPM} - \lambda_0$, $2\lambda_{QPM} - \lambda_1$, …, $2\lambda_{QPM} - \lambda_{N-1}$. These copies were sent into a DCF spool with length L which induced a wavelength dependent delay of 0, $\frac{\tau}{N}, \frac{2\tau}{N}, \ldots, \frac{(N-1)\tau}{N}$ on the copies ($\tau/N = \Delta\lambda \times L \times D$). Therefore, the DFT delays could be continuously tuned by changing $\Delta\lambda$ to achieve tunable optical DFT.

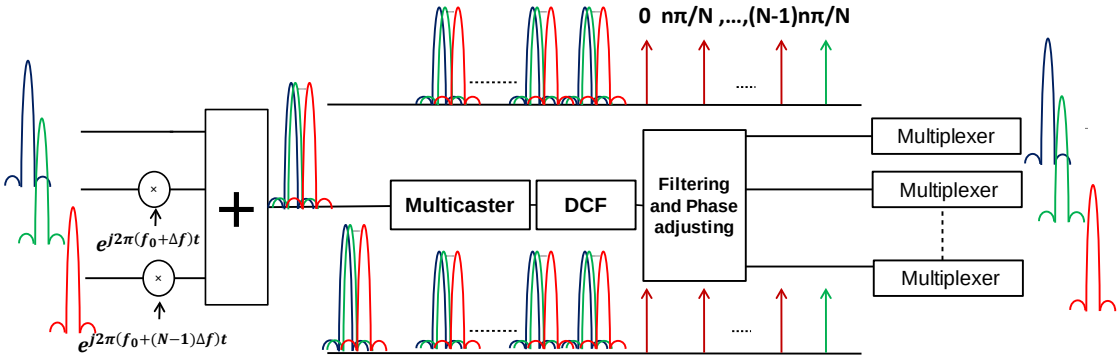

Figure 134. Conceptual block diagram of the reconfigurable and tunable optical DFT for OFDM demodulation

The signal copies as well as their corresponding dummy pumps were filtered altogether to maintain the coherency between the pumps and copies along the signal path. Moreover, the phases of the dummy pumps were adjusted to e^{j0}, $e^{j2\pi n/N}, \ldots, e^{j2\pi n(N-1)/N}$ with respect to the signal copies for demultiplexing of the n-th subcarrier. To achieve these two goals, a multiple output phase/amplitude programmable filter was utilized before the optical multiplexing stage. Finally, the second PPLN coherently added the delayed and phase adjusted copies to extract the n^{th} subchannel from the original signal.

The experimental set up is depicted in Figure 135. A phase modulator (PM), was driven by a 20/40-GHz clock tone in order to generate optical comb with 20/40-GHz spacings. The optical comb was amplified and sent through a circulator into the "common port" of a bi-directional multiport liquid crystal on silicon (LCoS) filter to de-interleave odd and even channels along with power equalization. The odd and even tones were then modulated to 10/20/40 Gbit/s DPSK in two separate optical modulators using PRBS 2^{31}-1 in order to generate independent DPSK signals on neighboring subcarriers. The data streams in the two paths were then manually synchronized using tunable optical delay lines, combined in a coupler, amplified and filtered to generate the OFDM input signal at ~1541.7 nm. Different number of subcarriers could be picked using the tunable LCoS filter.

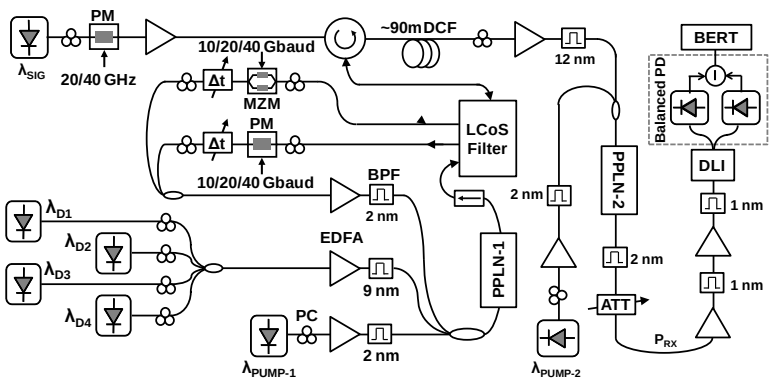

Figure 135. Experimental Setup for OFDM transmitter and tunable optical DFT for OFDM demultiplexing

PM: Phase Modulator
DCF: Dispersion compensating fiber
MZM: Mach-Zender Modulator
BPF: Bandpass Filter
PC: Polarization controller
PPLN: Periodically Polled Lithium Niobate
LCoS: Liquid Crystal on Silicon
DLI: Delay Line Inter-ferometer

The DFT part, on the other hand, consists of three stages. The OFDM signal was amplified to 300 mW, coupled together with another amplified (300 mW) CW pump ($\lambda_{\mathrm{PUMP-1}}$~1561.7 nm) and four CW lasers ($\lambda_{\mathrm{D1-4}}$) as the dummy pumps and sent into the PPLN waveguide. The PPLN had a QPM wavelength of ~1551.7 nm and generated four copies of the signal by cascaded SFG followed by DFG. The output of the first PPLN passed through the LCoS filter in order to filter the signal copies as well as their dummy pumps and apply the phases on the pumps for the DFT operation. A relative delay was introduced on the copies by sending the resulting signals and pumps through a ~90 m DCF spool. Using ~1.6 nm wavelength separation induced ~12.5 ps delay (quarter bit at 20 Gbit/s). In the last stage we used another PPLN with almost the same QMP wavelength and another CW pump to coherently multiplex the delayed and phase adjusted copies back on the same wavelength. The resulting signal contained a demultiplexed subchannel and was to have little interference from the other orthogonal subchannels at the right sampling time. Therefore, it could be filtered and sent to the preamplified receiver in order to perform BER measurements.

Figures 136 (a) and 136 (b) show the spectra of 2-tap and 3-tap DFT after the first (PPLN-1) and the second (PPLN-2) wavelength conversion stages. The eye diagrams are also shown for all subcarriers (SCs). To implement the 2-, 3- and 4-tap DFT at 20G, pump separations were set to ~3.2, ~2.4 and ~1.6 nm resulting in 1/2, 1/3 and 1/4 bit delay.

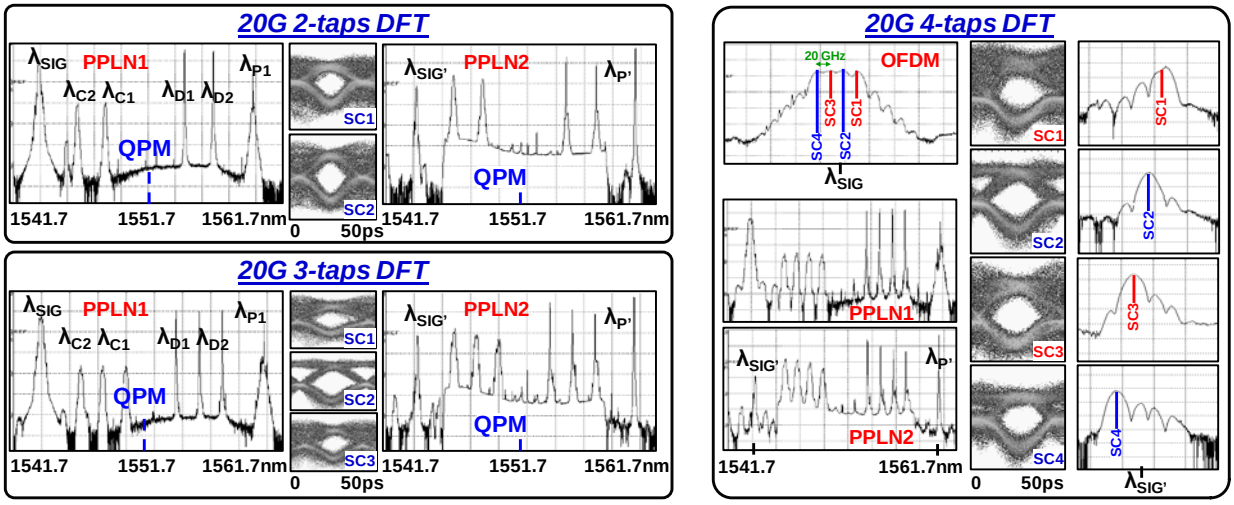

Figure 136. Optical spectra of the output of first and second stage and demultiplexed eye diagrams for a) 20G 2-taps, b) 20G 3-taps and c) 20G 4-taps along with demultiplexed spectra after the optical DFT

Figure 137 compares the BER performance of each demodulated subcarrier in 2-tap and 3-tap DFT scheme. By increasing the number of OFDM subcarriers, we observed that the power penalty reaches ~8 dB for 4 taps as compared to ~3 dB for 2 and 3 taps. In 3-taps individually, SC2 demodulator performed considerably better than SC1 and SC3 which could be a result of lower rise/fall time of SC1 and SC3 transmitter compared to SC2 transmitter which itself results in complete cancelation of SC1 and SC3 interference in SC2 demultiplexer. Indeed, for higher rise/fall time, introducing guard time was inevitable to achieve error free OFDM demodulation. Therefore, a 20 Gbaud 4-tap DFT for half baud rate (50% guard time) was implemented as shown in Figure 138. As plotted in Figure 139, a comparison between the power penalties at 10^{-9} BER reveals that by increasing the guard time from 0 to 50%, the penalties were reduced on average from ~7.5 dB to ~3.5 dB. As shown in Figure 140, where no guard time was used for 2-tone 40Gbit/s OFDM, the guard time was even more important for higher frequency spacing and higher baud rate as high power penalty (~10 dB) was observed on eye diagrams shown in Figure 140.

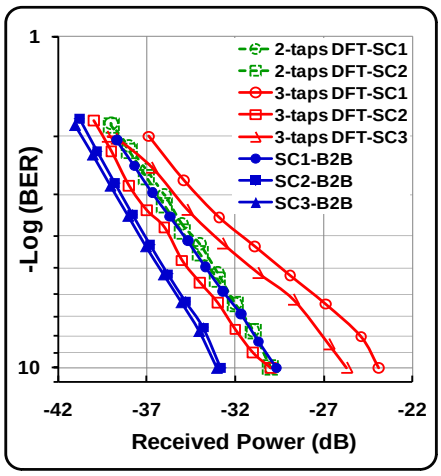

Figure 137. BER curves for different number of subchannels at 20 Gbit/s

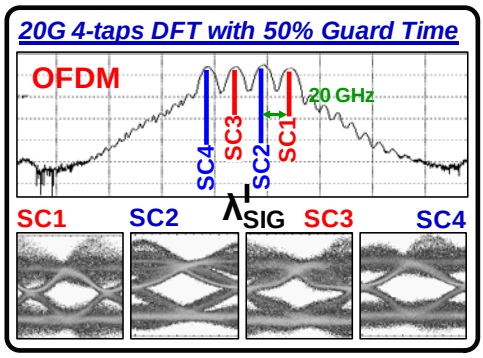

Figure 138. Input OFDM spectrum with 20GHz spacing and 50% guard time with the demultiplexed eye diagrams

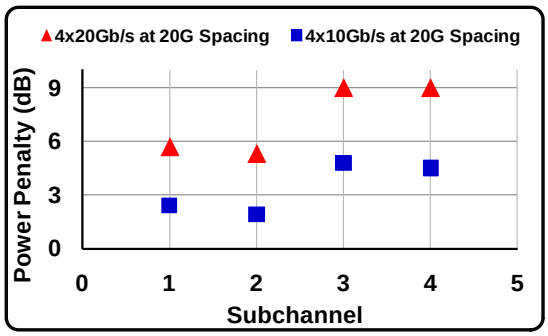

Figure 139. Power penalty comparisons for 20GHz spaced 4 tone OFDM with and without 50% guard time

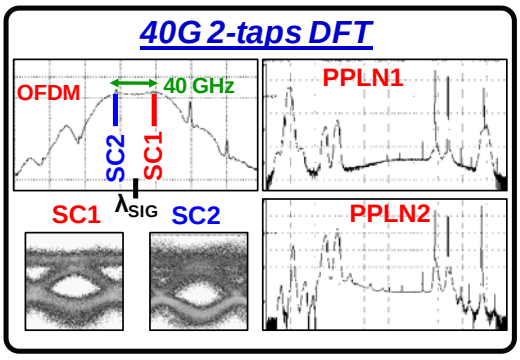

Figure 140. Input OFDM with 40GHz, first and second stage wavelength converter output specta and the demultiplexed eye diagrams

4.32. Experimental Performance of a Continuously Tunable 40-GHz Complex Weight Optical FIR Filter using Wavelength Conversion and Chromatic Dispersion

We have investigated the performance of a continuously tunable 40-GHz optical FIR filter using wavelength conversion and chromatic dispersion to achieve an optical FIR filter with complex taps. In our approach, $\chi^{(2)}$ processes in aPPLN waveguide was utilized for optical multicasting and multiplexing and DCF was used to realize the delays. Coherent multiplexing was made possible by reusing the same pumps in both nonlinear processes in the two PPLN waveguides. The tuning capabilities of the filter tap amplitudes (-9 to 0 dB), tap phases (0-2π) and free spectral rage (FSR) (~27 and 40 GHz) were experimentally demonstrated showing close agreement with theory. [37]

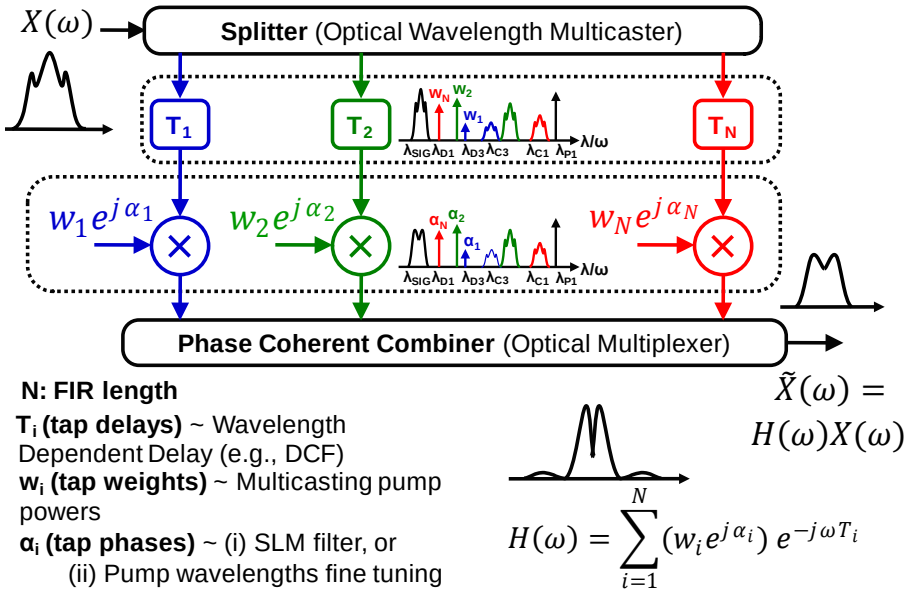

Figure 141. Conceptual block diagram of complex weight optical FIR filter implementation using conversion/dispersion delays

The conceptual block diagram of the tunable optical FIR filter with optical multiplexing is shown in Figure 141. An optical input signal at λ_{SIG} was multicast to several copies at different wavelengths ($\lambda_{C1\text{-}3}$) using a PPLN waveguide, by the cascaded $\chi^{(2)}::\chi^{(2)}$ processes of SFG followed by DFG using the dummy pumps ($\lambda_{D1\text{-}3}$). The signal copies were then sent through a spool of DCF to induce a small amount of wavelength dependent relative delay (T~D×Δλ) between the multicast signals. Therefore, the FIR length (number of taps), FIR delays (1/FSR), and FIR tap amplitudes were directly controlled by the dummy pumps. The FIR filter tap phases could be set by applying in line phase/amplitude programmable filter (spatial light modulator, SLM), or by simply adding a fine offset to the pump wavelengths.

.

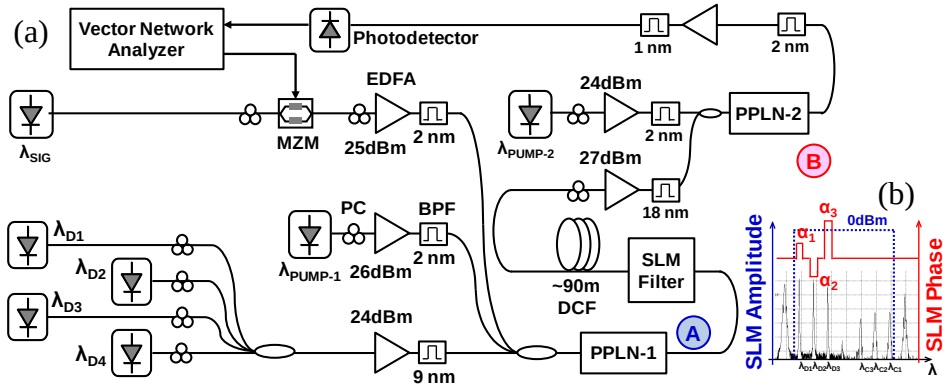

Figure 142. a) Experimental setup for the tunable optical FIR using conversion/dispersion delays. b) SLM filter amplitude and phase profile for applying phases on the pumps

The experimental setup for the tunable FIR filter is shown in Figure 142. A vector network analyzer (VNA) was used to scan the frequencies from 0 to 40 GHz. The output of the VNA

drove a Mach-Zehnder modulator at the quadrature bias point to modulate a ~1538.5 nm laser. The input signal was amplified, filtered and sent to a 4-cm PPLN waveguide (PPLN-1) along with an amplified pump laser at ~1562.5 nm. Four CW pump lasers ($\lambda_{D1\text{-}4}$) were coupled together, amplified and launched to the first PPLN waveguide. The QPM wavelength of the waveguide was set to ~1551 nm. The signal copies ($\lambda_{C1\text{-}4}$) are generated in the PPLN-1. The output of PPLN-1 was sent to an SLM that was used to filter the dummy pump lasers and the generated signal copies, and to control the phases of the pump laser prior to the second wavelength conversion stage, as shown in Figure 142(b). Instead of using the SLM, the phases of the taps can also be controlled by fine tuning of the pump wavelength (~3°/ pm). The filtered pumps and the signals were then sent through a ~180-m DCF in order to induce the relative delay. The pump lasers and the signal copies were then amplified and sent to a PPLN-2 (5 cm long waveguide) with QPM ~1551 nm. A pump laser at ~1563.5 nm was used for generation of the multiplexed signal at ~1538.5 nm. The multiplexed signal was then amplified, filtered and sent to a photoreceiver to be fed back to the VNA.

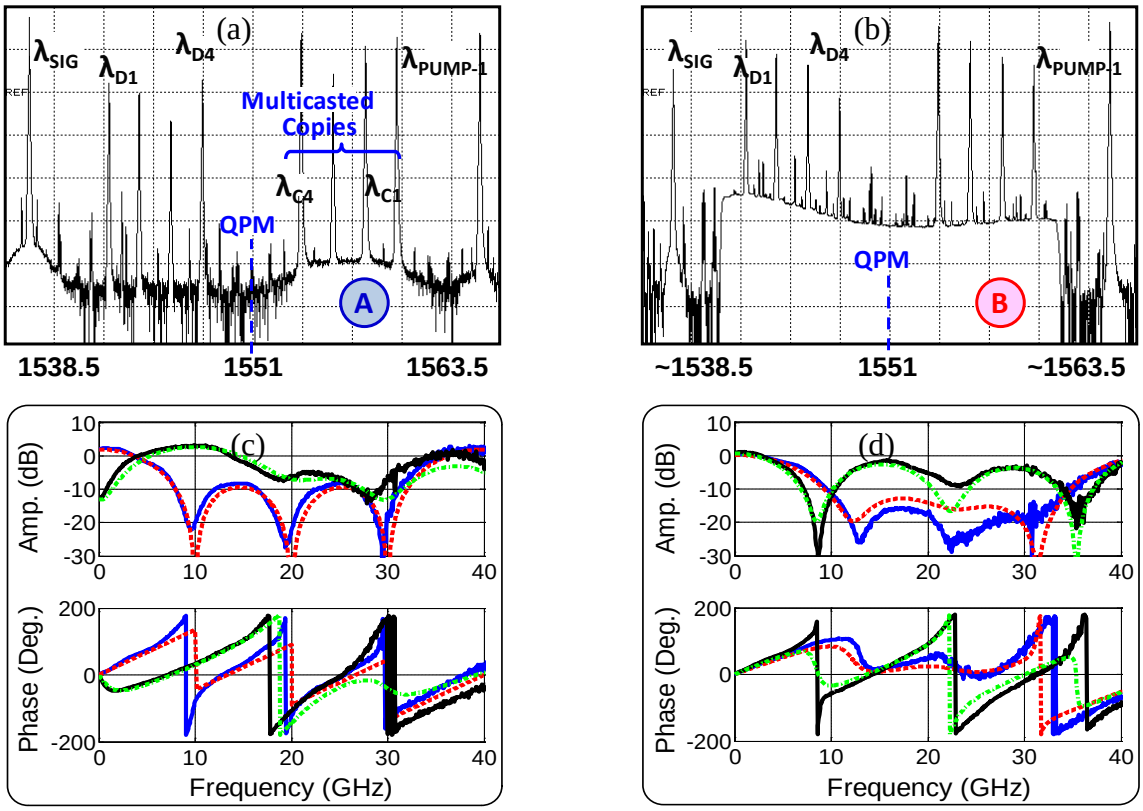

h = [1, 1, 1, 1] ∠ Φ

Solid blue (Exp.) & Dashed red (Sim) for Φ = [0,0,0,0]°

Solid black (Exp) & Dashed green (Sim) for Φ = [-135,135,0,0]°

h = A ∠ [0, 0, 0, 0]°

Solid blue (Exp.) & Dashed red (Sim) for A = [0.5,1,1,1]

Solid black (Exp) & Dashed green (Sim) for A = [1,0.125,0.5,1]

Figure 143. a) PPLN-1, b) PPLN-2 output spectrum, c&d) experimental and simulation RF response for length-4 FIR filters with 40 GHz FSR

Figure 144 (a,b) show the optical spectra for the two stages of wavelength conversion of a length-4 optical FIR with ~1.6 nm wavelength spacing (~25 ps delay, 40 GHz FSR). The RF

spectra shown in Figure 144 were normalized with respect to the system RF delay response. In Figure 144 (c), all taps were set to have equal amplitudes and their phases were tuned using the SLM. In Figure 144 (d), phases were kept constant and taps were varied by tuning laser powers in the first stage (3 dB attenuation for a 0.5 factor in tap amplitude). A length-3 FIR filter with FSR ~27 GHz is realized in Figure 145, where pump separations were set to 2.4 nm to induce ~37.5 ps delay between the taps. The tuning capabilities of the length-3 FIR were also demonstrated as shown in Figure 145 (c,d). Tap amplitudes were varied from 0 to -9 dB (1 to 0.125 in impulse response) and tap phases were tuned within 360°. The VNA measurement results showed a close agreement between the tunable complex weight optical FIR and the theory. The VNA used was limited to 40 GHz bandwidth; however, the FSR and the bandwidth of the proposed FIR filter could be potentially made wider (by choosing smaller DCF).

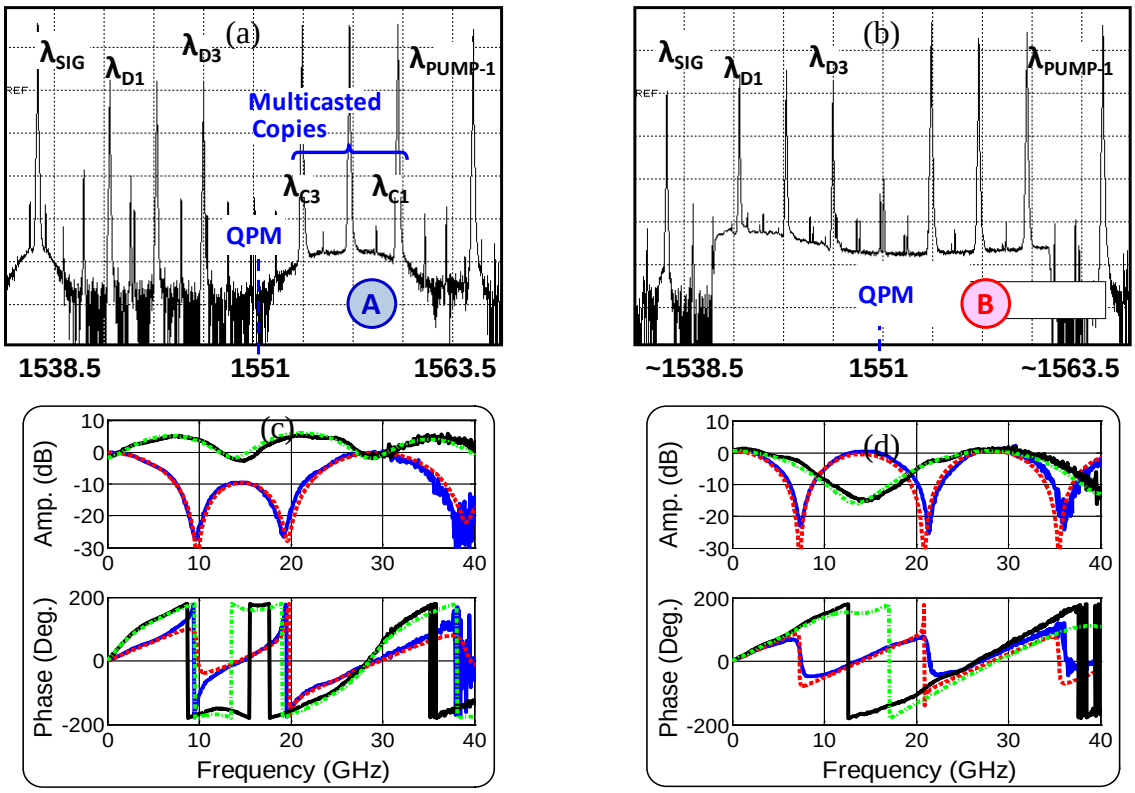

h = [1, 1, 1] ∠ Φ

Solid blue (Exp.) & Dashed red (Sim) for Φ = [0,0,0] °
Solid black (Exp) & Dashed green (Sim) for Φ = [180,-180,0]°

h = A ∠ [0, 0, 0]°

Solid blue (Exp.) & Dashed red (Sim) for A = [1,0.125,1]
Solid black (Exp) & Dashed green (Sim) for A = [0.5,1,0.25]

Figure 144. a) PPLN-1 b) PPLN-2 output spectrum, c&d) experimental and simulation RF response for length-3 FIR filters with ~27 GHz FSR

4.33. Demonstration of λ-Conversion of 160-Gbit/s PDM 16-QAM Using a Single Periodically-Poled Lithium Niobate Waveguide

We have also experiementally demonstrated wavelength conversion of 40-Gbaud single

polarization and 20-Gbaud PDM 16-QAM, both with an aggregate data-rate of 160 Gbit/s. A single PPLN waveguide in a bidirectional configuration was used to achieve polarization diverse operation. A power penalty of ~0.5 dB was obtained for optimal bias conditions of the PPLN waveguide. Power penalty measurements for varying pump powers show the window of linear operation for which transparent phase and amplitude conversion was achieved. [36]

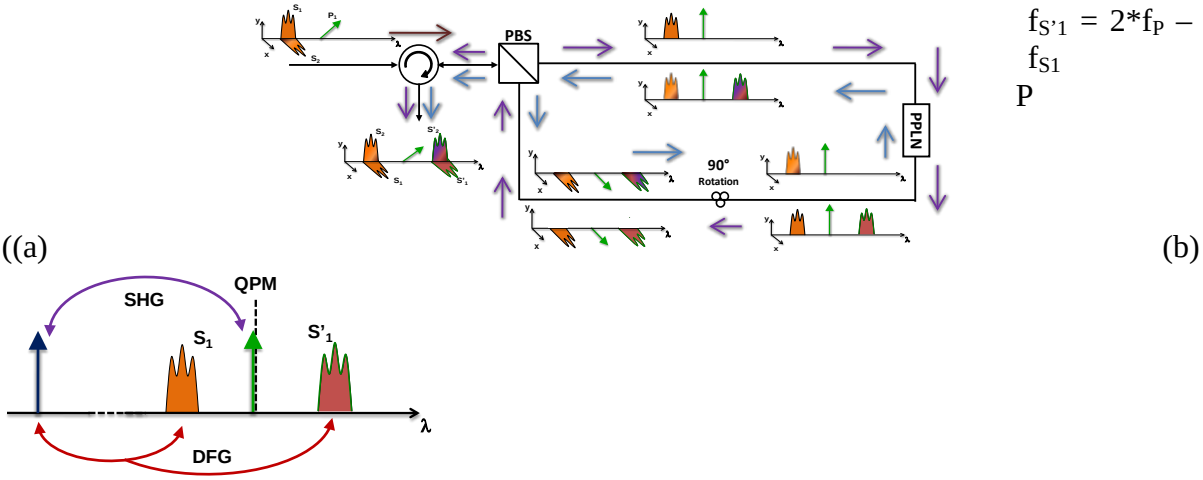

Figure 145. Conceptual diagram of transparent polarization (a) and phase and amplitude (b) conversion in a PPLN waveguide

The conceptual block diagram of this technique is shown in Figure 145. A polarization multiplexed signal and continuous wave (CW) pump aligned at 45° linear relative to the signal were inserted into the bi-directional wavelength converter through a circulator. A PBS/PBC separated the signal into the X and Y polarizations while the CW pump was split between the two polarizations. The X-polarization traversed the loop counterclockwise following the path of the blue arrows. It first experienced a 90° rotation so that the pump and the signal were aligned to the Y-polarization axis before passing through the PPLN. After passing through the PPLN, a copy of the data amplitude and phase was generated according to cascaded SHG/DFG, $f_{S'1} = 2*f_P - f_{S1}$, Figure 145 (b). Similarly, the Y-Polarization traveled in the opposite direction (clockwise) as shown by the purple arrows. It first passed through the PPLN to generate the wavelength converted copy of its data before being rotated by 90° so that it could pass backwards through the PBC. After passing back through the polarizing beam combiner, the recombined signal was directed out by the circulator. In general, the data signal need not be aligned in polarization and the setup yields polarization insensitive wavelength conversion due to its inherit polarization diversity.

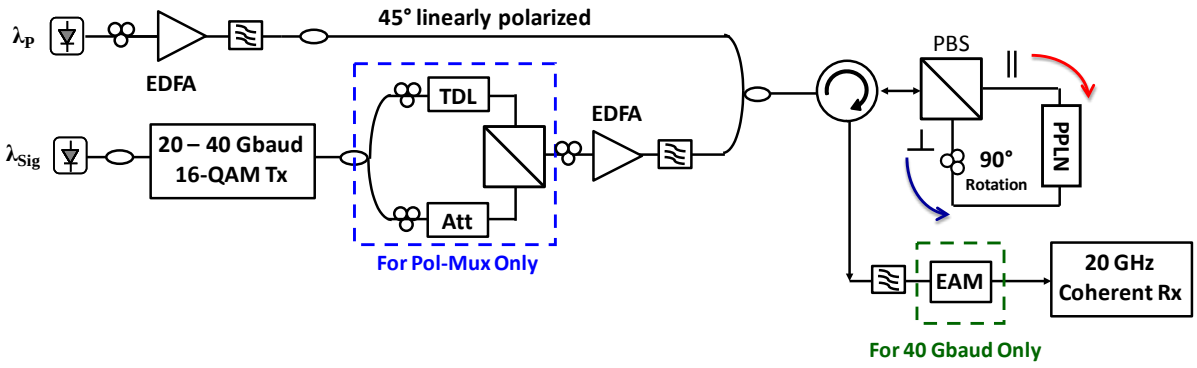

Figure 146. Experimental setup. A 20-Gbaud PDM 16-QAM or 40-Gbaud 16-QAM signal is generated and combined with a CW pump in a bidirectional PPLN based wavelength converter. An EAM is used for 40-Gbaud to 20-Gbaud down sampling followed by coherent detection

An experimental block diagram of our setup is shown in Figure 146. A laser at $\lambda_{Sig}\approx$1544.9 nm was first modulated with a QPSK waveform at the desired rate, 40 or 20 Gbaud. An integrated free-space multiplexer consisting of i) an optical split, ii) a 1-bit delay and 6-dB attenuation in one arm, and iii) recombining of the two arms, was used to convert the QPSK signal to 16-QAM. For 20 Gbaud PDM 16-QAM, polarization multiplexing was achieved by splitting the signal into two paths, de-correlating with a fiber delay, and recombining the signals using PBC/PBS to ensure orthogonality. Wavelength conversion was achieved in a bidirectional loop consisting of a PPLN waveguide with a QPM wavelength of 1549.9 nm, a PBS, a polarization controller set to rotate 90°, and a circulator to separate the data moving into and out of the loop. The incoming CW pump at $\lambda\approx$1549.9 was aligned 45° linearly polarized relative to the PBS such that the half of its power traveled in each direction around the loop. SHG followed by DFG were used to wavelength convert the signal ~10 nm longer in wavelength with an optical efficiency of -16 dB. After one pass around the loop, the pump, signal, and converted channels were recombined by the PBS and routed by the circulator to the receiver. The converted wavelength at $\lambda\approx$1554.9 nm was filtered off and sent to a pre-amplified coherent Rx for signal processing and BER measurements. Since our analog-to-digital converter was limited to ~20 GHz, an electro-absorption modulator (EAM) was used to down sample the 40-Gbaud 16-QAM signal to 20 Gbaud, prior to detection.

The experimental constellation diagrams and spectra are shown in Figure 147. For 40-Gbaud single polarization 16-QAM, Figure 147 (a), optimal conversion was obtained for a pump power of 16.2 dBm in both directions around the loop. By increasing the pump power the wavelength converter began to move into the depletion regime of operation and we started to see amplitude saturation of the converted signal, Figure 147(a)(bottom right). The highest amplitude level, corresponding to the four outside corners of the constellation, was compressed inward toward the second amplitude level, giving the constellation a rounded look. Figure 147 (b) shows the experimental constellations for 20-Gbaud PDM 16-QAM where optimal performance was obtained for pump powers of ~17 dBm in each direction. Figure 147 (c) shows the experimental spectra for the 40-Gbaud single polarization (top) and 20-Gbaud dual polarization (bottom).

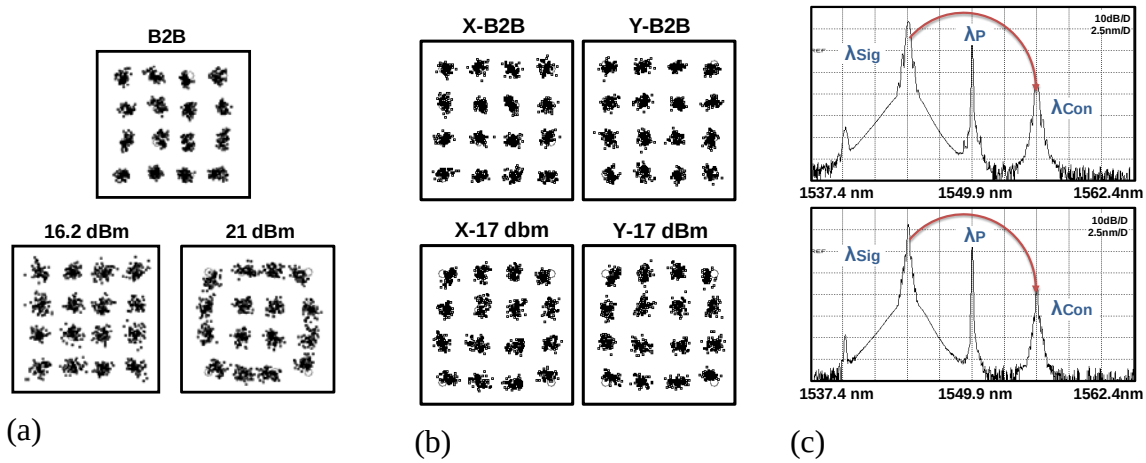

Figure 147. (a) Experimental constellation diagrams for 40-Gbaud single-polarization 16-QAM back-to-back (top) and after (bottom) conversion for pump powers of 16.2 dBm (left) and 21 dBm (right). (b) Experimental constellation diagrams for 20-Gbaud PDM 16-QAM back-to-back (top) and after wavelength conversion (bottom) for both polarizations. (c) Experimental spectra for 40-Gbaud single polarization (top) and 20-Gbaud PDM (bottom) 16-QAM

BER measurements were performed on the captured waveforms to assess the system performance. Figure 148(a) and (b) show the performance of 40-Gbaud single polarization 16-QAM and 20-Gbaud PDM 16-QAM respectively. Less than a 0.5 dB penalty for 40-Gbaud and ~0.6 dB penalty for 20-Gbaud exist for the wavelength converted signal at a BER of $1E^{-3}$. Figure 148(c) shows the measured relative power penalty for 40-Gbaud 16-QAM as a function of the pump power. The power penalty increased rapidly as signal depletion began to occur and the constellation amplitude levels became compressed. Increasing the signal power may prevent depletion and allow for the use of a higher power pump to improve conversion efficiency, but a higher power EDFA would be required and may reduce the signal-to-noise ratio of the system.

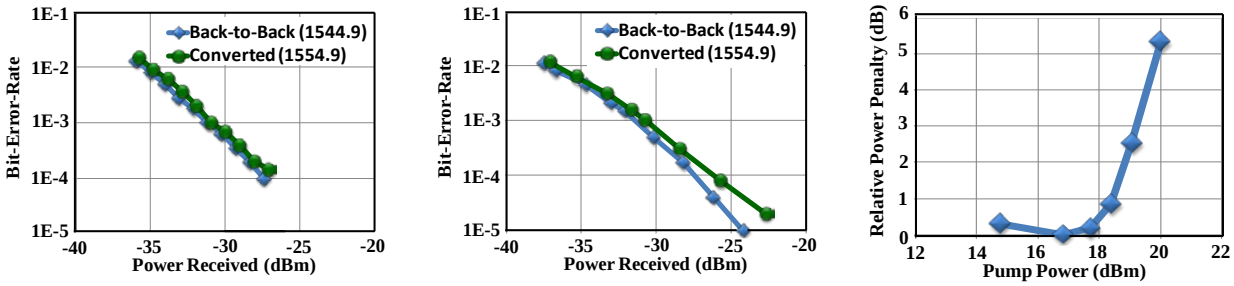

Figure 148. Bit-error-rate (BER) measurements for (a) 40-Gbaud 16-QAM and (b) 20-Gbaud PDM 16-QAM back-to-back and after wavelength conversion. (c) Relative power penalty vs. pump power for 40-Gbaud 16-QAM

4.34. Experimental demonstration of True Time Delays using Conversion/Dispersion with Flat Magnitude Response for Wideband Analog RF Signals.

We have experimentally demonstrated conversion/dispersion based True-Time-Delays (TTD)

up to 6.5 ns. The magnitude response was flattened to fluctuations <1 dB over 40 GHz of bandwidth by using an wavelength-offset pump in the wavelength conversion. In the 1-30 GHz range, root-mean-square (RMS) magnitude response fluctuations <0.2 dB were observed between different delay points. Over a measurement of 12 hours <2-dB magnitude response and $<10^{o}$ phase response fluctuation were measured for a 1 GHz band. The impulse response of the system for linear frequency-modulated (LFM) waveforms was calculated using experimentally obtained transfer functions. Peak-to-highest-sidelobe-ratios (PSLR) of 34.1 dB and 32.1 were calculated for the non-flat and flattened responses, respectively, where the ideal PSLR is 42.4 dB. [39]

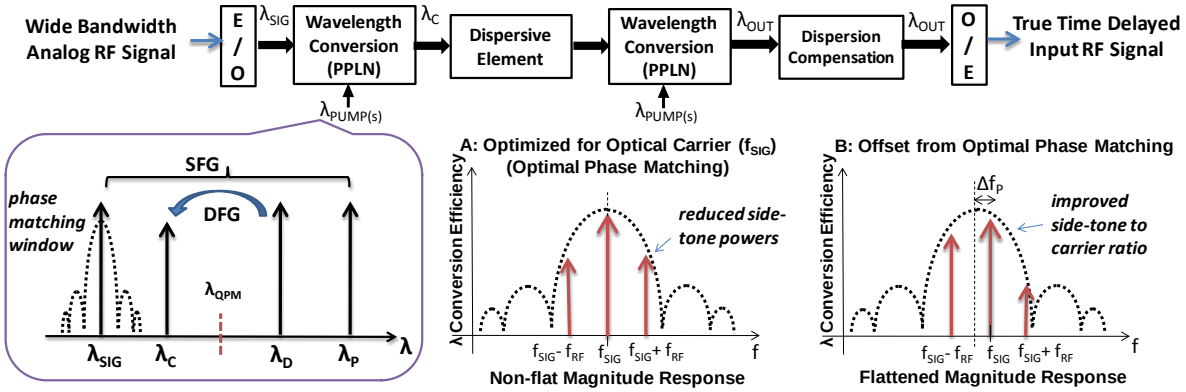

Figure 149. Block diagram of the TTD system using conversion dispersion based delays. Conceptual spectrum of a wavelength conversion in PPLN waveguide by cascaded SFG-DFG is shown. λQPM: Quasi-phase matching (QPM) wavelength

The conceptual block diagram is shown in Figure 149. A wideband analog RF signal was first modulated on an optical carrier ($\lambda_{SIG} = c/f_{SIG}$). The optical signal was then wavelength converted to λ_C using a PPLN waveguide and sent to a highly dispersive medium to induce relative delay. After the delay, it was converted back to the original wavelength and chromatic dispersion was compensated to recover the signal. The λ_C was generated by the cascaded $\chi^{(2)}::\chi^{(2)}$ processes of sum and difference frequency generation (SFG-DFG). For the SFG process, the phase matching window between the λ_{SIG} and the pump, λ_P, was approximately a $sinc^2$ function of phase mismatch. This was usually in the order of several 100s of pm. When wavelength conversion was optimized for minimum phase mismatch between the λ_{SIG} and λ_P, modulated side tones experienced less conversion efficiency compared to the carrier. This is shown with the Case-A in Figure 149. This results in a decreasing magnitude response with increasing RF frequency. However, a pump frequency offset (Δf_P) can be used to shift the matching window (as depicted by Case-B) to flatten the response. In this case, one of the side tones experienced higher conversion efficiency and could increase the side-tone to carrier ratio. When Δf_P was carefully chosen, a flattened magnitude response over wide bandwidths could be achieved.

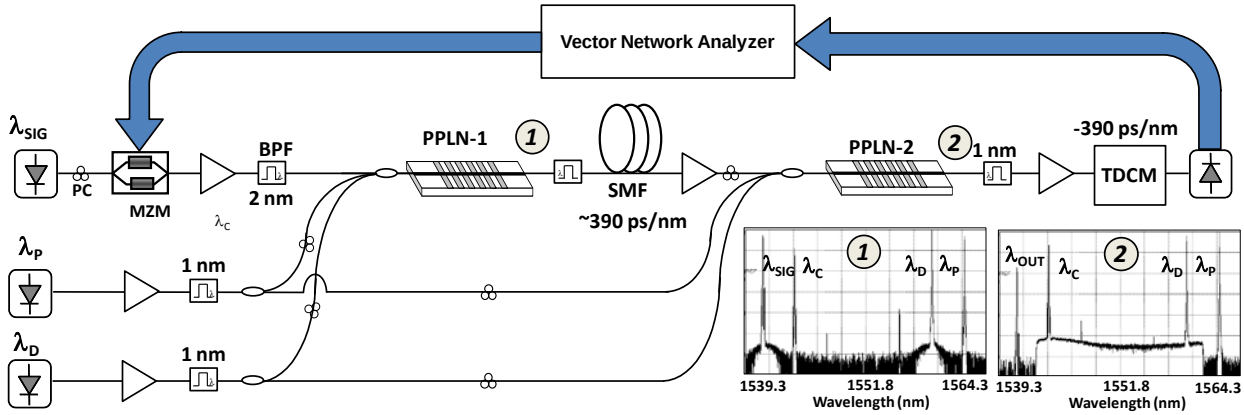

Figure 150. Experimental setup for the transfer function measurement. Spectra at output of the two PPLN waveguides are also shown (10 dB/div, 2.5 nm/div). BPF: bandpass filter, PC: polarization controller

An experimental block diagram of the true-time delay system is shown in Figure 150. A vector network analyzer (VNA: HP 8510C) was used for the acquisition of the S_{21} characteristics. The RF signal from the VNA was used to modulate the optical carrier (λ_{SIG} ~1541 nm) using an X-cut MZM with a 3-dB bandwidth of ~27 GHz and a |chirp factor| < 0.1. The modulation index was set to ~0.2 at 1 GHz and RF power driving the MZM was kept constant for the measured frequency range. The amplified and filtered signal was coupled with a pump (λ_{PUMP} ~1562.1 nm, for SFG process) and a probe pump laser (λ_D ~ tuned in the range 1543.0 -1559 nm for DFG process) and sent to the PPLN-1 waveguide with a QPM wavelength thermally set to ~1551.5 nm. The input polarizations were tuned to achieve highest efficiency. The wavelength converted signal (λ_C) was sent to a ~24 km spool of standard SMF with a dispersion of ~390 ps/nm to induce the wavelength dependent delay. The spectrum after the PPLN-1 (at point 1) is shown in the inset in Figure 150. The delayed signal was then filtered, amplified, and sent to the second PPLN waveguide (PPLN-2, with similar QPM) for the second wavelength conversion. The same laser pumps (λ_P and λ_D) were split and used for the second stage. Since the QPMs were set to be similar, the output of the second wavelength conversion (λ_{OUT}) was always at λ_{SIG}. The spectrum after PPLN-2 (point 2) is also shown in Figure 150. Tunable dispersion compensation module (TDCM) was set to -390 ps/nm and the output signal detected by a photodiode (PD) with ~37 GHz bandwidth operated in the linear regime.

The measured magnitude responses of the non-flat and flattened delay systems are shown in Figure 151. For the conventional delay case, two cascaded WCs at optimum SFG phase matching for the signal and pump lasers resulted in an ~13 dB RF power drop over 40 GHz of bandwidth. By using a 0.270 pm offset in the pump laser wavelength, the response of the system was flattened to < 1 dB fluctuation over 40 GHz. Due to the offset, the conversion efficiency slightly droped for the carrier, but increased for one of the side tones. We observed a ~2 dB RF power decrease for the flattened case compared to the non-flat optimum SFG case. Figure 152 shows a comparison of the side tone to carrier ratios for a modulation frequency of 25 GHz. For the conventional case, both the side tones were suppressed by ~7 dB by the cascaded WCs, resulting in the non-flat response. When flattened, the side tone closer to the optimum phase matching experienced larger conversion efficiency than the carrier and resulted in a relative ~4 dB increase in the tone/carrier ratio. The resulting output was not a perfect single side band

signal, since the other side tone was still partially converted. As shown in Figure 153, similar relative delays up to ~6.5 ns were achieved using a ~ 16 nm wavelength conversion range.

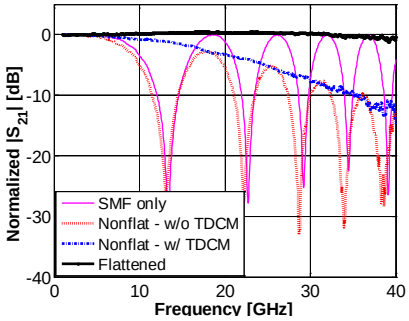

Figure 151. Normalized magnitude responses. The E/O/E response is subtracted

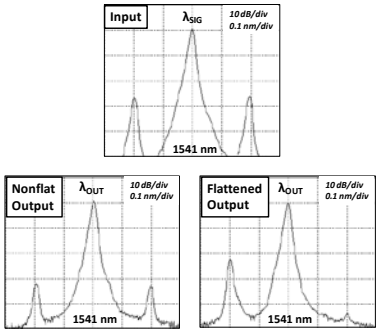

Figure 152. Spectra of input, and delayed output for non-flat and flattened cases (25 GHz)

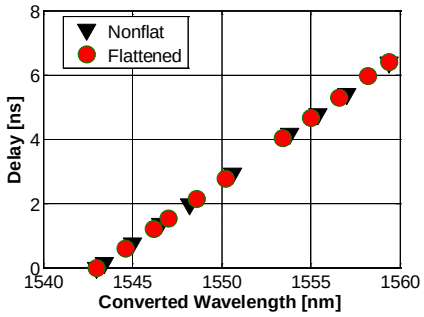

Figure 153. Relative delay for the non-flat and flattened delay systems

The magnitude response of the system for different delay values was compared. The lowest wavelength was taken as the reference and error between the reference and nine other wavelengths (with ~1.6 nm separation) was measured. The results for both the non-flat and flatted cases are shown in Figure 154. The relative magnitude error had less than <0.5 dB peak-to-peak (<0.2 dB RMS) fluctuations for frequencies <30 GHz. The error increases after 25 GHz which we believe was due to the limited MZM bandwidth (3-dB: 27 GHz) and the increasing V_π.

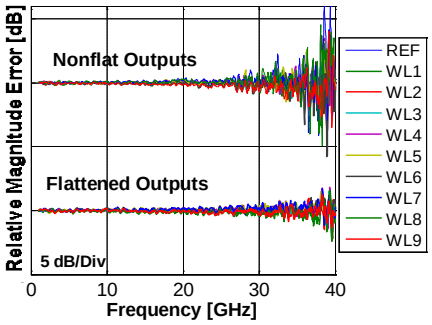

Figure 154. Relative magnitude errors with respect to the minimum delay case magnitude response. The RMS error is <0.2 dB for [1-30] GHz band

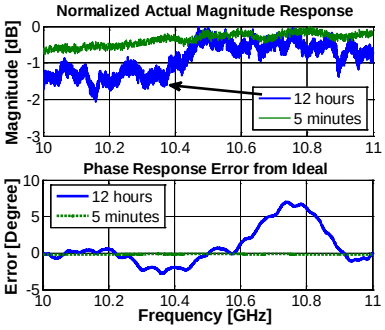

Figure 155. Magnitude response (including E/O/E) of flattened case measured in 12 hours with ~1.25 kHz steps vs. a fast scan

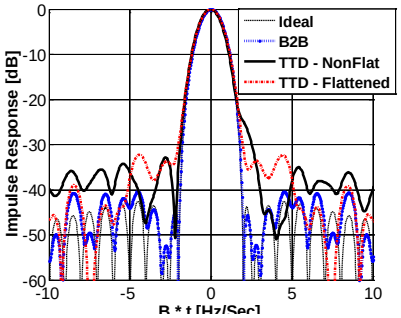

Figure 156. The calculated matched filter output using the experimental transfer function for non-flat and flattened cases

Shown in Figure 155 is the actual magnitude and the phase response (including E/O/E) of the flattened case for the 10-11 GHz range. In order to acquire the actual phase response, 1.25 kHz steps are used – resulting in a 12-hour measurement for the 1 GHz band. When the same band was measured without the SMF, the measurement was completed in 5 min (also shown in Figure 155). The results suggested the ripples in the magnitude and phase response were likely to be due to long term drifts (temperature, polarization, etc.) in the system. By using the 12-hour data in Figure 155 (10-11 GHz bandwidth), we have calculated the impulse response of the system for an ideal linear frequency-modulated pulse. PSLR of the ideal case using a Hamming window is ~ 42.4 dB. We have calculated PSLRs of 32.2 dB and 34.1 dB for the non-flat and flattened cases,

respectively. Since the 12-hour data used for these calculations might have more deviations, we believe actual results would be better than these calculated PSLRs.

4.35. Bit Depth and Sample Rate Tunable Digital to Analog Converter using Conversion/Dispersion Based Delays

We have also demonstrated a bit depth and sample rate tunable and reconfigurable optical digital to analog converter (DAC) using conversion/dispersion based delays with optical multicasting and optical and electrical multiplexing. 4-bit 10-GSample/s (3-bit 6.75 GSample/s) optical DAC was realized with ~2% (~1.5%) and ~5.6% (3%) error from theory for electrical and optical multiplexing, respectively. [38]

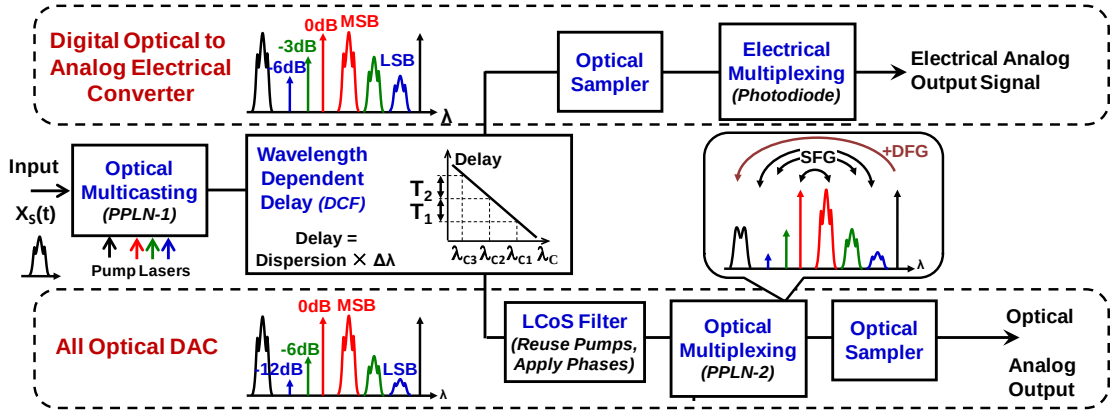

Figure 157. Conceptual block diagram of tunable digital to analog converter implementation using conversion/dispersion delays

The conceptual block diagram of the tunable optical digital-to-analog convertor (DAC) with both electrical and optical multiplexing is shown in Figure 157. An optical input signal at λ_{SIG} was multicast to several copies at different wavelengths ($\lambda_{C1\text{-}3}$) using a PPLN waveguide. The multicast copies were generated by the cascaded $\chi^{(2)}::\chi^{(2)}$ processes of SFG followed by DFG in a PPLN1 waveguide using the dummy pumps ($\lambda_{D1\text{-}3}$). The multicast signal copies were then sent through a spool of dispersion compensating fiber (DCF) to induce a small amount of wavelength dependent relative delay ($T\sim D\times\Delta\lambda$) between the multicast signals. Therefore, the number of taps, tap-delays, and tap-weight-magnitudes were directly controlled by the dummy pumps.

In order to realize DAC, there are two approaches to multiplex these copies: (i) *Electrical multiplexing*: In the first method, the power of each dummy pump must be 3 dB less than the power of previous dummy pump in order to achieve linear DAC (each bit weight is half of pervious bit weight). Then, the resulting copies are sent to a photodiode (PD) in order to electrically multiplex the copies. The multicast signal wavelengths are selected far enough apart such that the optical beat terms exist outside the bandwidth of the PD. (ii) *Optical Multiplexing*: In the second method another PPLN waveguide is utilized in order to optically multiplex signal copies. In the optical approach, the power of each dummy pump must be 6 dB less than the previous pump power since the optical fields are multiplexing in this method-power is equivalent to the square of optical field. The dummy pumps from the first PPLN output ($\lambda_{D1\text{-}3}$) were used as the SFG pumps with the corresponding signal copies ($\lambda_{C1\text{-}3}$) in the second PPLN. A pump, ($\lambda_{P\text{-}2}$), was introduced to generate the output multiplexed signal via the DFG process in the PPLN waveguide. Since the same corresponding pumps that generated the signal copies in the first

stage were used in the second stage, coherent multiplexing of these signal copies could be achieved. The signal also needed to be optically sampled by means of elctro-absorption modulator (EAM) in order to select an appropriate window of input bit stream.

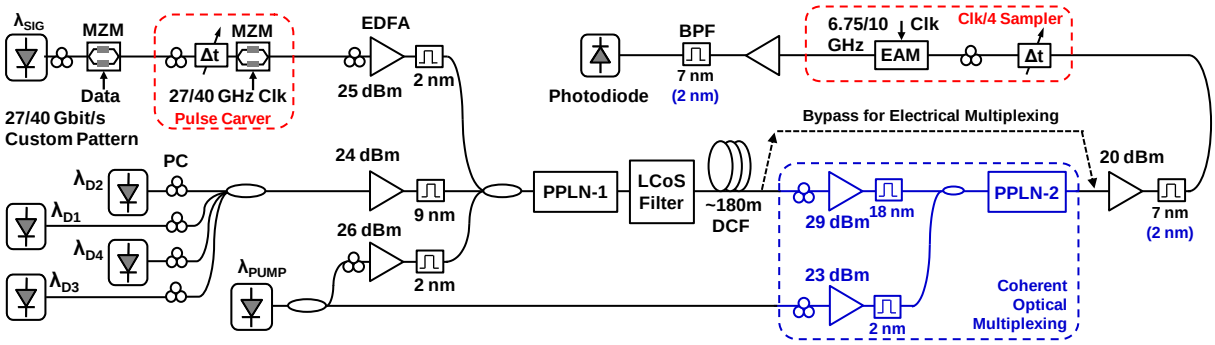

Figure 158. Experimental setup for the tunable DAC with optical and electrical multiplexing. PPLN: Peridically Polled Lithium Niabate Waveguide, LCoS: Liquid crystal on silicon, DCF: Dispersion Compensating Fiber, PC: Polarization Controller, BPF: Bandpass Filter

The experimental setup for the optical DAC is shown in Figure 158. A MZM was used to generate the input 40-Gbit/s OOK data at ~1540.5 nm. It was changed to 27-Gbit/s OOK for additional experiments. A programmable pattern generator was utilized in order to generate multiple patterns to produce different analog waveforms. Full-rate pulse carving was used. The input signal was amplified, filtered and sent to a 4-cm PPLN waveguide (PPLN-1) along with an amplified pump laser at ~1561.5 nm. Four CW pump lasers ($\lambda_{D1\text{-}4}$) were coupled together, amplified and launched into the PPLN waveguide. The QPM wavelength of the waveguide was set to ~1551 nm by temperature tuning. The signal copies at corresponding wavelengths ($\lambda_{C1\text{-}4}$) were generated by the cascaded SFG-DFG processes in the waveguide. The output of the PPLN-1 was sent to a liquid crystal on silicon (LCoS) based amplitude/phase programmable filter that was used to filter the dummy pump lasers and the generated signal copies, and to control the phases/amplitude of the pump laser prior to the second multiplexing stage. Instead of using the LCoS filter, the phases of the pumps were also controlled by fine tuning (+/- 10's of picometers) of the pump wavelength. The filtered pumps and the signals were then sent through a ~180-m DCF in order to induce the relative delay. To achieve optical multiplexing, the pump lasers and the signal copies were then amplified and sent to a 5-cm PPLN waveguide (PPLN-2) with QPM ~1551 nm (similar to PPLN-1). The pairs of pumps and signal copies that were symmetric to the QPM wavelength generate the phase coherent SFG signal based on the phases and the amplitudes of the pumps and the signal copies. The same pump laser at ~1561.5 nm was used for generation of the multiplexed signal at ~1540.5 nm. The multiplexed signal was then filtered and sent to an optical delay line followed by an EAM in order to sample an appropriate window of the bit stream. The resulting signal was then amplified, filtered and sent to a photodiode. In order to realize electrical multiplexing, the signal copies needed to be filtered and sent to the sampling stage after the DCF.

The performance of the tunable DAC was evaluated by comparing measurements of analog levels against the theoretical values. In the electrical multiplexing technique, the linearity of the DAC varies with the photodiode incident power. This is shown in Figure 159 on a 10-GSample/s DAC with 40-Gb/s input signal. Therefore, the photodiode power was varied to find the optimum incident power for the linearity of the DACs in this experiment (Figure 161). When optical

multiplexing is used, the electrical "field" levels of the optical DAC create the linear levels; however, because the photodiode output voltage was proportional to the intensity of light, the measured voltage levels had a quadratic form. This is can be seen in Figure 160, where the photodiode current is set to optimum values to demonstrate bit rate tunability of the optical DAC. In Figure 161, the incident power was swept for the "27-Gbits, 3-bit" and "40-Gbit/s, 4-bit" DACs for both optical and electrical multiplexing schemes. While higher incident power generally increased the signal to noise ratio, it also degraded the linearity of the DAC and receiver. Thus a trade off needed to be considered to choose the optimum photodiode incident power.

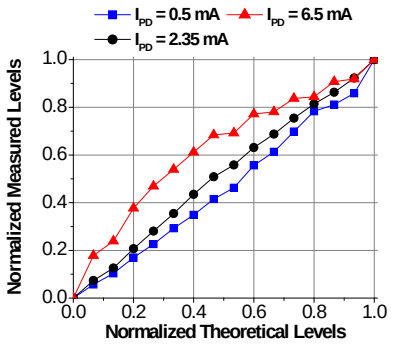

Figure 159. Linearity response of the 4-bit, 10 GSample/s DAC with electrical multiplexing

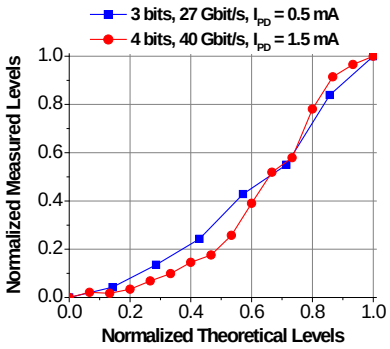

Figure 160. Quadratic power response (linear field amplitude) of optically multiplexed DAC

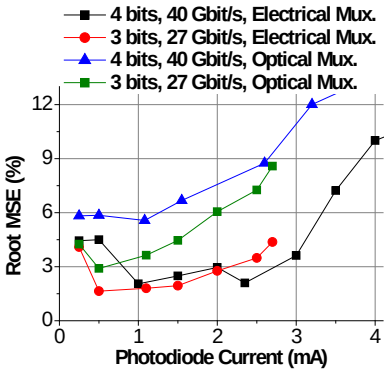

Figure 161. Root mean square error for optically/electrically multiplexed DAC versus photodiode current

To tune the bit rate (sample rate) of the DAC, the wavelength separation, $\Delta\lambda$, between the signal copies was set to ~1.6 nm (~2.4 nm), which resulted in ~25 ps (~37.5 ps) delay after passing through the ~150-m DCF. This created relatively one-bit-delayed copies for 4-bit 10-GSample/s (3-bit 6.75 GSample/s) DACs. Figures 160 and 161 show the sample rate tunability of the optically and electronically multiplexed DACs. A variety of waveforms are generated for each DAC as shown in Figs. 162-165 (b,c).

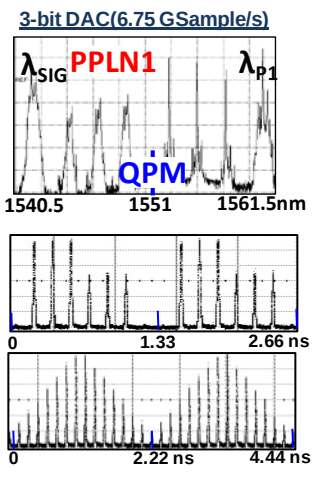

Figure 162. (a) Spectrum of the weighted multicasting in the first PPLN for a 3-bit DAC on 27 Gbit/s input. (b) Multilevel steps, (c) triangular wave

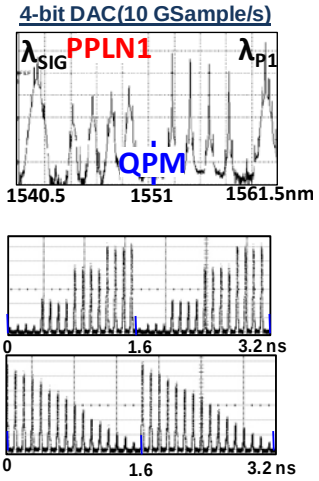

Figure 163. (a) Spectrum of the weighted multicasting in the first PPLN for a 4-bit DAC on 40 Gbit/s input. (b) Multilevel steps, (c) sawtooth wave

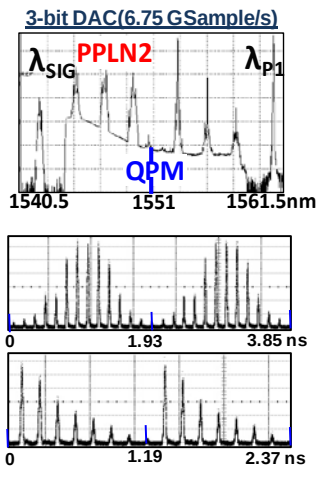

Figure 164. (a) Spectrum of the optical multiplexing in the second PPLN for a 3-bit DAC on 27 Gbit/s input. (b) Sine wave, (c) quadratic ramp

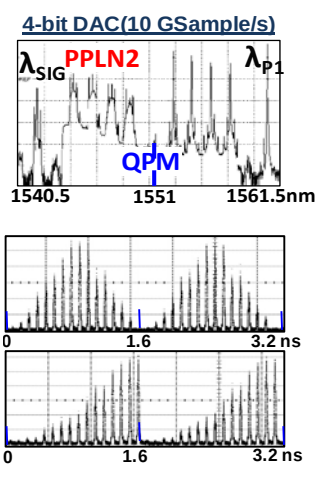

Figure 165. (a) Spectrum of the optical multiplexing in the second PPLN for a 4-bit DAC on 40 Gbit/s input. (b) Sine wave, (c) quadratic ramp

4.36. Demonstration of universal QAM encoder/converter using fully tunable complex-coefficient optical tapped-delay line

We experimentally demonstrated a reconfigurable and fully tunable QAM encoder/converter that operates on a lower order QAM signal and encodes/converts it to various higher order QAM formats. We used a coherent complex-weight optical tunable tapped-delay-line (OTDL) to simultaneously generate and sample 20 and 31 Gbaud BSPK/QPSK signals to 8-PAM and 4/8/16/64-QAM, thus increasing the spectral efficiency.

The conceptual block diagram of the QAM encoder/converter using optical TDL is shown in Figure 166. A lower order input QAM signal was sent into a system that simultaneously performs (i) tapped-delay-line phase-coherent-addition of consecutive symbols and (ii) optical sampling of the resulting signal. In order to encode a lower order QAM to a higher order QAM (e.g., QPSK to 64-QAM), every three consecutive symbols of the QPSK signal needed to be added with weights of [1,0.5,0.25] to generate a 64-QAM symbol. The result would be a 64-QAM signal at the baud rate of the QPSK signal which carries two redundant symbols in every three symbols, and occupies the same bandwidth.

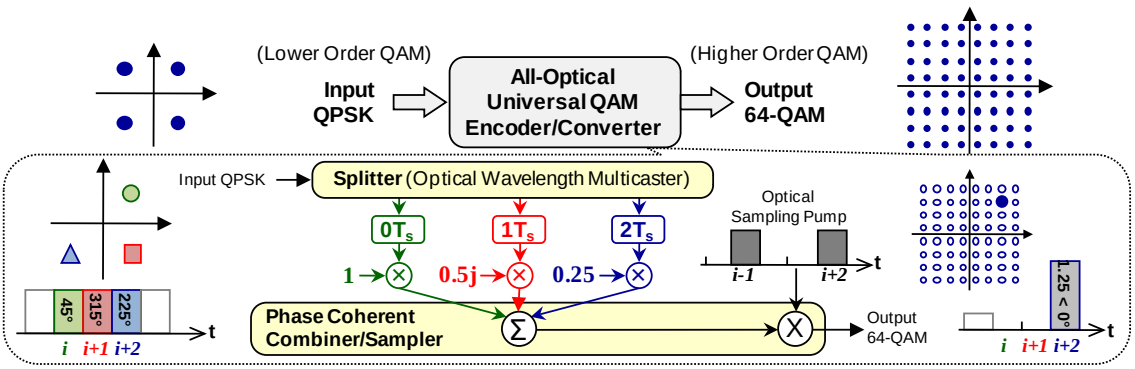

Figure 166. Conceptual block diagram of the QAM encoder/converter using optical tapped-delay line

In bandwidth-constrained systems, the redundancy could be eliminated by proper sampling to increase the "spectral efficiency". We used an "all-in-one" system that not only can manipulate and encode/convert any constellation points using basic rotation/addition functionalities, but also can sample the resulting signal simultaneously with multiplexing. As shown in Figure 167, an optical input signal at λ_{SIG} was multicast to several copies at different wavelengths ($\lambda_{C1\text{-}3}$) due to cascaded $\chi^{(2)}::\chi^{(2)}$ processes of cSFG-DFG in a PPLN waveguide using dummy pumps ($\lambda_{D1\text{-}3}$). The multicast signal copies then passed through a spool of DCF to induce a wavelength dependent relative delay of one symbol time ($T\sim D\times\Delta\lambda$) between the copies. Therefore, the number, delays, and amplitudes of the copies were directly controlled by the dummy pumps. To gain control of the phases of the copies (i.e., to rotate the constellation points), an in-line phase/amplitude programmable filter was used. The copies and their corresponding dummy pumps were filtered and sent into the second PPLN waveguide to be simultaneously multiplexed and sampled. Coherent addition of delayed and weighted copies was achieved by reusing the same dummy pumps from the first PPLN output ($\lambda_{D1\text{-}3}$) as the SFG pumps in the second PPLN. A CW pump (λ_P) was introduced to generate the output multiplexed signal via the DFG process in the second PPLN waveguide. The λ_P CW pump could be replaced with a pulsed pump to enable simultaneous multiplexing/sampling.

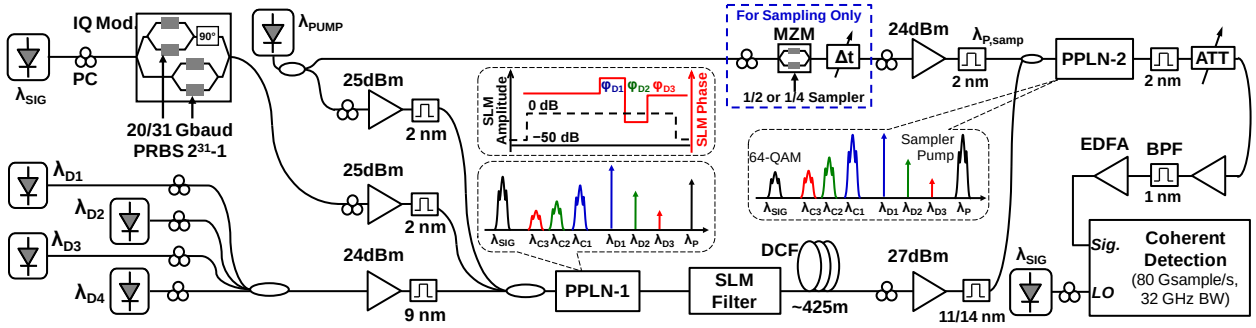

Figure 167. Experimental setup. PPLN: Periodically Poled Lithium Niobate Waveguide, SLM: Spatial Light Modulator, DCF: Dispersion Compensating Fiber, PC: Polarization Controller, BPF: Bandpass Filter, ATT: Attenuator, LO: Local Oscillator

The experimental setup is shown in Figure 167. An in-phase and quadrature (IQ) modulator was used to generate the input 20/31-Gbaud/s BPSK/QPSK signals (PRBS 2^{31}-1) at ~1541.5 nm. The input signal was amplified, filtered and sent to a 4-cm PPLN waveguide (PPLN-1) along with an amplified pump laser at ~1559.5 nm and one to four CW pump lasers

($\lambda_{D1\text{-}4}$). The quasi-phase matching (QPM) wavelength of the waveguide was temperature tuned to ~1550.5 nm. The output of PPLN-1 was sent into a programmable amplitude/phase filter (the SLM) which was based on a liquid crystal on silicon technology, to pass the dummy pump lasers ($\lambda_{D1\text{-}4}$) and the generated signal copies ($\lambda_{C1\text{-}4}$), and to write appropriate phases ϕ_{SLMi} on the "dummy pumps" before they were reused for multiplexing in PPLN-2. The filtered pumps and the signals were then sent through a ~425-m DCF in order to induce one symbol delay between the copies. To accommodate variable input baud rates, the wavelength separation between the dummy pumps (signal copies) was set to 0.95 nm (1.46 nm) for 31 Gbaud (20 Gbaud) signals to induce one symbol delay after the DCF. The pump lasers and the signal copies were then amplified and sent to a 5-cm PPLN waveguide (PPLN-2) with the same QPM as PPLN-1. Each copy (λ_{Ci}) mixed with the dummy pump that generated it (λ_{Di}) and thus the initial phase of the dummy pump got erased in the resulting SFG signal: $(\phi_{Sig}(t)+\phi_P-\phi_{Di})+(\phi_{Di}+\phi_{SLMi})-\phi_{P,samp}\equiv(\phi_P-\phi_{P,samp})+\phi_{Sig}(t)+\phi_{SLMi}$. The amplitude of the multiplexed signal was thus proportional to: $(A_{Sig}(t)A_PA_{Di}^*)A_{Di}A_{P,samp}^*(t)\equiv A_{Sig}(t)|A_{Di}|^2A_{P,samp}^*(t)$, i.e., 3 dB attenuation on a dummy pump power translated to a factor of 0.5 in the weighted copy amplitude. The pump laser at ~1559.5 could be modulated with a 1/2 or 1/4 sampling signal. The output was then filtered and sent to a pre-amplified receiver and coherent detection system (Agilent N4391A).

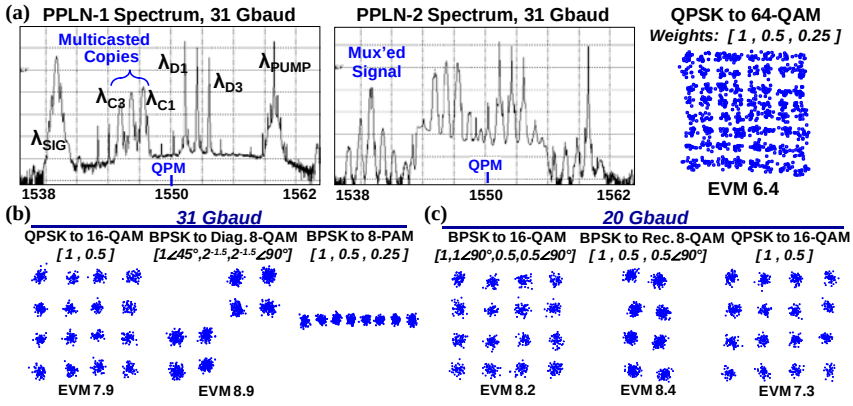

Figure 168. (a) Spectra of the 1st and the 2nd PLLN waveguides outputs and constellation of the generated 16-QAM. (b) and (c) Sample output constellations with 31 Gbaud and 20 Gbaud inputs

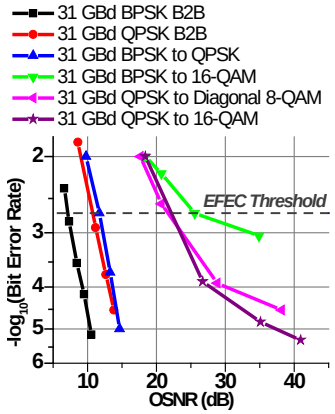

Figure 169. BER versus OSNR for non-sampled QAM encoder

The performance of the system was assessed by tuning the bit rate between 20 and 31 Gbaud and realizing various QAM encodings/conversions. Figure 168(a) shows the spectra for the multicasting (PPLN-1) and multiplexing (PPLN-2) stages for conversion of a 31 Gbaud QPSK signal to 64-QAM. Three copies were combined with weights of [1,0.5,0.25] to create 64-QAM with error vector amplitude (EVM) of 6.4. Figure 168(b,c) depict various constellation diagrams for BPSK/QPSK input signal converted to higher order QAMs at baud rates of 31/20 Gbaud. BER measurements for resulting formats are shown in Figure 169. The OSNR penalty at BER=2×10^{-3} was measured to be ~4.5 dB for BPSK to QPSK, i.e., only ~1 dB higher than a back-to-back measured QPSK. 16-QAM obtained from QPSK , and 16-QAM generated from BPSK, required ~3 dB and ~6 dB higher OSNR compared to a B2B 10 Gbaud 16-QAM, respectively. 10 Gbaud 16-QAM required ~19 dB OSNR to achieve BER of 2×10^{-3}.

The ability to tune the number of taps, baud rate, and simultaneous sampling of converted signal is presented in Figure 170. In Figure 170(a,b) the pump separation was set to 1.47 nm (0.95 nm) for 20 Gbaud (31 Gbaud) input signals, four (two) taps were used and the PPLN-2

pump was pulsed such that one symbol was sampled every four (two), thus creating sampling at 1/4 (1/2) of the baud rate. Therefore, the resulting QAM signals would have higher spectral efficiency. The BER curves of the sampled QAM signals are shown in Figure 171. The measured OSNR penalty was ~2 dB and ~8 dB for conversions of 31 Gbaud BPSK to 15.5 Gbaud QPSK and 31 Gbaud QPSK to 15.5 Gbaud 16-QAM, respectively.

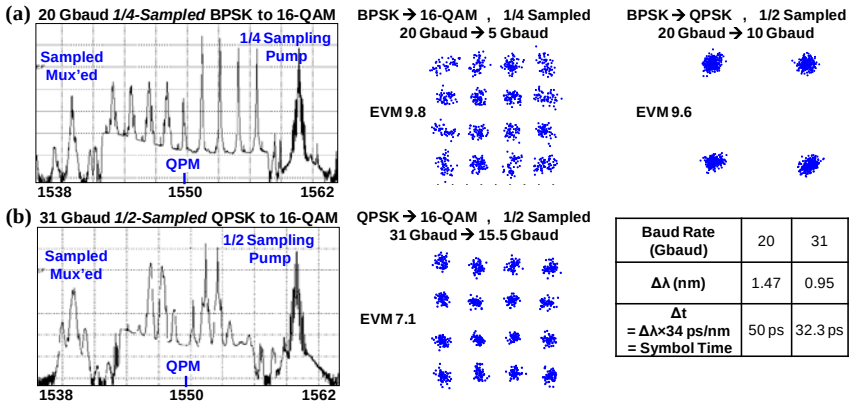

Baud Rate (Gbaud)	20	31
Δλ (nm)	1.47	0.95
Δt = Δλ×34 ps/nm = Symbol Time	50 ps	32.3 ps

Figure 170. (a) PPLN-2 output spectrum when pump is sampling at 1/4 rate, and corresponding constellations. (b) PPLN-2 spectrum and constellation when 1/2 rate sampling pump is used to generate 15.5 Gbaud 16-QAM from 31 Gbaud QPSK

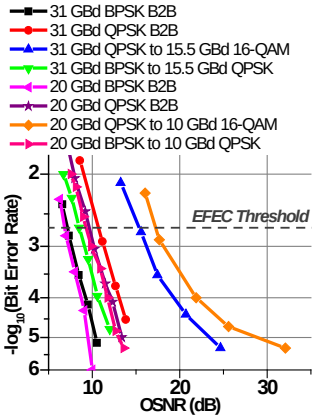

Figure 171. BER measurements versus OSNR with sampling pump

4.37. Demonstration of coherent multi-pattern correlator and all-optical equalizer enabling simultaneous equalization, wavelength conversion and multicasting

We have also demonstrated equalized QPSK/8-PSK signal after passing up to 25-km SMF-28 fiber by using tunable optical tapped-delay-line. We also demonstrated a tunable and reconfigurable optical correlator in conjugation with coherent detection to simultaneously search multiple patterns among BPSK/QPSK symbols in both 20 Gbaud and 31 Gbaud symbol rates.

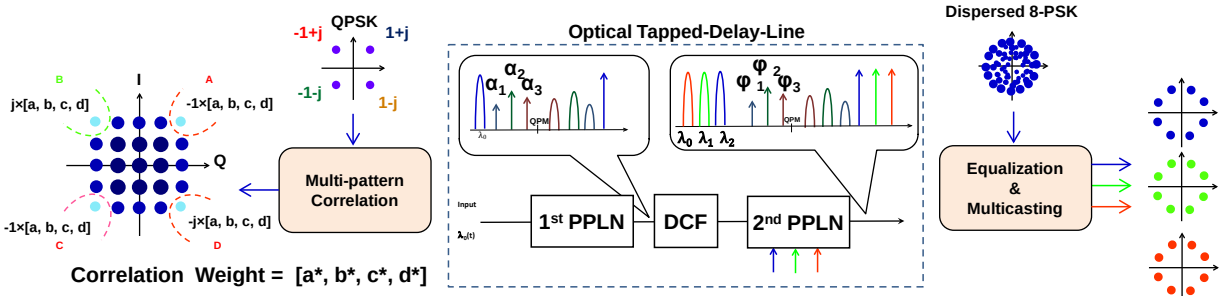

Figure 172. Block diagram of an Optical Tapped-Delay-Line as both multi-pattern correlator and equalizer

The conceptual block diagram of the coherent optical correlator/equalizer is shown in Figure 172. To realize optical tapped-delay-line (OTDL), an optical input signal at λ_0 was multicast to several copies at different wavelengths using a PPLN waveguide. The multicast signal copies were then sent through a spool of DCF to induce a small amount of wavelength dependent relative delay ($T \sim D \times \Delta\lambda$) between the multicast signals. Therefore, the number of taps, tap-delays, and tap-amplitude were directly controlled by the dummy pumps. In order to have control

of the tap-phases, the relative phases of the multicast copies with their corresponding dummy pumps need to be controlled before multiplexing by using an in-line phase/amplitude programmable filter. Coherent multiplexing was achieved by reusing the dummy pumps from the first PPLN output in the second PPLN as the SFG pumps to mix with their corresponding signal copies. To achieve high performance tunable equalizer, the relative delay needed to be set at the half symbol duration. The weights of the OTDL (amplitudes and phases), on the other hand, all depended on the amount of incoming data distortion. With this scheme, a CW pump would coherently add together three weighted delayed versions to produce an equalized signal. In the same way it was possible to perform wavelength conversion and/or multicasting of equalized signal by introducing multiple CW pumps to generate multiple equalized signals in different wavelengths (λ_0, λ_1 and λ_2 respectively).

For realization of a multiple pattern correlator, the delay needs to be set to the symbol duration and the weights of the dummy pumps must be equal to the conjugate of the target pattern. A QPSK symbol has four possible values: ±1±j. To indentify the appearance of four particular consecutive values [a,b,c,d] in a long pattern of QPSK symbols the correlator weights needed to be set to weights [a*, b*, c*, d*] . Then, patterns with [a, b, c, d], j × [a, b, c, d], -1 × [a, b, c, d], -j × [a, b, c, d] would create maximum amplitude. Thus, if the correlated signal was sent to a photodiode (direct detection) there was no way to distinguish between these patterns. On the other hand, by sending the result to the coherent receiver, each pattern was mapped to one constellation point due to their different phases which could be potentially used to recognize simultaneously all patterns with the same correlation weights. Such regions are indicated for 4-taps correlator in Figure 172.

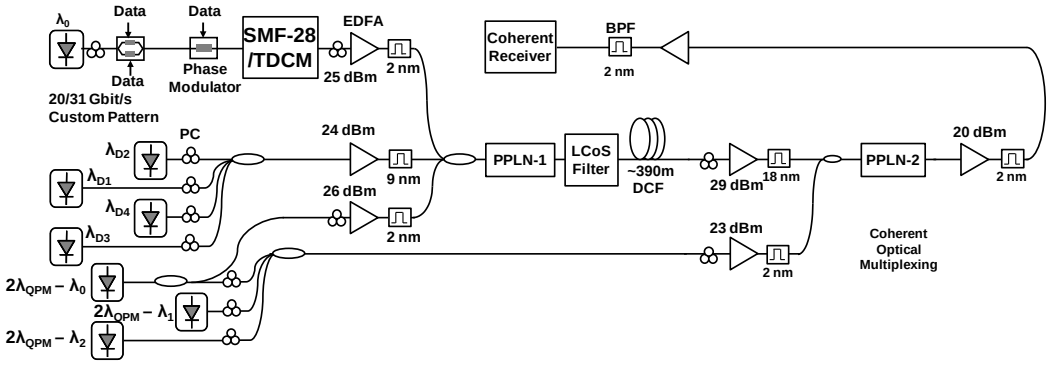

Figure 173. Experimental setup for correlator/equalizer

The experimental setup for the coherent correlator/equalizer is shown in Figure 173. A nested Mach-Zehnder modulator was used to generate the input 31- and 20-Gbit/s BPSK data (PRBS 2^{31}-1) and the 62-and 40-Gbit/s QPSK data (PRBS 2^{31}-1) at ~1541.440 nm. The resulting signal was sent to a phase modulator to generate 8-PSK signals at 93Gbit/s and 60 Gbit/s. A TDCM was employed to emulate dispersion on the input signal with two SMF-28 fibers with 10 and 25 Km lengths. The input signal was amplified, filtered and sent to a 4-cm PPLN waveguide (PPLN-1) along with an amplified pump laser at ~1560.75 nm. Four dummy pump lasers ($\lambda_{D1\text{-}4}$) were coupled together, amplified and launched into the first PPLN waveguide. The quasi-phase matching (QPM) wavelength of the waveguide was set to ~1550.7 nm by temperature tuning. The signal copies at corresponding wavelengths ($\lambda_{C1\text{-}4}$) were generated by the cascaded SFG-DFG processes in the waveguide. The output of the PPLN-1 was sent to a liquid crystal on

silicon based programmable filter used to filter the dummy pump lasers and the generated signal copies, and to control the phases of the pump laser prior to the second wavelength conversion stage, as shown in Figure 173. The filtered pumps and the signals were then sent through a ~390-m DCF or 180-m DCF in order to induce the relative delay. The dummy pump lasers and the signal copies were then amplified and sent to a 5-cm PPLN waveguide (PPLN-2) with QPM ~1550.7 nm. The pairs of pumps and signal copies that were symmetric to the QPM wavelength generate the phase coherent SFG signal based on the phases and the amplitudes of the pumps and the signal copies. A three pump laser at ~1560.75 nm, 1562.15 nm and 1563.55 nm was used for generation of the multiplexed signal at ~1540.7 nm, 1542.1 nm, and 1539.3 nm. The desired signal was then filtered and sent to a coherent receiver for obtaining constellation and BER measurement.

Figure 174 illustrates the optical equalizer performance. The IQ constellations of transmitted 20GBaud QPSK and 8-PSK signals after passing along 25-km SMF-28 fiber are shown in Figure 175(a). The equalized constellations in three different wavelengths along with optical spectra of first and second PPLN outputs are also depicted. A clean IQ constellation was obtained for each copy after equalization. BER measurements were performed on all equalized copies and the original signals for both cases 20 Gbaud QPSK and 8-PSK signals in Figure 174(e). Figure 174(b) shows the constellation of input and equalized signals of 31 GBaud QPSK after passing 10-km SMF-28 the optical spectra of PPLNs' outputs. The performance of the equalizer was evaluated in terms of constellation and OSNR penalties by emulating various amount of dispersion using the TDCM on 20/31Gbaud QPSK and 20Gbaud 8-PSK signals in Figure 174(c) and 9(d). Less than 1 dB OSNR penalty was achieved for up to 400 ps/nm on 20 Gbaud QPSK.

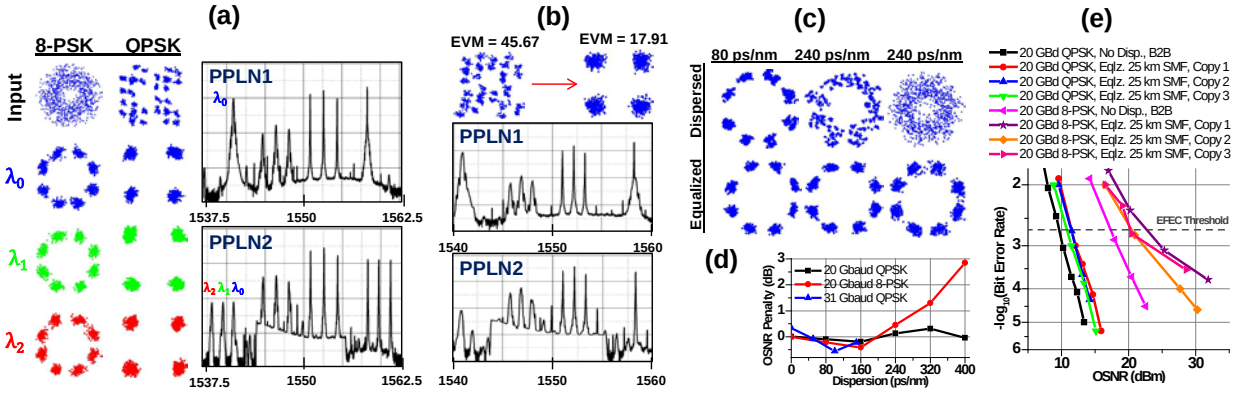

Figure 174. (a)20Gbaud 8-PSK and QPSK equalizing and multicasting. Equalizing of (b)31Gbaud QPSK,(c)different dispersion amount (d) OSNR penalty (e) BER

Figure 175 (a) shows the spectra of 4-tap correlator after the first (PPLN-1) and the second (PPLN-2) wavelength conversion stages. Figure 175 (b) illustrates the constellation of BPSK 4-taps correlation when the search pattern equals to [-1,1,1,-1]. Two constellation points with maximum amplitude correspond to two distinct patterns [-1,1,1,-1] and [1,-1,-1,1]. Searching for sequence [1+j, -1+j, 1-j, 1+j] or its product by j, -1 and -j on QPSK symbols, on the other hand, are shown in 175 (c). In its constellation, there were 4 points with maximum amplitude which correspond to 4 distinct patterns. 2- and 3-taps correlation on 20 Gbaud QPSK and 31 Gbaud QPSK are depicted in Fig 174 (d) and Fig 174 (e) respectively which compare the coherent detection results with eye diagrams. As can be seen, based on eye diagram analysis, exact pattern recognition was not possible since after direct detection there was no phase information whereas

one could potentially take advantage of amplitude and phase information on correlated signals in a coherent receiver to search multiple patterns at the same time.

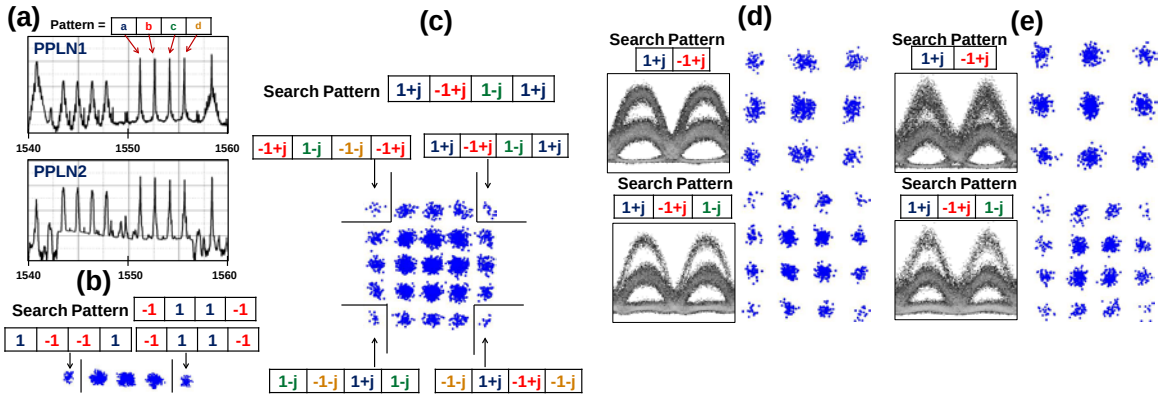

Figure 175. (a) optical spectrum the output of first and second PPLN,(b)searching [1,-1,-1,1] on 20 Gbaud BPSK symbols,(c)searching [1+j, -1+j, 1-j, 1+j] on 20Gbaud QPSK,(d) 2- and 3-tap 20 Gbaud correlated QPSK constellations, (e) 2- and 3-tap 31Gbaud correlated QPSK constellations

4.38. Experimental Characterization of Phase Tuning using Fine Wavelength Offset in a Complex-Coefficient Optical FIR Filter.

We proposed and characterized varying the tap phases of the complex-coefficient tunable conversion/dispersion based finite impulse response (FIR) filter by fine-tuning pump lasers. Full tap-phase tuning ($-\pi$ to π) is achieved by detuning the frequency of laser pumps by <10 GHz, with close agreement to the theory. We experimentally characterized the ability to utilize fine-tuning of pump lasers in conjunction with the dispersive element that is already in the system in order to induce tap delays without the need for a spatial light modulator. The required detuning depends on the difference between the pump and QPM wavelengths. [40]

The conceptual block diagram of the tunable optical tapped-delay-line is shown in Figure 176. Several copies at different wavelengths are generated by injecting multiple pump lasers at wavelengths ($\lambda_{D0\text{-}D3}$) into a PPLN waveguide (PPLN-1) for optical wavelength multicasting using a cascaded SFG/DFG process with a fixed pump at λ_p and a modulated signal at λ_s. The generated signal copies are then sent through a spool of DCF to induce a small amount of wavelength-dependent relative delay ($T \sim D \times \Delta\lambda$) between the signal copies. A Liquid Crystal on Silicon (LCoS) filter was utilized to compensate the offset phase between the taps and set the tap phases to those of the FIR filter. The phase offsets were introduced by the accumulated chromatic dispersion along the path between first and second nonlinear element. Here, we propose to set the tap phases by detuning the dummy pump wavelengths. The induced phase can be described by the following equation: $\delta\Phi_i = -2L\beta_2(\omega_i - \omega_{QPM})\delta\omega_i$, where $\beta_2, L, \omega_i, \omega_{QPM}$ and $\delta\omega_i$ are the group velocity dispersion parameter, DCF length, i^{th} dummy pump's angular frequency, PPLN quasi-phase matching (QPM) frequency and frequency detuning, respectively. It is worth noting that frequency detuning of dummy pumps also varies

the delay of the corresponding signal copy. This delay error is proportional to the frequency detuning and is negligible if the dummy pumps are far from the phase-matching wavelength. In the last stage, the delayed copies are coherently multiplexed into the original wavelength by reusing the dummy pump lasers.

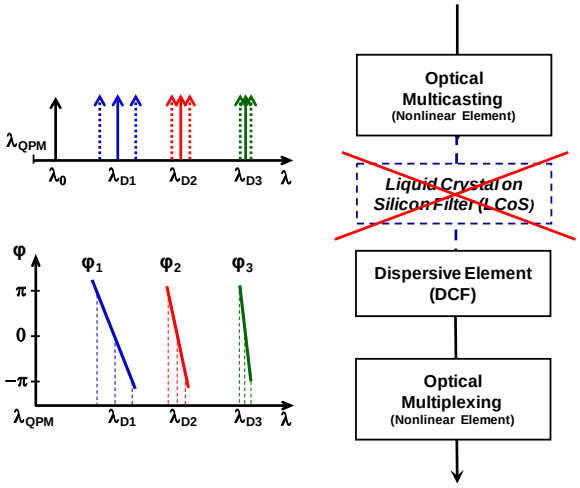

Figure 176. Conceptual block diagram of complex-weight optical FIR filter implementation using conversion/dispersion delays

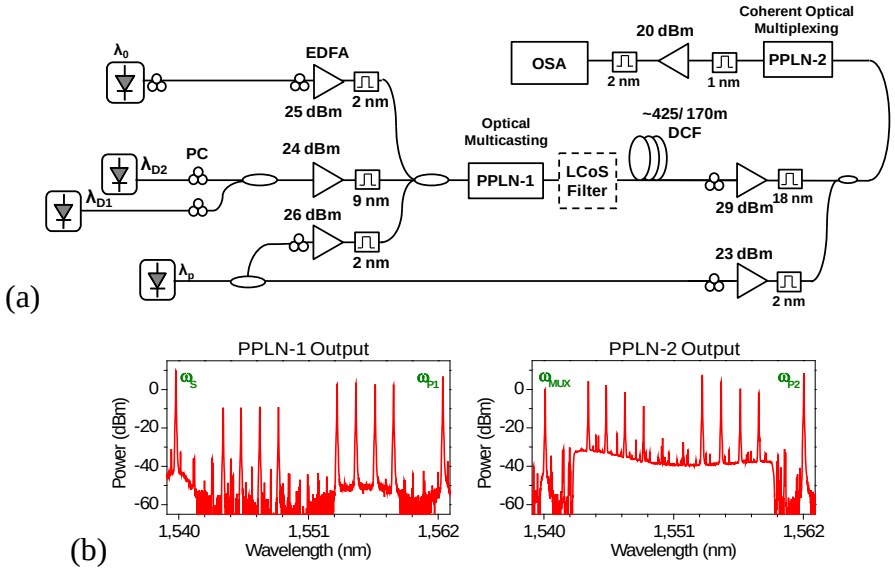

Figure 177. a) Experimental setup for the tunable optical FIR using conversion/dispersion delays. b) PPLN-1 and PPLN-2 output

The experimental setup for the tunable FIR filter is shown in Figure 177 (a). The input of the FIR was a CW laser at ~1538.5 nm that verifies the tap-phase variation with wavelength detuning. The input signal was amplified, filtered, and sent to a 4-cm-long PPLN waveguide (PPLN-1) along with an amplified pump laser at ~1562.5 nm. Two CW pump lasers ($\lambda_{1\text{-}2}$) were coupled together, amplified, and launched to the PPLN waveguide. The quasi-phase matching (QPM)

wavelength of the waveguide was set to ~1550 nm by temperature tuning. The output of PPLN-1 was sent to a filter based on LCoS technology that is used to filter the dummy pump lasers and the generated signal copies and to verify the phase variation formula. The filtered pumps and the signals were then sent through a ~425-m (34 ps/nm) or 175-m (15 ps/nm) DCF in order to induce the relative phase between CW copies. The pump lasers and the signal copies were then amplified and sent to a second PPLN waveguide (PPLN-2) (5-cm-long waveguide) with a QPM wavelength of ~1550 nm. The same pump laser was used for the generation of the multiplexed signal at the original signal's wavelength. The multiplexed signal was finally sent to an OSA.

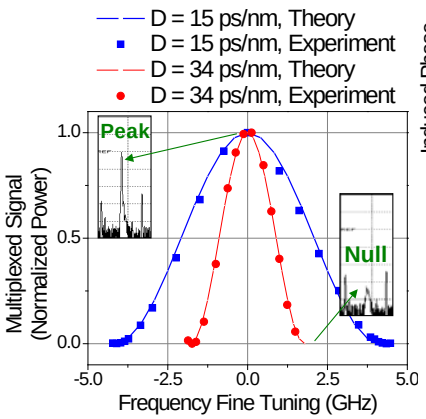

Figure 178. Theory and measured power of the optical multiplexed signal versus fine-tuning. Constructive and destructive interference

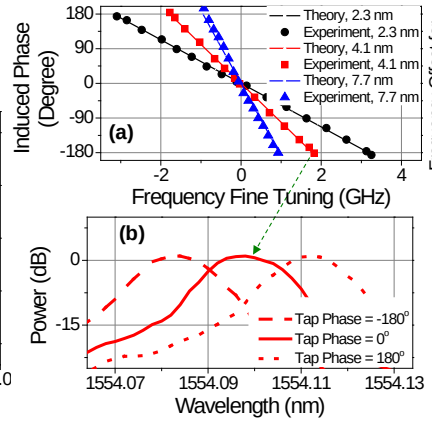

Figure 179. (a) Measured phase induced by frequency fine-tuning for various tap-QPM wavelength distances. (b) Fine-tuning of tap-1

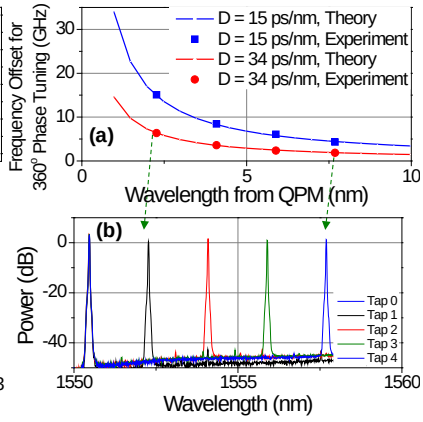

Figure 180. (a) Required frequency tuning for 2π phase shift on a tap for various DCF lengths vs. tap distance to QPM wavelength. (b) Spectrum

Figure 178 shows the constructive and destructive fringes created by frequency fine-tuning on a tap located at 4.1 nm from the QPM wavelength. For longer DCF lengths, the peaks and nulls become more sensitive to the frequency tuning, and the amount of phase can be derived from its $\cos^2$ form. Figure 179(a) depicts the theoretical and experimentally measured induced phase by fine-tuning of the tap wavelength. The experimental results show very close agreement with theory, showing a linear dependence of phase on laser fine-tuning. Fine-tuning of the middle (second) tap is depicted in Figure 179 (b). The amount of frequency fine-tuning required for 2π phase shift depends on the distance of the tap from the QPM wavelength (Figure 180 (a)). If longer DCF fibers are used, then coarser tuning will be required. However, for a given tap delay, there is a tradeoff between choosing longer DCFs and smaller wavelength spacing (i.e., more taps but shorter tap delay tuning range) and shorter DCFs and longer tap-tuning range. Interestingly, for both cases, the fine-tuning required can be made negligible compared to the tap-wavelength spacings.

4.39. Tunable Complex-Weight All-Optical IIR Filter Design based on Conversion/Dispersion Delays

We examined the design of a tunable optical infinite-impulse-response (IIR) filter based on conversion/dispersion delays. Design guidelines were studied to alleviate the effects of the inherent system propagation delay. We characterized the ability to extend the functionality of our approach from the FIR filter to IIR filters in order to achieve tunable IIR filters. The inherent

delay of the system, which could impose a limit on the IIR design, is shown to cause ripples. Design criteria and guidelines were presented to alleviate this limit, which is inherent to high speed IIR filers.

(a)

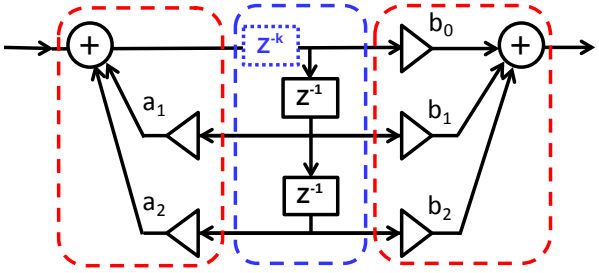

(b)

$$H(z) = \frac{z^{-k}\sum_{i=0}^{M} b_i z^{-i}}{1 + z^{-k}\sum_{i=0}^{N} a_i z^{-i}}$$

Figure 181. (a) Signal flow graph for DF-II IIR filter and (b) filter z-transform

The signal flow graph for the Direct-Form-II (DF-II) realization of IIR filter is shown in Figure 181(a). In this scheme, the delay section of the filter is shared between the feedforward and feedback (zeros and poles) sections. The z-transform of the filter impulse response is also shown in Figure 181(b).

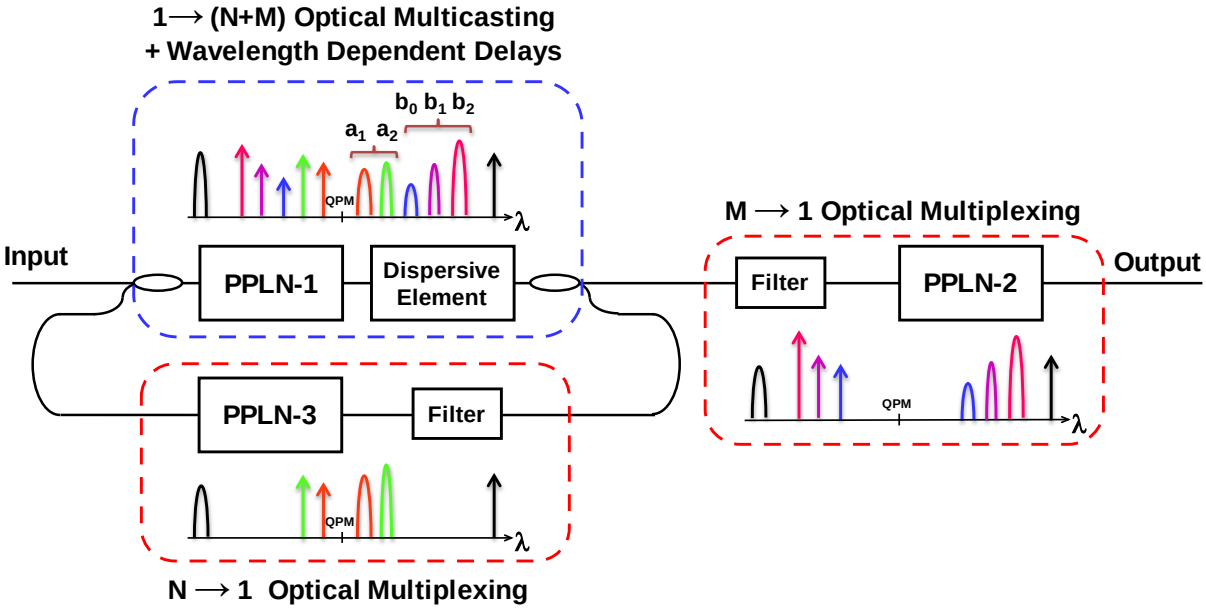

Figure 182. Proposed all optical and fully tunable IIR filter

Our proposed optical implementation of this digital filter is depicted in Figure 182(a). The delay stage is realized in two steps: first, we generate several copies at different wavelengths by injecting multiple dummy pump lasers at different wavelengths into the first PPLN (1→(N+M) Optical Multicasting). Then, a wavelength-dependent relative delay is induced between the generated signal copies by passing the PPLN-1 output through a dispersive element (e.g. dispersion compensation fiber, DCF). The output of this stage is then split into two separate paths: feedforward and feedback paths. Along the feedforward path, M signal copies are sent to the second PPLN along with their corresponding weighted dummy pumps in order to multiplex

them to the original wavelength (M→1 Multiplexing). In both feedforward and feedback paths, the associated amplitude and phase of the complex-weights are varied by dummy pumps' powers and fine-tuning of dummy pump wavelengths. In the feedback path, on the other hand, the N delayed signal copies with their dummy pumps are filtered and sent to the third PPLN in order to add the generated copies with associated complex weights (N→1 Multiplexing). The second PPLN output is then coupled with the input signal and sent to the system to close the feedback loop. Since maintaining the coherency between loop signal and input signal is necessary, the total loop length needs to be shorter than the coherence length of the input signal's laser linewidth. Moreover, any wavelength dependent element, including DCF, could inherently introduce some amount of propagation delay. This inherent delay in the IIR implementation results in the creation of new poles that cause amplitude and phase ripple in frequency response compared to the ideal filter (i.e. without propagation delay). Similar to the digital filter design methods in the electrical domain, here we propose a unit-cell for an optical IIR filter which ideally consists of two poles and two zeros. This unit-cell, however, would vary considering the propagation delay of the dispersive element.

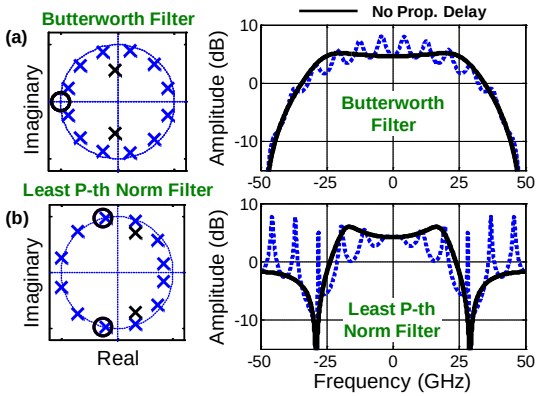

Figure 183. Filter zero-pole locations, amplitude and phase response for two cases with no extra and 10-bit inherent propagation delay in the system. (a) Least P-th norm optimal IIR filter and (b) Butterworth IIR filter design

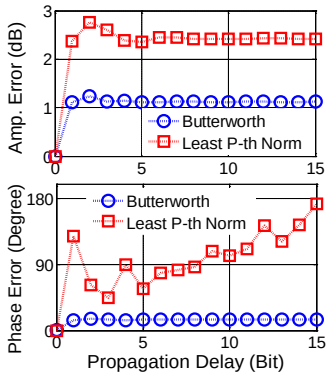

Figure 184. Average filter frequency response amplitude and phase error versus propagation delay for different filters

We considered a unit-cell IIR filter based on our OTDL technique for the analysis. The unit-cell designed here is a second order IIR filter. A 25-GHz lowpass digital optical IIR filter was designed using Butterworth and least p-th norm optimal techniques, as shown in Figure 183. The effect of inherent propagation delay is studied for these two filters designs. As can be observed in Figure 183, the propagation delay moves and adds some poles to the filter. These added poles fall around the unit circle and thus create ripples in both the amplitude and phase of the filter response (Figure 183). The heights of the amplitude ripples are inversely proportional to the distance from the poles to the unit circle. Therefore, in Figure 183(b), the filter with inherent 10-bit delay has larger ripples compared to the original design. Figure 179 depicts the mean absolute error for amplitude and phase of the two filters, when the inherent delay is varied beyond the ideal zero amount. As can be observed in the amplitude error, as the inherent delay increases, the error converges to a certain value that mainly depends on the original location of zeros and poles in the ideal system design. This is because the height of the ripples converges to a certain limit. The phase response, on the other hand, is more prone to ripples if the poles are close to the unit

circle. This is because when the poles fall outside the unit circle, they can induce a large phase and thus create large systematic phase offsets. In summary, the inherent delay causes ripples. These ripples can be made small enough if in the original design of the filter zeros and poles avoids creating extra poles near the unit circle.

4.40. Flexible, Reconfigurable Capacity Output of a High-Performance 64-QAM Optical Transmitter

We experimentally demonstrated a reconfigurable optical flexible transmitter to generate arbitrary optical QAM signals. Optical 16-QAM and 64-QAM is generated at EVM 8.5% and 7.2%, respectively. We demonstrated successful transmission through 80-km SMF-28 after compensating with 20-km DCF with negligible penalty.

Dramatic growth in data capacity demand in optical networks has necessitated a simultaneous increase in the data speeds of terminal transmitters. State-of-the-art transceivers are capable of providing 100-Gbit/s data rates per channel; these channels can employ the use of spectrally efficient higher-level modulation amplitude/phase formats as well as coherent technologies. Although these transmitters can provide enormous data pipes, two specific challenges remain: (1) there will be a large discrepancy between high-rate and low-rate data channels, such that the large capacity of a single data channel from the transceiver will often not be required and be under-utilized, and (2) the large capital investment in terminal transmitters are often not efficiently utilized. A laudable goal would be to have transmitters whose extremely large capacity can be tailored and shared among many different channels, as the traffic demands vary in a dynamic, heterogeneous network. Flexible, reconfigurable bandwidth allocation can enable optimal use of terminal equipment as well as create new opportunities for scalable, cost-effective network architectures. [41]

One potential approach to achieving such a flexible transmitter is the use of optical nonlinearities to perform reconfigurable multiplexing of different data channels, such that the capacity and data constellation can be reapportioned among different output wavelengths; i.e., data can emerge as a single 64-QAM signal or as three independent QPSK signals. Wave-mixing using nonlinearities have: (a) >THz bandwidths, (b) minimal noise generation, (c) wavelength conversion of a data channel, and (d) transparency to the data bit rate and modulation format. Previously, methods for a flexible transmitter have been reported in which: (a) IQ modulators on individual frequency combs allocate the bandwidth and (b) elastic optical path network using OFDM and variable-bandwidth wavelength crossconnects.

We have demonstrated a flexible, reconfigurable capacity output of a high-performance 64-QAM optical transmitter. We used nonlinearity based optical signal processing to achieve reconfigurability and flexibility in allocation of capacity per channel and bandwidth.

The conceptual block diagram of a flexible capacity QAM transmitter is shown in Figure 185. Multiple electrical signals are input to the system, and the output capacity can be configured by changing the lasers configuration into the transmitter. In the flexible transmitter, many QPSK signals at various wavelengths are generated in order to convert the electrical signals to the optical domain. The optical QPSK signals are then injected into an optical system that generates various higher order QAM signals at different wavelengths from the QPSK signals.

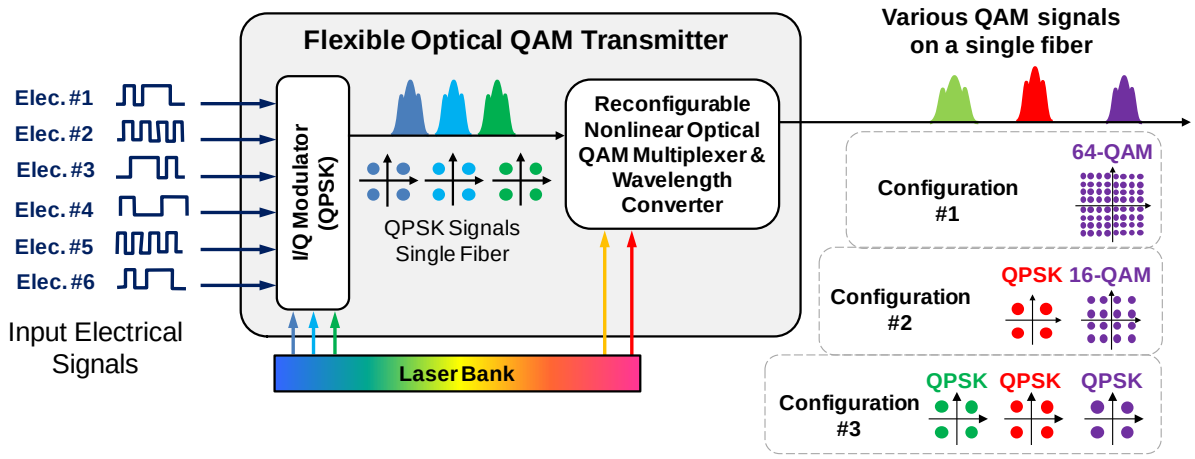

Figure 185. Block diagram of an optical flexible transmitter

The optical QAM multiplexer/wavelength converter utilizes a series of cascaded second order nonlinear wave mixings (i.e., SHG, DFG and SHG) in PPLN waveguides in conjunction with DCF to create the output. In the optical QAM multiplexer, a CW pump (E_{CW}) at the quasi-phase-matching (QPM) wavelength of the PPLN waveguide is injected to the PPLN waveguide together with the QPSK signals ($E_{Di}(t)$). This generates copies of the signals at new wavelengths with complex fields $|E_{CW}|^2(E_{Di}(t))^*$. The original QPSK signals, their copies, and the CW pump are sent into a DCF that induces one symbol delay between the original signal and its copy; then, they are sent to the second PPLN waveguide for multiplexing along with another QPSK signal ($E_P(t)$). Because all signals and pumps are on the same optical path, coherency is preserved. According to SFG, DFG and SHG rules, the multiplexed signal becomes proportional to $\Sigma |E_{CW}|^2(1+\alpha|E_{Di}(t)|^2 e^{j(\varphi(t)-\varphi(t-T))})(E_P(t))^*$. This gives the multiplexing an equation of multiplexing of $E_{Di}(t)$ and $E_P(t)$. Thus, although the phase of $E_{Di}(t)$ is lost in the process, because of one symbol delay, the difference of the phase is preserved and used for multiplexing. Because nonlinear mixings can be controlled by reconfiguring the pump lasers, the transmitter can simultaneously allocate capacity on different wavelengths, flexibly and reconfigurably.

The experimental setup for the flexible transmitter is shown in Figure 186. A nested Mach-Zehnder modulator was used to generate the 40-Gbit/s QPSK data (PRBS 2^{31}-1) at ~1558.2, 1556 and 1555 nm. The resulting signals were sent to the WDM filter to be separated and decorrelated. The two QPSK signals at 1556 and 1555 nm were then combined with the CW pump laser and sent to the first PPLN (5-cm length) waveguide after enough amplification to generate phase conjugate of the original signal. The output of the first PPLN waveguide was then passed through the DCF to induce one bit delay between input signals and their corresponding phase conjugate copies. The signals, their copies, and the CW pump lasers as well as the QPSK signal at 1558.2 were then sent to the second PPLN (4-cm length) waveguide to generate the desired output. The output signal was then sent to a 80 km SMF-28 fiber spool and 20 km DCF. The resulting signal was then sent to the coherent receiver to obtain I-Q constellation and to measure BER. Coherent homodyne detection with a local oscillator was used to recover the amplitude and phase of the 64-QAM signal. The signal was sampled at 80 GSample/s rate. Since the signals were at 20-Gbaud, this sampling rate was large enough (above Nyquist sampling rate); therefore, we used digital signal processing techniques offline to perform phase/frequency tracking and synchronization to obtain the phase/amplitude of every data symbol.

Figure 187(a) illustrates the optical spectrum of the first stage in which the phase conjugate copies of the original QPSK signals were generated at corresponding wavelengths. These copies were used in the second stage to generate the output signal.

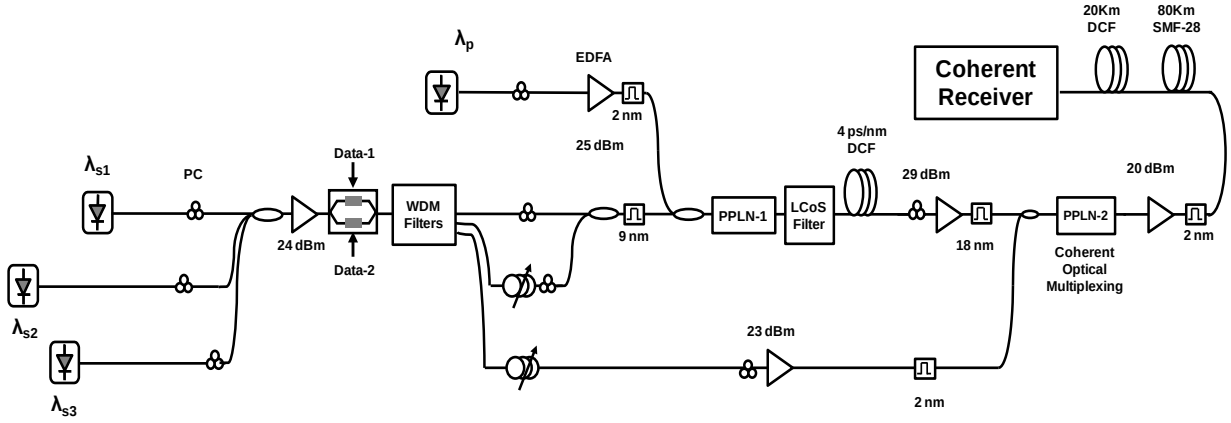

Figure 186. Experimental setup for optical flexible transmitter

In order to realize the first configuration, an offset 16-QAM signal, which was generated by multiplexing two QPSK signals and a CW pump laser with approriate phases and amplitudes. The third QPSK signal was multiplied by this 16-QAM signal by DFG mixing in PPLN-2 and thus "rotated" it, to generate a 64-QAM signal. The second PPLN output as well as the final I-Q constellation are depicted in Figure 187(b). Using the proposed flexible transmitter, a 64-QAM with EVM ~7 % was achieved.

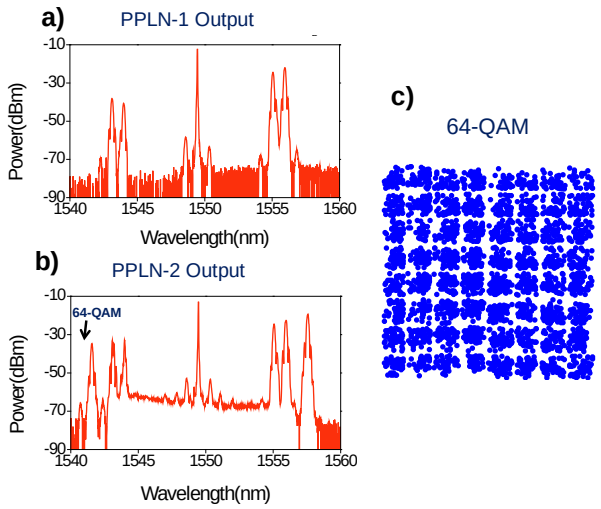

Figure 187. (a) PPLN-1 and (b) PPLN-2 output and (c) generated 64-QAM

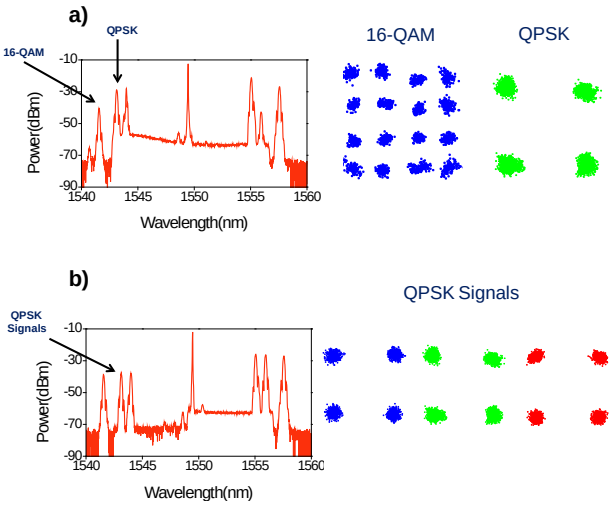

Figure 188. (a) Generated QPSK and 16-QAM (b) three QPSK signal generation

For reconfiguration, the setup (Figure 186) is the same and the only things that needed to be tuned were the filters. The first nonlinear stage was the same for all three cases, where two QPSK signals were sent into the PPLN and a phase-conjugate copy was created for each. For the second configuration, similar to the previouse one, two QPSK were multiplexed to generate a 16-QAM at the first output channel. The second output, on the other hand, was a copy of the third QPSK signal at the output. The LCoS filter blocked a QPSK original signal (Figure 188(a)),

such that we were left with a shifted QPSK that was being mixed/multiplied by the third QPSK to generate the 16-QAM output signal. Also, since the original signal for the first QPSK was blocked, its phase-conjugate copy passed the second nonlinear stages without contributing in the multiplexing (16-QAM); thus, it was the QPSK output.

In Figure 188(b), the transmitter was reconfigured to generate three QPSK signals at 1542.17, 1543.8 and 1545.4 nm. To generate three QPSK signals: The LCoS filter and the 18-nm filter blocked the phase-conjugate copies (Figure 188(b)). Therefore, at the output of the second PPLN, we had three copies that represent our three output QPSK signals. For all QPSK signals, an EVM of ~11 % was achieved.

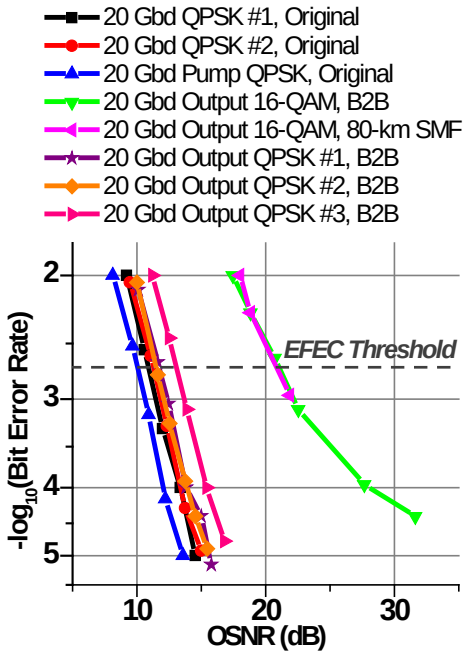

Figure 189. BER measurements on the flexible transmitter output

Figure 189 shows the BER for all scenarios. The 16-QAM was transmitted through 80-km SMF-28 and 20-km DCF to evaluate transmission capability. The OSNR penalty after 100-km transmission is negligible.

5. Conclusions

We have demonstrated dramatic enhancements in the performance and functionality of tunable optical delay lines; we showed up to 3.6 μs of tunable optical delay for OOK, DPSK and DQPSK modulation formats. Fundamentally, we used tunable wavelength conversion combined with inter-channel chromatic dispersion and intra-channel dispersion compensation to achieve continuously tunable optical delays. Extremely long delays (3.6 μs) at high bit-rates (>100 Gbit/s) were demonstrated with minimal data distortion (BER of 1E-9) that met the POPS program goals. We also demonstrated delays for different data modulation formats, including on-off-keying and spectrally efficient differential-quadrature-phase-shift-keying.

We used: (i) low dispersion slope, highly nonlinear fiber to achieve wide-bandwidth wavelength conversion based on four-wave mixing, and (ii) a highly dispersive element with low dispersion slope to introduce a large linear change in time delay as a function of wavelength. Since the dispersive element also introduces data-destroying intra-channel chromatic dispersion, we mitigated dispersion in order to achieve a low bit-error-rate. Towards this end, we made use of spectrally efficient differential-quadrature-phase-shift-keying which increased the tolerance to all orders of dispersion.

In general, we studied various high-data-rate signal-processing applications that make use of POPS-enabled tunable optical delays. We demonstrated that tunable optical delays can potentially be used in a dynamic, reconfigurable, and heterogeneous optical system.

During the POPS program, many fundamental sub-systems for nonlinear optical signal processing were demonstrated and studied. Future research in the field will benefit from these techniques to enable high speed processing of data signals in multiple data channels. Using coherent homodyne detection, more advance modulation formats can be utilized in which optical amplitude, phase and polarization represent information. Nonlinear signal processing using tapped-delay-lines, for example, could be regarded as a technique for parallel and high capacity data processing.

6. References

1. Xiaoxia Wu, Louis Christen, Omer F. Yilmaz, Scott R. Nuccio, and Alan E. Willner, “Optical 10–20 and 20–40 Gbits/s Pseudorandom Bit Sequence Data Multiplexing Utilizing Conversion/Dispersion Based Tunable Optical Delays”, Optics Letters, Vol. 33, Issue 13, pp. 1518-1520 (2008).
2. Louis Christen, Irfan Fazal, Omer F. Yilmaz, Xiaoxia Wu, Scott Nuccio, Alan E. Willner, Carsten Langrock, Martin M. Fejer, “Tunable 105 ns Optical Delay for 80 Gbps RZ-DQPSK, 40 Gbps RZ-DPSK, and 40 Gbps RZ-OOK Signals using Wavelength Conversion and Chromatic Dispersion”, Proc. of Optical Fiber Communications Conference (OFC), San Diego, CA, Feb. 2008.
3. Omer F. Yilmaz, Louis Christen, Xiaoxia Wu, Scott R. Nuccio, Irfan Fazal, and Alan E. Willner, “Time-Slot-Interchange of 40 Gb/s Variable Length Optical Packets Using Conversion/Dispersion Based Tunable Delays”, Optics Letters, Vol. 33, Issue 17, pp. 1954-1956 (2008).
4. S. R. Nuccio, O. F. Yilmaz, S. Khaleghi, L. Christen, I. Fazal, and A. E. Willner, “503 ns, Tunable Optical Delay of 40 Gb/s RZ-OOK using Additional λ-Conversion for Increased Delay and Reduced Residual Dispersion”, Proc. of Optical Fiber Communications Conference (OFC), San Diego, CA, March 2009.
5. O. F. Yilmaz, S. R. Nuccio, S. Khaleghi, and A. E. Willner, “Optical Multiplexing of Two 21.5-Gbit/s DPSK Signals into a Single 43-Gbit/s DQPSK Channel with Simultaneous 7-Fold Multicasting in a Single PPLN Waveguide”, Proc. of Optical Fiber Communications Conference (OFC), San Diego, CA, March 2009.
6. Xiaoxia Wu, Antonella Bogoni, Omer F. Yilmaz, Scott R. Nuccio, and Alan E. Willner, “Optically Concatenated 4-Fold 40-Gbit/s Multicasting, 4-Fold 40-to-160-Gbit/s Multiplexing, and 160-to-40-Gbit/s Demultiplexing Using Highly Nonlinear Fiber”, Proc. of Optical Fiber Communications Conference (OFC), San Diego, CA, March 2009.
7. X. Wu, A. Bogoni, S. R. Nuccio, O. F. Yilmaz, A. E. Willner, " 320-Gbit/s Optical Time Multiplexing of Two 160-Gbit/s Channels Using Supercontinuum Generation to Achieve High-Speed WDM-to-TDM", Proc. of the Conference on Lasers and Electro-Optics (CLEO), Baltimore, MD, May 2009.
8. O. F. Yilmaz, S. R. Nuccio, X. Wu, A. E. Willner; "Tunable N-Fold Multicasting and Pulsewidth of 40 Gb/s Channels by Variable Periodic Slicing of a Supercontinuum," accepted to the Conference on Lasers and Electro-Optics (CLEO), Baltimore, MD, May 2009.
9. S. R. Nuccio, O. F. Yilmaz, X. Wu, A. E. Willner, "Fine (<0.5 ps) and Course Tuning (>15 ps) of Optical Delays using Acousto-optic Mixing with a 1-pm Tunable Laser," Proc. of the Conference on Lasers and Electro-Optics (CLEO), Baltimore, MD, May 2009.
10. O. F. Yilmaz, S. R. Nuccio, Z. Bakhtiari , X. Wu, J. Wang, L. Zhang, and A.E. Willner, "Wavelength Conversion and 9-fold Multicasting of a 21.4 Gbit/s DPSK Data Channel using Supercontinuum Generation," in Nonlinear Optics: Materials, Fundamentals and Applications, OSA Technical Digest (CD) (Optical Society of America, 2009), paper PDPA3.

11. Xiaoxia Wu, Scott Nuccio, Omer F. Yilmaz, Jian Wang, Antonella Bogoni, Alan E. Willner, "Controllable Optical Demultiplexing Using Continuously Tunable Optical Parametric Delay at 160-Gbit/s with with <0.1-ps Resolution," Optics Letters, Vol. 34, Issue 24, pp. 3926-3928 (2009).

12. Xiaoxia Wu, Jian Wang, Omer F. Yilmaz, Scott R. Nuccio, Antonella Bogoni, Alan E. Willner, " Bit-rate-variable and order-switchable optical multiplexing of high-speed pseudorandom bit sequence using optical delays," Optics Letters, Vol. 35, Issue 18, pp. 3042-3044 (2010).

13. Scott R. Nuccio, Omer F. Yilmaz, Salman Khaleghi, Xiaoxia Wu, Louis Christen, Irfan Fazal, and Alan E. Willner, "Tunable 503 ns Optical Delay of 40-Gb/s RZ-OOK and RZ-DPSK using a Wavelength Scheme for Phase Conjugation to Reduce Residual Dispersion and Increase Delay," Optics Letters, vol. 34, no. 12, pp. 1903-1905, 2009.

14. Omer F. Yilmaz, Scott R. Nuccio, Xue Wang, Jian Wang, Irfan Fazal, Jeng Yuan Yang, Xiaoxia Wu, Alan E. Willner, "Experimental Demonstration of 8-Fold Multicasting of a 100 Gb/s Polarization-Multiplexed OOK Signal Using Highly Nonlinear Fiber," Proc. of Optical Fiber Communications Conference (OFC), San Diego, CA, March 2010.

15. Jian Wang, Zahra Bakhtiari, Yinying Xiao-Li, Omer Yilmaz, Scott Nuccio, Xiaoxia Wu, Hao Huang, Jeng-Yuan Yang, Yang Yue, Alan E. Willner, "Experimental Demonstration of Data Traffic Grooming of a Single 10-Gbit/s TDM Tributary Channel between Two 160-Gbit/s WDM Channels," Proc. of Optical Fiber Communications Conference (OFC), San Diego, CA, March 2010.

16. Jian Wang, Zahra Bakhtiari, Yinying Xiao-Li, Scott Nuccio, Omer Yilmaz, Xiaoxia Wu, Jeng-Yuan Yang, Yang Yue, Irfan Fazal, Alan E. Willner, "Phase-Transparent Optical Data Exchange of 40-Gbit/s DPSK Signals Using Four-Wave-Mixing in a Highly Nonlinear Fiber," Proc. of Optical Fiber Communications Conference (OFC), San Diego, CA, March 2010.

17. Xiaoxia Wu, Antonella Bogoni, Omer F. Yilmaz, Scott R. Nuccio, Jian Wang, and Alan E. Willner, "8-Fold 40-to-320-Gbit/s Phase-Coherent WDM-to-TDM Multiplexing and 320-to-40-Gbit/s Demultiplexing Using Highly Nonlinear Fibers," Proc. of Optical Fiber Communications Conference (OFC), San Diego, CA, March 2010.

18. S. R. Nuccio, O. F. Yilmaz, X. Wang, A. E. Willner, "Experimental Demonstration of All-Optical Polarization Multiplexing and Polarization Demultiplexing between Two 50-Gbit/s Channels and a Single 100-Gbit/s Channel," Proc. of Optical Fiber Communications Conference (OFC), San Diego, CA, March 2010.

19. S. R. Nuccio, O. F. Yilmaz, X. Wu, and A. E. Willner, "Fine Tuning of Conversion/Dispersion Based Optical Delays with a 1-pm Tunable Laser using Cascaded Acousto-Optic Mixing," Optics Letters, Vol. 35, Issue 4, pp. 523-525 (2010).

20. Xiaoxia Wu, Hao Huang, Jian Wang, Xue Wang, Omer F. Yilmaz, Scott R. Nuccio, Alan E. Willner, "Simultaneous Two-Channel Wavelength Conversion of 40-Gbit/s DPSK WDM Signals without Additional Pumps", in OSA CLEO 2010, San Jose, CA.

21. Jian Wang, Omer F. Yilmaz, Scott R. Nuccio, Xiaoxia Wu, Zahra Bakhtiari, Yinying Xiao-Li, Jeng-Yuan Yang, Hao Huang, Yang Yue, Irfan Fazal, Robert W. Hellwarth, Alan E.

Willner, “Data Traffic Grooming/Exchange of a Single 10-Gbit/s TDM Tributary Channel between Two Pol-Muxed 80-Gbit/s DPSK Channels” OSA CLEO 2010, San Jose, CA.

22. S. R. Nuccio, O. F. Yilmaz, X. Wang, J. Wang, X. Wu, and A. E. Willner, "1.16 μs Continuously Tunable Optical Delay of a 100-Gb/s DQPSK Signal Using Wavelength Conversion and Chromatic Dispersion in an HNLF," in OSA CLEO 2010, San Jose, CA.
23. O. F. Yilmaz, S. Nuccio, J. Wang, X. Wu, and A. E. Willner, "Multicasting of 40-Gbit/s NRZ-OOK Data into 24 RZ Copies Using a Single Pump and Supercontinuum Generation," in OSA CLEO 2010, San Jose, CA.
24. S. R. Nuccio, O. F. Yilmaz, X. Wang, H. Huang, J. Wang, X. Wu, and A. E. Willner, “Higher-Order Dispersion Compensation to Enable a 3.6-μs Wavelength-Maintaining Delay of a 100-Gb/s DQPSK Signal,” Optics Letters, Vol. 35, Issue 17, pp. 2985-2987 (2010).
25. Jian Wang, Hao Huang, Xue Wang, Jeng-Yuan Yang, and Alan E. Willner, "Multi-channel 100-Gbit/s DQPSK data exchange using bidirectional degenerate four-wave mixing," Opt. Express 19, 3332-3338 (2011)
26. Antonella Bogoni, Xiaoxia Wu, Scott R. Nuccio, and Alan E. Willner, "640 Gb/s All-Optical Regenerator Based on a Periodically Poled Lithium Niobate Waveguide," J. Lightwave Technol. 30, 1829-1834 (2012)
27. J. Wang, S. R. Nuccio, J. Yang, H. Huang, X. Wu, A. Bogoni, and A. Willner, "50-Gbaud/s Optical Addition and Dual-Directional Subtraction of Quaternary Base Numbers using Nonlinearities and 100-Gbit/s (D)QPSK Signals," in Photonics in Switching, OSA Technical Digest (CD) (Optical Society of America, 2010), post deadline paper PDPWG2.
28. Jian Wang, Scott R. Nuccio, Hao Huang, Xue Wang, Jeng-Yuan Yang, and Alan E. Willner., “Optical data exchange of 100-Gbit/s DQPSK signals”, Optics Express, Vol. 18, Issue 23, pp. 23740-23745 (2010).
29. Jian Wang, Zahra Bakhtiari, Scott R. Nuccio, Omer F. Yilmaz, Xiaoxia Wu, and Alan E. Willner, “Phase-transparent optical data exchange of 40-Gbit/s differential phase-shift keying signals”, Optics Letters, Vol. 35, Issue 17, pp. 2979-2981 (2010)
30. O. F. Yilmaz, J. Wang, S. Khaleghi, S. R. Nuccio, X. Wu, and A. E. Willner, “Pre-Conversion Phase Modulation of Input Differential Phase-Shif-Keying Signals for Wavelength Conversion and Multicasting Applications Using Phase-Modulated Pumps,” Optics Letters, Vol. 36, Issue 5, pp. 731-733 (2011).
31. J. Wang, S. R. Nuccio, X. Wu, O. F. Yilmaz, and A. E. Willner, “Orthogonal Tributary Channel Grooming Exchange of 160-Gbit/s Pol-Muxed DPSK Signal,” Optics Express, Vol. 18, Issue 16, pp. 16995-17008 (2010).
32. A.E. Willner, S.R. Nuccio, “Recent Advances in Tunable Optical Delays and Their Applications”, Invited Paper, Society of Photo-Instrumentation Engineers (SPIE) Photonics West, Conference 7949, paper 7949-7, Jan. 2011, San Jose, CA (SPIE, Bellingham, Wash., 2011).
33. Salman Khaleghi, Omer F. Yilmaz, M. Reza Chitgarha, Irfan M. Fazal, and Alan E. Willner, “80-Gbit/s DQPSK Optical Tapped-Delay-Line Equalization using Finely Tunable Delays, Phases and Amplitudes,” Proc. of Optical Fiber Communications Conference (OFC), Los

Angeles, CA, March 2011.

34. M. R. Chitgarha, S. Khaleghi, Omer F. Yilmaz, Jeng-Y Yang, and A. Willner, "Demonstration of Baud-Rate-Variable and Channel-Spacing-Tunable Demultiplexing of 10-40-Gbaud OFDM Subcarriers using a Multi-Tap Optical DFT," Proc. of Optical Fiber Communications Conference (OFC), Los Angeles, CA, March 2011.
35. S. Nuccio, Z. Bakhtiari, Omer F. Yilmaz, and Alan E. Willner, "Wavelength-Conversion of 160-Gbit/s PDM 16-QAM Using a Single Periodically-Poled Lithium Niobate Waveguide," Proc. of Optical Fiber Communications Conference (OFC), Los Angeles, CA, March 2011.
36. Salman Khaleghi, M. Reza Chitgarha, Omer F. Yilmaz, Alan E. Willner, and Michael Haney, "Experimental Performance of a Continuously Tunable 40-GHz Complex Weight Optical FIR Filter using Wavelength Conversion and Chromatic Dispersion," Accepted for publication to Conference on Lasers and Electro-Optics 2011, Baltimore, May 2011.
37. Mohammad R. Chitgarha, Salman Khaleghi, Omer F. Yilmaz, Alan E. Willner, "Bit Depth and Sample Rate Tunable Digital to Analog Converter using Conversion/Dispersion Based Delays," in 37th European Conference and Exposition on Optical Communications, OSA Technical Digest (CD) (Optical Society of America, 2011), paper We.10.P1.48.
38. Omer F. Yilmaz, Lior Yaron, Salman Khaleghi, M. Reza Chitgarha, Moshe Tur, Alan Willner, "True Time Delays using Conversion/Dispersion with Flat Magnitude Response for Wideband Analog RF Signals," Optics Express, Vol. 20, Issue 8, pp. 8219-8227 (2012).
39. Salman Khaleghi, Mohammad Reza Chitgarha, Omer F. Yilmaz, Moshe Tur, Michael W. Haney, Carsten Langrock, Martin M. Fejer, Alan E. Willner, "Experimental Characterization of Phase Tuning using Fine Wavelength Offset in a Complex-Coefficient Optical FIR Filter," in CLEO: Science and Innovations, OSA Technical Digest (online) (Optical Society of America, 2012), paper CM2B.4, San Jose, CA, May 2012.
40. M. R. Chitgarha, S. Khaleghi, Z. Ma, M. Ziyadi, O. Gerstel, L. Paraschis, C. Langrock, M. M. Fejer, and Alan E. Willner, "Flexible, Reconfigurable Capacity Output of a High-Performance 64-QAM Optical Transmitter," accepted to ECOC 2012.

List of Acronyms, Abbreviations, and Symbols

AM	Amplitude modulation
BER	Bit error ratio
BPF	Band-pass filter
BPSK	Binary phase shift keying
CD	Chromatic dispersion
DAC	Digital to analog converter
DCF	Dispersion compensating fiber
DEMUX	Demultiplexing
DFG	Difference frequency generation
DFT	Discrete Fourier transform
DFWM	Degenerate four wave mixing
DGD	Differential group delay
DLI	Delay line interferometer
DQPSK	Differential quadrature phase shift keying
EVM	Error vector magnitude
FEC	Forward Error Correction
FIR	Finite impulse response
FSR	Free spectral range
FWM	Four wave mixing
HNLF	Highly nonlinear fiber
IIR	Infinite impulse response
IQ	In-phase and quadrature
LCoS	Liquid crystal on silicon
MLL	Mode locked laser
MUX	Multiplexer
MZM	Mach-Zehnder modulator
ODL	Optical delay line
OFDM	Orthogonal frequency division multiplexing
OOK	On-off keying
OSNR	Optical signal to noise ratio

OTDL	Optical tapped-delay-line
PM	Phase modulation
PMD	Polarization mode dispersion
POPS	Parametric Optical Processes and Systems
PPLN	Periodically poled lithium niobate
PRBS	Pseudo-random binary sequence
QAM	Quadrature amplitude modulation
QPM	Quasi-phase matching
QPSK	Quadrature phase shift keying
RZ	Return to zero
SFG	Sum frequency generation
SLM	Spatial light modulator
SMF	Single mode fiber
SPM	Self phase modulation
TDCM	Tunable dispersion compensating module
TDL	Tapped delay line
TSI	Time-slot interchange
XPM	Cross phase modulation
ZDW	Zero dispersion wavelength